

Nanostructured Metal Oxide-Based Microfluidic Biosensors for Point-of-Care Diagnostics

Md. Azahar Ali

A Dissertation Submitted to
Indian Institute of Technology Hyderabad
In Partial Fulfillment of the Requirement for
The Degree of Doctor of Philosophy



भारतीय प्रौद्योगिकी संस्थान हैदराबाद
Indian Institute of Technology Hyderabad

Department of Biomedical Engineering

February, 2014

Declaration

I declare that this written submission represents my ideas in my own words, and where others' ideas or words have been included, I have adequately cited and referenced the original sources. I also declare that I have adhered to all principles of academic honesty and integrity and have not misrepresented or fabricated or falsified any idea/data/fact/source in my submission. I understand that any violation of the above will be a cause for disciplinary action by the Institute and can also evoke penal action from the sources that have thus not been properly cited, or from whom proper permission has not been taken when needed.



(Signature)

MD. AZAHAR ALI

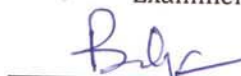
BO11P1002

Approval Sheet

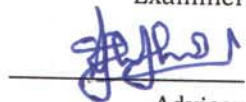
This thesis entitled "Nanostructured Metal Oxide-Based Microfluidic Biosensors for Point-of-Care Diagnostics by Md. Azahar Ali is approved for the degree of Doctor of Philosophy from IIT Hyderabad.



Prof. Soumyo Mukherji
Department of Biosciences and Bioengineering
IIT-Bombay, Powai
Examiner



Prof. B. D. Gupta
Department of Physics
Indian Institute of Technology Delhi, Delhi
Examiner



Adviser
Dr. Renu John
Assistant Professor, Department of Biomedical Engineering
Indian Institute of Technology Hyderabad



Co-Advisers
Prof. Bansi Dhar Malhotra
(Head, Biotechnology Department, Delhi Technological University, Ex Scientist, CSIR-
National Physical Laboratory
(and)

Dr. Ved V. Agrawal
Scientist, CSIR-National Physical Laboratory, New Delhi



Dr. Ashok Kumar Pandey
Assistant Professor, Department of Mechanical Engineering
Indian Institute of Technology Hyderabad
Chairman

Acknowledgements

First and foremost I bow down to divine almighty for providing me inspiration and constant strength to achieve milestones in life which can add meaning to it. Despite only having one name on the cover, this thesis would not have been possible without the input of others whose assistance has been invaluable. I am highly indebted to my supervisors, Prof. Bansi. D. Malhotra, Department of Biotechnology, DTU, Delhi, Dr. Renu John, Biomedical Engineering, IIT Hyderabad, and Dr. Ved V. Agrawal, CSIR-NPL, New Delhi for providing me an opportunity to work under their esteemed guidance. Their scientific perception and friendship are perhaps only surpassed by their courage in allowing me to explore the vast scientific landscape in order to train me as a freethinking independent scientist at the end of the journey. They made me realize that apart from knowing my subject and hard work, I need passion and imagination, to invent and discover. Without their help and support, I would never have been here today.

I would like to express my kind regards to Prof. R. C. Budhani, Director, National Physical Laboratory, New Delhi for taking active interest in my work and providing necessary facilities at CSIR-National Physical Laboratory. I am grateful to Dr. A. M. Biradar, Head, Engineering Material Division and Biomedical Instrumentation Section, National Physical Laboratory, New Delhi for their interest and encouragement at various stages. I would especially like to thank my doctoral committee members; Dr. Ashok Pandey, Dr. Anand Mohan, Dr. Vinod Janardhanan and Dr. Parag D. Pawar for their valuable suggestions and encouragement. I would like to thank Dr. Rajeev Chopra, Head, HRDG group, NPL. I would like to acknowledge Prof. Ashok Mulchandani, University of California, Riverside and Prof. Ashutosh Sharma, IIT Kanpur for the valuable suggestions. I would like to express my gratitude to Dr. G. Sumana, Dr. Pratima R. Solanki, Mr. M. K. Pandey, and Dr. A. Kaushik for their valuable suggestions. I received and their years of hands-on experience. I cannot forget to thank the useful, valuable discussions, help and for their awesome companion on many occasions at the tea stall. I have enjoyed the pleasant working environment at the Biomedical Instrumentation Section, NPL and I would also thank to all my friends for helping me in lab and their kind cooperation.

I have spent my valuable time with my research mates Saurabh Srivastva, Manoj K. Patel, Chandan Singh, Kamil Reza, Chandra Mouli Pandey, Aditya Sharma, Rachna Sharma, Nawab Singh, Shipra Solanki, Mukta Tyagi, Amrita, Dr. Nirmal Prabhakar, Dr. Renu Singh, Dr. Nisha, Dr. Jay Singh, Dr. Manish Singh, Surendra Yadav, Saurabh Kumar, Suveen Kumar, Appan Choudhary and Dr. Pinky Anand. I would like to extend my sincere thanks to all of them to have supported me at every moment. I cannot explain how thankful I am to all my friends Vimal, Hanu, Praveen, Narendra, Manjoosha, Sindhu, Kirtana, Barik, Kunal, Tasleema, Tilak, Mukesh, Sandeep, Mr. K. N. Sood, Mr. Jay, Dr. V. Reddy, Dr. Maumita Chakrabarty, Dr. Zimple Matharu, Dr. Chetna Dhand, Dr. P. Chavhan and Dr. Anjali. I found them always been there for me. No matter where I go, they will always remain in my heart.

I would like to thank my family who has been the cornerstone of my existence. I express my deepest sense of gratitude to all my family members especially my Father, Mother, Brothers and Sisters, who have stayed up nights by my side when I required them.

What more I should say about them, they will always be in my heart. Last but not the least, I would like to acknowledge all the people who made this journey comfortable, enjoyable and marked every moment of time as the source of inspiration and sensation.

I would like to acknowledge the Council of Scientific and Industrial Research for awarding me scholarship to carry out the research work because without their support my work would have remained just a dream. Finally, I would like to thank Allah for giving me the most precious friends and lab members, who loved me unconditionally and stood by my side like a rock. Most importantly, they gave me the space and freedom to flourish.

Md. Azahar Ali

**Dedicated to
my beloved parents, brothers and sisters**

Abstract

The potential research on microfluidic devices for detection of biomolecules has recently intensified due to its application in point-of-care (POC) diagnostics for global health care. Early detection plays an imperative role to determine predisposition to disease (prevention) or the outcome of disease (monitoring and prognosis). There is a significant need for POC diagnostics devices as perceived from biohazard threats, the spread of infectious disease, home testing and monitoring. The POC diagnostics can provide a convenient and immediate response to a patient test sample. The POC diagnostics can be attained via use of transportable, portable, and handheld instruments such as blood glucometer, cholesterol meter etc. and test kits. It includes testing of blood or urine for pathogens, glucose, cholesterol, blood gas, coagulation, biomarkers, hemoglobin, pregnancy etc. Cheaper, smaller, faster, and smarter devices are the main merits of POC diagnostics for detection of various target analytes. A number of clinical biochemical studies such as blood gas, glucose/lactate/cholesterol, nucleic acid sequence analysis, proteins/peptides, combinatorial synthesis, toxicity monitoring, immunoassays, and forensic analysis are also focused areas for developing microfluidic biochips.

Recently, there is an increasing demand to integrate advanced biosensors into “Lab on a chip” systems by introducing microfluidics. Efforts are being made to increase the resolution, accuracy and miniaturization for detection of biomolecules along with microfluidic integrated unit for sample pre-processing. Due to their portability, faster response and flexibility of microfluidic devices, it has the potential to fulfill a number of unmet needs for diagnostics. Microfluidic devices are known to offer important opportunities for modern research, especially for the clinical diagnosis due to their numerous advantages. It is a technology which manipulates minute volumes (from 10^{-6} to 10^{-18} litres) in micron-size channels and containers, becoming so called “Labs on a Chip”. Current research for improving biological assays has yielded a wealth of techniques via miniaturization of existing methods and the development of novel analytical approaches. Presently, the microfluidic devices have become an interesting subject in many academic laboratories for chemical and biological analysis with new physical phenomena which are not accessible in macroscopic labs. Microchannels, microvalves, micropumps etc. are few main components that control fluid flow through the microfluidic devices for POC applications. The POC biosensor consists of a transducer and a bioreceptor element which combines with a signal condition circuit. Some biosensors have been successfully commercialized for POC

application such as blood glucose biosensor. Blood, saliva, urine etc. are the common body fluids used for diagnostics and can be sampled directly from the organs.

Microfluidic chips are also known as laboratory of microfluidic chips, which can be used for synthesis of materials, sample preparation, reaction, separation, detection and cell culture and sorting. It offers various advantages such as very low reagent/sample consumption, and waste generation, fast reaction times, high reaction efficiency and a large surface to volume ratio. Miniaturization of these devices can increase throughput and allows multiplexing platform and massive parallelization for integration of several assays analyses. The 'microfluidically' produced result from these the medical decision making devices can bring precision to the art of medical diagnostics. Therefore, microfluidics has received much more attention from the researchers in recent years.

Nanomaterials are experiencing a rapid development in recent years due to their potential applications in the field of electronics, catalysis, ceramics, magnetic data storage, structural components, biomaterials and biosensors. Nanostructured metal oxides show increased surface-to-volume ratio, chemical activity, mechanical strength, electrocatalytic properties and enhanced diffusivity. Nanostructured materials involve the tailoring of materials at atomic level to attain unique properties, which can be suitably manipulated for desired applications. The nanostructured metal oxides such as titania (TiO_2), silica (SiO_2), iron oxide (Fe_3O_4), cerium oxide (CeO_2), zinc oxide (ZnO), zirconia (ZrO_2), nickel oxide (NiO) etc. are widely used to fabricate electrochemical biosensors. Utilization of these nanostructured materials has been found to enhance the biosensor sensitivity, selectivity, detection limit and reproducibility. In particular, the biofunctionalization of these materials could provide excellent electrocatalytic properties. In biosensor fabrication, the method of immobilization of desired biomolecules onto a biocompatible and electroactive electrode is generally the first and major concern. A successful nano-matrix can be an excellent candidate to immobilize or integrate biomolecules on transducer surface and efficiently maintain the functionality of the biomolecules. There are still challenges such as miniaturization, automation and integration of the nanostructured-based biosensors to microfluidics. Utilization of nanoparticles, nanotubes and nanowires in microfluidic assembly is currently of much interest for injection, separation, and detection. The small volumes and short reaction length may allow a sensitive detection. Their integration with a microfluidic platform through a combination of microfabrication and nanomaterial synthesis allows unique functionality to the device. Using these smart integrated microfluidic systems, many advances have been achieved for electrochemical and optical detection of

biomolecules such as antigens, enzymes, antibodies, DNA hybridization and oligonucleotides. Thus, nanostructured materials and the carbon composite can be used to enhance the biosensing signal. This thesis focuses on improving the detection limits, selectivity and sensitivity using nanomaterials in the most common detection techniques in microfluidics, i.e., electrochemistry, and electronic detection.

Coronary artery disease is one of important issue that has been found to cause human deaths in all developed countries. Recently, the risks of high blood cholesterol levels have increased worldwide. The high blood cholesterol levels may lead to cardiovascular diseases including arteriosclerosis. The atherosclerosis is known to be a critical condition in which arteries becomes blocked due to the accumulation of cholesterol. Deposition of cholesterol on the walls of arteries can form plaques resulting in blockages and interruption of the blood circulation that can cause angina and myocardial infarction. Thromboembolism can occur due to the bursting of these plaques. Hence, cholesterol has become one of the important parameter for POC testing. Lipids are not soluble in water and allow sufficient transport of cholesterol and other lipids called lipoproteins. The four major categories of lipoprotein are known as chylomicron (CM), low density lipoprotein (LDL), very low-density lipoprotein (VLDL) and high density lipoprotein (HDL). There is a significant interest for POC diagnostics applications using Lab-on-a-chip, and microfluidic devices to detect desired target analytes or biomolecules such as free cholesterol, total cholesterol, low density lipoprotein etc. in human blood.

Electrochemical detection technique has become an attractive technique for POC biosensor devices due to label-free detection and higher signal to noise ratio resulting in high sensitivity and excellent selectivity. Besides these, the electrochemical detection offers numerous advantages such as easy detection, low cost, low-power requirements, inherent miniaturization, portability, and high degree of compatibility with advanced micromachining technologies. These properties allow electrochemical detection enormously suitable to be integrated with miniaturized microfluidic systems. However, the sluggish heterogeneous electron transfer rates in electrochemical detection of some materials on transducer surface may lead to decreased sensitivity with time. This thesis shows some aspects on the fabrication of low cost nanostructured metal oxides like anatase-TiO₂, NiO and chitosan-TiO₂, carbon nanotubes-NiO composites based microfluidic devices for free/total cholesterol and LDL detection. The major role of nanostructures materials in these microfluidic devices are the immobilization or functionalization of enzymes and antibodies on its microfluidic transducer surface. The nanomaterials used as microfluidic electrodes

can overcome these problems because of their very high surface area may lead to higher stability and large amperometric currents. Several methods are available for the estimation of cholesterol, LDL etc. in clinical laboratories such as ultracentrifugation, nuclear magnetic resonance (NMR) spectroscopy, electrophoresis, chromatography, Friedewald method etc. These techniques are tedious, expensive, time consuming and have lesser reproducibility and hence are not desirable in clinical laboratories. Additionally, the accuracy/precision is the major limitation of these methods. In order to develop efficient detection strategies for cholesterol, LDL etc., the POC microfluidic biosensors are very attractive choice towards clinical health-care.

Chapter 1 gives an overview of the importance of POC diagnostics with microfluidic-based biosensors for detection of biomolecules. First part of thesis gives an introduction to POC biosensors with its merits and demerits as reported in research literature. A historical background of microfluidic devices with its current research activities has been pictured. A brief description relating to the suitable materials used for microfluidic fabrication has been given. Particularly, utilization of nanostructured metal oxides and carbon materials for attachment of biomolecules and their integration with microfluidic assembly have been described. Besides this, efforts have been made to discuss the possible aspects for suitable detection strategies using microfluidic assembly to improve biosensor efficacy in terms of sensitivity, selectivity and stability compared to that of other methods. Electrochemical-based biosensors and their integration to microfluidic biochips for detection of various biomolecules such as cholesterol, LDL etc. have been described. The importance of cholesterol and LDL detection in human blood serum using microfluidic technique and their advantages and disadvantages has been explained. The motivation of the work relating to construction of the microfluidic system towards POC diagnostics has been highlighted. The first chapter concludes with an overview of the entire thesis.

Chapter 2 deals with basic principles construction of microfluidic devices such as fluidic transports, scaling effect, diffusion, mixing etc. Various components and materials for microfluidic devices have been explained in this chapter. Besides this, the principle, characteristics and various types of biosensors have been demonstrated. A brief literature survey on biosensor has been presented. Significant features in design of biosensors construction have been explained. The electrochemical technique and various immobilization processes for microfluidic biosensor fabrication have been illustrated. In particular, the efforts have been made to focus on utilization of nanomaterials in POC biosensor with appropriate references to existing research literature. The importance and applications of synthesized nanostructured metal oxides such as TiO_2 , NiO and their

nanocomposites with chitosan and carbon nanotubes (CH-TiO₂ and CNT-NiO) in microfluidic biosensors have been included in this chapter. The importance and prospects of cholesterol and lipid profile in human serum samples have also been explained. Salient features of enzyme, antibodies etc. used for fabrication of electrochemical cholesterol and LDL detection systems have been described.

Chapter 3 gives a broad overview of various materials, fabrication and characterization techniques that has been adopted in this thesis for the development of microfluidic biosensors. In this chapter, attempts have been made to give details for fabrication of PDMS microchannels using various steps of soft lithography. The description of how patterned microelectrodes (indium tin oxide; ITO) can be fabricated using wet chemical etching and photolithography techniques has been given. An overview of the chemical synthesis of nanomaterials has also been included. The sol-gel synthesis of anatase-TiO₂ and its composite with chitosan has been discussed. The co-precipitation synthesis of NiO, chemical vapor deposition of CNTs synthesis and its composite with carbon nanotubes are explained in this chapter. The synthesized nanoparticles, composites based electrodes or bioelectrodes have been characterized using various spectroscopic and microscopic techniques. Details of spectroscopic techniques such as UV-visible (UV-vis), X-ray diffraction (XRD), Fourier transform infrared (FT-IR), Raman, Zeta potential and X-ray photoelectron are described. The principles of different microscopic techniques such as scanning electron microscopy (SEM), atomic force microscopy (AFM) and transmission electron microscopy (TEM) that are used to characterize the electrodes/bioelectrodes have described in this chapter. Electrochemical studies such as cyclic voltammetry, chronoamperometry, chronocoulometry and impedance spectroscopy techniques have been illustrated. Finally, efforts have been made to discuss the basics of chronoamperometric (CA), cyclic voltammetry (CV) and impedance spectroscopy (EIS) that were employed to characterize the developed microfluidic biosensor devices.

Chapter 4 describes the experiments and results relating to the fabrication of nanostructured anatase-TiO₂ based microfluidic platform for free cholesterol estimation. I have highlighted the role of anatase-TiO₂ in the microfluidic system. The results of XRD, FT-IR, UV-Vis AFM and TEM of this integrated microfluidic system have been described. The electrochemistry of the fabricated microfluidic biochip has been observed using EIS and CV studies. The desired flow rate of cholesterol solution through the channel has been optimized by tuning flow rate with the help of a syringe pump. Finally, free cholesterol

concentration (0.64–10.3mM) has been estimated using electrochemical technique. This microfluidic system shows excellent sensitivity, reproducibility and selectivity.

In order to improve the adsorption capability of biomolecules on microfluidic transducer surface, a better candidate, chitosan modified TiO₂ nanoparticles has been utilized to monitor total cholesterol. The Brunauer–Emmett–Teller (BET) studies are used to quantify the specific surface area and pore size distribution of titania nanoparticles before and after chitosan incorporation. The bienzyme functionalized mesoporous anatase titania-chitosan (antTiO₂-CH) nanocomposite has been characterized using electron microscopy, UV-visible, FT-IR and XPS. The electrochemistry for effective electrochemical area, surface coverage, flow rate etc. has been investigated using CV, EIS and chronoamperometric techniques. Finally, esterified cholesterol has been detected using EIS spectroscopic technique. Results of the proposed nanocomposite (antTiO₂-CH) based microfluidic biosensor have been described.

Chapter 5 deals with studies relating to nickel oxide nanorods (NR-NiO) integrated with microfluidic device for total cholesterol detection. I have focused to describe the importance and role of nanostructured NiO to develop the microfluidic biosensor. Results relating to the confirmation of synthesized materials (NR-NiO) have been illustrated using various microscopic and spectroscopic techniques. The electrochemical characterization of the proposed microfluidic device has been carried out using CV and EIS. Finally, the total cholesterol concentration has been estimated using this proposed microfluidic device. Potential merits and demerits of this microfluidic biosensor have been explained. In conclusion, the nanostructured NiO has been found to be an interesting material for the integration with microfluidic system as well as biomolecules attachment. However, there are still considerable challenges to be addressed improving in the biosensing characteristics for cholesterol and LDL detection in microfluidic system. Thus, efforts have been made to form a composite material with carbon nanotubes and nanostructured NiO for fabrication of microfluidic biosensor, which is the topic of research for next chapter.

Chapter 6 covers the step by step fabrication process of a novel microfluidic nanobiochip based on a composite comprising of nanostructured NiO and carbon nanotubes (CNTs), as well as the biochip's use for total cholesterol estimation. This chapter contains the overview relating to the application of CNT and its nanocomposite with NiO for microfluidic biosensor development. The fabrication of the microfluidic biochip using CNT-NiO nanocomposite has been demonstrated. The biochip is immobilized with a bienzyme, composed of cholesterol esterase and cholesterol oxidase, and integrated with PDMS

microchannels. Additionally, this chapter includes results of experiments on toxicity effect of these synthesized CNTs, NiO nanoparticles and CNT-NiO in A549 cell line and the characterization of the CNT-NiO nanocomposite using XRD, Raman and XPS. The morphological studies have been investigated using SEM and TEM techniques. The electrostatic interaction between NiO and CNTs has been confirmed using Zeta potential measurement. The electrochemical properties of this proposed microfluidic biochip have been investigated using CV and EIS studies. The chronoamperometric response of the biochip has been measured as a function of the cholesterol oleate concentration. This Chapter also demonstrates an impedimetric-Lab on a chip (*i*LOC) immunosensor for the label-free detection of blood low density lipoprotein (LDL) using this synthesized CNT-NiO nanocomposite material. The studies relating to fabrication of a biosensing platform for LDL concentration detection have also been described. In order to measure electrode surface areas, diffusion coefficients and charges with respect to time and the mechanisms and rate constants for chemical reactions coupled to electron transfer reactions, the chronocoulogram (CC) have been carried out for various electrodes at same step potential. Electrochemical impedance properties of the proposed *i*LOC and potentials optimization for biosensing have been investigated. Finally, the impedimetric response for the *i*LOC as a function of LDL concentration has been carried out. This platform is also suitable to observation and studying the antibody-antigen interactions on this transducer surface.

Chapter 7 summarizes the work reported in this thesis and highlight the major conclusions derived from various experimental reported in this thesis. A careful analyses of future prospects of this work towards a practical microfluidics-based POC sensor realization has been analysed. Detection of multi-analytes such as LDL, VLDL, HDL, cholesterol and triglyceride based on this microfluidic system is one of the potential challenges that can be realized with minor modifications. Future direction towards fabrication of electrode arrays and selective deposition of biofunctionalized nanomaterials could be easily feasible with recent advances in microfabrication technology. Advances in microfluidic technologies have provided an exciting opportunity to integrate photonics and microfluidic at micron-size scales to leverage the combined advantages resulting in a totally new area of research termed as optofluidics. New possibilities towards POC applications can be realized using a microscope in combination with optofluidic channels.

Nomenclature

POC: Point-of-care
 μ TAS: Micro total analysis systems
LOC: Lab-on-a-chip
DNA: Deoxyribonucleic acid
PNA: Peptide nucleic acid
HIV/AIDS: Human immunodeficiency virus/ Acquired immunodeficiency syndrome
PDMS: Polydimethylsiloxane
GC: Chromatographic
IBM: International business machine
MEMS: Microelectromechanical system
BioMEMS: Biological microelectromechanical system
PCR: Polymerase chain reaction
RT-PCR: Real time- polymerase chain reaction
cm: Centimetre
 μ m: Micrometre
mm: Millimetre
nm: Nanometre
IUPAC: International union of pure and applied chemistry
SPR: Surface plasmon resonance
SWCNT: Single walled carbon nanotube
MWCNT: Multiwalled carbon nanotube
CdSe: Cadmium selenide
Au: Gold
 H_2O_2 : Hydrogen peroxide
SARS: Acute respiratory syndrome
 In_2O_3 : Indium oxide
CNT: Carbon nanotube
fm: Femtomolar
mM: Millimolar
nM: Nanomolar
A: Ampere
nA: Nanoampere
mA: Milliampere
 μ A: Microampere
mV: Millivoltage
V: Voltage
NP: Nanoparticles
CH: Chitosan
ZnO: Zinc oxide
NMOx: Nanostructured metal oxides
 TiO_2 : Nanostructured titania
Ant: Anatase
NiO: Nickel oxide
NR-NiO: Nickel oxide nanorods
 SiO_2 : Silica
 Fe_3O_4 : Iron oxide
 CeO_2 : Cerium oxide
 ZrO_2 : Zirconia
 Al_2O_3 : Aluminum oxide
 CeO_2 : Cerium oxide

MgO: Magnesium oxide
 Fe₃O₄: Iron oxide
 BaO: Barium oxide
 CuO: Copper oxide
 V₂O₅: Vanadium oxide
 CHD: Coronary heart disease
 CEs: Cholesterol esters
 PLs: Phospholipids
 TGs: Triglycerides
 ChEt: Cholesterol esterified
 ChOx: Cholesterol oxidase
 AAB: Anti-apolipoprotein B 100
 CM: Chylomicron
 LDL: Low density lipoprotein
 VLDL: Very low-density lipoprotein
 HDL: High density lipoprotein
 NCEP: National cholesterol education program
 ITO: Indium tin oxide
 XRD: X-ray diffraction
 FT-IR: Fourier transform infrared
 BET: Brunauer–Emmett–Teller
 UV-vis: Ultraviolet visible
 AFM: Atomic force microscopy
 TEM: Transmission electron microscopy
 XPS: X-ray photoelectron
 SEM: Scanning electron microscopy
 FE-SEM: Field emission- scanning electron microscopy
 CV: Cyclic voltammetry
 CA: Chronoamperometry
 EIS: Electrochemical impedance spectroscopy
 NMR: Nuclear magnetic resonance
 RIA: Radio immuno assay
 ρ : Density of the fluid
 μ : Dynamic viscosity of the fluid
 ∇ : Napla operator
 $v(u,v,w)$: Velocity vector
 $\frac{D}{Dt}$: Total derivative operator
 U: Average flow velocity
 L: Characteristic length
 R_e : Reynolds-number
 K_n : Knudsen number
 λ : Mean free path
 S: Scaling factor
 PMMA: Polymethylmethacrylate
 PC: Polycarbonate
 SAM: Self assembled monolayer
 ISFET: Ion-sensitive field effect transistor
 BioFET: Biological-field effect transistor
 ss: Single-strand
 3D: Three-dimensional
 2D: Two-dimensional

1D: One-dimensional
 IEP: Isoelectric point
 ChOx: Cholesterol oxidase
 GOx: Glucose oxidase
 HRP: Horseradish peroxidase
 IgG: Immunoglobulin G
 Urs: Urease
 AutoCAD: Auto computer-aided design
 HCl: Hydrochloric acid
 HNO₃: Nitric acid
 H₂O: Water
 BSA: Bovine serum albumin
 NHS: N-hydroxysuccinimide
 EDC: N-ethyl-N0-(3-dimethylaminopropyl carbodiimide)
 EDTA: Ethylenediaminetetraacetic acid
 KOH: Potassium hydroxide
 TGA: Thioglycolic acid
 DMSO: Dimethyl sulfoxide
 CVD: Chemical vapor deposition
 NIR: Near infra-red
 FWHM: Full width at half maximum
 PGSTAT: Potentiostat/galvanostat
 CE: Counter electrode
 WE: Working electrode
 RE: Reference electrode
 DA: Differential amplifier
 CF: Current follower
 Q: Charge
 t: Time
 ω : Radial frequency (radians/s)
 f: Frequency
 CPE: Constant phase element
 C_{dl}: Double layer capacitance
 k_f : Forward electron-transfer rate constant
 k_b : Backward electron-transfer rate constant
 k₀: Electron transfer rate
 τ : Time constant
 R: Gas constant,
 T: Temperature
 N: Electron transferring constant of the redox couple,
 F: Faraday constant
 C: Concentration of the redox couple in the bulk solution
 R_s: Electrolyte
 R_{CT}: Charge-transfer resistance
 ET: Electron transfer
 Z_w: Warburg impedance
 IHP: Inner Helmholtz plane
 OHP: Outer Helmholtz plane
 C_o: Concentration of oxidant at the electrode surface
 C_o^{*}: Concentration of oxidant in the bulk
 C_R: Concentration of reductant at the electrode surface,

η : Overpotential
 α : Reaction order
 A_{ec} : Electrochemical surface area,
eV: Electron volt
PBS: Phosphate buffer saline
 μ L: Microlitre
mL: Millilitre
nL: Nanolitre
mg: Milligram
 μ g: Microgram
mg: Milligram
dL: Decilitre
Pa: Pascal
 ΔP : Pressure difference
w: Width
SNR: Signal to noise ratio
NaCl: Sodium chloride
 δ : Depression angle
MTT: Methyl thiazol tetrazolium
RPMI: Rosewell Park Memorial Institute
AVEDEV: Average deviation
TO: Transverse optical
LO: Llongitudinal optical
Ni: Nickel
fcc: Face-centered cubic
FAD: Flavin adenine dinucleotide
Hb: Hemoglobin

Contents

Declaration.....	ii
Approval Sheet	iii
Acknowledgements.....	iv
Dedication.....	ivi
Abstract.....	vii
Nomenclature	xixiv
Chapter 1: Introduction and Overview	1
1.1 Point-of-care diagnostics	3
1.2 A historical snapshot of microfluidics devices	5
1.3 State-of-the-art biosensors	12
1.4 Integration of nanomaterials with microfluidics	15
1.5 Importance of cholesterol	17
1.6 Motivation of the work	21
1.7 Objectives of the thesis	21
1.8 Thesis overview	22
1.9 Conclusions.....	24
Chapter 2: Principles of microfluidics, biosensors and applications of nanostructured metal oxides.....	25
2.1 Introduction	27
2.2 Principle of microfluidics	27
2.2.1 Governing equations.....	27
2.2.2 Reynolds number and laminar flow.....	28
2.2.3 Turbulent flow	30
2.2.4 Turbulent flow	30
2.2.5 Pressure driven flow	30
2.2.6 Scaling effects	31
2.2.7 Capillary flow.....	31
2.2.8 Diffusion and mixing.....	32
2.2.9 Electrokinetics	32
2.3 Components of microfluidic devices	34
2.4 Materials for microfluidic devices	34
2.5 Biosensors.....	36
2.5.1 Characteristics of biosensors	39

2.5.2	Electrochemical biosensor	39
2.5.3	Amperometric/potentiometric biosensor	39
2.5.4	Impedimetric/capacitive biosensor	40
2.5.5	Optical biosensor	41
2.5.6	Piezoelectric sensor	41
2.5.7	Enzymatic biosensor.....	41
2.5.8	Immunosensor	43
2.5.9	Nucleic acid biosensor.....	46
2.6.0	Whole cell biosensor	46
2.7	Immobilization of biosensors.....	46
2.8	A brief literature survey of nanostructured metal oxides.....	49
2.8.1	Titanium dioxide	50
2.8.2	Nickel oxide	51
2.8.3	Carbon nanotubes	53
2.9	Conclusions.....	55
Chapter 3: Materials and Experimental Techniques		57
3.1	Introduction.....	59
3.1.1	Fabrication of PDMS microchannels	59
3.1.2	Mask fabrication.....	60
3.1.3	SU-8 photoresist	60
3.1.4	Exposure	60
3.1.5	Post exposure bake	61
3.1.6	Development	61
3.1.7	PDMS molding.....	61
3.1.8	Precautions	64
3.2	Wet chemical etching.....	64
3.2.1	ITO ($\text{In}_2\text{O}_3:\text{SnO}_2$) etching by chemical process	64
3.2.2	ITO etching using photolithography.....	64
3.3	Chemical synthesis of nanomaterials.....	65
3.3.1	Sol gel method.....	66
3.3.2	Chemical and reagents.....	67
3.3.3	Sol-gel synthesis of anatase- TiO_2	67
3.3.4	Synthesis of chitosan and anatase- TiO_2 composite	69
3.3.5	Co-precipitation method.....	70
3.3.6	Co-precipitated synthesis of nNiO	70

3.3.7	Synthesis of carbon nanotubes	71
3.3.8	Synthesis of CNT-NiO composite.....	71
3.4	Characterization techniques	72
3.4.1	UV-Vis spectroscopy.....	72
3.4.2	Fourier transform infrared spectroscopy	73
3.4.3	Raman spectroscopy	75
3.4.4	X-ray diffraction.....	75
3.4.5	Scanning electron microscopy.....	76
3.4.6	Transmission electron microscopy	78
3.4.7	Atomic force microscopy	78
3.4.8	Zeta potential and BET studies.....	79
3.4.9	X-ray photoelectron spectroscopy	81
3.5.0	Electrochemical techniques	81
3.5.1	Electrochemical cell	81
3.5.2	Cyclic voltammetry	83
3.5.3	Chronoamperometry and chronocoulometry.....	86
3.5.4	Impedance spectroscopy.....	88
3.4	Conclusions.....	92

Chapter 4, Part I: Nanostructured anatase-TiO₂ based microfluidic platform for free cholesterol estimation93

4.1	Introduction.....	95
4.2.0	Experimental section	96
4.2.1	Fabrication of microfluidic biosensing platform	96
4.2.2	Precautions	97
4.3	Result and discussions	97
4.3.1	X-ray diffraction studies.....	97
4.3.2	UV-Visible studies	98
4.3.3	FT-IR studies.....	98
4.3.4	AFM studies	101
4.3.5	TEM studies	101
4.3.6	EIS studies	101
4.3.7	CV studies	102
4.3.8	Scan rate studies	102
4.3.9	Effect of diffusion.....	102
4.4.1	Effect of pH.....	103

4.4.2	Estimation of microfluidic parameters	104
4.4.3	Estimation of free cholesterol.....	104
4.4.4	Selectivity studies.....	105
4.4.5	Potential merits and demerits of this fabricated microfluidic.....	107
4.4.6	Conclusions	108
Part II: Mesoporous titania-chitosan nanocomposite based microfluidic biochip for total cholesterol detection		110
4.5	Introduction.....	110
4.5.1	Biosensing platform.....	111
4.6	Results and discussions.....	114
4.6.1	UV-visible, FT-IR, Raman and BET surface analysis	114
4.6.2	XPS studies.....	117
4.6.3	Morphological studies	119
4.6.4	Cyclic voltammetric studies	120
4.6.5	Chronoamperometric studies.....	122
4.6.6	EIS studies	122
4.6.7	Impedance response studies	125
4.6.8	Reproducibility studies.....	127
4.6.9	Effect of stability and specificity.....	127
4.7.0	Potential merits and demerits	130
4.8	Conclusions.....	130
Chapter 5: Highly efficient microfluidic biochip based on nanostructured nickel oxide.....		133
5.1	Introduction.....	135
5.2	Experimental section.....	136
5.2.1	Fabrication of microfluidic biosensor.....	136
5.2.2	Precautions	137
5.3	Results and discussions.....	138
5.3.1	XRD studies	138
5.3.2	Raman studies.....	138
5.3.3	FT-IR studies.....	140
5.3.4	TEM studies	140
5.3.5	Electrochemical characterization.....	141
5.3.6	Scan rate studies	142
5.3.7	Effect of flow rate.....	143

5.3.8	Electrochemical response studies	143
5.3.9	Effect of interferents, stability and reproducibility	147
5.4.0	Potential merits and demerits of this microfluidic biosensor	148
5.5	Conclusions.....	149
Chapter 6: Microfluidic biochip based on CNT-NiO nanocomposite cholesterol estimation.....		151
6.1	Introduction.....	153
Part I: CNT-NiO nanocomposite-based biochip for total cholesterol estimation		155
6.2.0	Experimental.....	155
6.2.1	Cell proliferation studies.....	155
6.2.2	Fabrication of microfluidic biochip platform.....	156
6.3	Results and discussions.....	158
6.3.1	XRD studies.....	158
6.3.2	Raman studies	158
6.3.3	XPS studies.....	159
6.3.4	Zeta potential studies.....	161
6.3.5	Cytotoxicity studies	163
6.3.6	Morphological studies analysis.....	165
6.3.7	Electrochemical properties	167
6.3.8	Chronoamperometric response studies	171
6.3.9	Reproducibility studies	174
6.4.0	Selectivity and stability studies.....	174
6.5	Conclusions.....	175
Part II: CNT-NiO nanocomposite based impedimetric-Lab on a chip for LDL detection.....		176
6.6	Biosensing platform.....	176
6.7	Results and discussions.....	176
6.7.1	FT-IR studies.....	176
6.7.2	UV-Vis studies	177
6.7.3	Chronocoulometric studies.....	178
6.7.4	Electrochemical impedance properties of <i>i</i> LOC.....	180
6.7.5	Impedimetric response of <i>i</i> LOC.....	183
6.7.6	Selectivity and stability studies.....	184

6.7.7	Potential merits of this fabricated microfluidic platform	184
6.8	Conclusions.....	185
Chapter 7: Summary of the work and future prospects		187
7.1	Summary of the work.....	189
7.2	Future prospects	193
Figures		
1.1	Historical snapshot of microfluidics technology with time	6
1.2	The length scales of microfluidic device and biological based micro-fabrication....	8
1.3	The chemical formula of (a) cholesterol (free), and (b) cholesteryl ester.....	17
1.4	(i) The structure of lipoprotein molecule and (ii) LDL particle model.....	18
2.1.1	Microfluidic platforms classified according to main liquid propulsion principle...	29
2.1.2	Schematic description the fluids flow for (a) laminar and (b) turbulent.....	29
2.1.3	Schematic representation of a typical pressure-driven fluid flow.....	33
2.1.4	Schematic of the configuration of charges in a channel under electroosmotic conditions showing the mobile charges the diffusive and fixed charges in the Stern layer.....	33
2.1.5	Main components of biosensor	38
2.1.6	Schematic representation of (i) a three electrode based microfluidic biosensor and (ii) a typical biosensor	38
2.1.7	Schematic representation of reactions used in enzymatic biosensors such as (i) catalytic conversion of glucose into gluconic acid in the presence of potassium ferricyanide. At the surface of electrode, electron generated by conversion of Fe (II) to Fe (III), (ii) catalytic conversion of glucose into gluconic acid and H ₂ O ₂ thereafter electron generation by electrochemical oxidation, (iii) biochemical reaction of urea biosensor and (iv) biochemical reaction of cholesterol biosensor	43
2.1.8	Schematics presentation of an antibody	45
2.1.9	Immunological reaction	45
2.2.0	Various immobilization techniques for biosensor construction.....	48
2.2.1	Different NMOx and their biosensing applications	52
2.2.2	(i) The principle of CNT construction from graphene sheet along the chiral vector \vec{C} and (ii) MWCNT	54
3.1.1	Schematic representation of step by step PDMS microchannel fabrication using SU 8 negative photoresist	62
3.1.2	(a) After exposing the photoresist pattern on Si wafer (negative and positive tone) and (b) chemical structure of SU 8	62
3.1.3	Photograph of a PDMS microchannel	63
3.1.4	ITO patterning via wet chemical etching process.....	63
3.1.5	Schematic representation of the crystalline structure of TiO ₂	68

3.1.6 Chemical structure of chitosan	69
3.1.7 (i) The absorption spectra of Cys-CdS quantum dots using UV-visible spectrophotometer model, Perkin Elmer, Lambda 950	74
3.1.8 (i) Schematic diagram of the operation of FT-IR, Perkin-Elmer, Model 2000 and (ii) FT-IR spectra of reduced graphene oxide film.....	74
3.1.9 (a) Energy level diagram for Raman spectroscopy. The shift in wavelength between the excitation light (λ_e) and the scattered light (λ_s) is related to Raman shift (ΔV in cm^{-1}) according to: $\Delta V = (1/\lambda_e) + (1/\lambda_s)$. (b) Raman spectra of pristine CNTs and COOH functionalized CNTs.....	77
3.2.1 Bragg diffraction.....	77
3.2.2 (A) TEM instrument (TEM, JEOL JEM-2000 EX) and (B) TEM image of gold nanoparticles.....	80
3.2.3 (i) Schematic representation of zeta potential and (ii) XPS of the C1s region of rGO deconvoluted into characteristic peaks	80
3.2.4 Electrochemical cell circuit for electrochemical measurement	82
3.2.5 (i) Input signal or excitation signal for CV measurement and (ii) output signal of a CV.....	84
3.2.6 Electrochemical system that includes electron transfer along with its Randles equivalent circuit	84
3.2.7 CV studies of various fabricated electrodes such as (a) NiO/ITO, (b) NiO-CdS/ITO and (c) AAB/NiO-CdS/ITO.....	86
3.2.8 (i) Current vs. time for chronoamperometric measurement and (ii) charge vs. time for chronocoulometric studies	87
3.2.9 Chronoamperometric response of rGO/ITO electrode have been conducted in PBS, 50 mM, pH 7.0, 0.9% NaCl at the potential -0.3 V	88
3.3 A Nyquist plot of EIS measurement.....	91
3.3.1 EIS spectra of various electrodes in PBS solution (50 mM, pH 7.4, 0.9% NaCl) containing 5 mM $[\text{Fe}(\text{CN})_6]^{3-/4-}$	91
4.1.1 Pictorial representation of the microfluidic system for cholesterol detection.....	97
4.1.2 XRD spectrum of TiO_2 powder and (b) UV-visible spectra of ant-TiO ₂ /ITO film.....	99
4.1.3 FT-IR studies of (a) ant-TiO ₂ /ITO and (b) ChOx/ant-TiO ₂ /ITO.....	99
4.1.4 (a) AFM images for ant-TiO ₂ /ITO electrode and (b) AFM for ChOx/ant-TiO ₂ /ITO bioelectrode	100
4.1.5 Histogram plot for average size of ant-TiO ₂ nanoparticles	100
4.1.6 (a) (i) EIS studies of (a) ant-TiO ₂ /ITO electrode and ChOx/ant-TiO ₂ /ITO bioelectrode, (ii) The CV of (a) ant-TiO ₂ /ITO electrode and (b) ChOx/ant-TiO ₂ /ITO bioelectrode at scan rate (30 mV/s) in PBS (50 mM, pH 7.0, 0.9% NaCl) containing 5mM $[\text{Fe}(\text{CN})_6]^{3-/4-}$	101

4.1.7 (i) CV of ChOx/ <i>ant</i> -TiO ₂ /ITO bioelectrode as a function of scan rate in PBS (50mM, pH 7.0, 0.9% NaCl) containing 5mM [Fe(CN) ₆] ^{3-/4-} and (ii) CV for different flow rates (0-50μL/min) as a function of flow rate [inset: Diffusivity for <i>ant</i> -TiO ₂ /ITO electrode]	103
4.1.8 CV of ChOx/ <i>ant</i> -TiO ₂ /ITO bioelectrode as a function of pH of the buffer solution (inset: plot between the current response and pH of solution).....	104
4.1.9 (a) CV curves of ChOx/ <i>ant</i> -TiO ₂ /ITO bioelectrode at different cholesterol concentration, (b) linear plot of response studies of ChOx/ <i>ant</i> -TiO ₂ /ITO bioelectrode as a function of cholesterol concentration (50–400 mg/dl and (c) CV curves of ChOx/ <i>ant</i> -TiO ₂ /ITO bioelectrode in presence of interferents studies. (d) Shows current responses of various interferents	106
4.2.0 a) Reproducibility studies for different bioelectrodes at same flow rate and (b) stability studies of the ChOx/ <i>ant</i> -TiO ₂ /ITO bioelectrode (inset: current response vs days).....	107
4.2.1 Functionalization of bienzyme onto <i>ant</i> TiO ₂ -CH surface for cholesterol detection.....	113
4.2.2 3D optical profilometric image for (a) ITO on glass film, (b) <i>ant</i> TiO ₂ -CH film on ITO.....	114
4.2.3 A photograph of the fabricated microfluidic biochip	114
4.2.4 (i) UV visible spectra of chitosan (a), <i>ant</i> TiO ₂ nanoparticles (b) and <i>ant</i> TiO ₂ -CH (c), (ii) FT-IR spectra of (a) <i>ant</i> TiO ₂ film, (b) <i>ant</i> TiO ₂ -CH/ITO and (c) ChEt-ChOx/ <i>ant</i> TiO ₂ -CH/ITO film. (iii) Raman spectra of TiO ₂ and <i>ant</i> TiO ₂ -CH showing pure anatase phase. (iv) The N ₂ adsorption and desorption isotherms of <i>ant</i> -TiO ₂ nanoparticles, inset shows the pore size distribution of <i>ant</i> -TiO ₂ nanoparticles	116
4.2.5 (i) Wide scan XPS of various films, (ii) XPS spectra of the C1s region of <i>ant</i> TiO ₂ -CH film after deconvolution, (iii) the C1s region of ChEt-ChOx/ <i>ant</i> TiO ₂ -CH film, (iv) N 1s core level spectra of <i>ant</i> TiO ₂ -CH film and (v) N 1s core level spectra of ChEt-ChOx/ <i>ant</i> TiO ₂ -CH film	118
4.2.6 (a) FE-SEM image of <i>ant</i> TiO ₂ nanoparticles and (b) <i>ant</i> TiO ₂ -CH. (c) FE-SEM image of <i>ant</i> TiO ₂ -CH film with enzyme immobilization	120
4.2.7 (i) CV of (a) <i>ant</i> TiO ₂ -CH/ITO electrode and (b) ChEt-ChOx/ <i>ant</i> TiO ₂ -CH/ITO bioelectrode in PBS solution (50 mM, pH 7.0, 0.9% NaCl) containing 5 mM [Fe(CN) ₆] ^{3-/4-} , (ii) CV of ChEt-ChOx/ <i>ant</i> TiO ₂ -CH/ITO bioelectrode as a function of scan rate [20-160 (mV/s)] in ascending order, inset: anodic and cathodic peak current vs (scan rate mV/s) ^{-1/2} , (iii) CA response current vs flow rate (μL/min) of (a) <i>ant</i> TiO ₂ -CH/ITO electrode and (b) ChEt-ChOx/ <i>ant</i> TiO ₂ -CH/ITO bioelectrode, and (iv) EIS of (a) <i>ant</i> TiO ₂ -CH/ITO electrode and (b) ChEt-ChOx/ <i>ant</i> TiO ₂ -CH/ITO bioelectrode, (inset: zoom image)	123
4.2.8 (i) EIS spectra of ChEt-ChOx/ <i>ant</i> TiO ₂ -CH/ITO bioelectrode as a function of flow rate (0.01-5.0μL/min), inset: plot between charge transfer resistance (R _{ct2}) and flow rate (μL/min) and (ii) EIS spectra of ChEt-ChOx/ <i>ant</i> TiO ₂ -CH/ITO bioelectrode at different potential (0.1-0.7 V), inset: the plot between R _{ct2} value and logarithm of potential	125
4.2.9 Randles equivalent circuit model for EIS measurement.....	126
4.3 (i) Dispersion angles versus potentials for ChEt-ChOx/ <i>ant</i> TiO ₂ -CH/ITO bioelectrode, (ii) EIS response spectra of ChEt-ChOx/ <i>ant</i> TiO ₂ -CH/ITO bioelectrode as a function of cholesterol oleate concentration (at flow rate of 1μL/min), (iii) plot between R _{ct2} and	

concentration of cholesterol oleate [2-500 mg/dl] and (iv) the microfluidic sensor linear fit curve between EIS response and logarithm of cholesterol oleate concentration in the range of 2-500 mg/dl	128
4.3.1 The selectivity studies in presence of various interferents	129
5.1.1 The microfluidics chip used for total cholesterol detection.....	137
5.1.2 X-Ray diffraction pattern of NR-NiO nanorods onto ITO film (inset: powder XRD pattern of NiO nanorods).....	139
5.1.3 Raman spectroscopy studies of NiO nanorods (inset: UV visible studies of NR-NiO of NR-NiO/ITO film)	139
5.1.4 FT-IR spectra of (a) NR-NiO/ITO film and (b) ChEt-ChOx/NR-NiO/ITO film...	140
5.1.5 HR-TEM analysis of (a) synthesis NiO nanorods (inset: zoom image nanorods), (b) single nanorods micrograph with length 36.7nm and width 8.3nm (inset: SAED pattern of NiO nanorods), (c) lattice fringes of as-synthesis NR-NiO different planes (inset: lattice fringe for (111) plane and zoom image) and (d) ChEt-ChOx immobilization onto NR-NiO (inset: image at low resolution).....	142
5.1.6 (i) EIS of (a) NR-NiO/ITO electrode and ChEt-ChOx/NR-NiO/ITO bioelectrode (inset: Randles equivalent circuit model for EIS measurement and (ii) CV of (a) NR-NiO/ITO electrode and (b) ChEt-ChOx/NR-NiO/ITO bioelectrode in PBS solution (50 mM, pH 7.0, 0.9% NaCl) containing 5 mM $[\text{Fe}(\text{CN})_6]^{3-/4-}$	143
5.1.7 CV of ChEt-ChOx/NR-NiO/ITO bioelectrode as a function of scan rate [30-110 (mV/s) ^{-1/2}]... ..	144
5.1.8 Diffusivity of NR-NiO/ITO electrode at different flow rates using syringe pump [inset: CV response of NR-NiO/ITO electrode at different flow rates (10-70 $\mu\text{L}/\text{min}$)]......	145
5.1.9 Calibration curve for this microfluidic biosensor between peak current and different concentration of cholesterol oleate (25-400 mg/dl) (inset: CV response of ChEt-ChOx/NR-NiO/ITO bioelectrode as a function of cholesterol oleate concentration	147
5.2.0 (i) Studies using different interferents for the ChEt-ChOx/NR-NiO/ITO bioelectrode. Current response is plotted as a function of different analytes. (ii) Stability studies of the ChEt-ChOx/NR-NiO/ITO bioelectrode as a function of days.....	148
6.1.1 The schematic of the microfluidic biochip used for total cholesterol detection (the ordered arrangement of this microsystem is assumed).....	157
6.1.2 (a) The photograph of real microfluidic biochip for cholesterol detection and (b) the enlarged view of optical microscopic image of the microfluidic biochip.....	157
6.1.3 (i) The X-ray diffraction pattern of CNT-NiO and (ii) the Raman spectroscopy spectra of (a)NiO nanoparticles and (b) CNT-NiO	159
6.1.4 (i) The wide-scan X-ray photoelectron spectra (XPS) of various films. (ii) The XPS spectra of the C1s region of the CNT-NiO film after deconvolution; (iii) the C1s region of the ChEt-ChOx/CNT-NiO/ITO film; and (iv) the N1s core-level spectra of the ChEt-ChOx/CNT-NiO/ITO film	160
6.1.5 (a) Zeta potential studies of dispersed NiO nanoparticles in water solution (b) Zeta potential studies of dispersed CNT in water solution	162

6.1.6 CNT-NiO composite has reduced toxicity as compared to CNT alone. The A549 cells plated at 5×10^3 cells per well in 96 well tissue culture plate were exposed to growth medium containing indicated concentration of nanoparticles for 24 hrs. The cells were treated with MTT for 1 hr and then relative reduction of MTT to formazan by cells was calculated. The relative reduction of MTT is presented as % proliferation with respect to cells not exposed to any nanoparticles (Ctrl). The error bars show AVEDEV	162
6.1.7 CNTs exposure significantly attenuates the ability of A549 cells to reduce MTT dye to formazan compared to NiO nanoparticles or CNT-NiO composite. A549 cells exposed to indicate concentration of CNTs, NiO or NiO-CNT composite for 24 hours are incubated in the presence of 1 mg/ml MTT for 1h. The cells are imaged using Nikon eclipse microscope at 100x magnification.....	164
6.1.8 (i) SEM studies of COOH functionalized CNT, (ii) CNT-NiO film on indium tin oxide (ITO) coated glass substrate and (iii) SEM image of NiO nanoparticles	165
6.1.9 The HR-TEM analysis of (i) the NiO nanoparticles, (ii) an individual CNT (inset: the SAED pattern of the CNT), (iii) the CNTs modified with NiO nanoparticles, and (iv) an atomic-scale image of a CNT-NiO (inset: lattice fringes of the CNT)	166
6.2.1 (i) CV of different electrodes in PBS solution (50 mM, pH 7.0, 0.9% NaCl) containing 5 mM $[\text{Fe}(\text{CN})_6]^{3-/4-}$, (ii) the chronoamperometric (current-time) response of CNT-NiO/ITO electrode as a function of flow rate [0.01-5 $\mu\text{L}/\text{min}$], inset: current vs flow plot, (iii) the chronoamperometric response of ChEt-ChOx/CNT-NiO/ITO electrode as a function of flow rate [0.01-20 $\mu\text{L}/\text{min}$], inset: current vs flow plot and (iv) EIS spectra of electrodes	169
6.2.2 CV studies ChEt-ChOx/CNT-NiO/ITO bioelectrode as a function of scan rate [30-100 (mV/s)], inset: (i) anodic and cathodic peak current vs square root of scan rate and (ii) anodic and cathodic peak current vs square root of scan rate.....	171
6.2.3 (i) The chronoamperometric response of the ChEt-ChOx/CNT-NiO/ITO-based biochip as a function of the cholesterol oleate concentration (0.25-12.93 mM) in a PBS solution containing 5 mM of $[\text{Fe}(\text{CN})_6]^{3-/4-}$. The experiment was controlled using a syringe pump attached to the inlet of the microsystem (inset: the response current as a function of the cholesterol concentration obtained for both (a) ChEt-ChOx/CNT-NiO/ITO and (b) CNT-NiO/ITO electrodes). (ii) A calibration plot showing the logarithm of the cholesterol concentration (mM) and the amperometric current of the biochip during sensing. (iii) Real sample analysis.....	173
6.2.4 Reproducibility studies of the ChEt-ChOx/CNT-NiO/ITO microfluidics bioelectrodes under similar conditions. (ii) Stability studies of the ChOx-ChEt/CNT-NiO/ITO bioelectrode and (iii) selectivity studies of the ChOx-ChEt/CNT-NiO/ITO-based biochip.....	175
6.2.5 FT-IR spectra of (a) CNT-NiO/ITO film and (b) BSA-AAB/CNT-NiO/ITO film.....	177
6.2.6 (A) UV-Visible studies and (B) $(\alpha h\nu)^2$ versus energy plots of various films.....	178
6.2.7 (i) CC plots (charge-time) for CNT-NiO/ITO (a) electrode and BSA-AAB/CNT-NiO/ITO (b) bioelectrode, and (ii) charge (Q) vs. $t^{1/2}$ plot of CNT-NiO/ITO (a) electrode and BSA-AAB/CNT-NiO/ITO (b) bioelectrode.....	179
6.2.8 (i) Potential-dependent chronocoulometric responses for the BSA-AAB/CNT-NiO/ITO bioelectrode at different potential (1.0-5.0 V), (ii) chronocoulometric responses	

at different flow rate (0.01-15 $\mu\text{L}/\text{min}$) and (iii) Q vs. $t^{1/2}$ plot for different flow rates (inset: slope; $Q/t^{1/2}$ vs flow rate plot)	180
6.2.9 (a) EIS spectra of CNT-NiO/ITO electrode (i) and BSA-AAB/CNT-NiO/ITO bioelectrode (ii), (b) EIS spectra of BSA-AAB/CNT-NiO/ITO bioelectrode as a function of potential (V), (c) plot between charge transfer resistance (R_{ct}) and potential (V) and (d) EIS responses of BSA-AAB/CNT-NiO/ITO bioelectrode as function of LDL concentration	181
6.3.1 (a) Linear sensor calibration plot of <i>i</i> LOC, (b) EIS spectra of <i>i</i> LOC without BSA-AAB for control experiment, (c) sensing and control experiment plots as a function of LDL concentration and (d) $1/R_{ct}$ and $1/\text{concentration}$ plot for association constant	183

Tables

1.1 Area-wise applications of microfluidic devices	10
1.2 Milestones and achievements relevant to biosensors	14
1.3 Classifications of lipoproteins with concentration	19
1.4 Classification of lipoproteins	20
2.1.1 Various methods for immobilization of biomolecules with advantages and disadvantages	47
4.1.1 Characteristics of microfluidics based cholesterol biosensor along with those reported in literature	108
4.1.2 Pore size distribution from BET data	119
4.1.3 The atomic concentration (%) and full width half maxima (FWHM) of C, O and N elements present in antTiO ₂ -CH/ITO and ChEt-ChOx/antTiO ₂ -CH/ITO electrodes from XPS analysis	119
4.1.4 Sensing characteristics of cholesterol biosensor along with those reported in literature	129
5.1.1 Sensing characteristics of cholesterol biosensor along with those reported in literature	148
6.1.1 The atomic concentration (%) of the elements C, Ni, O, and N present in the CNT-NiO/ITO and ChEt-ChOx/CNT-NiO/ITO films obtained from XPS analysis	161
6.1.2 The sensing characteristics of the ChEt-ChOx/CNT-NiO/ITO based biochip designed for total cholesterol estimation	174
References	196
Publications	217

CHAPTER 1

Introduction and Overview

1.1 Point-of-care diagnostics

Point-of-care (POC) diagnostics is considered important in the clinical scenario of diseases as well as for treatment of patients. Early diagnostics plays an imperative role in determining pre-disposition to a disease (prevention) or the outcome of disease (monitoring and prognosis) [1-15]. POC devices are generally small, portable, handheld, faster and cost-effective devices. These devices can be used for bedside, near-patient, satellite or remote, and decentralized testing. POC devices provide a convenient and immediate response to the patients and clinical care team [1, 2]. By utilizing POC testing devices, results could be made available quickly to the clinical care team thereby facilitating immediate clinical decision and treatment device [4-6]. Numerous tests including blood glucose, blood gas concentration, coagulation, expression of cardiac markers, drugs of abuse, pregnancy, Hb, urine analysis and infected diseases etc. could be feasible with POC devices [1-15]. POC testing can be achieved via use of portable devices such as blood gluco/lactate meter, creatinine analyzer, C-reactive protein analyzer, pulse co-oximeter, cholesterol meter etc. With the goal of getting, cheaper, smaller, faster, and smarter, the POC devices seems to be one of the most favoured technologies of the coming generation of the health care diagnostic devices [16].

Currently health care is an active field of intellectual engagement for emerging technologies. Various techniques are used towards the discovery, delivery of chemicals for diagnosis and treatment of human diseases [17]. The outbreak of new or re-emerging infectious diseases along with changing lifestyles has led to an urgent need towards the faster development of POC devices that could be used for effective therapeutic interventions [18]. It may be noted that even simple routine biochemical tests require well-trained technicians and expensive laboratory infrastructure with continuous supply of chemicals resulting in high costs. Such diagnostic challenges have necessitated the development of new technologies nearer to the patient sites and are termed as the POC diagnostics. POC diagnostics are commonly described as analytical testing platforms that can be used both in a clinical laboratory and in the vicinity of a patient via portable equipments [19]. Therefore, the entire clinical community is witnessing a paradigm shift from the conventional diagnostic devices to miniaturized and automated POC devices that can fulfill the increasing demand of medical sector including direct unprocessed specimen utilization and the minimum need of electronic or mechanical maintenance. The POC has the potential to provide rapid and accurate information on desired biochemical tests required by increasing population of patients in emergency rooms at reasonable costs [20]. An ideal diagnostic device should provide a suitable environment for interaction of a desired analyte present in a sample with the bio-recognition molecule (e.g., protein/ lipid/ nucleic acid/ whole cell) immobilized on to the sensor surface [5, 6]. Until recently, development of such devices was considered unachievable due to the extensive variability in biological

samples resulting in unreliable clinical data and the complexity of the electronics that are needed to support it.

Compared to the core laboratory analysis, potential demand for POC devices have increased in the past two decades due to its several advantages [7]. The annual growth rate of POC (12 %) indicates that 40 % of laboratory tests are predicted to be conducted on POC devices within the next decade [18]. The POC test can be performed at an outpatient clinic or patient's home or even at a primary care provider's office desk. POC testing can be accomplished in mobile transport vehicles such as ambulances, helicopters, fire engines, cruise ships and the space shuttles. The short therapeutic time offers improved patient outcome by reducing delays in waiting time for laboratory results and can prevent such bottlenecks [21]. Thus, POC devices would certainly result in improved physician efficacy by minimizing the turn-around time and better fitting within clinical workflow. The characteristics such as portability, rapid result, small sample volume, no sample processing, and ease of use have promoted the use of POC devices in patient health care [22].

The applications of POC diagnostics have grown rapidly towards the medical health care [23]. A number of clinical biochemical studies such as blood gas, glucose/lactate/cholesterol, nucleic acid sequence analysis, proteins/peptides, combinatorial synthesis, toxicity monitoring, immunoassays, and forensic analysis are the focused areas for developing the micro total analysis systems (μ TAS) or Lab-on-a-chip (LOC) [24]. Detection of nucleotides and peptides of any cancer such as breast, prostate, oral, lung etc. is very important for early diagnostics. One of the most successful examples of POC testing device is the iSTAT device from Abbott Laboratories (Abbott Park, IL, USA). This iSTAT analyzer uses microfabricated electrodes coupled with an electrochemical detection unit that measures various electrolytes, blood gases, glucose, lactate and hematocrit [13]. In the last decade, extensive research has been taking place on POC devices using microfluidic, LOC, microarrays etc. technologies in the realm of enzymatic, DNA, proteomic and immunoassays analysis. The modern POC diagnostics devices utilize immunoassay technology via antigen-antibody binding. In addition, POC diagnostics devices are widely used to determine various specific protein biomarkers such as glycated hemoglobin, C-reactive protein, D-dimer, troponin I or T, prostate-specific antigen, human immunodeficiency virus, influenza, chlamydia, and hepatitis [6, 7]. A traditional urine test at home for diabetics and kidney-disease patients can be performed by POC devices. The home POC devices can measure the pregnancy hormone human chorionic gonadotropin for pregnancy test. An ideal POC diagnostic device uses a minute amount of unprocessed sample that is collected from the patient directly [25]. Efforts have been made to detect multiple biomarkers for accurate POC tests with high sensitivity and short turn-around time. These devices would be safer to use in a hospital, user friendly and easy to operate by non-technical experts.

Chong et al. have fabricated paper-based microfluidic POC diagnostic devices for drug metabolism monitoring [26]. Ahn et al. have demonstrated the disposable smart Lab on a chip (LOC) for POC clinical diagnostics [1]. Cheng et al. have reported the enhanced performance of a POC CD4+ T-cell counting microchip through monocyte depletion for HIV/AIDS diagnostics [3]. Gervais et al. have developed toward one-step POC immunodiagnostics using capillary-driven microfluidics and PDMS substrates [5]. Gubala et al. have reviewed the status and future prospects of POC diagnostics [7]. Myers et al. have reviewed the innovations in optical microfluidic technologies for POC diagnostics [11]. Sandhu et al. have described the synthesis and applications of magnetic nanoparticles for biorecognition and POC medical diagnostics [12]. Soper et al. have developed the POC biosensor systems for cancer diagnostics/prognostics [27]. Tüdos et al. have described the trends in miniaturized total analysis systems for POC testing in clinical chemistry [13]. Wang et al. have developed electrochemical biosensors towards POC cancer diagnostics [28]. Chin et al. have reported the POC diagnostic devices for health care [29]. Choi et al. have reviewed the microsystem toward point-of-care detection of nucleic acids and proteins [30]. However, there are many challenges yet to be addressed in ideal POC device with desired characteristics. Various challenges including miniaturization, all-peripheral instrumentation, faster implementation etc. needs more attention remain before these technology can be translated to be efficient POC devices.

1.2 A historical snapshot of microfluidics devices

Microfluidics is a new branch of science and technology in which significant progress has been made in the past two decades. The microfluidics has a long history from basic research to diagnostic products. This technique has revolutionized the chemical and biochemical analysis of biomolecules. A major milestone in microfluidics could soon lead to stand-alone, self-powered chips that can diagnose diseases within minutes [31]. An overview of the state-of-the-art microfluidic technology with time line is depicted in the Figure 1.1. Initially, researchers manipulated liquids at high precision using gas chromatography, high-pressure liquid chromatography, and capillary electrophoresis [32]. In 1950s, the biological fluids molecules are controlled precisely by utilizing inject printing technologies and are known as the first microfluidic device. In 1970s, IBM started to commercialize these printers. Terry et al. developed a silicon micromachined based gas chromatographic (GC) air analyzer at Stanford University [33]. In terms of fluid propulsion within microchannels with sub-millimetre cross sections, the year 1979 set a milestone when a miniaturized GC was realized by Terry et al. on a Si wafer. In the 20th century, many researchers have investigated the applications of MEMS (microelectromechanical system) in biology, chemistry and biomedical fields. The nineties witnessed the integration of bioanalytical and microelectronics disciplines which can be considered the birth of microfluidics. Manz et al. introduced the

concept of miniaturized total chemical analysis systems (μ TAS) and developed the microfluidic high-pressure liquid chromatography systems and microfluidic capillary electrophoresis in 1992 [34]. In 1996, George M. Whitesides introduced soft lithography using PDMS (polydimethylsiloxane) for fabrication of microfluidic devices. These researchers demonstrated that the utilization of polymers in microfluidics is easier, more flexible and less expensive than silicon or glass [35-37]. Whitesides et al. have reviewed the origin and future of microfluidic devices and fabricated a new platform for POC diagnostics, cellular and developmental biology [38]. In 2000, the efforts have been made to develop laboratories on a chip that integrates almost all diagnostic operations performed in a hospital on a single microfluidic chip. It has been observed that the majority of microfluidic devices are still fabricated using silicon or glass. These materials are known to be expensive and the process is time-consuming and requires access to specialized facilities. Thus, they are marginally useful in research requiring rapid evaluation of prototypes.

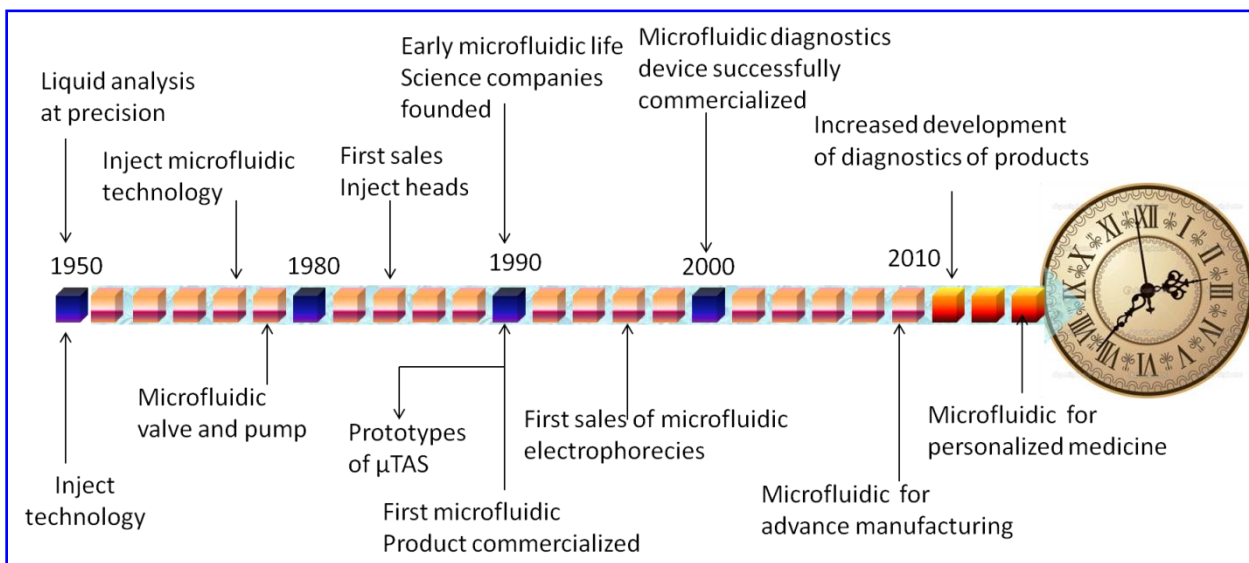


Figure 1.1 Historical snapshot of microfluidics technology with time [15].

Microfluidics is currently one of the most promising technologies to meet the growing needs in healthcare for faster processing of samples, accurate and reliable results, parallelization and miniaturization [39]. It is an extremely attractive technology because of its ability to manipulate minute volumes of a fluid within given spatial dimensions and the ease of multiplexing and integration onto compact, portable devices for on-chip testing [40]. The fluid volumes of interest are typically measured in order of microlitres (10^{-6} L) to picoliters (10^{-12} L), and flow rates generally do not exceed more than a few microlitres per minute [41]. Various biological fluids such as blood serum, breast milk, sweat,

synovial fluid, tears, urine, saliva, sebum (skin oil) etc. are most commonly used in microfluidics, and can be precisely controlled and manipulated. Due to the small size and dimensions of the microfluidic systems, both energy and chemical consumption are drastically reduced. Due to laminar flow regime, it can perform liquid-liquid extraction, sample fractionation and immuno-affinity extraction between two parallel flows. Fluidic behaviour in laminar flow regime can be used for performing various sample pre-treatments and process.

The range of applications of microfluidics is rapidly growing in fields of biotechnology and healthcare for faster processing of given samples, to obtain accurate and reliable results [42]. Extensive research has been carried out in the last decade towards the development of microfluidics technology proposing exciting possibilities in the realm of glucose, urea and cholesterol assays analysis, deoxyribonucleic acid (DNA)/polymerase chain reaction (PCR) analysis, proteomic analysis involving proteins/peptide, immunoassays and toxicity monitoring and microarrays [43]. The developments in microfluidics have been very promising to people in industry as well as research that resulted in adoption of these platforms for clinical diagnostics [29]. The increased surface-to-volume ratio of microfluidic systems can be an advantage when working with immobilized materials such as enzymes, DNA and antibodies [44]. Furthermore, advances in microfluidics, arrays, and sensors promise to revolutionize the detection of pathogens *in vivo* and *in vitro* in the environment through the development of LOC devices [45]. In addition, a vast area for research in cell culture applications has recently evolved via exploiting its ability to mimic *in vivo* like conditions of cellular micro-environment [46]. Microfluidics can provide more realistic *in vitro* environments for small-scale biological species of interest. The applications of microfluidics towards various fields such as biochemical assays, cell/organ analysis, synthesis, digitization and PCR have been described. Working with such minute volumes of fluids, microfluidic devices can be used to achieve exceptional performance in terms of parameters such as sensitivity, speed, and spatial resolution [47]. Microfluidics-based sensor can be used to detect target analytes with sensitivity as good as one part per billion. For example, an ink-jet droplet generator can print an image with approximately one million discretely controlled droplets in an area of 1 cm². However, still there is a strong need of such devices that rely on several qualitative and quantitative results including simple ‘yes’ and ‘no’ result. This will instantly remove the heavy burden on the conventional diagnostics methodology that hinders testing of thousands of samples within a given point of time. Moreover, a high-throughput system for handling a large number of samples must be instant and utilize very small chemical volumes to keep the cost of the device at an affordable level. The comparative length scales for several biological structures, as well as common micro-fabrication structures used in microfluidics devices as shown in Figure 1.2.

The recent trends to miniaturize, automate and parallelize assays address these issues directly while simultaneously increasing resolution and accuracy. There is an effort to miniaturize and integrate sample pre-processing with analyte detection. These microsystems integrate scaled-down laboratory functions and processes to a miniaturized chip format and are known as “Lab-on-a-chip” or bio-microelectromechanical systems (bio-MEMS) [48]. There is an increasing demand to integrate multiple platforms into LOC systems by introducing microfluidics [49]. Thus, a Lab-on-a-chip is an analytical device which integrates several or one functions on a single device in microscale size. Usually, it is a microchip-based system that (similar to the micro total analytical system or μ TAS) contains all liquid handling steps on the chip to perform the analysis [50]. The μ TAS includes all the necessary steps to perform various analyses such as sampling, dilution, sample filtration, chemical reactions, separation and detection. However, all steps in the analytical procedure need not necessarily be integrated on the chip [50]. MEMS are made up of elements in the range of 1 to 100 μ m in size and devices can be fabricated in very small size such as 20 μ m-1.0 mm [51]. The MEMS devices are fabricated through the deposition of material layers, patterning by photolithography and etching to produce the required shapes [51]. These micro-systems are being employed in fields such as biology, microelectronics, physics, engineering and other related areas.

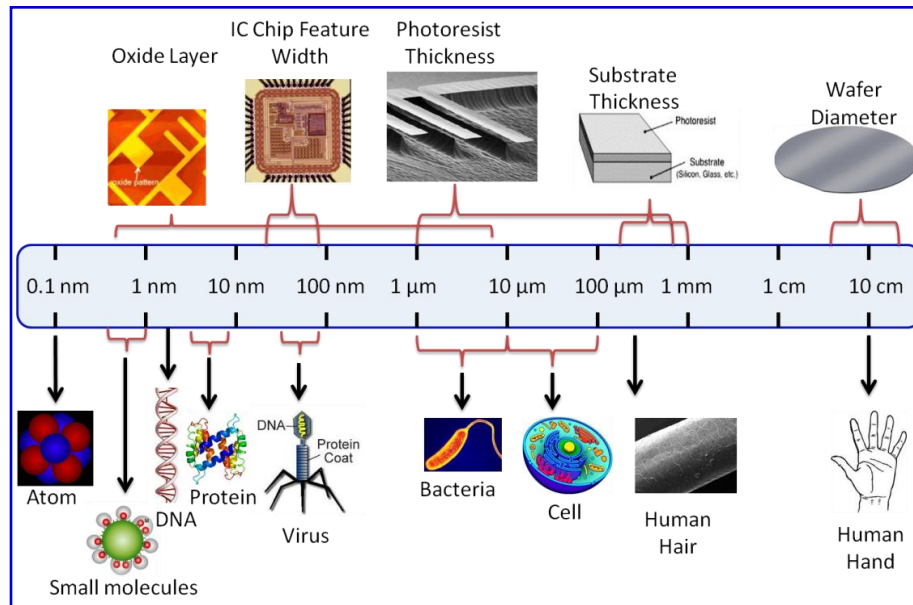


Figure 1.2 The length scales of microfluidic device and biological based micro-fabrication.

The active microfluidic devices have been found to have many disadvantages such as high cost, difficulty in integration and complex fabrication/control circuitry [52]. Thus, the passive microfluidic devices based on valves, passive filters, mixers, extractors, membranes and passive actuators have recently been fabricated [52]. The passive microfluidic devices have no external power requirement for device operation and offers ease of integration, continuity in substrate material, rapid prototyping, low cost, and possibility of use without active control. With microscale fluid regulators such as pumps, valves, mixers etc. can be integrated with the LOC, the analytical performance of these platforms can be greatly enhanced. Advances in microfluidics and LOC technology have resulted in altogether exciting and promising approach to integrate optics and fluidics part at micron-size scales to leverage the combined advantages. All these studies can be brought to commercial reality by precisely controlling spatial and temporal factors such as cell–cell and cell–matrix interactions, oxygen and nutrients delivery, metabolites removal etc. [53]. Optofluidic elements that can manipulate light inside a microchannel level were also demonstrated [54]. Principles of optical microscopic imaging coupled with fluorescence tags and surface plasmon resonance-based detection were explored and demonstrated as effective biosensing platforms for detection and quantification of various biomolecules. Microfluidics systems were adapted for imaging intracellular events like cell division, migration etc. Microfluidic devices allow the generation on a single chip of a large number of crystallization conditions (temperature, pH, humidity etc.). Application of microfluidics spread to many other areas such as sugar testers, drug screening, microprocessor cooling, chemical microreactor and micro fuel cells. Table 1.1 summarizes different potential application of microfluidic devices.

Table 1.1 Area-wise applications of microfluidic devices [55]

Area	Applications
Clinical Analysis	Rapid analysis of blood and bodily fluids, point of care diagnostics, enzymatic analysis, electrochemical detection, cell counting and sorting etc.
Miniaturized analytical system Genomics and proteomics	Rapid, high density sequencing, DNA finger printing, combinational analysis, forensic analysis, gene expression analysis, integration with fluids with DNA arrays.
Chemical/biological warfare defense	Early detection and identification of pathogen and toxins, early diagnosis, triage etc.
High throughput screening	Combinatorial synthesis and assaying for drugs and toxicological assays
Environmental testing	<i>In situ</i> analysis of environmental contamination etc.
Biomedical devices	Devices for <i>in vivo</i> drug delivery, <i>in vivo</i> monitoring for diseases and conditions, single molecule detection etc.
Sample separation	Purification of biological analysis for further analysis
Biomimetic analysis	Development of machines that mimic biological functions
Studies of chemical reaction	Enzyme substrate
Amplifications of nucleic acids/sequences	PCR, RT-PCR etc.
Flow of fluids	Studies on diffusion through small channels, laminar flow studies etc.
Small scale organic synthesis	Combinatorial synthesis
Bioimaging analysis	Optofluidics application based on surface plasmon resonance coupled with fluorescence tags molecules, nanoparticulate imaging contrast agents for <i>in vitro</i> and <i>in vivo</i> biosensing devices

Andersson et al. have described the cell sorting, trapping and sampling using microfluidic devices [56]. Sorger et al. demonstrated integrated microfluidic devices for rapid detection of protein biomarkers in patient samples [16]. Haeberle et al. have critically reviewed the microfluidic platforms for LOC applications [9]. Dinh et al. have developed a multifunctional biochip functionalized with nucleic acid and antibody receptors that are specific to gene fragments of *Bacillus anthracis* and *Escherichia coli*, respectively [57]. Dong et al. have fabricated a microfluidic array device for immunoassays analysis with screen printing technology [4]. Kovarik et al. have demonstrated the fabrication of μ TAS, and its integration with other techniques such as optics, acoustics, biomimetics, electricity and magnetism [58]. The recent advances of microfluidic devices for drug discovery, target selection, pre-clinical tests, clinical trials, chemical synthesis, formulations studies and product management have been extensively reviewed by Kang et al. [59]. Weibel et al. have described the applications of microfluidics in chemical biology [60]. Hansen et al. have demonstrated the microfluidics in structural biology for smaller, faster and better performance [61]. Fiorini et al. have described the biotechnological applications of microfluidics for

potential development of health care devices [62]. Thus, adoptions of these microfluidic platforms in the development of POC diagnostics devices are promising to the researchers working in this area.

The reasons for miniaturising analytical devices originate from two sources: economic benefits and increased analytical/technical performance of the analysis. However, both are interrelated; an improved analysis can have economic impact due to faster analysis, higher sample throughput and lower reagent consumption. The several advantages of downscaling analytical systems are listed below [62]

- Higher sample throughput
- Multiplexing
- Automation
- Integration
- Portability
- Manufacturing cost
- Disposability
- Lower energy consumption
- Reduced chemical consumption
- Laminar flow
- Improved separation efficiency
- Short diffusion paths
- Increased surface-to-volume ratio
- Faster heat dissipation

Higher sample throughput may result in improved separation performance, multiplexing, and/or faster analysis due to short diffusion paths for analytes and reagents. Multiplexing can be achieved by construction of parallel analysis lines integrated on the same chip. In addition, chemical reactions can proceed faster because of improved thermal transport such as heat dissipation. Microchip with channel systems for multiple liquid-handling step, along with the MEMS-based detection systems can provide automated and compact devices. Both integration and automation are prerequisites for efficient portable analyzers.

An ideal diagnostic device should provide a suitable environment for interaction of desired analyte present in a sample with the bio-recognition molecules that are immobilized on to the sensor surface [15]. An ideal microfluidic device can multiplex more than 100 analytes within 1 minute that may be a variety of proteins, enzymes, antibodies and nucleic acids. It can be used to detect a concentration as low as picomolar to femtomolar within a large dynamic range. It provides higher selectivity, excellent sensitivity, zero cross talk, false positives and there would be no cross contamination between samples

from different patients for simultaneous reading. These devices may be impervious to water and cannot be damaged easily. Due to utilization of transparent materials in microfluidic devices, fluids flow can be monitored optically resulting in new technologies based on optical read-out. In addition, these devices would have a longer battery life and can have a good shelf life at temperatures from -55°C to 55°C . The flow control, filtration/processing of the sample, antifouling surface, wettability, signal generation and receptor attachment are all highly dependent on the properties of materials used for the construction of microfluidic devices. The precise control of the materials is essential for the proper working a POC device.

1.3 The state-of-the-art biosensors

A biosensor is an analytical device consisting of a biological sensing element and a transducer that converts a biological response into a measurable signal, whose magnitude is proportional to the concentration of a specific chemical or set of chemicals [63]. Biosensors are used in our daily life, such as in health care diagnostics, food safety and environmental monitoring. Health care is one of the main areas where biosensors find a lot of applications, such as monitoring of glucose, cholesterol, urea, lactate, lipoproteins etc. in human blood serum, saliva or sweat [64].

In 1962, Clark introduced an oxygen electrode at Cincinnati Children's Hospital [65]. This is the first glucose enzyme-electrode that relied on a thin layer of glucose oxidase entrapped over an oxygen electrode via a semipermeable dialysis membrane. The term "biosensor" was introduced by Cammann in 1977 [66]. The IUPAC definition of a biosensor, however, was introduced more recently as 1999 to 2001. Electrochemical detection has been employed to monitor the oxygen consumed by the enzyme-catalyzed reaction between glucose and glucose oxidase in presence of oxygen. A negative potential was applied to the platinum cathode for a reductive detection of the oxygen consumption. The method of detection is based on the decrease in oxygen concentration that is proportional to glucose concentration. The Clark's technology was transferred to Yellow Spring Instrument Company, which launched the first dedicated glucose analyzer for diabetes mellitus in 1975. Table 1.2 gives the milestones and achievements relevant to biosensors [63]. This proposed oxygen-electrode is known as first generation of biosensor which is oxygen dependent. In the first generation biosensors, the normal product of the reaction diffuses to the transducer and causes the electrical response. The second generation biosensors involved the specific 'mediators' between the reaction and the transducer in order to generate improved response. Thus, this generation of biosensor depends on mediator but does not depend on oxygen for biochemical reaction. In 1980, the efforts have been focused on the development of mediator-based 'second-generation' biosensors by introducing the commercial strips for self-monitoring of blood glucose. In third generation biosensors, the reaction causes the response and does not involve any mediator diffusion [67]. In these

biosensors thus, the direct electron transfer (ET) between the biomolecules (enzyme, antibody, DNA etc.) and the electrode surface excluding any intermediate ET reactions with redox mediators. Wang et al. have described the advances in electrochemical glucose biosensors [68]. Pumera et al. have reviewed the electrochemical biosensors based on nanoscale materials as biomolecule tracers, including gold nanoparticles, quantum dots for DNA and protein multiplexing, novel nanobiolabels as apoferritin, liposomes and enzyme tag loaded carbon nanotubes [69]. Thus, the electrochemical detection plays an important role in development of biosensors because of the low cost, ease of use, portability, label-free operation, simplicity and higher signal to noise ratio. Details of biosensor with a brief literature survey, types of biosensors and methods of immobilization have been illustrated in the Chapter 2.

Common methods of detection for electrochemical biosensors involve measurement of current, voltage, conductance, capacitance and impedance. Chornokur et al. have developed an impedance-based miniaturized biosensor for ultrasensitive and fast prostate-specific antigen detection [70]. Dubuisson et al. have reported a label-free DNA electrical detection platform using graphene [71]. An electrochemical biosensor for early detection of cervical cancer has been by demonstrated Chandra et al. [72]. Jie et al. have reported an electrochemiluminescence immunosensor based on CdSe nanocomposite for the detection LDL [73]. Singh et al. have reported the nanoparticle-enhanced sensitivity of a nanogap-interdigitated electrode array impedimetric biosensor [74]. Researchers have explored various biosensor platforms for the detection of target analytes including cholesterol and LDL. There are many different ways to construct a biosensor. The choice of the transduction process and transducer material is critically dependant on fabrication of the sensing layer on the transducer surface. It is known that the biosensors are promising analytical tools applicable in different areas for clinical diagnosis and many other applications. The miniaturization, multiplexing and parallelization of the biosensor fabrication are the important issues for POC applications. Thus, the biosensor integrated microfluidic platforms for detection of desired analytes can play an important role in POC diagnostics.

Electrochemical detection is being increasingly used for enzymatic analysis and hence is an attractive choice for microfluidics systems because of higher sensitivity arising due to higher signal-to-noise ratio and improved ratio of faradaic-to-charging current [75]. The size of the electrode affects mass transport of the redox active species to and from the electrode surface and the bulk solution that may perhaps influence the electrochemical response [76]. Compared to macro-sized conventional electrodes, micro-electrodes offer many advantages including reduced charging current, high mass transport which is dominated by radial diffusion, immunity to ohmic drop and small RC constant. The small electrode surface area of the electrode can significantly reduce the charging current due to smaller small double layer capacitance. The higher faradaic current compared to that of non-faradaic current of microelectrode provides enhanced detection limit. The microelectrodes can generate small amount of

currents resulting in a negligible ohmic drop of potential. Electrochemical impedance spectroscopic (EIS) method has recently received considerable attention for the detection of biomolecules towards the POC applications [77]. Impedance spectroscopy is the study of the resistive and capacitive behaviour of an electrode–electrolyte interface by means of electrochemical transportation of electrons in a given frequency domain [78]. The impedimetric method is known to be a non-destructive, sensitive and label-free analytical detection technique that relates a bio-recognition event occurring at an electrode/electrolyte interface [78]. Besides this, EIS can be used to obtain information on biomolecular interactions, amount of adsorbed proteins, surface charge densities and the magnitude of adsorption coefficient [79]. The EIS uses a small perturbation (usually sinusoidal) which reduces the matrix interference and rapidly responds to the change caused due to binding of an analyte with the immobilized bio-recognition element on the transducer surface [77-79].

Table 1.2 Milestones and achievements relevant to biosensors [63]

Year	Contributions	References
1956	Leland C. Clark Jr. (1918 – 2005) presented his first paper about the oxygen electrode. In 1962, Clark and Ann Lyons from the Cincinnati Children’s Hospital developed the first glucose enzyme electrode.	[80, 65]
1959	Rosalyn Sussman Yalow (born 1921) and Solomon Aaron Berson (1918 – 1972) developed the radioimmunoassay which allows the very sensitive determination of hormones such as insulin based on an antigen–antibody reaction. Today the RIA technology is surpassed by enzyme–linked immunosorbent assay because the colorimetric or fluorescent detection principles are favored over radioactive-based technologies.	[81]
1963	Garry A. Rechnitz together with S. Katz introduced one of the first papers in the field of biosensors with the direct potentiometric determination of urea after urease hydrolysis. At that time the term “biosensor” had not yet been coined. Thus, these types of devices were called enzyme electrodes or biocatalytic membrane electrodes.	[82]
1967	G.P. Hicks und S.J. Updike introduced the first practical enzyme electrode immobilizing the enzyme within a gel. In 1970, Bergveld introduced the ion selective field effect transistor.	[83]
1972	Betso et al. showed for the first time that direct electron transfer of cytochrome c could be realized at mercury electrodes.	[84]
1973	Ph. Racinee and W. Mindt (Hoffmann La Roche) developed a lactate electrode	[71]
1975	The first commercial biosensor was introduced for diabetes patients	[68]

1976	First microbe - based biosensors	[85]
1980s	Self - assembled monolayers start to receive considerable attention in the scientific community and are employed in biosensor research	[86]
1981	Oxidation of NADH at graphite electrodes is described for the first time	[87]
1983	First surface plasmon resonance immunosensor	[88]
1984	First ferrocene - mediated amperometric glucose biosensor by Cass et al.	[89]
1988	Adam Heller and Yinon Degani introduced the electrical connection (“ wiring ”) of redox centers of enzymes to electrodes through electron-conducting redox hydrogels	[90]
1988	Direct ET by means of immobilized enzymes was introduced	[91]
1990	Bartlett et al. introduce mediator - modified enzymes	[92]
1997	IUPAC introduced for the first time a definition for biosensors in analogy to the definition of chemosensors	[93]
2002	Schuhmann et al. introduced the use of electrodeposition paints as immobilization matrices for biosensors. In 2007, an implanted glucose biosensor operated for five days.	[94, 95]

1.4 Integration of nanomaterials with microfluidics

Nanomaterials with at least one of their dimensions ranging from 1 to 100 nm scale have been predicted to provide unique physical and chemical properties due to the quantum size effect, surface effect, surface-to-volume ratio and macro-quantum tunnel effect. Different techniques can control the size of materials at the nanoscale dimensions. The nanosensors, nanoprobe and other nanosystems are revolutionizing the fields of POC biosensors to enable rapid analysis [96]. Metal nanoparticles such as gold, silver, nickel etc. are widely used in biosensor development. These nanomaterials provide the amplification of signal transduction in biosensor technologies thereby improving the characteristics of biosensors. They can be used to obtain the enhanced immobilization of biomolecules due to the ultrafine surface area. Nanomaterials exhibit good catalytic properties that are different from their bulk material properties due to their high surface area, and high edge concentration. In addition, the nanoparticles on the surfaces of electrodes can be used to improve electron transfer that improves the biosensor efficacy.

Law et al. have reported the development of a nanoparticle-enhanced biosensor by integrating both the nanoparticles and immunoassay sensing technologies into a phase interrogation surface plasmon resonance (SPR) system for detecting antigen at a concentration as low as the femtomolar range [97]. Claussen et al. have developed an electrochemical H₂O₂ biosensor using single walled carbon nanotubes

(SWCNTs) networks decorated with Au-coated palladium nanocubes [98]. Wang et al. have reviewed nucleic acid conjugated nanomaterials for enhanced molecular recognition. A free-standing flexible conductive reduced graphene oxide/nafion hybrid films by a solution chemistry that utilizes self-assembly and directional convective-assembly towards the biosensor application has been reported Choi et al. [99]. Zamolo et al. have developed an ultrasensitive electrochemiluminescence-based sensor for the detection of palytoxin using CNTs [100]. Saddiqui et al. have developed the vertically aligned carbon nanofiber electrode arrays using electrochemical impedance spectroscopy [101]. Mahmoud et al. have developed a picomolar detection system of protease using peptide/single walled CNT/gold nanoparticle-modified electrode [102]. A label-free, electrical detection of the severe acute respiratory syndrome (SARS) virus N-protein with In_2O_3 nanowire biosensors utilizing antibody mimics as capture probes has been developed by Ishikawa et al. [103]. Luo et al. have fabricated a boron-doped diamond nanorod forest electrode and demonstrated their application in nonenzymatic amperometric glucose biosensing [104]. However, these materials need several steps of surface treatment for attachment of biomolecules.

To use a biosensor at outside of the laboratory, it either has to be as simple or automated with regard to sample processing and reagent addition. Automation and miniaturization of analytical techniques, as well as the development of on-line and remote sensing devices can be achieved using microfluidic biosensor technology. Use of nanoparticles (NPs), nanotubes and nanowires in microfluidic assembly is currently of much interest in various fields such as biomedical, physics, chemistry etc. Their integration with a microfluidic platform through a combination of microfabrication and nanomaterial synthesis allow the unique functionality of the device. Using this smart integrated microfluidic system, many advances are achieved for electrochemical and optical detection of biomolecules such as antigen, enzymes, antibodies, DNA hybridization and oligonucleotides. Recently, this advanced technology has been explored in the field of biosensors and biochips. Nanostructured materials such as metal oxide nanoparticles, carbon, and polymeric materials, have been widely investigated to enhance the biosensing signal. Choi et al. have demonstrated the application of nanoparticles for the detection of biomolecules, their integration with nanopatterning and the microfluidic technologies for molecular diagnosis [105]. Most biological samples are known to have in a liquid medium, thus the biosensors can be combined with compelling fluid handling systems. Lee et al. have developed an integrated ZnO surface acoustic wave microfluidic for cancer diagnostics [106]. Other than biosensing applications, microfluidic could act as a novel route for the synthesis of controlled nanostructured materials.

Nanostructured metal oxides (NMOx) have recently captured increased interest for the development of microfluidic biosensors. To fabricate an efficient microfluidic biosensor, it is critical to select an appropriate NMOx for immobilization of the desired biomolecules. Details and importance of

nanostructured titania (TiO₂), nickel oxide (NiO) and their composites such as chitosan-TiO₂ and CNT-NiO have been described in the next Chapter.

1.5 Importance of cholesterol

Coronary heart disease (CHD) is one of the important issues that can cause the human death in all developed countries. CHD is a disease in which a waxy substance called plaque builds up inside the coronary arteries]. These arteries supply oxygen-rich blood to the heart muscle. The atherosclerosis is a known to be a critical condition in which arteries becomes blocked due to the accumulation of cholesterol [100]. Deposition of cholesterol inside walls of arteries can form plaques resulting in blockages and interruption of the blood circulation that can causes heart attack, angina and myocardial infarction. Over time, plaque can become harden or rupture. Hardened plaques narrow the coronary arteries and reduce the flow of oxygen-rich blood to the heart. In ruptured plaque, a blood clot can form on its surface resulting in a complete block of blood flow through a coronary artery. Thromboembolism is another condition that can occur due to the bursting of these plaques. If the flow of oxygen-rich blood to the heart muscle is reduced or blocked, angina or a heart attack can occur. Hence, the estimation of cholesterol in blood has become an important parameter for POC diagnostics.

Cholesterol is a janus-faced molecule and is a waxy, fat like substance found in all animal products such as meats, eggs and dairy products [107]. It is useful in cell membranes and controls the membrane permeability and fluidity. It can produce sex hormones, and can form bile acids, which are necessary for the digestion of fats. Recently, the risks of high blood cholesterol levels are increased worldwide. The high blood cholesterol levels may lead to cardiovascular diseases including arteriosclerosis. In blood stream, the human body can make cholesterol in the liver and it can absorb cholesterol from the diet. It is an important component for the metabolism of fat soluble vitamins, including vitamins A, D, E, K and insulates nerve fibers. It is known that 70% of cholesterol exists in ester form and 30% as free form in a blood sample. The chemical formulas of (a) free cholesterol and (b) cholesterol ester have been shown in Figure 1.4.

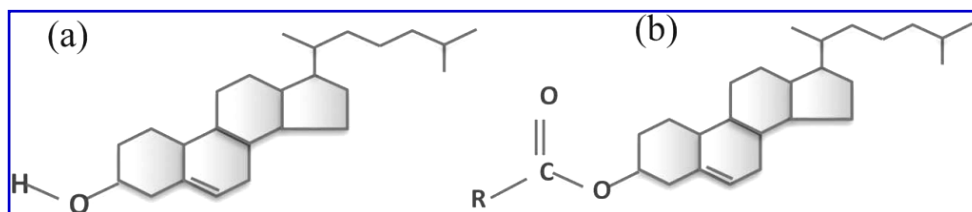


Figure 1.3 The chemical formula of (a) cholesterol (free), and (b) cholesteryl ester [108].

Cholesterol [(3 β)-cholest-5-en-3-ol; molecular formula: C₂₇H₄₆O, molecular mass: 386.6 g/mol] is a family of polycyclic compounds [Figure 1.3 (a)], it is known to be a sterol. In plasma, three major types of lipids namely cholesterol, phospholipids (PLs), and triglycerides (TGs) are present. Additionally, in plasma lipoprotein, cholesterol is found in free form that can esterified to long-chain fatty acids called cholesterol esters (CEs) [Figure 1.3 (b)] which can form covalent and non-covalent linkages in animal tissues. Lipoprotein is composed of lipid and protein which forms a particle via non-covalent bonds. In addition, it consists of a non-polar lipid of PLs, free cholesterol and proteins. The main function of lipoprotein is to transport cholesterol or TGs around the human body. The four major categories of lipoprotein are known as chylomicron (CM), low density lipoprotein (LDL), very low-density lipoprotein (VLDL) and high density lipoprotein (HDL) [109].

- ✓ Desirable - Less than 200 mg/dL (desirable level corresponding to lower risk for heart disease)
- ✓ Borderline high - 200 to 239 mg/dL (borderline high risk)
- ✓ High - 240 mg/dL and above (high risk)

High cholesterol levels in the blood are associated with various disorders such as hypertension, atherosclerosis, nephrosis, myxedema, jaundice and myocardial infarction [107]. Low levels of cholesterol may result in hyperthyroidism, anaemia and malabsorption. Thus, it is very important to develop the POC devices for estimation of cholesterol. In this regard, microfluidic biosensor can provide an efficient, simple and reliable detection strategy for its regular quantification.

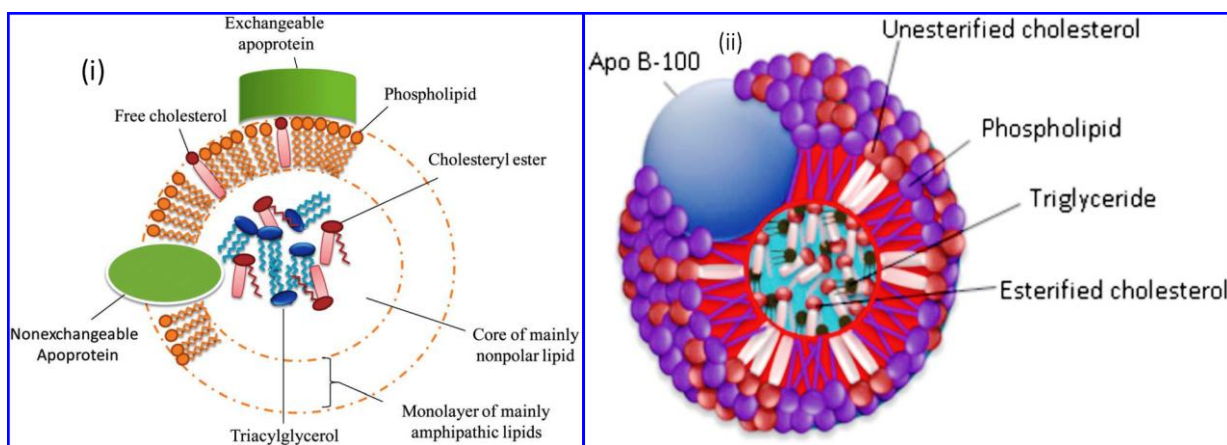


Figure 1.4(i) The structure of lipoprotein molecule and (ii) LDL particle model [110].

The physical and chemical characteristics of lipoproteins (density range between 1.019 and 1.063 kg/L) are listed in Table 1.3. LDL particles vary in size and density and can carry 60–70% of the total serum cholesterol. The core of a lipid particle consists of CEs and TGs which are surrounded by PLs, free cholesterol and apolipoproteins (proteins) [Figure 1.4(i)]. Apolipoprotein B 100 is amphipathic in nature and highly insoluble in aqueous solution that can interact with lipid moieties of lipoproteins and is specialized to facilitate several biochemical steps in lipid metabolism. Figure 1.4(ii) is a pictorial schematic model of the LDL particle. Hydrophobic core LDL particle contains CEs and TGs where the hydrophilic outer shell of LDL contains the PLs and free cholesterol. Classifications of lipoproteins are shown in the Table 1.4. The major component of atherogenic lipoproteins is the apo B 100 which has been identified by the National Cholesterol Education Program (NCEP). High density lipoprotein (HDL) is the smallest lipoprotein and carry 20– 30% of the total serum cholesterol [102]. The two major apolipoproteins of HDL are known as Apo A-I and apo A-II. All the apolipoproteins except apo B-100, are helical with a hydrophobic and a hydrophilic domain. HDL transports cholesterol away from arteries thus, it is known to be as good cholesterol (which can remove excess cholesterol in the blood and can help to protect you against heart diseases).

Table 1.3 Classifications of lipoproteins with concentration [110]

Lipoproteins	Concentration (mg/dL)	Classification	Risks
LDL cholesterol	<100	Optimal	Heart attack, Stroke, Hypercholesterolemia, Cardiovascular disease
	100-129	Near or above optimal	
	130-159	Borderline	
	160-189	High	
	≥ 190	Very High	
HDL cholesterol	<40	Low	
	≥60	High	

Table 1.4 Classification of lipoproteins [110]

Class	Density (kg/L)	Diameter (nm)	Protein (%)	Free Cholesterol (%)	Esterified Cholesterol (%)	Phospho-lipids (%)	Triglycerides (%)
HDL	1.063-1.21	8-15	33	7	40	46	6
LDL	1.019	18-24	25	11	50	29	10
VLDL	0.95-1.006	30-52	10	7	18	20	55
CM	<0.95	80-1200	<2	2	3	8	85

Currently, several methods including ultracentrifugation, nuclear magnetic resonance (NMR) spectroscopy, electrophoresis, chromatography, Friedewald method etc. are being used for the estimation of cholesterol, LDL etc. in the clinical laboratories. The ultracentrifugation techniques are tedious, time consuming and have poor reproducibility thus, this method is not considered practical for use in clinical laboratories. However, ultracentrifugation can be considered as a reference method for estimation of HDL and LDL cholesterol. Another common method is Friedewald calculation which is used to detect LDL cholesterol from human serum sample. The Friedewald Eq. (1.1) is given by [102]

$$\text{LDL-cholesterol} = \text{TC} - \text{HDL-cholesterol} - \text{TG}/5 \text{ (mg/dL)} \quad \text{Eq. 1.1}$$

In large scale studies, this method is commonly used in the clinical laboratory. However, the accuracy/precision is the major limitation of this method. Electrophoresis techniques can be used to detect lipids such as cholesterol and triglycerides (TGs) due to the differences in the size and charges of various lipoproteins. This method can be used for qualitative analysis of lipoproteins though it may not give a quantitative picture. Both ultracentrifugation and electrophoresis have disadvantages especially when the workload is high for routine tests in clinical laboratories. Chromatography technique is used to separate lipoproteins such as high density lipoprotein (HDL), low density lipoprotein (LDL), very large low density lipoprotein (VLDL) and CM from serum samples. The stability of this strategy is poor, due to using two columns with subsequent determination of cholesterol concentration using an online enzymatic reaction.

In order to develop an efficient, fast and cost effectiveness detection strategy for cholesterol, LDL etc. the POC devices can play critical role in health-care diagnostics. An electrochemical technique for rapid detection of cholesterol using PDMS microchip capillary electrophoresis based on the enzymatic reaction have been reported by Ruecha et al. [111]. A very small volume of whole blood is only needed

for a fingerstick POC test and results are available soon after sampling, which is advantageous in self-management of hypercholesterolemia. Earlier detection and disease management and cost-effectiveness are some other advantages offered by POC diagnostics. Researchers have also focused the nanostructured materials for electrochemical detection of cholesterol, LDL and triglyceride etc. Solanki et al. have reported a biosensor based on nanostructured cerium oxide film for triglyceride detection [112]. Nanostructured iron oxide platform has been developed for impedimetric cholesterol detection [113]. Electrophoretically deposited polyaniline nanotubes based electrode platform has been developed for cholesterol of detection [114]. Such techniques could perhaps be used for selective determination of HDL-C and LDL-C for POC. However, the miniaturization and requirement of huge amount of sample/reagent are the main disadvantages of the POC devices.

1.6 Motivation of the work

This research work is an effort to explore the possibility of developing low cost, simple, efficient and highly reliable strategy for detection of biomolecules, more specifically, cholesterol for its routine quantification. Having outlined, the exceptional qualities associated with microfluidics, the main focus of this research is to integrate microfluidics to realize compact POC devices. It is aimed at improving the state of art POC devices by structural innovation brought in through the recent developments in nanotechnology. Incorporation of nanostructured metal oxides on electrode surface would improve the biosensor efficacy such as detection limit, sensitivity, selectivity, detection time and long term functional stability of the devices.

Though this research is applicable to a wide variety of biomolecules, free, total and LDL cholesterol have been chosen as the targeted candidates for detection, due to its high importance in clinical health care and point-of-care applications. With this motivation, the main objectives in this thesis are described in the next Section.

1.7 Objectives of the thesis

The objective of this thesis is to design, develop, and characterize various microfluidic chips incorporating biofunctionalized nanostructured materials for POC diagnostics. To construct the microfluidic biosensors, PDMS has been selected as a suitable material for the fabrication of different microchannel architectures. The studies are aimed at “Development of nanostructured metal oxide-based microfluidic biosensors for the detection of free/total cholesterol and low density lipoproteins”. To achieve this objective, the following steps have been envisaged:

1. Development and fabrication of microfluidic PDMS channels and ITO microelectrodes to complete the biochips.

2. Explore various nanomaterials for the modification of microfluidic electrodes and functionalization e. g.
 - a. Anatase-titania (TiO₂) nanoparticles
 - b. Chitosan modified titania nanoparticles
 - c. Nickel oxide (NiO) nanorods
 - d. Nickel oxide and carbon nanotubes composite
3. The biofunctionalization of these microfluidic electrodes with various biomolecules such as enzyme, antibody etc. and their characterization using various spectroscopic and morphological techniques.
4. Electrochemical detection (using cyclic voltammetry, chronoamperometry, impedance spectroscopy etc.) of cholesterol and LDL.

I have selected some suitable nanostructured materials such as TiO₂, NiO and their composites with chitosan and carbon nanotubes to be integrated with microfluidic assembly. Studies are carried out to immobilize these nanostructured microfluidic electrodes with biomolecules/proteins (cholesterol oxidase, cholesterol esterase, anti-apolipoprotein B, bovine serum albumin) via physical adsorption and covalent interactions. A systematic optimization of these microfluidic biochips is carried out by changing these proposed nanostructured metal oxides for cholesterol detection. In addition, characterization of these nanostructured metal oxides and their biofunctionalization is carried out. Comparative studies of these microfluidic biosensors for cholesterol detection are also investigated.

1.8 Thesis overview

The objective of this thesis is to design and develop various microfluidic chips that are capable of assembling biofunctionalized nanostructured materials for POC diagnostics. To construct the microfluidic biosensors, PDMS has been chosen as a suitable material for fabrication of different microchannels architectures using soft lithography technique in order to control the biological fluids such as cholesterol, LDL with buffer solutions. The patterned microelectrodes of indium tin oxide on glass substrate have been fabricated using photolithographic and wet chemical etching techniques. I have selected some suitable nanostructured materials such as TiO₂, NiO and their composites with chitosan and carbon nanotubes to integrate with microfluidic assembly. These nanostructured materials with biomolecules have been characterized using various spectroscopic and microscopic techniques. These synthesized materials have been utilized in the microfluidic systems in order to improve the biosensor efficacy. In this thesis, I have highlighted the materials synthesis and construction of highly efficient microfluidic biosensors for POC applications. Free cholesterol, total cholesterol and LDL cholesterol are the target analytes which I have selected to monitor electrochemically using these proposed microfluidic devices.

Chapter 1 of this thesis gives a brief description of the POC diagnostics, a historical snapshot of microfluidic biosensors, utilization nanostructured metal oxides in biosensors and their integration for biomolecules detection with literatures survey. Motivation of thesis has been described in this Chapter. I have illustrated the importance of various target analytes such as free, total cholesterol and LDL detection using microfluidic assembly. Electrochemical detection and their integration of microfluidic biochips for various biomolecules such as cholesterol, LDL etc. detection have been demonstrated. The importance of cholesterol and LDL detection in human blood serum using microfluidic technique and their advantages/disadvantages has been added. In the Chapter 2, the basic principle and construction of microfluidics devices such as fluidic transports, scaling effect, diffusion, mixing etc. have been described. Microfluidic components and materials have been illustrated in this Chapter. A brief literature survey on microfluidics devices has been included. A brief introduction of biosensor principle, characteristics, types of biosensors and immobilization techniques has been presented. The importance and applications of synthesized nanostructured metal oxides such as TiO_2 , NiO and their nanocomposites with chitosan and carbon nanotubes (CH- TiO_2 and CNT-NiO) in microfluidic biosensors have been included in this Chapter.

Chapter 3 deals with a broad overview of various materials, fabrication and characterization techniques that have been adopted in this thesis for the development of microfluidic biosensors. Attempts have been made to give detailed of PDMS microchannels fabrication using various steps of soft lithography. I have described the wet chemical etching and photolithography techniques for patterned microelectrodes (indium tin oxide; ITO) fabrication. I have also illustrated an overview of the chemical synthesis of nanomaterials. Various characterization tools and methods have been discussed in this Chapter. The Chapter 4 describes the experimental and results relating to the fabrication of nanostructured anatase- TiO_2 based microfluidic platform for free cholesterol estimation. The results of XRD, FT-IR, UV-visible, AFM and TEM of this integrated microfluidic system have been illustrated. Free cholesterol has been estimated using electrochemical technique using this proposed microfluidic POC biosensor. Additionally, I have prepared another candidate of chitosan modified TiO_2 nanoparticles for total cholesterol detection using microfluidic assembly. Chapter 5 gives the details of nickel oxide nanorods (NR-NiO) integration with microfluidic device for total cholesterol detection. Potential merits and demerits of this proposed microfluidic biosensor have been illustrated.

Chapter 6 explains the step by step fabrication process of a microfluidic biochip based on a composite comprising of nanostructured NiO and carbon nanotubes (CNT-NiO) for total cholesterol and LDL estimation. The fabrication of the microfluidic biochip using CNT-NiO nanocomposite has been explained. Additionally, I have investigated the toxicity effect of these synthesized CNT, NiO and CNT-

NiO in A549 cell line. I have characterized the CNT-NiO composite using various techniques such as XRD, Raman, XPS SEM and TEM. The electrochemistry of this proposed microfluidic biochip has been investigated using CV and EIS studies. The chronoamperometric results of the biochip for cholesterol oleate detection have been discussed. The Chapter 7 gives an overview of thesis summary and future prospects. The conclusion for each chapter has been described. A future prospect of the work including limitations and a new direction has been demonstrated.

1.7 Conclusions

In conclusion, I have given an introduction of POC diagnostics devices. A historical snapshot of microfluidic devices for detection of biomolecules has been highlighted. The state-of-the-art biosensors and their integration with microfluidics POC devices have been included. An overview of biosensors with the importance of nanomaterials has been explained with references to existing research literature. The next Chapter deals with the description of microfluidics. The basics principle and construction of biosensors have described. The details on nanostructured metal oxides have also been illustrated.

CHAPTER 2

Principles of Microfluidics, Biosensors and Applications of Nanostructured Metal Oxides

2.1 Introduction

This Chapter paves the basic principles of microfluidic devices including fundamentals of fluidic transportation, mixing, diffusion and scaling effects. The various components and materials for microfluidic devices have been illustrated. An overview of biosensor principle, types and immobilization techniques have been described. Current developments in nanostructured metal oxides/composites and their applications in biosensing devices have also been explained.

2.2 Principle of microfluidics

Microfluidic platforms find applications in many fields using the pressure driven laminar flow, lateral flow tests, linear actuated devices, centrifugal microfluidics, microfluidic large scale integration, electrokinetics, electrowetting and surface acoustic waves as depicted in Figure 2.1.1 [115-117]. Mark et al. have reported that a microfluidic platform provides a set of fluidic unit operations, which are designed for easy combination within a well-defined fabrication technology [115]. A microfluidic platform provides a generic and consistent way for miniaturization, integration, automation and parallelization of bio-chemical processes. Utilization of fluid transport models in light of the development of microfluidic devices have found many applications towards the drug design, delivery and detection, diagnostic devices. Many researchers have focused on specific microdevices using valves, pumps, actuators, mixers and reactors, sensors, and three-dimensional channels networks [116]. The transport processes including mixing, reactions, and separations in micro-domain play an important role in lab-on-a-chip devices. In a microchannel, the low-Reynolds numbers inherent in most microfluidic systems lead to laminar flows that can be predicted and designed in a uniform fashion. Researchers have investigated the fundamental transport and scaling principles of micro/nanofluidic flows for manipulation and analysis [115, 117]. Kamholz et al. have demonstrated the molecular diffusion in pressure-driven laminar flow in microfluidic channels [118]. Pamme et al. have described the fluid flow separations using microfluidic platform [119]. Fluid separation in microfluidics is commonly used in electrophoresis and chromatography via filtration and centrifugation. Liu et al. have explained mixing of two fluids in a microchannel [120]. Sudarsan et al. have described fluid mixing in planar spiral microchannels [121]. In a microfluidic flow, the continuum approximation of different fluidics characterization is important since it allows us to analyze with the same governing principles developed for macroscale fluid mechanics.

2.2.1 Governing equations

Fluid flow in micro or nanochannels with a characteristic length of more than 10 nm, the flow of a Newtonian, isotropic, and incompressible fluid can be described respectively by the continuity equation, and the Navier-Stokes equation [122]. The continuity equation is given by

$$\frac{Dp}{Dt} + \rho \operatorname{div}\nabla = 0 \quad \text{Eq. 2.1.1}$$

where ∇ is the Laplace operator, $\frac{D}{Dt}$ is the total derivative operator in a three-dimensional Cartesian coordinate system and is given by

$$\frac{D}{Dt} = \frac{\partial}{\partial t} + u \frac{\partial}{\partial x} + v \frac{\partial}{\partial y} + w \frac{\partial}{\partial z} = \frac{\partial}{\partial t} + (\mathbf{v} \cdot \nabla) \quad \text{Eq. 2.1.2}$$

and $\mathbf{v}=(u,v,w)$ is the velocity vector. The Navier-Stokes equation is derived from Newton's 2nd law is given by

$$\rho \frac{D\mathbf{v}}{Dt} = \rho \mathbf{F} - \nabla p + \mu \nabla^2 \mathbf{v} \quad \text{Eq. 2.1.3}$$

where ρ is the density of the fluid and μ is the dynamic viscosity of the fluid.

2.2.2 Reynolds number and laminar flow

Fluid flow can be characterized by the Reynolds-number which is a dimensionless number [123]. It can be defined as the ratio of inertial to viscous forces of the liquid in motion and is given by Eq. 2.1.4

$$\frac{\text{Inertial Force}}{\text{Viscous Force}} = \frac{\rho u L}{\mu} \quad \text{Eq. 2.1.4}$$

where u is the average flow velocity, L is the characteristic length, μ is the dynamic viscosity, and ρ is the density of the fluid. The kinematic viscosity of water being $\nu = 10^{-6} \text{ m}^2/\text{s}$, the Reynolds number is of the order of 1. Typical Reynolds numbers vary from 10^{-4} to 1. Thus, a laminar flow would mean that the streamlines are locally parallel and that even obstacles in the flow will not induce any turbulence. Resistance per length of the channel wall increases when the channel diameter narrows. When downscaling to the microlevel, the flow resistance increases rapidly with narrowing channel diameter, compared to larger channels. This is the reason why laminar flow occurs in microchannels; viscous force dominates due to large surface to volume ratio. Details and importance of Reynolds number have been described by Squires et al. [124]. Schematic description of fluid flow for (a) laminar and (b) turbulent is shown in Figure 2.1.2. Fluidic molecules transported in a parallel and predictable fashion, with no disruption between the layers is called laminar flow. At low velocities the fluid tends to flow without lateral mixing. In a laminar flow, the motion of particles of the fluid is very orderly with all particles moving in straight lines parallel to the channels walls. Laminar flow tends to occur at lower velocities, below the onset of turbulent flow.

The Knudsen number has great importance in gas dynamics. It provides a measure of how rarefied a flow is, or how low the density is relative to the length scale of the flow. The Knudsen number is given by

$$K_n = \lambda/L \quad \text{Eq. 2.1.5}$$

where λ is the mean free path given in and L is some length scale characteristic of the flow.

The different regimes of behavior are:

- ✓ **Re** \ll 1 viscous effects dominate inertial effects
- ✓ **Re** \approx 1 viscous effect comparable to inertial effects
- ✓ **Re** \gg 1 inertial effects dominate viscous effects

In channel flows is,

- ✓ **Laminar**, when $Re < 2300$
- ✓ **Transient**, when $2300 < Re < 4000$
- ✓ **Turbulent**, when $4000 < Re$

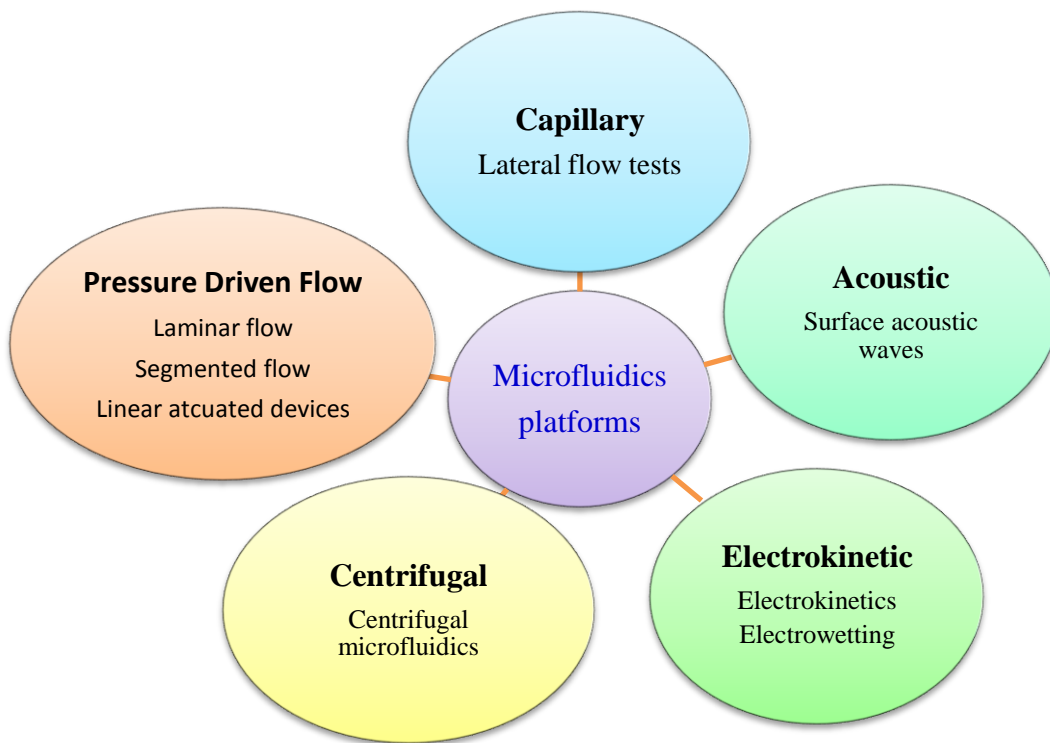


Figure 2.1.1 Microfluidic platforms classified according to main liquid propulsion principle [115].

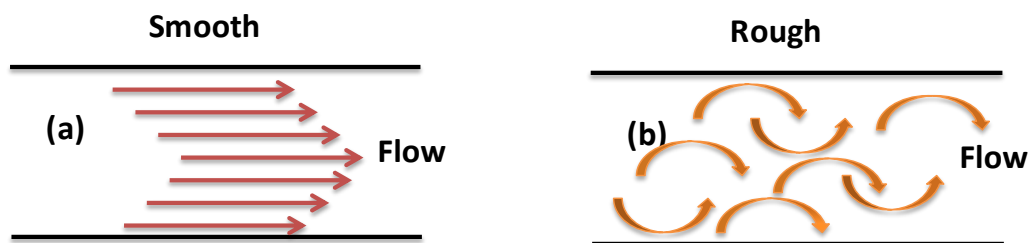


Figure 2.1.2 Schematic description the fluids flow for (a) laminar and (b) turbulent

2.2.3 Turbulent flow

In turbulent flow, fluid molecules move in an irregular and unpredictable fashion. In this flow, the speed of the fluid molecules at a point continuously undergoes changes in both magnitude and direction. In turbulent flow vortices, turbulent flow occurs in general at high flow rates and with larger pipes.

2.2.4 Transitional flow

It is a mixture of turbulent and laminar flow. In this flow, turbulence occurs in the centre of the pipe while flow near the edges is laminar. During flowing, such flows behave in different manners in terms of their frictional energy loss. In this flow, the fluid molecules acquire an irregular fluctuation under an external disturbance.

2.2.5 Pressure-driven flow

In micro-domain, a pressure-driven flow can be characterized by liquid transport mechanisms based on pressure gradients resulting in stable laminar flow profiles [125]. In fluid mechanics, the pressure-driven flow at no-slip boundary condition states that the fluid velocity at the walls must be zero. The pressure-driven flow produces a parabolic velocity profile and allows the straight forward way of moving fluid molecules in a microfluidic device. External or internal pressure sources such as syringes, pumps or micropumps, gas expansion principles, pneumatic displacement of membranes, etc. can be used to control liquid in microchannels. The samples and reagents can be injected through the inlet of chip either batch-wise or in a continuous mode. The main drawback of using pressure as a means of transport is that the pressure driven flow will display a non-uniform velocity profile. Sia et al. have described the details of pressure-driven flow in microfluidic devices [126]. Schematic representation of typical pressure driven fluid flow is shown in Figure 2.1.3. It can be difficult to maintain the smoothness of the flow when using pumps to drive the flow in small microfluidic channels.

In case of linear actuated devices, the liquid movement can be controlled by mechanical displacement such as a plunger. Fluid control is limited to a one-dimensional path, where the flow is dominated only in a linear fashion without branches. Segmented flow illustrates the principle of using small liquid droplets immersed in a second immiscible continuous phase (gas or liquid) as stable micro-confinements within the microchannels [115]. In this case, flow can be transported using pressure gradients and can be merged, split, sorted, and processed without any dispersion in microchannels. In centrifugal microfluidics, all processes are controlled by centrifugal force, Euler force, Coriolis force and capillary force [127].

Active pumping: Precise flow control in microfluidics is a key parameter to the proper functioning of devices. In active pumping, the fluid flow can be controlled using external sources, like mechanical displacement, centripetal force and electrical fields [128]. Syringe pump is one of the simplest

microfluidic pump widely used in laboratories. In order to move the plunger of syringe pump at a constant speed, a stepper motor can be used. It can be used for a wide range of volumes and flow rates. Main disadvantages are large dead volumes and significant flow hysteresis. Active pumping is confined to the research laboratories only.

Passive pumping: The fluid flow rate in microfluidics can be manipulated using passive valves. Driving forces to move liquids in passive microfluidics are chemical gradients on surfaces, osmotic pressure, and permeation in PDMS or capillary forces. This microfluidic flow occurs spontaneously and is appealing, owing to their portability, zero power consumption and low dead volumes. These devices are attractive because of their low cost. A disadvantage is that the flow rates of fabricated devices are set in the design and thus can only be varied to a limited degree.

2.2.6 Scaling effects

In microfluidics, the scaling law is a physical phenomena and it can be different for different microscale devices compared to that of macroscale devices. The device miniaturization can change the ratio of different physical effects leading to new fluidic behaviours with new applications [129]. Squires et al. have reviewed various scaling effects for microfluidic devices at a nanolitre scale [130]. For example, surface tension dominates over gravitational forces, electric fields tend to be far more influential than pressure gradients and molecular diffusion becomes more significant relative to bulk fluid displacement. In particular, the fluid properties such as diffusion time, distance and surface-to-volume will be varied. The change of the spatial dimension or the size of the fluidic component of interest is characterized by the scaling factor, $S = l/l_0$, where l_0 is the reference size. Miniaturization indicates that the scaling factor is smaller than unity ($S < 1$). On the other hand, different forces occurring in the micro- and nanoscale are categorized as surface forces and volume forces. The surface forces (surface tension and viscous friction) are proportional to the surface area, while volume forces such as weight, buoyancy force, or inertial force are proportional to the volume. The scaling of the ratio between surface force and volume force is given by

$$\frac{\text{Surface force}}{\text{Volume force}} = \frac{A}{V} = \frac{L^2}{L^3} = \frac{1}{L} = S^{-1} \quad \text{Eq. 1.1.4}$$

where L , A , and V are the characteristic length, surface area, and volume, respectively.

2.2.7 Capillary flow

Fluid molecules can be transported via capillary action or capillary forces which results from the interaction of liquid, gas and solid surfaces, at the interface between them. For example capillary flow is utilized for a common commercially available pregnancy test strips for the intake of sample. In this case, the fluidic molecules are driven by capillary forces [131] and their movement is controlled by the

wettability and feature size of the porous or microstructured substrate. A color change can be seen in the detection area due to the chemical reaction.

2.2.8 Diffusion and mixing

Mixing strategies in microfluidics can be either active or passive depending on the operational mechanism. The active mixers utilize the external forces, beyond the energy associated with the flow for performing mixing. Mixing of fluids in microfluidics are difficult because flow is typically laminar and it depends on diffusion. Researchers have proposed different approaches for fluid mixing in microfluidics. Sudarsan et al. have demonstrated mixing of fluids in microfluidic devices [121]. In addition, the passive mixers avoid the problems by exploiting characteristics of specific flow fields to mix species without application of external electrical or mechanical forces. Passive mixers are reliable and cost effective compared to active mixers. Microfluidic platforms have been used to manipulate the distribution of chemical species. The chemical separations, for example, physically separate components of a multispecies mixture so that the quantities of each component can be analyzed and useful species can be concentrated or purified from a mixture [120]. Many biochemical assays such as DNA microarrays, require that a reagent be brought in contact with the entirety of a functionalized surface, i.e., that the reagents in the system are well mixed. The mixer benefits from a short path and efficient mixing at the cost of increased complexity in fabrication and packaging.

2.2.9 Electrokinetics

Another well known transport process in microfluidic devices is the use of electrokinetic flow [132]. In electrokinetics, the fluidic operations are controlled by electric fields acting on electric charges, or electric field gradients acting on electric dipoles. Depending on fluids, several electrokinetic effects such as electroosmosis, electrophoresis, dielectrophoresis, and polarization may produce in the microfluidic channel. The electrokinetic flow arises when a polar liquid is brought in contact with the solid channel wall when subjected to an electric field. Once the wall comes in contact with the polar liquid, the wall surface acquires an electric charge. This will cause the relocation of charges inside the liquid yielding a thin layer of ions at the wall surface oppositely charged to the charge of the wall. This is known as the Stern layer. Outside the Stern layer another thicker layer of excess charges is formed known as the diffuse layer. This layer contains an excess of charges of the same polarity as those in the Stern layer. The ions within the Stern layer are fixed whereas those in the diffused layer are mobile. Figure 2.1.4 shows the schematic of the representation of charges in a channel under electroosmotic conditions.

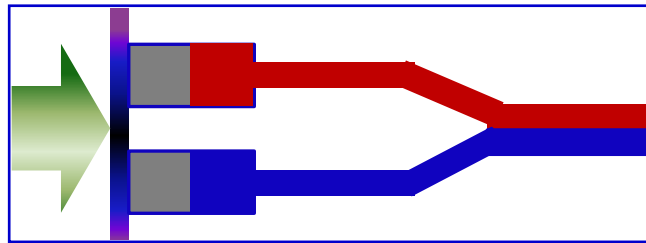


Figure 2.1.3 Schematic representation of a typical pressure-driven fluid flow

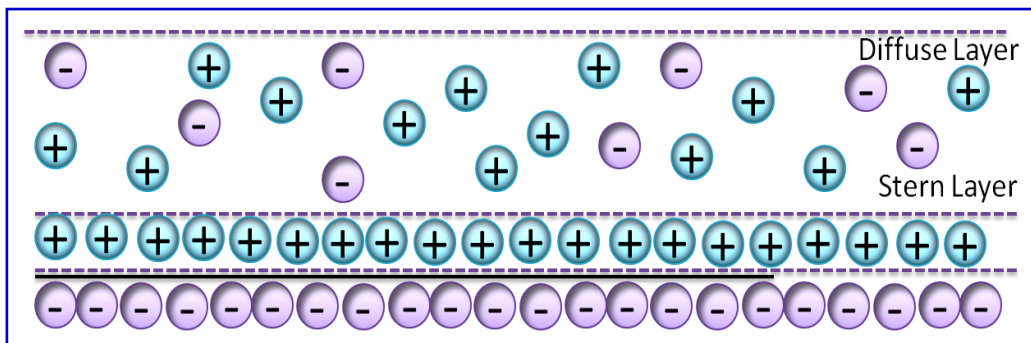


Figure 2.1.4 Schematic of the configuration of charges in a channel under electroosmotic conditions showing the mobile charges the diffusive and fixed charges in the Stern layer.

The electric fields in microchannels can cause bulk fluid motion and the velocity of this motion is linearly proportional to the applied electric field. The velocity is dependent on both the material used to construct the microchannel and the solution in contact with the channel wall. This motion is known as electroosmosis, and stems from electrical forces on ions in the electrical double layer, a thin layer of ions that is located near a wall exposed to an aqueous solution. If the fluid velocity is interrogated at millimetre resolution, (e.g. the fluid flow can be observed by a light microscope), the fluid flow in a channel of uniform cross-section appears to be uniform. On the other hand, if the fluid velocity is interrogated with the nanometre resolution, the fluid velocity would be uniform far from the wall, but it would decay to zero at the wall over a length scale of λ_D ranging from approximately 0.5–200 nm. However, this flow comes with its own complications, as its velocity distribution is different from pressure driven flow. It is sensitive to chemical features at the interface, since applied electric field can also move particles relative to the fluid or cause Joule heating (i.e., resistive heating) throughout the fluid. The electrowetting platforms utilize droplets immersed in a second immiscible continuous phase (gas or liquid) as stable micro-confinements. The droplets inhabit a hydrophobic surface that contains a one or two dimensional array of individually addressable electrodes. By varying voltages between electrodes, the droplets can be generated, transported, merged, split and processed.

2.3 Components of microfluidic devices

The microchannel in microfluidics system is an important component that can be used to control biological fluids, buffer solution etc. in uniform fashion [118, 126]. For coupling between two or more microfluidic systems, or between a microfluidic system and the exterior world, microchannel can be used. Other control elements such as valves and pumps, are complicated to be fabricated using silicon technology and then difficult to be integrated onto lab-on-a-chip systems. However, the use of ‘soft’ technologies based on elastomers offer elegant possibilities for valves and pumps. The injection of fluids is a practical difficulty and it does not always have a simple solution, especially when the sample is very small and not amplifiable (for example, proteins extracted from a single cell). The sample can be diluted to a large volume so that it can be manipulated more easily. However, this creates a series of difficulties, including the need for sensitive instrumentation. The injection of minute quantities of fluid remains an open problem in the management of fluid volumes.

2.4 Materials for microfluidic devices

Materials such as silicon, glass, polymers, plastics (cyclic olefin copolymer or polystyrene), paper (nitrocellulose or cellulose), waxes, and adhesives have been used to fabricate microfluidic devices [133]. In early microfluidic systems, silicon was used as a substrate owing to the wealth of existing microfabrication production. Many researchers have used standard photolithography and etching

processes to construct microfluidic channels of precise dimensions on silicon wafers. However, the focus shifted from silicon to glass substrates due to the number of advantages of glass over silicon. Glass is a transparent material since it allows the visualization of on-chip processes and is more compatible with electroosmotic flow than conductive silicon. In addition, glass can be easily bonded to a second substrate than silicon. The characteristics of glass such as surface stability, solvent compatibility, easy of fabrication etc. are beneficial for practical realization of a microfluidics device [134]. Nie et al. have reported a POC device that can be used to detect glucose, cholesterol, lactate, and alcohol etc. in blood or urine using patterned chromatographic paper (Whatman 1 Chr) [135]. This technique allows the reproducible conformal contact between the electrode and the paper channel and can be easily scaled to large numbers, requires a smaller quantity of analyte solution. Silicon has the added advantage that it can combine on-chip electronics with microfluidic networks. Besides this, silicon supports the most precise geometrical tolerance, which is becoming increasingly important as channel dimensions continue to decrease. Though from a cost point of view, PDMS is simpler and universal material for microfluidic applications compared to both glass and silicon wafers.

Polymeric materials including polydimethylsiloxane (PDMS), polymethylmethacrylate (PMMA), polycarbonate (PC) etc. show superior properties such as chemical resistance, aging, mechanical, optical etc. over glass and silicon for a number of reasons [134, 136]. The last 10 years have witnessed a shift from silicon to polymeric micromachining as a low-cost alternative for the fabrication of microfluidic devices. In soft lithographic microfabrication, PDMS behaves like an elastic solid that maintains its molded structure when cured. The use of PDMS for microfluidic applications was first presented by George M. Whitesides in the mid-1990s [35-37]. In this method the elastomeric monomer is poured over a master mold structure (typically a silicon wafer with an inverse photoresist structure of the channel geometry) and is then cured. The cured structures can be simply peeled from the master and bonded to a planar substrate, forming the microchannel structures. The master mold can be reused multiple times to replicate devices. Details of this method have been described in the materials & methods section of Chapter 3.

The PDMS, PC or PMMA have been widely used in majority of microfluidic research laboratories. The PDMS behaves like an elastic soft material that maintains its molded structure. It offers low cost, flexibility, and rapid prototyping. PDMS is known to have poor chemical compatibility with many organic solvents as it tends to swell upon contact, making it mainly suitable for aqueous applications. Modification of the PDMS surface is unstable over time. PDMS adsorbs small molecules and it can be deformed under pressure of pneumatic valves. High pressure operation on PDMS devices can lead to large alteration of channel geometry and hence is not desirable. Though, PDMS has gained widespread acceptance in the field of microfluidics, glass and silicon certainly have increased utility in

fabrication of microfluidic devices. Other polymers including PMMA and PC have also been explored for microfluidic applications. These materials adopt techniques like hot embossing and injection molding for device fabrication. PMMA is a thermoplastic material for high-resolution photoresists and it can be patterned into microchannels or other structures by hot embossing. In addition, PMMA is optically transparent and can be patterned by laser cutting. However, PMMA can restrict light transmission in the UV range, which limits its applicability in sensing. PMMA can easily be integrated with metal electrodes and its surface can be functionalized for electrochemical sensing applications. PMMA is also used as an intermediate material for fabrication of microfluidic devices. Plecis et al. have demonstrated the fabrication of microfluidic devices based on glass–PDMS–glass technology [137]. Quake et al. have described the micro-nanofabrication using soft materials [138]. Sia et al. have described the fabrication of PDMS based microfluidic devices for biological studies [126].

Surface modification of PDMS using various techniques such as air/oxygen/argon plasma, UV/ozone and corona discharge etc. can produce silanol terminations (SiOH) on its surface thereby leading to increased hydrophilicity. Hydrophilicity of PDMS is limited to a period of 20-30 minutes and is subjected to swelling in organic solvents. PDMS can restrict detection of shorter wavelength (near 400 nm). Bodas et al. have described the formation of more stable hydrophilic surfaces of PDMS by plasma and chemical treatments [139]. Permanent modification of PDMS surface using various chemical treatments has been investigated. Wu et al. have developed a facile approach to modify PDMS using a vinyl-terminated initiator that is mixed with Sylgard 184 (PDMS oligomer and curing agent) [140]. But the modified PDMS surface becomes unstable over time. Bodas et al. have developed another approach to modify hydrophobic surface of Sylgard 184 PDMS using oxygen plus C_2F_6 and 2-hydroxyethyl methacrylate with exposure time of 15 min [139] and observed that the hydrophilicity of PDMS surfaces are increased to 2 days and 10 days, respectively. Researchers have modified the PDMS surface by self assembled monolayer (SAM) to reduce swelling resulting in improved stability [141].

2.5 Biosensors

A sensor is a device that detects or measures a physical property and records, indicates or otherwise responds to it. A transducer is a device that converts an observed change (physical or chemical) into a measurable signal. It is an analytical device that enables the identification and quantification of an analyte of interest from a sample matrix, for example, water, food, blood, or urine [142]. A biosensor is an analytical device incorporating a biological sensing element connected to a transducer. Various definitions and terminologies are used depending on the field of applications. According to the IUPAC definition, “A biosensor is a self-contained integrated device which is capable of providing specific quantitative or semi-quantitative analytical information using a biological recognition element which is in

direct spatial contact with a transducer element” [142]. The “specific biological element” recognizes a specific analyte and, the changes in the sensor surface due to interaction of biomolecules or reaction are usually converted into electrical signal by the transducer. The bio-element may be an enzyme, antibody, antigen, living cells, nucleic acid, lectine, hormone, and tissues, etc. The bio-element is very specific to the analyte to which it is sensitive. It does not recognize other analytes. The large variety of sensor-elements includes electric current, electric potential, intensity and phase of electromagnetic radiations, mass, conductance, impedance, temperature, viscosity, and so on. The “sensor” element transduces the change in the biomolecules into an electrical signal. Various components of a biosensor is shown in the Figure 2.1.5. The basics of biosensors, its various types and immobilization methods are discussed in this section.

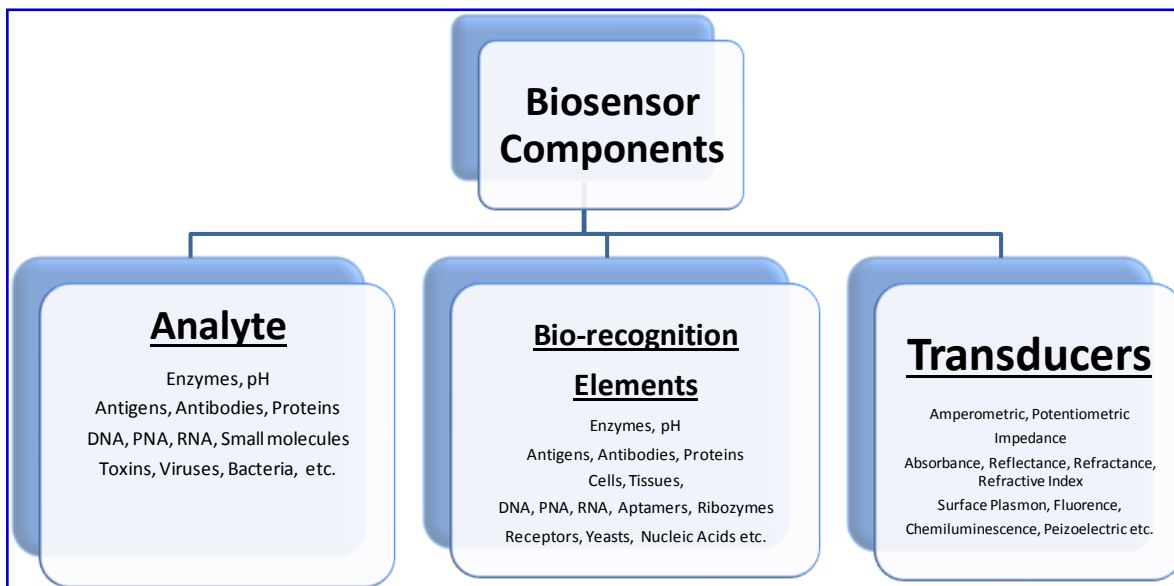


Figure 2.1.5 Main components of biosensor

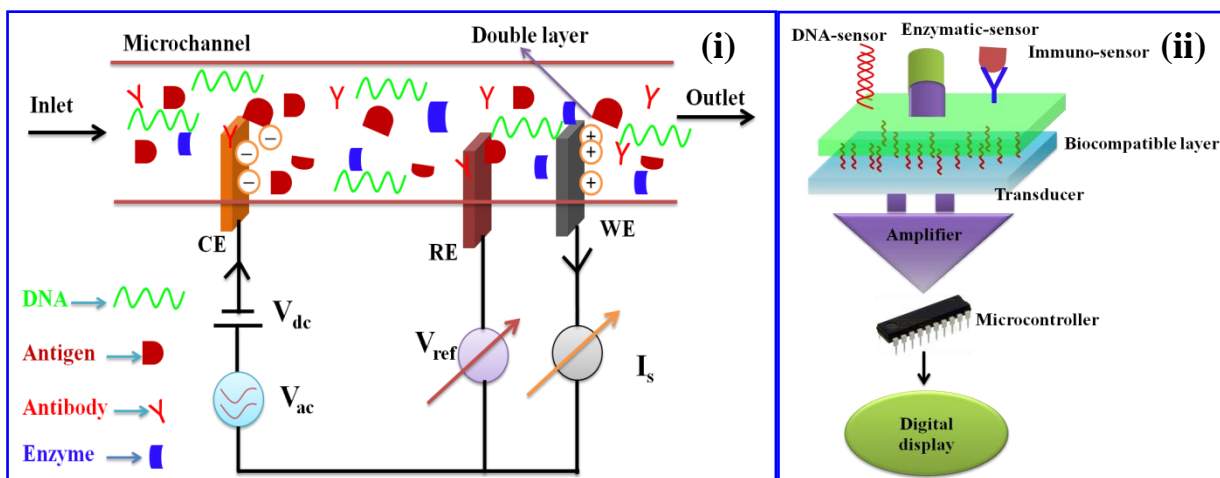


Figure 2.1.6 Schematic representation of (i) a three electrode based microfluidic biosensor and (ii) a typical biosensor.

2.5.1 Characteristics of biosensors

- i. Accuracy
- ii. Sensitivity and specificity – no environmental interference,
- iii. Measurement range –susceptible to saturation?
- iv. Speed of response –e.g. nerve agents
- v. Re-usability – antibody based often not re-usable due to tight interactions
- vi. Self-testing/ calibration
- vii. Physical robustness
- viii. Cost – capital, running
- ix. Acceptability and ease of use by users
- x. Product-safety

2.5.2 Electrochemical biosensor

An electrochemical biosensor measures current, voltage, impedance or capacitance based on an enzymatic catalysis of a reaction that produces electrons. This biosensor consists of a reference electrode, a counter electrode and a working electrode. In this biosensor, the target analyte involve an enzymatic reaction that takes place on electrode surface. This reaction on sensor surface can cause the electron transfer through the double layer that produces a current or can contribute to the double layer potential that produces a voltage. The rate of flow of electrons or measured current or potential is directly proportional to the analyte concentration at a fixed potential or zero current, respectively. Electrochemical biosensors can detect desired analytes without damaging the system [143]. In this configuration, bio-receptor molecules are either coated onto or covalently bonded to a transducer surface. The bio-receptor molecules react specifically with target analytes to be detected. Based on their operating principle by which chemical information is converted to a measurable signal, electrochemical sensor can be classified into three categories namely: potentiometric, amperometric and impedimetric, biosensors. Construction of an electrochemical cell for electrochemical biosensors measurement has been described in the next Section. Types of electrochemical biosensor are given below.

2.5.3 Amperometric/potentiometric biosensor

Amperometric sensors [144] measure the current change resulting from a chemical reaction between electroactive materials while a constant potential is being applied [Figure 2.1.7(i)]. The observed change in the current is related to the concentration of the species in solution. The working electrode of the amperometric biosensor is usually either a noble metal, ITO or a screen-printed layer covered by the bioreceptor-element. By applying potential, the current (typically in nA to mA range) is measured due to

the conversion of electroactive species generated in the enzyme layer at the electrode surface. Several amperometric biosensors have been investigated for the estimation of various target molecules [145]. Potentiometric biosensors are based on ion-sensitive field effect transistors (ISFET), graphene-FET or bioFET as shown in Figure 2.1.7 (ii & iii). In the case of ISFET, the output signal can be measured due to ions (H^+ , pH etc.) accumulated at the ion-selective membrane interface. Carbon materials such as carbon nanotubes, graphene, etc. are explored for detection of biomolecules by varying drain potential/current in FET devices. Mao et al. have grown graphene vertically for the development of FET potentiometric biosensor [146].

2.5.4 Impedimetric/capacitive biosensor

The impedance spectroscopy is a label-free technique that has been widely used for probing various types of biomolecular interactions such as enzymatic, immunosensors, DNA hybridization and protein-protein interactions [147]. When a target biomolecule interacts with a probe-functionalized surface, the electrical properties of the surface (e.g., dielectric constant or resistance) can change exclusively due to the presence of the target molecules. Thus, no label is required for impedance sensing. The electrical impedance can measure the resistance of an electrochemical cell when a voltage is applied. It can be defined as the ratio of the voltage to the current in the frequency domain. Impedance-based biosensors measure the electrical impedance of an interface with constant DC bias conditions. In an electrochemical cell, various phenomena such as electrode kinetics, redox reactions, diffusion and molecular interactions occur at the electrode surface that influences the flow of electrons for impedance analysis. The most interesting formats for evaluating electrochemical impedance data are the Nyquist and Bode plots.

Capacitive biosensors utilize the change in dielectric properties and/or thickness of the dielectric layer at the electrolyte-electrode interfaces, due to the interaction of biomolecules. An ideal capacitor has the ability to store charge and thus, the electric capacitance between the working electrode and the electrolyte is $C = \epsilon_0 \epsilon A/d$; where, A is the area, d is the separation between the plates, ϵ_0 is the dielectric constant and ϵ is the relative static permittivity. The circuit construction and basic theory of impedance/capacitive measurement has been explained in next Chapter. Lee et al. have developed an electrochemical impedance biosensor with aptamer-modified pyrolyzed carbon electrode for label-free protein detection [148]. Lee et al. have reported the strategy for one-chip electronic detection of DNA hybridization using precision impedance-based CMOS array sensor [149]. Wang et al. have developed a TiO_2 nanowire bundle microelectrode based impedance immunosensor for rapid and sensitive detection of *Listeria monocytogenes* [150].

2.5.5 Optical biosensor

In an optical biosensor, the transduction process induces a change in some optical property of input light, namely absorption, transmission, reflection, refraction, phase, amplitude, polarization or frequency in response to the physical or chemical change produced by the biorecognition process [151]. Optical biosensors offer several advantages like high selectivity and specificity, remote sensing, isolation from electromagnetic interference, label free detection, real-time measurements and multi parameters detection. They can operate non-invasively or minimally invasive for *in vivo* measurements [152].

One reliable and highly sensitive optical method for biosensor application is surface plasmon resonance (SPR). SPR is an optical phenomenon occurring at the interface between noble metals (e.g. silver, gold etc.) and dielectric materials that results in collective oscillations of the conductive electrons induced by light [153-155]. This change in SPR angle characteristics is the actual monitored signal, and the change over time form the sensorgram. Many researchers have investigated different approaches to fabricate gold nanoparticles [156] with various shapes and characteristics for label-free detection of biological molecules, such as glucose, cholesterol, low density lipoprotein and DNA via SPR. Recently, Feltis et al. demonstrated a low-cost handheld SPR-based immunosensor for the toxin ricin [157]. Luo et al. developed a multilayer PDMS array consisting of multiple gold spots for the real-time observation of immunocomplex formation using SPR [158].

2.5.6 Piezoelectric sensors

In a piezoelectric sensor, the piezoelectric effect is exploited to measure strain, force, pressure or acceleration by converting them to an electrical signal. In this mode, sensing molecules are attached to a piezoelectric surface wherein the interactions between the analyte and the sensing molecules set up mechanical vibrations that can be translated into an electrical signal proportional to the amount of the analyte. An example of such a sensor is quartz crystal micro or nano balance. Major disadvantage of piezoelectric sensors is that they cannot be used for truly static measurements [159].

2.5.7 Enzymatic biosensor

Enzymatic biosensors provide a powerful platform for the POC diagnostics. In an enzymatic biosensor, enzyme is immobilized onto a suitable transducer and it produces a specific signal upon reaction with an analyte. The main purpose is to convert an enzymatic reaction into a suitable analytical signal (electrochemical, colorimetric, optical properties etc.). The thrust is towards developing biosensors for the easy detection of the most important parameters like blood-sugar, urea and cholesterol that may serve as an indicator about the onset of a disease.

Ever since the proposal of glucose biosensor in 1962 [65], several devices based on electrochemical biosensors have been developed [65]. Most of these devices are based on enzyme-functionalized screen-printed disposable electrode strips that work on the principle of amperometric detection. These hand-held POC testing devices help in self monitoring as well as getting quick, reliable and accurate results using small volume of samples. Quantitative analysis of glucose via biosensor primarily follows two mechanisms which are presented in Figure 2.1.7 (i and ii) [160]. Many approaches have been followed to obtain improved characteristics of glucose sensing devices by coupling it with microfluidics. Hou et al. have reported glucose microfluidics chip based on polymethyl methacrylate (PMMA) using CO₂ laser and hot plate press bonding fabrication technique [161]. Compared to conventional detection methods, this chip has the advantage of self rotation effect resulting in improved mixing in a micromixer and promises rapid and low cost detection of glucose. Recent developments in nanotechnology and engineering have enabled immobilization of enzymes on to nanoparticles and nanostructures, which in turn can be functionalized on to the electrodes. Yu et al. fabricated a microfluidic chip where enzymes were immobilized on the single-walled carbon nanotube onto the PDMS channel [162].

Accurate determination of urea level in a biological sample is considered very important since change in urea concentration in blood (8-20 mg/dL) is an indicator for several diseases such as renal failure, hepatic failure, nephritic syndrome, etc. Generally, urease and glutamate dehydrogenase enzymes are used for the determination of urea level in the biological samples. Urease converts urea into hydrogen bicarbonate and ammonia whereas glutamate dehydrogenase converts ammonium ions, α -ketoglutarate and nicotinamide adenine dinucleotide (NADH) to L-glutamate and NAD⁺ as shown in Figure 2.1.7(iii). Electrons generated after conversion of NADH to NAD⁺ are measured for the estimation of urea concentration [163]. Microfluidics-based urea biosensors are of great demand in diagnosis because of high sensitivity, low consumption of materials/reagents, fast response time/reaction time, portability and high accuracy along with reusability. Nanomaterials have recently been used for immobilization of urease. Srivastava et al. immobilized enzymes covalently onto the gold electrode through self assembled monolayer with the help of 10-carboxy-1-decanthiol [164]. Sensitivity and detection range have been found to be improved when enzymes are immobilized on titania-zirconia composite [165]. The biochemical reaction of cholesterol detection is shown in the Figure 2.1. 7 (iv).

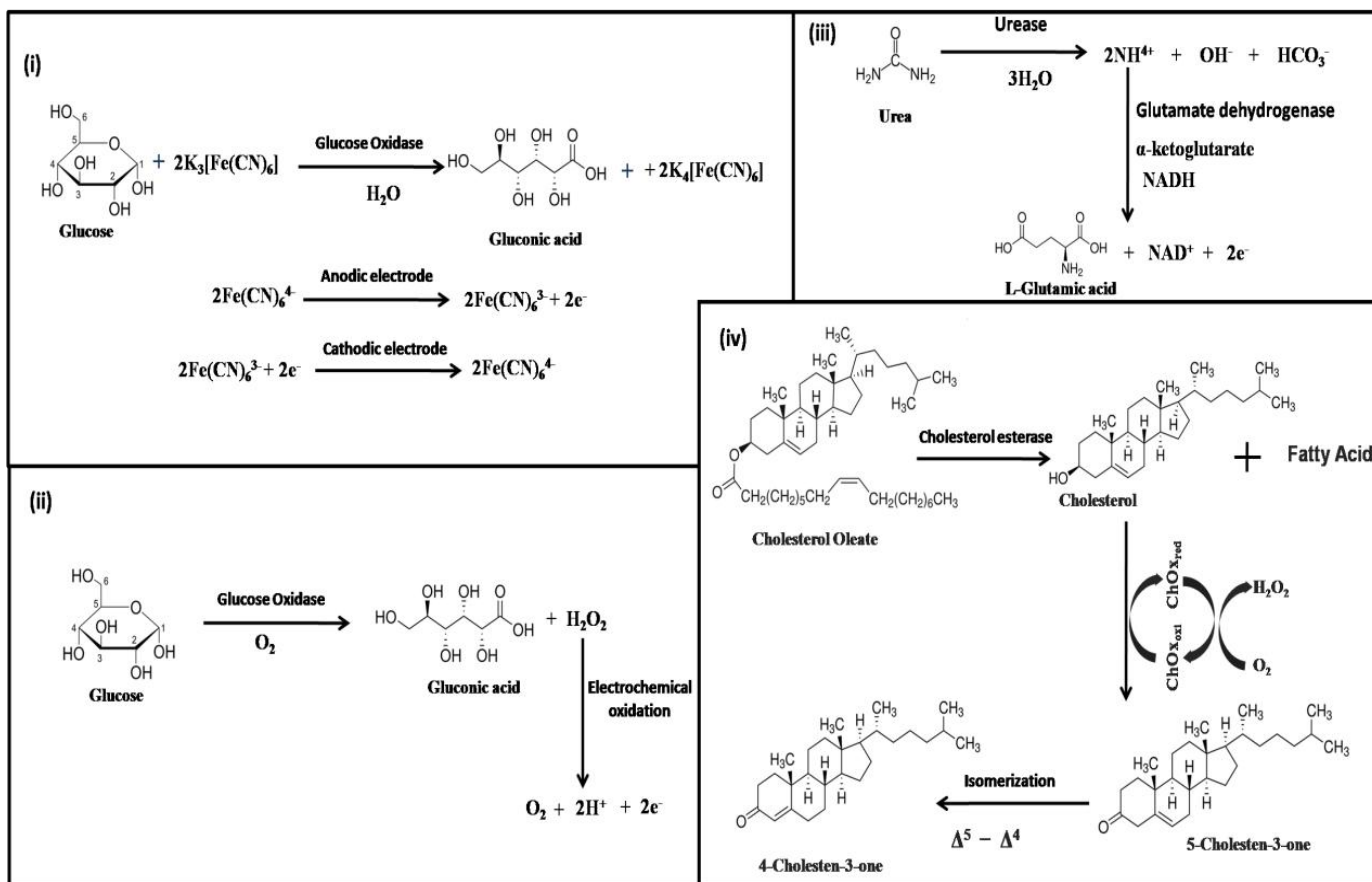


Figure 2.1.7 Schematic representation of reactions used in enzymatic biosensors such as (i) catalytic conversion of glucose into gluconic acid in the presence of potassium ferricyanide. At the surface of electrode, electron generated by conversion of Fe (II) to Fe (III), (ii) catalytic conversion of glucose into gluconic acid and H_2O_2 thereafter electron generation by electrochemical oxidation, (iii) biochemical reaction of urea biosensor and (iv) biochemical reaction of cholesterol biosensor [160].

2.5.8 Immunosensor

Immunosensor is based on an immunochemical reaction comprising of antigen or antibody as the recognition element that is spatially in contact with a transducer surface [166]. Immunosensor based devices can be used to detect immunocomplex formation by measuring change in resistance, current, refractive index, capacitance etc. A conventional immunoassay uses a monoclonal antibody comprising of a 'Y' shaped structure containing two antigen binding sites [Figure 2.1.8]. However, the antigen binding to an antibody involves highly specific interaction, making the immunoassay highly reproducible and highly specific, suitable for a range of target analytes for biosensing applications [Figure 2.1.9]. However, biological components like antibodies are very expensive and the conventional immunoassays are time consuming [167]. In this context, microfluidics integrated immunosensors would yield (i) sensitive detection, (ii) reduced biological component cost by using very minute volumes, (iii) increased functionality for surface treatment, (iv) decreased diffusion distance and fast detection times (v) portability etc. and thus, making it viable for POC diagnostics. The development of microfluidics coupled immunosensor platforms has gained immense attention towards an efficient and reliable biosensor.

The immunosensors play an important role in the development of POC devices for detection of food pathogens, bacteria and virus due their high specificity and sensitivity and both label or label free rapid detection [167]. Many researchers have investigated label-free detection of different biological molecules, such as aflatoxins, low density lipoproteins, etc. using integrated SPR microfluidic devices. However, label free detection suffers with non-specific binding on the sensor surface. Reliability and stability are some of the other challenges that can be addressed by using reference electrode. On the other hand, labeled immunosensor measures a molecule attached to a receptor by optical, fluorescence or amperometric detection. Fluorescence microscopy can be used to detect fluorophores at a surface density even below 1 fluorophore/ μm^2 with a corresponding concentration of analyte in solution in the picomolar range. The electrochemical detection of a given label has several advantages such as high sensitivity and low cost. However, some of the disadvantages include washing and separation steps, increased complexity of the assay etc. Despite these interesting developments, the microfluidics immunosensor are yet to hit the commercial market. One of the major problems that delay the commercialization is the inability of integration and optimization of peripheral and supporting accessories on a single platform.

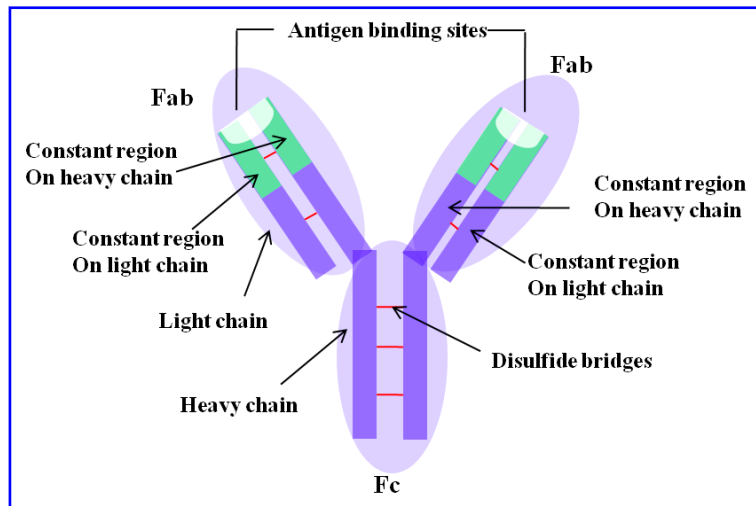


Figure 2.1.8 Schematic presentation of an antibody

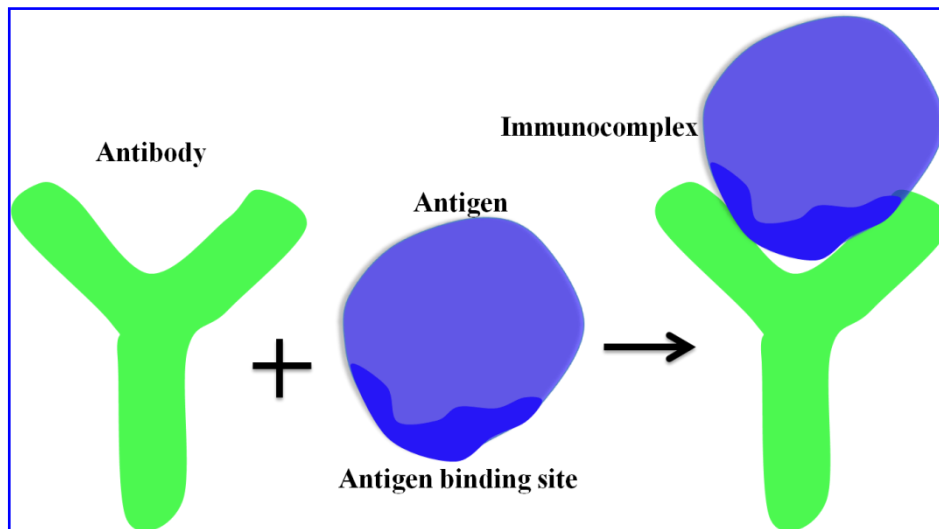


Figure 2.1.9 Immunological reaction

2.5.9 Nucleic acid biosensor

A nucleic acid or DNA sensor is a biosensor that integrates a nucleic acid as the biological recognition element and an electrode as the electrochemical signal transducer [168]. Currently, DNA biosensors technologies are of much interest owing to their great promise for rapid and low-cost detection of specific DNA sequences. These technologies commonly rely on the immobilization of a single-strand (ss) oligonucleotide probe onto optical, electrochemical, or mass-sensitive transducers [168]. The probe DNA is specific to recognize the complementary DNA (called duplex) target sequence via hybridization resulting in a change in the measurable signal. Chen et al. have developed a simple and ultrasensitive electrochemical DNA biosensor based on DNA concatamers [169].

2.6.0 Whole cell biosensor

The whole-cell biosensor is constructed through the immobilization of cells, microorganisms or bacteria that act as sensing element instead of purified enzymes. The sensing element of whole-cell biosensor recognizes specific species of interest. Main critical point in the development of the modern cell-based biosensors is the immobilization of cells onto transducers in cellular conditions. Olaniran et al. have developed a whole-cell bacterial biosensor for rapid and effective monitoring of heavy metals and inorganic pollutants in waste water [170].

2.7 Immobilization of biosensors

Immobilization or functionalization of biomolecules on a transducer surface is an important step to construct a biosensor [171]. The selectivity, stability, sensitivity and reproducibility of the biosensor are the dominant parameters that can be improved by determining an effective method for immobilization. Various methods have been reported for the immobilization of desired bio-molecules onto solid support materials. Figure 2.2.0 describes the various immobilization techniques and Table 2.1.1 summarizes the merits and demerits of these techniques.

Table 2.1.1: Various methods for immobilization of biomolecules with advantages and disadvantages [171].

Method	Advantages	Disadvantages
Entrapment and encapsulation	<ul style="list-style-type: none"> • Gentle treatment • No direct chemical modification • Specificity of biocatalyst and analyte interaction retained 	<ul style="list-style-type: none"> ✓ Applicable for small analyte detection ✓ High diffusion barrier to both substrate and product transport ✓ Continuous loss of biocatalyst
Covalent binding	<ul style="list-style-type: none"> • Low diffusional resistance • Strong binding force between biocatalyst and matrix • Not affected by adverse conditions of pH, ionic strength 	<ul style="list-style-type: none"> ✓ May involve harsh/toxic chemicals ✓ Matrix not regenerable ✓ Frequently occurring loss of activity
Cross-linking	<ul style="list-style-type: none"> • Used in conjunction with entrapment to reduce loss of biocomponent activity 	<ul style="list-style-type: none"> ✓ Harsh treatment with toxic chemicals ✓ Covalent linkages formed amongst protein molecules rather than matrix
Adsorption	<ul style="list-style-type: none"> • Gentle treatment of biocatalyst • No modification of biological component • Matrix can be regenerated • Maximal retention of activity 	<ul style="list-style-type: none"> ✓ Very weak bonds ✓ Susceptible to changes in pH, temperature, ionic strength

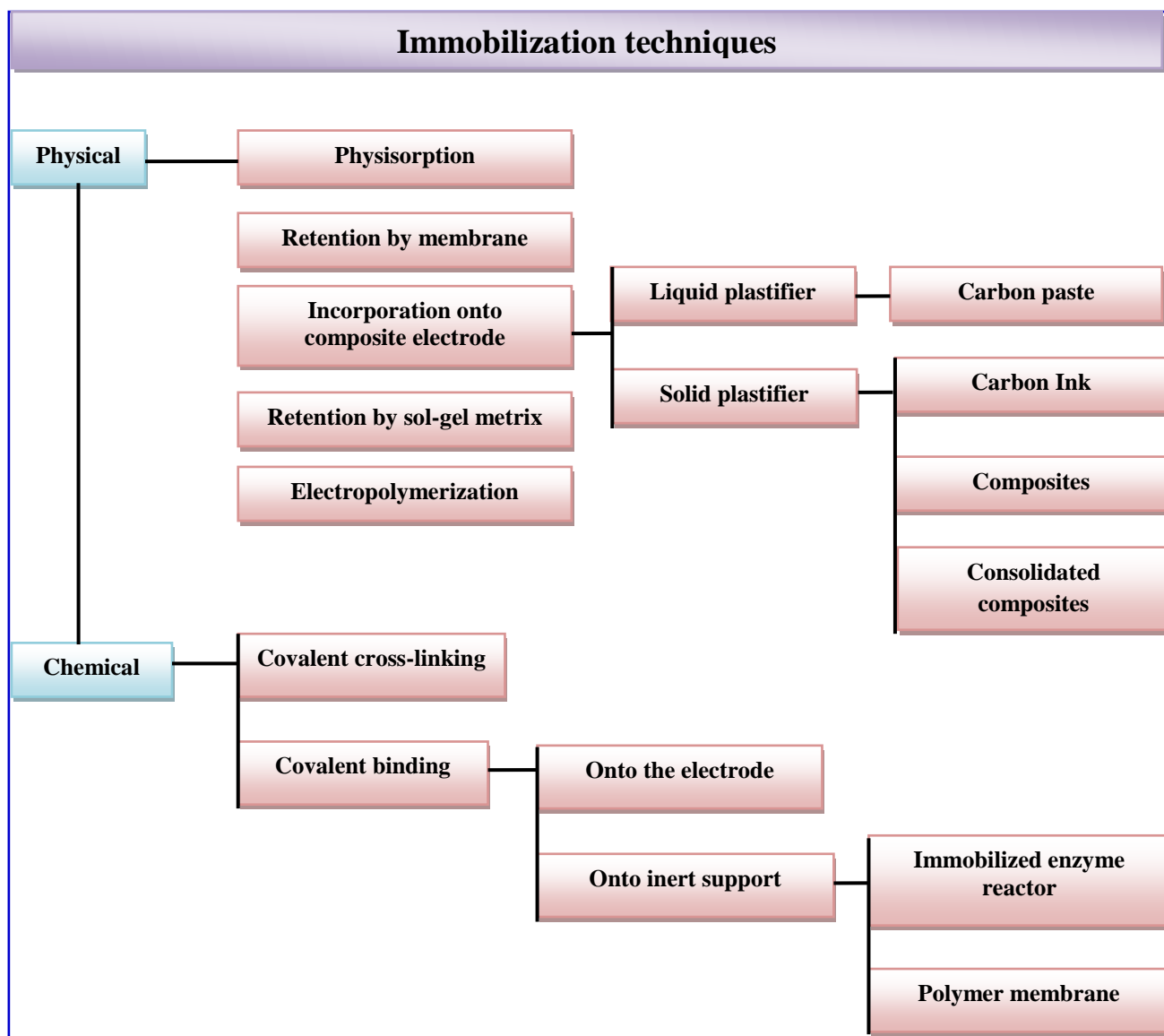


Figure 2.2.0 Various immobilization techniques for biosensor construction

2.8 A brief literature survey of nanostructured metal oxides

Nanomaterials, especially nanostructured metal oxides (NMOx) have been extensively explored to develop biosensors [172]. Nanoparticles, nanocages, nanobelts, nanotubes, nanofibers, nanorods etc. of metal oxides are widely used as a transducer materials for electrochemical biosensors. NMOx have been used to catalyze biochemical reactions in the biosensor and have been predicted to exhibit novel functions. Consequently, the NMOx are being explored for application in drug delivery, tissue engineering, non-invasive sensors, *in vitro* and *in vivo* intracellular imaging, and biosensing [172]. The common NMOx includes Al_2O_3 , SiO_2 , TiO_2 , ZrO_2 , ZnO , CeO_2 , MgO , Fe_3O_4 , BaO , CuO , and V_2O_5 utilized in the development of biosensor. In biosensor, these NMOx are known to play important role for immobilization of biomolecules and direct electron transfer between electrode and electroanalyte. Efforts are being made to explore the prospects and future challenges of NMOx for the development of microfluidic biosensing devices. To fabricate an efficient microfluidic biosensor, it is critical to select an NMOx that is suitable for immobilization of the desired biomolecules. The formation of a bio-interface depends on the characteristics of NMOx such as effective surface area, surface charge, biocompatible, energy, roughness, porosity, functional groups, and hygroscopic nature. The biomolecules (enzyme, antibody, DNA etc.) can bind with NMOx via physical adsorption or covalent interaction. The physical adsorption of a biomolecule with NMOx arises due to weak interaction known as *Van der Waals* electrostatic interaction depends on the surface morphology and net surface electric charge. The covalent binding of a biomolecule to an NMOx depends on the availability of functional groups that can be engineered during the chemical reactions of NMOx preparation. It has been observed that the rate of electron transfer depends on the NMOx–biomolecule functionalization. In addition, the microenvironment of NMOx can help an enzyme to retain its suitable conformational change that enhances the signal transduction and stability. Various NMOx and their biosensing applications have described in the Figure 2.2.1. Solanki et al. have demonstrated the prospects of various metal oxides in the field of biosensor technology [172]. Chang et al. have proposed a high-sensitive detection strategy for carbohydrate antigen using a gold/ZnO thin film SPR-based biosensor [173]. Ahmad et al. have developed a highly sensitive amperometric cholesterol biosensor based on Pt-incorporated fullerene-like ZnO nanospheres [174]. Xiao et al. have described the growth of metal–metal oxide nanostructures on freestanding graphene paper for flexible biosensors [175]. Levine et al. developed a real-time, multiplexed electrochemical DNA detection using an active complementary metal-oxide-semiconductor biosensor array with integrated sensor electronics [176]. Kim et al. have developed an amperometric glucose biosensor based on sol-gel-derived zirconia/nafion composite film as encapsulation matrix [177]. Neouze et al. have described the surface functionalization of metal oxides nanoparticles using organic ligand [178]. The surface functionalization of NMOx plays an important role in attachment of biomolecules as well as in fabrication of the

bioelectrode. It can also reduce the aggregation of nanoparticles on a transducer surface. The main compounds used for surface functionalization of metal oxide nanoparticles are phosphonates and silanes. This may include alkoxysilane, $\equiv\text{Si-OR}$ (R=alkyl), hydrogenosilane, $\equiv\text{Si-H}$, or chlorosilane, $\equiv\text{Si-Cl}$, reagents. The main advantage of silanes is that they provide numerous functionalities such as amino, cyano, carboxylic acid, epoxy groups, etc. However, the surface functionalization may lead to more than one step of chemical treatment on biosensor resulting in device complexity. Thus, efforts have been made to immobilize biomolecules on desired nanostructure metal oxides surface via electrostatic interaction. Among the various NMOx, the two candidates namely TiO_2 and NiO have been chosen to be integrated with microfluidic biosensor in this work. More details of TiO_2 and NiO are described below.

2.8.1 Titanium dioxide

Titanium dioxide (TiO_2) has attracted much interest in biomedical applications due to their high sensitivity and specificity for rapid analyte detection [179-185]. It offers high sensitivity due to their tunable band gap (1.8 and 4.1 eV) that depends on its crystal structure. The different crystalline structures can be obtained by tuning temperature during annealing. TiO_2 has four crystalline polymorphs namely rutile, anatase, brookite and titanium dioxide (B). The titanium dioxide has been widely used in cosmetics, paints, ointments, toothpaste, etc. Researchers have utilized nanostructured TiO_2 in various fields such as photovoltaics, electrochromics, battery and electrochemical biosensors. The size and shape of nanostructured TiO_2 is predicted to play an important role in the construction of the biosensor. The high surface area of TiO_2 nanoparticles can be used to enhance the biofunctionalization on transducer surface. The crystalline nature of nanostructured TiO_2 may be used to improve the heterogeneous charge transfer between electrode and bulk solution. Viticoli et al. have discussed the direct electron transfer to construct a third-generation biosensors using TiO_2 nanostructured film. Cao et al. have developed a glucose biosensor using three-dimensional (3D) macroporous TiO_2 . In addition, the nanostructured TiO_2 provides optical transparency, biocompatibility, environmental safety and excellent electrochemical conductivity which improve the biosensor characteristics. The good biocompatibility of TiO_2 helps to decrease the enzyme inactivation rate. Ayob et al. have reported synthesis of TiO_2 nanowire for detection of DNA [179]. Bao et al. have developed the nanostructured TiO_2 for direct electrochemistry and glucose biosensor applications [181]. Chavhan et al. have utilized TiO_2 platform for detection of ascorbic acid [180]. Jardinier et al. used the atomic layer deposition of TiO_2 photonic crystal waveguide biosensors [182]. Li et al. have developed a glucose biosensor using TiO_2 sol-gel derived prussian blue nanoparticles [183]. Direct electrochemistry of hemoglobin on vertically aligned carbon hybrid TiO_2 nanotubes and its highly sensitive biosensor performance has been described by Liu et al [184]. Si et al. have demonstrated

hierarchically structured one-dimensional TiO₂ for protein immobilization, and mediator-free glucose sensing [185]. Nanostructured TiO₂ has found wide applications in detection of biomolecules.

Nanocomposite materials consist of two or more phases, where one of the phase is in nanoscale dimensions. The structure, physical and chemical properties of these composite materials result in unique and fascinating mechanical, electrical, thermal, optical, electrochemical, and catalytic properties. Carrara et al. have synthesized a nanocomposite material of poly(o-anisidine) and TiO₂ for biosensor applications [186]. Tak et al. have developed a ZnO–CNT hybrid nanocomposite based urea biosensor [187]. In addition, the nanocomposite based on inorganic materials and organic polymers for the fabrication of biosensors has been considered recently. Metal oxide-chitosan (bio-polymer) nanocomposite materials show the excellent film-forming ability, biocompatibility, non-toxicity, susceptibility to chemical modification and cost-effectiveness. It can act as a stabilizing agent for biomolecules immobilization. This chitosan polymer material can be used to reduce the agglomeration of metal oxide nanoparticles. Feng et al. have used a nanoporous CH–CeO₂ nanocomposite matrix for the immobilization of single stranded DNA probe for detection of cancer gene [188]. Malhotra et al. have developed the metal oxide–CH based nanocomposite for cholesterol biosensor [189].

2.8.2 Nickel oxide

NiO is a p-type with stable wide band gap semiconducting metal oxide that exhibits anodic electrochromism, and is being studied for applications in supercapacitors, smart windows, and dye-sensitized photocathodes. In addition, NiO (II) is a functional material that has received much attention due to its applications in various fields, such as catalysis, fuel cell electrodes, gas sensors, antiferromagnetic layers, biosensor and p-type transparent conducting films. Nanostructured NiO has aroused much interest for development of health care devices. It provides the large surface area, high conductivity, catalytic activity, high carrier mobility, biocompatibility, stability, and excellent electrochemical properties. The high isoelectric point (IEP) of NiO (~10.7) can be helpful to immobilize biomolecules with low IEP via electrostatic interactions. The nanostructured NiO with different morphologies such as nanostrips, nanoparticles, nanowires, nanorods, nanoflakes and nanospheres have been obtained by various methodologies namely precursor thermal decomposition method, template method, calcination, aqueous solution method and chemical co-precipitation method. Salimi et al. have described direct electron transfer and electrocatalytic activity properties of glucose oxidase and NiO nanoparticles [190]. Pang et al. have demonstrated the selective synthesis of nickel oxide nanowires and length effect on their electrochemical properties [191]. Niu et al. have developed a highly sensitive and selective nonenzymatic glucose biosensor using three-dimensional porous nickel nanostructures [192]. Kavitha et al. have synthesized the high-quality NiO nanorods for electrochemical and antibacterial

properties [193]. Xiong et al. have synthesized mesoporous NiO with various hierarchical nanostructures by quasi-nanotubes/nanowires/nanorods self-assembly for supercapacitor application [194]. Yadav et al. have developed nanostructured NiO film for application to fish freshness biosensor [195]. The attempts have been made to synthesize nanostructured NiO via chemical route for biosensing applications. The nanostructured NiO allows direct functionalization with biomolecules due to high isoelectric point (10.6). The high surface to volume ratio, excellent electrocatalytic and charge transfer properties of NiO improves the biosensor sensitivity and detection limit. In addition, the hydroxide formation $[\text{Ni}(\text{OH})_2]$ of NiO can be easily integrate with microfluidic system to develop a miniaturized analytical device for detection of biomolecules.



Figure 2.2.1 Different NMOx and their biosensing applications [172].

2.8.3 Carbon nanotubes

Carbon nanotubes (CNTs) have attracted much attention in the fabrication of nanodevices [196]. The surface chemistry and electronic properties of CNTs make them an ideal material for use in chemical and biosensing applications. Single walled carbon nanotubes (SWCNT) and multiwalled carbon nanotubes (MWCNT) are both widely used in biosensors. The graphene sheet (one atom- thick sheets of graphite) can be rolled up to prepare SWCNT. Structurally, only one cylinder is termed SWCNT whereas multiwalled carbon nanotubes (MWCNT) consist of two or more concentric graphene cylinders. The graphene can wrap along the honeycomb graphene structure and is given by chiral vector \vec{C} which is a result of a pair (n, m) of integers that correspond to graphene vectors \vec{a}_1 and \vec{a}_2 . The principle construction of CNTs from a graphene sheet along the chiral vector \vec{C} is shown in Figure 2.2.2(i). It can be formed by rolling a graphene sheet into a cylinder along an (m, n) lattice vector in the plane. The key parameters of a nanotube are the (m, n) indices which determine the diameter and chirality. The chiral angle between hexagons and the tube axis, CNTs can be either metals or semiconductors, with band gaps that are relatively large (~0.5 eV for typical diameter of 1.5 nm) or small (~10 meV). The (n, 0) structure is called “zigzag” and the structure where n = m (n,n) is called “armchair”. Another type of CNT construction, which can be characterized by the equation where n > m > 0, is called “chiral”. The chirality determines the mechanical, electronics, optical etc. of CNT. The diameter of CNTs varies from a few nanometres in the case of SWCNT to several tens of nanometres in the case of MWCNT. The structure of MWCNT is shown in Figure 2.2.2(ii). The lengths of the CNT are usually found in the micrometre range. Timur et al. have developed of a microbial biosensor based on CNTs modified electrode [197]. Martinez et al. have demonstrated a label-free DNA biosensors based on functionalized CNTs field effect transistors [198]. Abdolahad et al. a vertically aligned CNT-based impedance biosensor for rapid and high sensitive detection of cancer cells [199]. Wang et al. have reviewed CNTs based electrochemical biosensors [200]. The unique properties of CNTs make them extremely attractive biosensor field and electrochemical detection.

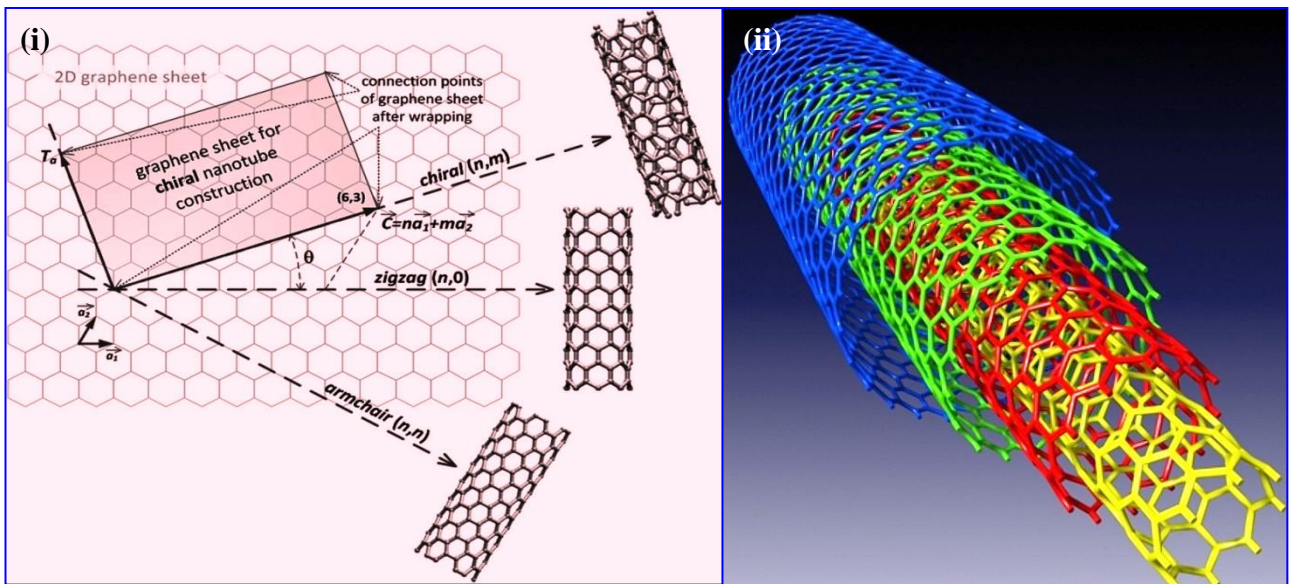


Figure 2.2.2 (i) The principle of CNT construction from graphene sheet along the chiral vector \vec{C} [201] and (ii) MWCNT (www.turbosquid.com).

The multifunctional properties of CNTs would result in improved efficacy of biosensor fabrication. CNTs are known to be an exciting material due to their flexibility, enhanced electrical conduction and act as a mediator for desired electrochemical biosensing. It improves the electro-activity of biomolecules leading to fast electron transfer. The chemical treatment of CNTs sidewalls might provide an additional impetus towards functionalization of biomolecules. This covalent interaction makes the enhanced performance of high enzyme or antibody loading. I have chosen CNTs (multiwalled) to construct the microfluidic device for point-of-care application due to low cost and ease of synthesis. CNTs may act as nanoelectrode that can be integrated with biomolecules to communicate with the outside environment by electron transportation. Therefore, the electronic properties of CNTs can be advantageous for chemical functionalization with a moiety and altering the structure whose intrinsic properties are electrically tunable. However, the poor solubility of CNTs in an aqueous media continues to be a concern. In order to improve the dispersion or agglomeration of CNTs, I have focused to integrate metal oxide (such as NiO) with CNTs. Ayala et al. decorated carbon nanotubes with nanostructured nickel particles via chemical methods [202]. Zhu et al. have used the CNTs beaded with ZnO nanoparticles for ultrafast nonlinear optical switching [203]. Zhang et al. have developed a highly sensitive nonenzymatic glucose sensor has been developed based on CNT-NiO [204]. Claussen et al. have reported an electrochemical biosensor of nanocube-augmented CNT networks [205]. The fabrication and results of the CNT-NiO nanocomposite based microfluidic biochip are described in Chapter 4 and 6.

2.9 Conclusions

This Chapter illustrates the basic principles towards the construction of microfluidics and biosensors. The literature surveys for microfluidics and biosensors have been discussed. A detailed overview of biosensors and various immobilization techniques have been described. Applications of nanostructured materials in fabrication of biosensors have been explained. In particular, the role and importance of nanostructured metal oxides such as TiO₂, NiO and composites materials (TiO₂-CH, CNT-NiO) and their integration with biological as well as microfluidic systems have been described. In the next Chapter, the different materials, methods and various characterization tools used in experimental studies are discussed.

CHAPTER 3

Materials and Experimental Techniques

3.1 Introduction

This Chapter gives a broad overview of various materials, fabrications and different characterization tools that have been adopted in this thesis for the development of microfluidic biosensors. The Chapter begins with the description of how PDMS microchannels can be fabricated using soft lithography. The various steps followed in the fabrication of PDMS microchannels have been discussed. Additionally, the steps involved in establishing microelectrodes for the biosensors have been explained. Modifications of the microelectrodes for various application including biofunctionalization using various nanostructured materials and composites such as TiO₂, NiO, TiO₂-CH and CNT-NiO are the major highlight of this chapter. The experimental techniques used for the synthesis of the nanostructured materials as well their surface modification have been explained. This is followed by description of all experimental protocols and procedures involved in biofunctionalization of electrodes. A discussion and justification on the various tools such as ultraviolet-visible spectroscopy (UV-Vis), Fourier transform infrared spectroscopy (FT-IR), X-ray diffraction (XRD), X-ray photoelectron spectroscopy (XPS), Zeta potential, Raman spectroscopy, transmission electron microscopy (TEM), atomic force microscopy (AFM) and scanning electron microscope (SEM) that are employed for the characterization of these synthesized materials, has been added in this chapter. Finally, efforts have been made to discuss the various electrochemical techniques such as chronoamperometric, cyclic voltammetry and impedance spectroscopy employed to characterize the developed microfluidic biosensor devices.

3.1.1 Fabrication of PDMS microchannels

Photolithography is a binary pattern transfer technique, where there is no gray-scale, color, or depth transferred to the image. Photolithography is an optical technique for transferring pattern onto a photosensitive substrate. It is similar to the lithographic printing process. Patterns are first transferred to an imagable photoresist layer. Photoresist is a liquid that can be spread out onto a substrate, exposed with a desired pattern, and developed into a selectively placed layer for subsequent processing [206].

The PDMS microfluidic channels (rectangular) have been fabricated by soft lithography technique [207]. It is termed as soft because of the use of soft elastomeric materials such as PDMS, PMMA etc. In soft lithography, instead of using a rigid photomask, a patterned elastomer is used as a stamp, mold, or mask to create the micro-patterns/structures. Replica molding, micro-contact printing, micromolding, and micro-transfer molding are some of the popular methods that are used in soft lithography. Figure 3.1.1 shows the schematic diagram of the creation of PDMS microchannel. Stepwise fabrication process has been described below.

3.1.2 Mask fabrication

Auto computer-aided design (AutoCAD™) software has been used to design various masks needed for PDMS microchannel fabrication. The desired digitally designed mask is printed on to an optical transparency sheet using a high-resolution printer.

3.1.3 SU-8 photoresist

There are two types of photoresist namely positive and negative. In positive, the photoresist is exposed with UV light, wherever the underlying material has to be removed. The UV light changes the chemical structure of the resist so that it becomes more soluble in the developer solution. The exposed resist is then washed away by the developer solution, leaving windows of the bare underlying material. Therefore, the mask contains an exact copy of the pattern that remains on the Si wafer. In the case of negative resists, exposure to the UV light causes the negative resist to get polymerized, and more difficult to dissolve. Therefore, the negative resist remains on the surface wherever it is exposed, and the developer solution removes only the unexposed portions. Mask used for negative photoresist, therefore, contains the inverse of the pattern to be transferred [Figure 3.1. 2(a)].

SU-8 is an epoxy-based photoresist [Figure 3.1. 2(b)] viscous polymer that is used to print microstructures of high aspect ratio (> 20). The SU-8 has a maximum absorption for ultraviolet light at a wavelength of 365 nm (g-line). On exposure it undergoes a long molecular chain cross-linking causing the solidification of the material under exposure. Gamma butyrolactone is the primary solvent of SU-8 series. It is highly transparent in the UV region and can allow thick (hundreds of micrometers) microstructures with nearly vertical side walls. After exposure and development, its highly cross-linked microstructure gives the material high stability against chemicals and radiation damage.

The SU-8 photoresist (negative) is first spun onto a Si wafer using the photoresist spinner at a speed that achieves the required thickness. In order to get a 100 μm thick layer of SU-8 using SU-8 100, the wafer is spun at 500 rpm for 5 s, to spread out the photoresist, then at 1500 rpm for 30 s, to achieve the final thickness. The wafer should then be soft baked for the required time at the required temperature. The soft bake time is 10 min at 65°C, and 30 min at 90°C. The two-step baking is carried out to reduce internal stresses owing to thermal effects.

3.1.4 Exposure

The photomask is used to clamp between the Si/SU-8 substrate and a blank glass plate. The photoresist is exposed in a UV light at a dose of 400 mJ/cm^2 .

3.1.5 Post exposure bake

A post-exposure baking is performed to crosslink selectively the exposed portions of the photoresist for 1 min at 65°C and 10 min at 95°C.

3.1.6 Development

SU-8 developer is poured in a beaker, and a spray bottle with new SU-8 developer is prepared. The sample is developed in the SU-8 developer until all unexposed SU-8 is removed. To determine whether all the unexposed SU-8 is removed, the sample is removed from the beaker, rinsed with new developer, rinsed with isopropyl alcohol, and then blown dry gently with nitrogen air.

3.1.7 PDMS molding

PDMS is a group of polymeric organosilicon compounds that is referred to as silicones. The chemical formula for PDMS is $\text{CH}_3[\text{Si}(\text{CH}_3)_2\text{O}]_n\text{Si}(\text{CH}_3)_3$, where n is the number of repeating monomer $[\text{SiO}(\text{CH}_3)_2]$ units and is shown in Figure 3.1. 1. The PDMS oligomer and crosslinking prepolymer of PDMS agent from a Sylgard 184 kit is mixed in a ratio of 10:1. A convenient way of mixing these agents is to place both in a disposable plastic bag, heat seal, and mix manually. The mixture can then be placed under vacuum for degassing. The PDMS mixture is poured onto Si/Su-8 mold and cured for 1 h at 65°C. After cooling, the PDMS can be carefully peeled off from the mold. This process creates a microchannel of the desired pattern. In our case, the channel height and width are 200 μm each and the length is 2 cm. The microchannel having reservoirs at the end are fabricated by punching holes at desired position in the PDMS slab. The PDMS film is sealed to a flat glass electrode surface to complete the microfluidic channel. If these are immediately pressed together, a tight bond will be created [Figure 3.1.3]. Otherwise, oxygen plasma can be used to treat both the glass substrate and the PDMS film for tight-sealing the channel.

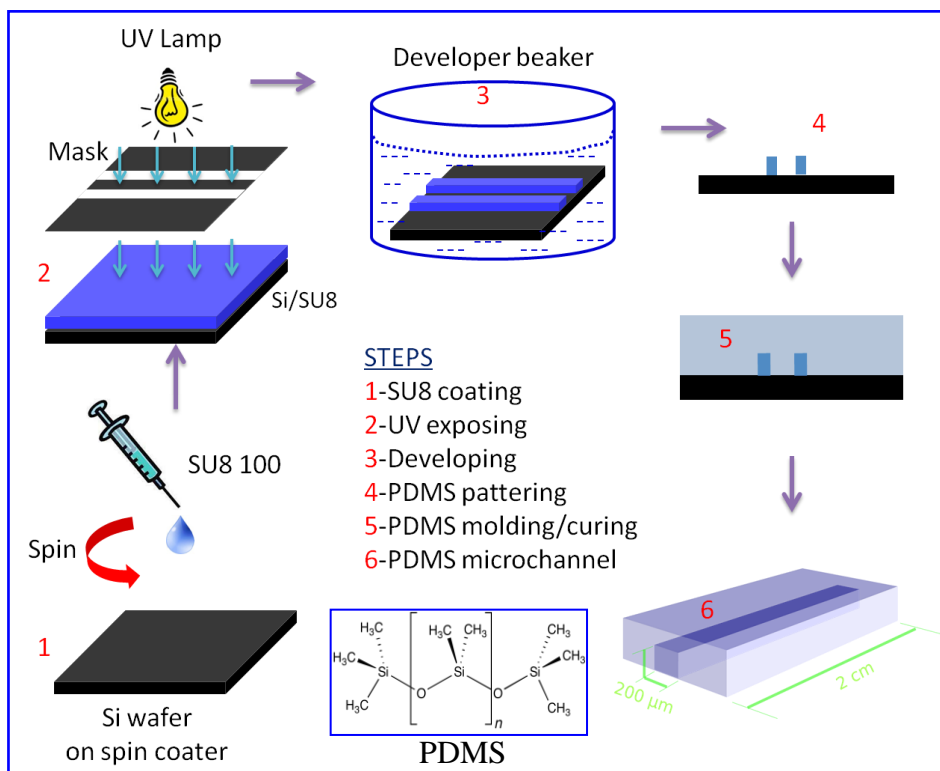


Figure 3.1.1 Schematic representation of step by step PDMS microchannel fabrication using SU 8 negative photoresist.

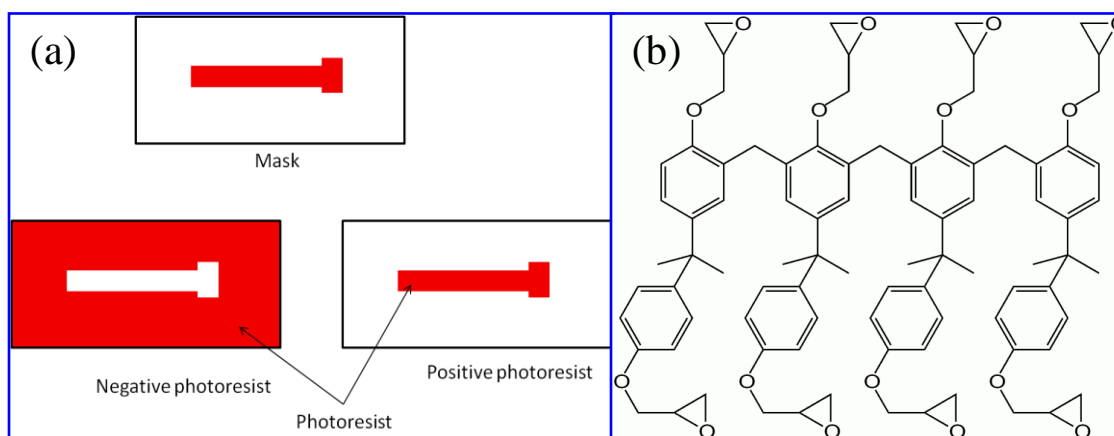


Figure 3.1.2 (a) After exposing the photoresist pattern on Si wafer (negative and positive tone) and (b) chemical structure of SU 8.

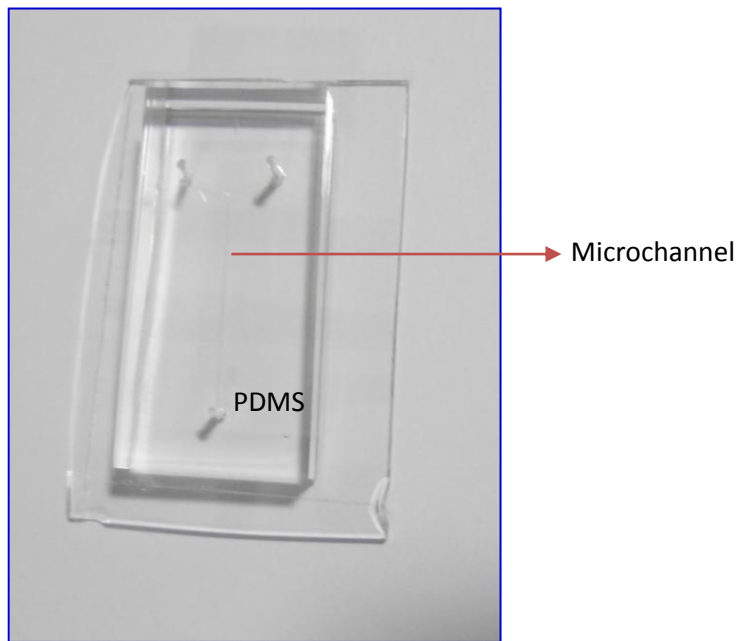


Figure 3.1.3 Photograph of a PDMS microchannel

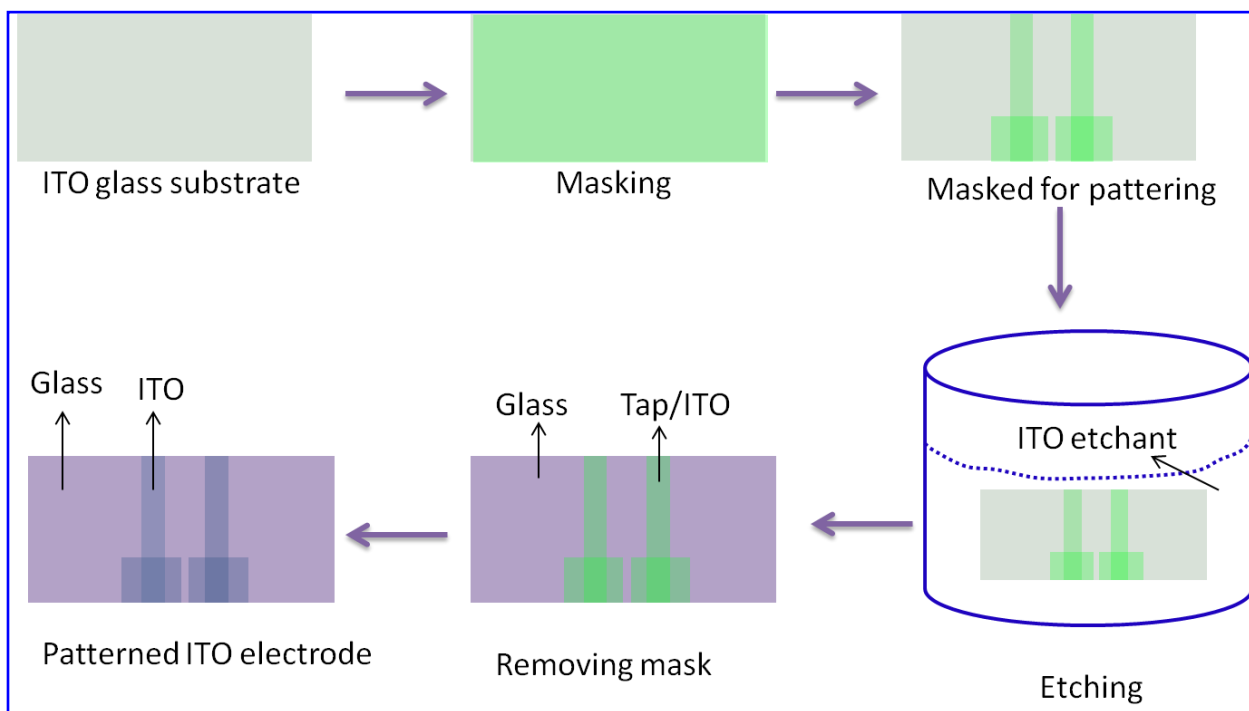


Figure 3.1.4 ITO patterning via wet chemical etching process

3.1.8 Precautions

- i. The aligner has the ability to align masks to the existing patterns for multiple exposure steps.*
- ii. All bake times are given with respect to baking on a hot plate.*
- iii. Handle and store under nitrogen. This material has an extremely low flash point (-18°C).*
- iv. After all baking steps, the sample must be allowed to cool slowly (at least 15 min) to room temperature before any further processing is done, to reduce internal stresses. This thermal relaxation time is crucial for survival of the mold.*

3.2 Wet chemical etching

Chemical etching technique is used to remove layers selectively from the desired substrate. It is a low cost and easy process widely used in microfabrication [208]. In chemical etching, the masking material is a photoresist which can be patterned using photolithography. This technique is used for etching ITO in order to fabricate microfluidic electrode.

3.2.1 ITO ($\text{In}_2\text{O}_3:\text{SnO}_2$) etching by chemical Process

Patterned microelectrode of dimensions $0.2 \times 2.5 \text{ cm}^2$ is fabricated onto indium tin oxide (ITO) coated glass slide ($2.5 \times 3.5 \text{ cm}^2$) by wet chemical etching process using ITO etchant [Hydrochloric acid (HCl) + nitric acid (HNO_3) + water (H_2O) (1:0.1:1) at 40°C] [209]. For this process, ITO glass substrate is masked with the commercially available cello masking tape film. The masking tape is removed from entire substrate except the desired two patterned ITO electrode (electrode dimension: $0.2 \times 2.5 \text{ cm}^2$) using a sharp razor blade. After masking, the substrate is dipped on ITO etchant for 15 min. This etchant is selectively used to etch the ITO from the entire substrate and the ITO etchant cannot react with the masked area. Thus, after etching, the remaining mask is removed to form patterned ITO electrode on glass substrate. Various steps of chemical etching have been illustrated in Figure 3.1.4.

3.2.2 ITO etching using photolithography

Photolithographic technique has been used for the fabrication of patterned ITO microelectrodes with help of wet chemical method. Two patterned microelectrodes comprising of dimensions ($0.2 \times 2.5 \text{ cm}^2$) have been prepared on ITO coated glass slide of size $2.5 \times 3.5 \text{ cm}^2$ by photolithographic technique. The ITO glass is cleaned with acetone prior to use. First, the positive photoresist (Shipley 1811) is spin coated onto ITO glass substrate at 3000 rpm for 20 s. In order to remove solvent, the photoresist coated substrate is soft baked using a hot plate for 1 min. Then, the substrate is exposed to UV radiation for 5 min through a given optical mask (high resolution black printed transparent sheet). The substrate is dipped in a positive photoresist developer solution for 10s to develop the pattern. The chemical ITO etchant (Zinc dust + HCL solution 15%) is used to etch ITO from exposed region [210]. After, ITO etching the remaining

photoresist onto ITO is removed by acetone. This patterned ITO electrode is then cleaned with acetone via sonication for 10 minutes and then with dichloromethane for 10 minutes, and finally washed thoroughly with water several times. These clean electrodes are placed in a vial wherein a mixture of $\text{H}_2\text{O}:\text{H}_2\text{O}_2$ (30%): NH_3 (25%) (5:1:1) is added and stirred for 1 h at 70°C . Then, the slides are washed with plenty of water and dried in an oven at 100°C for 4 h.

Optically transparent ITO electrode has excellent chemical functional property for the fabrication of microfluidic biosensors. The surface of ITO coated substrate can be easily hydrolyzed or hydrophilic via chemical treatment ($\text{H}_2\text{O}:\text{H}_2\text{O}_2$: NH_3) by introducing OH groups and can be directly modified by sol gel metal oxide via electrostatic interaction. Thus, ITO electrode is a suitable candidate for deposition of sol gel nanoparticles and immobilization of biomolecules in order to fabricate microfluidic biosensor.

3.3 Chemical synthesis of nanomaterials

Various methods for preparation of metallic and metal oxides nanoparticles like different gas phase and vacuum methods have been reported since the early 1980s [211, 212]. There are many methods for preparation of nanomaterials, including both attrition and pyrolysis. In attrition, macro- or micro-scale particles are kept in a ball mill, or a size-reducing mechanism. In pyrolysis, a vaporous precursor (liquid or gas) is enforced through an orifice at high pressure and burned. Pyrolysis often results in aggregates and agglomerates rather than single primary particles. Interestingly, chemical route for the synthesis of nanoparticles including sol-gel technique and colloidal synthesis route has also been developed. These materials possessed many attractive properties which are attributed to the high volume fraction of interfacial structures that are dissimilar from the crystalline structures of the core [211, 212]. The studies have been extended to nanocomposites, and very interesting properties with respect to toughness and strength have been reported [212]. Additionally, nanostructured powders attained through flame pyrolysis process have been commercialized for a long time, e.g. SiO_2 or TiO_2 . Nanoparticles prepared through colloidal chemistry in liquid environments, industry (e.g. the fabrication of water glass), and also in biology. The stability of colloidal nanoparticles plays an important role in industrial and biosensing applications. The electrostatic stabilization is one of the mechanisms arising from van der Waals attraction and is counterbalanced by the repulsive Coulomb forces acting between the negatively charged colloidal particles in order to prevent the aggregation of the colloidal particles. The use of this chemical colloidal route show the ways to interesting concepts for the research on nanomaterials synthesis.

The sol-gel process is a wet-chemical technique (also acknowledged as chemical solution deposition) broadly used in the fields of materials and biomedical science. These techniques are used primarily for the fabrication of metal oxides starting from a chemical solution (*sol*, abbreviated for solution), which proceeds as the precursor for an integrated network (or *gel*) of either discrete particles or

network polymers. In all these studies, typical precursors are metal alkoxides and metal chlorides, which experiences hydrolysis and polycondensation reactions to figure either a elastic solid network or a colloidal suspension (or dispersion) which is a system composed of discrete (often amorphous) submicrometer particles dispersed to various degrees in a host fluid. The idea of zeta potential tailoring the surface modification for compatibility or specific reactivity is mentioned only in very few literatures. To facilitate a sufficient amount of dispersion, the particle surface should be compatibilized to the matrix and surface modification of the nanoparticles turn out to be a crucial means for the advance of suitable processing routes, or, reactive monomers are initiated into a given polymer, nucleation and growth have to be directed. This critical size range (or particle diameter) typically ranges from nanometers (10^{-9} m) to micrometers (10^{-6} m).

3.3.1 Sol gel method

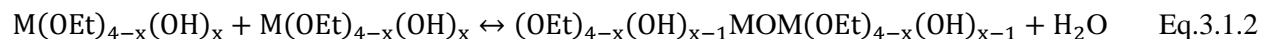
Sol-gel method is a wet chemical process for synthesis of colloidal dispersions of inorganic and organic-inorganic nanomaterials such as oxides and oxide-based nanohybrids [213]. Although the fabrication of different forms of final products requires some specific considerations, the fundamentals and general approaches in the synthesis of colloidal dispersions are the same. Sol-gel process offers many advantages, including low processing temperature and molecular level homogeneity. Sol-gel process is particularly useful in making complex metal oxides, temperature sensitive organic-inorganic hybrid materials, and thermodynamically unfavorable or metastable materials.

Typical sol-gel process consists of two steps namely; hydrolysis and condensation of precursors [214]. Precursors can be either metal alkoxides or inorganic and organic salts. Organic or aqueous solvents may be used to dissolve precursors, and catalysts are often added to promote hydrolysis and condensation reactions [Eq. (3.1.1 & 3.1.2)]:

Hydrolysis:



Condensation:



Hydrolysis and condensation reactions are both multiple-step processes, occurring sequentially and in parallel. Each sequential reaction may be reversible. Condensation results in the formation of nanoscale clusters of metal oxides or hydroxides, often with organic groups embedded or attached to them. These organic groups may be due to incomplete hydrolysis, or introduced as non-hydrolysable organic ligands. The size of the nanoscale clusters, along with the morphology and microstructure of the final product, can be tailored by controlling the hydrolysis and condensation reactions.

3.3.2 Chemical and reagents

The curing agent (Sylgard 184) has been obtained from Dow Corning (Midland, MI, USA). SU8-100 negative photoresist, positive photoresist (Shipley-1818) and SU8 developer have been purchased from Microchem (Newton, MA, USA). ITO coated glass slides of thickness $\sim 150\text{-}300 \text{ \AA}$ having a resistance of 50 \Omega/sq have been procured from Vin Karola Instruments. Titanium (IV) butoxide, chitosan, 2-methoxy ethanol, nickel nitrate $[\text{Ni}(\text{NO}_3)_2] \cdot \text{H}_2\text{O}$, potassium hydroxide (KOH), have been purchased from Sigma Aldrich, USA.

The desired chemicals such as titanium (IV) butoxide, 2-methoxy ethanol, chitosan powder, nickel nitrate and potassium hydroxide have been purchased from Sigma Aldrich, USA. All biological chemicals such as cholesterol, cholesterol oxidase, cholesterol esterase, low density lipoprotein (LDL; MW: 3500 kda), apolipoprotein B-100 (AAB; MW: 515 kda), bovine serum albumin (BSA), N-hydroxysuccinimide (NHS), N-ethyl-N0-(3-dimethylaminopropyl carbodiimide) (EDC) are of analytical grade and have been purchased from Sigma Aldrich. The surfactants such as polidocanol (Brij) and ethylenediaminetetraacetic acid (EDTA) have been purchased from Sigma Aldrich, USA.

3.3.3 Sol-gel synthesis of anatase-TiO₂

Typical precursors are metal alkoxides and metal chlorides that undergo hydrolysis and poly condensation reactions to form a colloid of solid nanoparticles dispersed in a solvent. Sol-gel derived materials have diverse applications in optics, electronics, energy, space, biosensors, medicine (e.g., controlled drug release) and separation (e.g., chromatography) technology. Many researchers have employed sol-gel technique for fabrication of nanostructured metal oxide films on solid substrates for sensing applications [215].

To synthesize TiO₂ nanoparticles, the starting material, i.e. titanium (IV) butoxide is dissolved in 2-methoxy ethanol in order to prepare 5(wt%) precursor sol solution. The resulting sol is then hydrolyzed by drop wise addition of catalytic amount of H₂O and nitric acid under continuous stirring. After completion of the hydrolysis, the sol is kept for aging for about 2 h at ambient temperature to polymerize the gel. The obtained transparent sol-gel solution is used to deposit film onto patterned ITO electrode on glass substrate using dip coating method. The TiO₂ films are initially dried at an intermediate temperature of $\sim 110^\circ\text{C}$ for half an hour and finally annealed at 450°C for 2 h in air atmosphere. The proposed reactions involved in the synthesizes of TiO₂ films onto ITO substrate are shown in Eq. 3.1.3. Figure 3.1.5 shows the schematic representation of the crystalline structure of TiO₂.

3.3.4 Synthesis of chitosan (CH) and anatase-TiO₂ composite

The chemical structure of CH is shown in Figure 3.1.6. It is a linear polysaccharide composed of randomly distributed β -(1-4)-linked D-glucosamine (deacetylated unit) and N-acetyl-D-glucosamine (acetylated unit) [217]. It can be prepared by treating shrimp and other crustacean shells with the alkali sodium hydroxide. A CH (0.50%) solution is prepared by dissolving CH (50 mg) in 100 mL of acetate buffer (0.05 M, pH 4.2) solution. Calculated amount of anatase TiO₂ (antTiO₂) nanoparticles is dispersed in the CH solution (5 mg/ml) by stirring at room temperature and is sonicated for 30 minutes. A highly viscous solution of CH with uniformly dispersed antTiO₂ nanoparticles is obtained. The selective deposition of antTiO₂-CH solution is carried out on this fabricated patterned ITO electrode through a dip coating technique. Initially, the glass substrate with ITO microelectrode is masked using masking tape and only the desired electrode is selectively exposed by removing the masking tape over it. The substrate is then dried at 40°C for about 1 h after which the remaining masking tape film is removed from the substrate. This process results in a glass substrate containing antTiO₂-CH/ITO (unmasked region) and bare ITO electrode (masked region). The antTiO₂-CH/ITO film is washed with deionized water to remove any unbound particles.

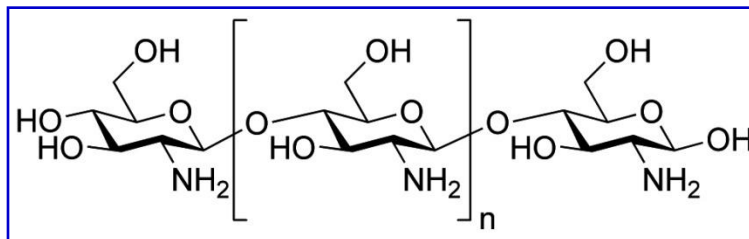


Figure 3.1.6: Chemical structure of chitosan

3.3.5 Co-precipitation method

Co-precipitation is defined as the precipitation of one compound simultaneously with one or more other compounds to form mixed crystals [218]. Nanostructured metal oxides with controlled size, shape and structure can be synthesized using chemical, physical and biological routes. Among the various techniques, co-precipitation method for the synthesis of nanoparticles have become very popular and gained wide acceptance. The chemical synthesis of nanomaterials involves three steps, namely nucleation, growth and termination of reaction *via* precipitation of required precursor ion in solution phase. Reaction temperature and reagent conditions provide a rudimentary control of these three steps. The control of shape, size, stability and assembly of nanoparticles are achieved by incorporating different solvents, templates and capping agents such as polymeric molecules and biomolecules. The co-precipitation process is a very suitable method for synthesis of oxide powders. The main components of a solution consist of a solute and a solvent. Solution may be homogeneous mixtures (a physical combination of substances), which can be solid, liquid, or gas. There are three main mechanisms of co-precipitation namely; inclusion, occlusion, and adsorption. An inclusion happens when the impurities occupy a lattice site in the crystal structure of the carrier, known as crystallographic defect. This can occur when the ionic radius and charge of the impurity are similar to that of the carrier. An occlusion happens when an adsorbed impurity becomes physically trapped inside the crystal as it grows. An adsorbate is an impurity that is weakly bound (adsorbed) to the surface of the precipitate.

3.3.6 Co-precipitated synthesis of nanostructured nickel oxide (nNiO)

nNiO can be prepared using sol-gel, reverse-micelle, laser induced fragmentation and microwave irradiation techniques. The controlled growth and high aspect ratio of synthesized nanowires is a challenge for functionalization with biomolecules including antibodies. The nNiO film has recently been used for immobilization of single stranded DNA via electrostatic interactions for Kala-azar detection [219]. A composite of NiO–CH based cholesterol biosensor has recently been reported via immobilization of cholesterol oxidase [220].

In order to synthesize nNiO [221], the nickel nitrate $\{\text{Ni}(\text{NO}_3)_2 \cdot 6\text{H}_2\text{O}; 0.5 \text{ M}\}$ and 0.2 M of potassium hydroxide (KOH) are dissolved in deionized water to which KOH solution is added drop wise with constant stirring at room temperature (25°C) until pH 9.0 is reached. A green precipitate of $\text{Ni}(\text{OH})_2$ thus obtained is centrifuged followed by washing with deionized water until neutral pH is achieved. This solution was dried at 80 °C overnight. A nickel hydroxide gel is formed as shown in the reactions below. The $\text{Ni}(\text{OH})_2$ based films are calcinated at 400°C for about 2 h to form nNiO.



A transparent viscous solution of nNiO is obtained on the ITO coated glass plate via dip-coating technique. To control the shape of nNiO, we have optimized the pH value of Ni(OH)₂ solution before calcination.

3.3.7 Synthesis of carbon nanotubes

Precursors such as xylene, methane, ethylene, acetylene, benzene, and carbon monoxide are most commonly used for synthesis of MWCNT. Chemical vapor deposition (CVD) is one of the most popular methods for producing CNTs [222]. In this technique, thermal decomposition of a hydrocarbon vapour is achieved in the presence of a metal catalyst [Figure 3.1.6]. It is also known as thermal CVD or catalytic CVD and offers better control on the growth parameters. The process involves passing a hydrocarbon vapor (typically 15–60 min) through a tubular reactor in which a catalyst material is present at sufficiently high temperature (600–1200 °C) to decompose the hydrocarbon. CNTs grow on the catalyst in the reactor, which are collected upon cooling the system to room temperature. Volatile materials (ferrocene) directly turn from solid to vapor, and perform CVD while passing over the catalyst kept in the high-temperature zone. Pyrolysis of the catalyst vapor at a suitable temperature liberates metal nanoparticles in-situ (process is known as floating catalyst method). Alternatively, catalyst coated substrates can be placed in the hot zone of the furnace to catalyze the CNTs growth. The CNTs (90%) are synthesized by catalytic CVD using a mixture of ferrocene acting as catalyst and toluene as a hydrocarbon source [222]. These CNTs are purified and functionalized through refluxing in concentrated nitric acid/sulphuric acid solution, generating a large number of COOH groups on the nanotubes surface.

3.3.8 Synthesis of CNT-NiO composite

Drop-wise addition of 0.2 M KOH (potassium hydroxide) solution along with COOH-terminated CNT to 0.5M Ni(NO₃)₂·6H₂O (nickel nitrate) solution in de-ionized water with constant stirring results in blackish green precipitate of nickel hydroxide [Ni(OH)₂] at pH of ~11.8. Excess solvents are evaporated resulting in the precipitate that is dried at 80°C for 24 h resulting in a transparent viscous solution of nickel hydroxide modified CNT. This precipitate is maintained at pH 10.0. The thick gel-like Ni(OH)₂ modified CNT solution is deposited onto patterned ITO electrodes on glass substrate via dip coating. The electrodes are initially dried at ~110°C for about 1 h and finally annealed at 400°C in ambient conditions for about 2 h to remove any solvent resulting in the formation of CNT(0.1%)-NiO and CNT(0.2%)-NiO onto ITO surface.

3.4 Characterization techniques

The prepared nanoparticles, composites based electrodes/bioelectrodes have been characterized using various spectroscopic techniques such as UV-Vis, FT-IR, Raman, XRD, Zeta potential and XPS. The different microscopic techniques such as SEM, AFM and TEM have been used to characterize the fabricated microfluidic electrodes. Electrochemical studies such as CV, chronoamperometry (CA), chronocoulometry (CC) and EIS techniques have been carried out to investigate the electrochemical properties and detection of biomolecules.

3.4.1 UV-Vis spectroscopy

The absorption or reflectance spectroscopy uses light in the visible and adjacent (near-UV and near-infrared) ranges [223]. In the region of electromagnetic spectrum, the molecules undergo an electronic transition resulting in the changes of electronic structure of ions through the excitations of bonded and non-bonded electrons. In this process, the promotion of electrons happens from the ground state to higher energy states. For visible and ultra-violet spectrum, electronic excitations occur in the range 200-900 nm. There are many factors which influence the relative energies of molecular orbitals (i.e., solvents, position/conformation of substituents, etc.) and information of these factors is necessary in electronic spectroscopy. The strength of electronic spectroscopy lies in its ability to measure the extent of multiple bond or aromatic conjugation within molecules or macromolecules. Longer the conjugation, longer is the maximum wavelength of the absorption spectrum. It can be useful to identify the conducting state of metal oxide nanoparticles as well as carbon materials. The technique is used in a quantitative way to determine concentrations of an absorbing species in solution, using the Beer-Lambert law [Eq. 3.1.7].

$$A = \log_{10}(I_0/I) = \epsilon \cdot c \cdot L \quad \text{Eq. 3.1.6}$$

where, A is the measured absorbance, I_0 is the intensity of the incident light at a given wavelength, I is the transmitted intensity, L the pathlength through the sample, and c the concentration of the absorbing species. For each species and wavelength, ϵ is a constant known as the extinction coefficient. The absorbance of nanoparticles is found to decrease as particle size decreases resulting in a sharp increase of the binding energy. It is a very useful technique to compare between bulk and nanomaterials as well as particles size estimation using effective mass approximation model.

$$\Delta E = \left(\hbar^2 \pi^2 / 2R^2\right) \left(\frac{1}{m_e} + \frac{1}{m_h}\right) - \frac{1.8e^2}{\epsilon R} \quad \text{Eq. 3.1.7}$$

where, ΔE is the increase of the band gap energy, $\epsilon = 5.7$ is the relative dielectric constant, and $m_e = 0.19 m_0$ and $m_h = 0.8 m_0$ are the effective masses of electrons and holes, respectively.

In our studies, the UV-visible spectroscopy has been used to confirm the formation of sol-gel derived nanostructured TiO₂, TiO₂-CH, NiO, CNT, and CNT-NiO and find their band gap energies. These measurements have been carried out using a UV-visible spectrophotometer (Perkin Elmer, Lambda 950) with the resolution of 0.05-5 nm (NIR resolution: 0.2-20 nm) in the wavelength range from 175-3300 nm using Deuterium and Tungsten halogen light sources. Figure 3.1.6(i) shows an example of the absorption spectrograph obtained from cysteine capped cadmium sulfide (Cys-CdS). It has been found that the value of the radius of Cys-CdS quantum dots is about 4-6 nm.

3.4.2 Fourier transform infrared (FT-IR) spectroscopy

FT-IR technique provides information about the various functional groups present in the compound [224]. It involves absorption of electromagnetic radiation in the infrared region of the spectrum, which results in changes in the vibration energy levels of molecule. The FT-IR spectrum represents the molecular absorption and transmission, creating a molecular fingerprint of the sample. Usually, most molecules have vibrations in the form of stretching, bending etc. FT-IR is an interesting technique in identifying organic compounds that have polar chemical bonds (such as OH, NH, CH etc.) with good charge separation (strong dipoles). A Michelson interferometer [Figure 3.1.8(i)] is used for the FT-IR measurement. Light from the polychromatic infrared source is collimated to a beam splitter, where, 50% of the light is refracted towards a fixed mirror and 50% is transmitted towards a moving mirror. Light is reflected from the two mirrors back to the beam splitter and 50% of the original light passes into the sample. One beam travels through a fixed length and the other is constantly changing as the mirror moves, the signal which exits the interferometer is the result of these two beams “interfering” with each other. The resulting signal is called an interferogram and is measured with all frequencies simultaneously. The measured interferogram signal cannot be interpreted directly. Thus, the decoding of the individual frequencies is required and can be accomplished via the well-known mathematical technique called the Fourier transformation. This transformed spectrum can be used for desired analysis.

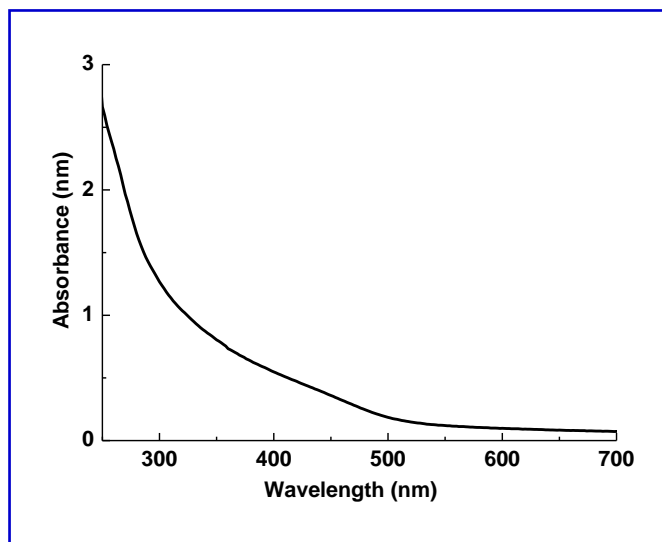


Figure 3.1.7 The absorption spectra of Cys-CdS quantum dots using UV-visible spectrophotometer model, Perkin Elmer, Lambda 950

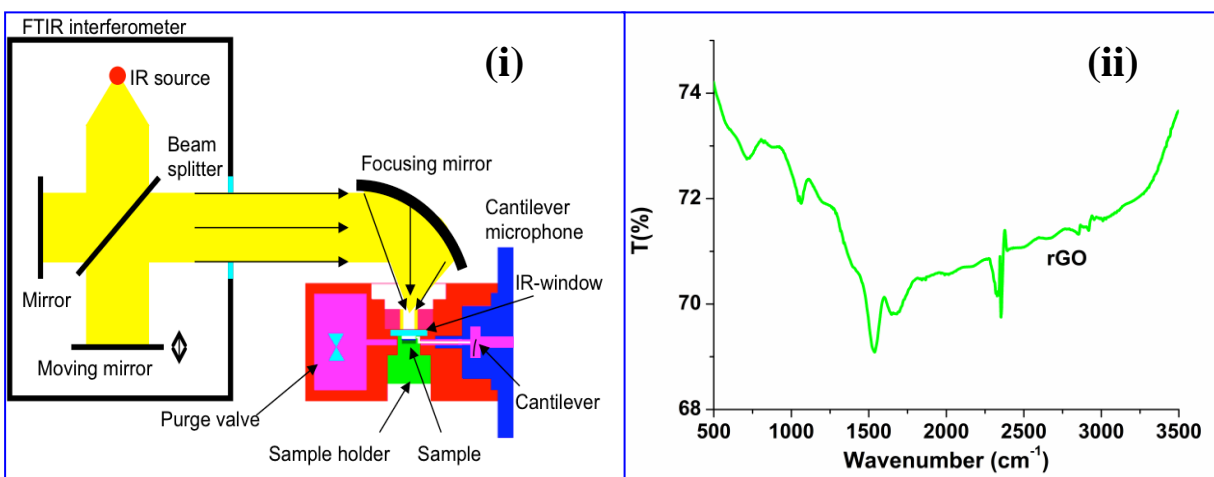


Figure 3.1.8 (i) Schematic diagram of the operation of FT-IR, Perkin-Elmer, Model 2000 (www.gasera.fi), and (ii) FT-IR spectra of reduced graphene oxide film.

In this thesis, the FT-IR measurements have been carried out to confirm the presence of metal oxide nanoparticles, composites and their functionalization with biomolecules such as enzymes, antibodies etc. Since every functional group has a unique vibration energy, the IR spectra is indication of their fingerprints. The prepared samples have been characterized using this technique and their descriptions have been included in the results and discussion sections. A FT-IR spectrum of reduced graphene oxide

(rGO) film is shown in Figure 3.1.8 (ii) as an example. The peaks seen at 1600-1700 cm^{-1} is indication of the functional COOH groups on rGO.

3.4.3 Raman spectroscopy

Raman spectroscopy allows the detection and identification of molecules through their unique vibrational and rotational energy level structures [225]. When a strong light source (laser) is focused on a substance, most of this energy will be scattered elastically. This process is called Rayleigh scattering. The molecules of the substance get excited to a virtual electronic state and would immediately fall back to their original state by releasing a photon [Figure 3.1.9(a)]. The energy of this scattered photon is equal to that of the incoming light. A molecule may also fall back from an excited electronic state to an energy state that is higher (Stokes type scattering) or lower (anti-Stokes type scattering) than the original state. The difference in energy between the incoming and scattered photon (Raman shift) corresponds to the energy difference between vibrational energy levels of the molecule. The different vibrational modes of a molecule can therefore be identified by recognizing Raman shifts (or 'bands') in the inelastically scattered light spectrum [Figure 3.1.9(a)].

A wide variety of substances such as minerals, organic molecules, fluids, gases etc. can be identified directly through Raman studies. The Raman scattering is effective for covalent bonds, and very weak for ionic bonds. However, the infra-red spectroscopy also measures the vibrational energies of molecules. The absorption of light in the infrared region of the spectrum, offers a spectrum that corresponds to specific vibrational modes. For Raman active molecules, there should be a change in the polarizability of the molecule during the vibration indicating that molecules undergo a positional change. FT-IR active molecules should undergo dipole moment change during their vibrations. Thus, when a molecule is symmetrical, e.g. O_2 , no FT-IR absorption peaks can be observed, since the molecule cannot change its dipole moment. Figure 3.1.9 (a) shows a simplified energy level diagram for Raman spectroscopy. Raman spectra of pristine CNTs and COOH functionalized CNTs shown in Figure 3.1.9(b). It can be seen that the intensities of the disorder and graphitic peaks are changed due to functionalization of CNTs.

3.4.4 X-ray diffraction (XRD)

In order to investigate the crystallographic structure, crystalline size (grain size) and preferred growth orientation of nanostructured samples, the XRD technique has been used. The XRD pattern can be recorded using an X-ray diffractometer, wherein the peak broadening data are obtained by measuring the average of peak broadening in the five strongest diffraction peaks. The mean crystallite size can be

determined from the peak broadening in the X-ray diffraction spectrum using the Debye-Scherrer Eq. 3.1.7

$$D = 0.9\lambda / \beta \cos \theta \quad \text{Eq. 3.1.7}$$

where, D is the average crystallite size (\AA), λ is the wavelength of X-rays (Cu $K\alpha$: $\lambda = 1.5418 \text{\AA}$), θ is the Bragg diffraction angle, and β is the full width at half maximum (FWHM) (in radians).

For a crystalline solid sample, the beams are scattered from lattice planes separated by a distance d (interplanar). The scattered waves interfere constructively, but they remain in phase since the path length of each wave is equal to an integer multiple of the wavelength. The path difference between two waves undergoing scattering is given by $2 d \sin\theta$, where θ is the scattering angle. The condition for constructive interference from successive crystallographic planes (h , k , and l) of the crystalline lattice, is given by Bragg's law, as

$$2d \sin\theta = n\lambda \quad \text{Eq. 3.1.8}$$

where, n is an integer, and λ is the wavelength. The diffraction pattern may be obtained by measuring the intensity of scattered waves as a function of scattering angle. The intensities known as Bragg peaks are obtained in the diffraction pattern, when scattered waves satisfy the Bragg condition [Figure 3.2.1].

XRD measurements have been carried out using the model: Max 2200 diffractometer, Rigaku with Cu $K\alpha$ radiation of 1.54\AA . The voltage and the current of X-ray tube were 40 KV and 40 mA, respectively. A step scanning is performed with a step size of $0.01^\circ/\text{step}$ and the integration time of 8 s/step to get noise free XRD graph.

3.4.5 Scanning electron microscopy (SEM)

SEM is a very useful technique and widely used to study the surface morphology and topography. It provides high-magnification and can have resolution of a few nanometers. Tungsten is used to emit monochromatic electrons with typical energy of 20-30 keV. These electrons are focused by condenser lenses to form a beam with a very fine spot size ~ 1 to 5 nm . This beam passes through a pair of scanning coils in the objective lenses that deflects the beam in a raster fashion over the sample surface. This beam of primary electrons interacts with sample volume ranging from less than 100 nm to $5 \text{ }\mu\text{m}$ and generates signals (secondary electrons, internal currents, photon emission etc.). These signals are detected by detectors. The final image is produced on the screen through cathode ray tube. In addition, SEM can provide information about the sample composition near the surface and is known as energy dispersive spectroscopy. In the present work, SEM has been used to study the morphology of nanostructured metal

oxides and its nanocomposite-based film. A LEO microscope (image b) has been used for all the measurements.

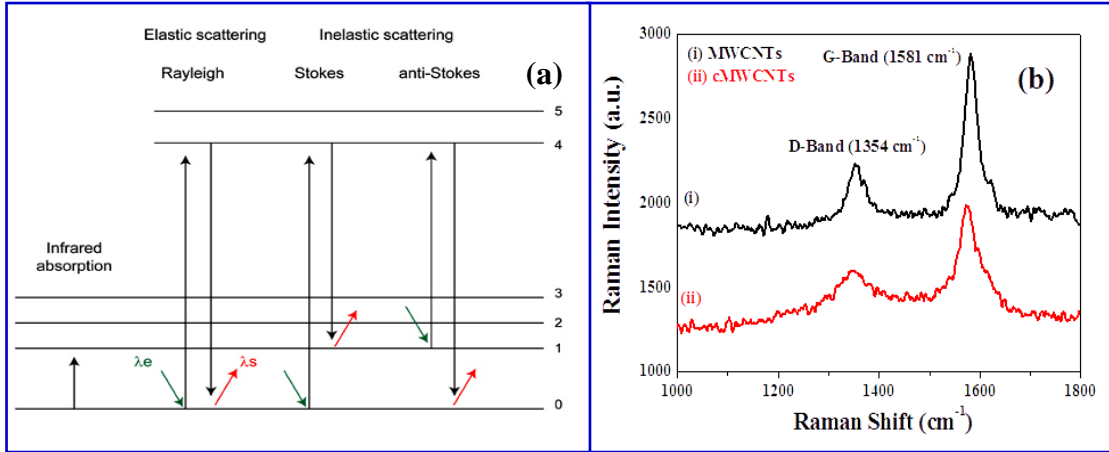


Figure 3.1.9 (a) Energy level diagram for Raman spectroscopy. The shift in wavelength between the excitation light (λ_e) and the scattered light (λ_s) is related to Raman shift (ΔV in cm^{-1}) according to: $\Delta V = (1/\lambda_e) + (1/\lambda_s)$. (b) Raman spectra of pristine CNTs and COOH functionalized CNTs.

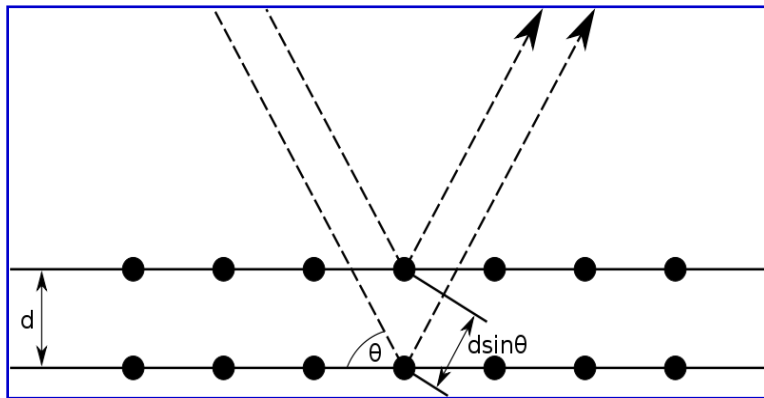


Figure 3.2.1 Bragg diffraction

3.4.6 Transmission electron microscopy (TEM)

The TEM studies have been carried out to investigate the morphological shape, size and distribution of nanomaterials [226]. Figure 3.2.2(A) represents the schematic of a TEM. A thin solid specimen (< 200 nm) is bombarded in vacuum with a monoenergetic focused beam of electrons. The high resolution results from the smaller de Broglie wavelength associated with high-energy electron beam and its ability to focus the electron beam. For example, electrons having energy of 100 keV corresponds to a de Broglie wavelength of 3.7×10^{-3} nm. TEM operates with the electron beams having energy in the range of 20-200 keV. The spatial resolution is large for higher energy electron beams. The beam has sufficiently high energy to propagate through the specimen. The transmitted electron signals are magnified by a series of electromagnetic lenses. TEM offers two modes to study a desired specimen: image and diffraction. The image mode contrast must be induced in order to produce image for analysis. Many contrast-forming mechanisms exist and the interpretation of images is complicated due to the interplay of the different mechanisms. The most common imaging techniques in TEM are mass-thickness imaging, diffraction imaging and phase contrast imaging. In the diffraction mode, the pattern of the diffracted electrons is obtained from the electron-illuminated sample. When the electron beam is incident on the sample, scattering events occur since all the illuminated parts of the sample act as scattering sources. Interference causes coherently scattered beams when Bragg's law is fulfilled. The coherently scattered beams are recorded as a "spot". This spot pattern of the diffracted electron beam from the selected sample area is called the selected area electron diffraction (SAED) pattern. It provides information about the crystalline structure and crystal orientation. A key requirement for TEM samples is the electron transparency, as a thick sample would cause too many interactions leaving no intensity in the transmitted beam. A thick sample also increases the risk of multiple scattering of electrons and the resulting image would be difficult to interpret. In the present work, TEM samples have been prepared by dispersing powder sample in ethanol using sonication and a small drop of that solution is casted onto a carbon coated copper grid. Figure 3.2.3(B) show an example of TEM image of gold nanoparticles.

3.4.7 Atomic force microscopy (AFM)

AFM is a high-resolution scanning probe microscopic technique. It consists of a cantilever with a sharp tip (or probe) at its end which is used to scan the specimen surface [227]. The cantilever is made using silicon with a tip radius of curvature on the order of nanometer. When the tip is brought in proximity of a sample surface, force between the tip and the sample results a deflection of the cantilever according to Hooke's law. Different kinds of forces such as mechanical contact force, *Van Der Waals* force, capillary force, chemical bonding, electrostatic forces, magnetic forces etc. can be measured using AFM. The deflection is measured using a laser spot reflected from the top surface of the cantilever into an array of

photodiodes. The AFM can be operated in contact mode or dynamic (non-contact or "tapping") mode. In static mode, the cantilever is dragged across the surface of the sample and the contours of the surface are measured directly using the deflection of the cantilever. In dynamic mode, the cantilever is externally oscillated at or close to its fundamental resonance frequency or a harmonic. If the tip was scanned at a constant height, it may collide with the surface resulting in damage. Thus, a feedback mechanism is employed to adjust the tip-to-sample distance to maintain a constant force between the tip and the sample. The tip or sample is mounted on a 'tripod' of three piezo crystals, each responsible for scanning in the three (x, y and z) directions.

3.4.8 Zeta potential and Brunauer-Emmett-Teller (BET) studies

Zeta potential is a measure of the magnitude of the electrostatic or charge repulsion or attraction between particles [228], and is one of the fundamental parameters known to affect stability. Its measurement reveals detailed insight into the causes of dispersion, aggregation or flocculation, and this information can be applied to improve the formulation of dispersions, emulsions and suspensions. Figure 3.2.3(i) shows a microscopic portion of a particle surface immersed in water. Zeta potential is defined as the electrical potential at the shear plane with respect to the bulk liquid. Colloidal particles dispersed in a solution are electrically charged due to their ionic characteristics and dipolar attributes. Each particle dispersed in a solution is surrounded by oppositely charged ions called the fixed layer. Outside the fixed layer, there are varying compositions of ions of opposite polarities, forming a cloud-like area. This area is called the diffuse double layer, and the whole area is electrically neutral. When a voltage is applied to the solution in which particles are dispersed, particles are attracted to the electrode of the opposite polarity, accompanied by the fixed layer and part of the diffuse double layer, or internal side of the "sliding surface". Zeta potential is considered to be the electric potential of this inner area including this conceptual "sliding surface". As this electric potential approaches zero, particles tend to aggregate. The NiO nanoparticles and carbon nanotubes have been characterized using measured Zeta potential. The pore size distribution and total surface area of the TiO₂ and antTiO₂-CH are calculated by means of the BET and Barrett-Joyner-Halenda (BJH) methods and Autosorb software (Quantachrome Instruments, USA). BET explains the physical adsorption of gas molecules such as nitrogen multilayer adsorption on a solid surface. This method is utilized to evaluate the precise specific surface area of materials as a function of relative pressure using a fully automated analyzer. The technique includes external area and pore area evaluations in order to determine the total specific surface area in m²/g yielding important information in studying the effects of surface porosity and particle size in many applications.

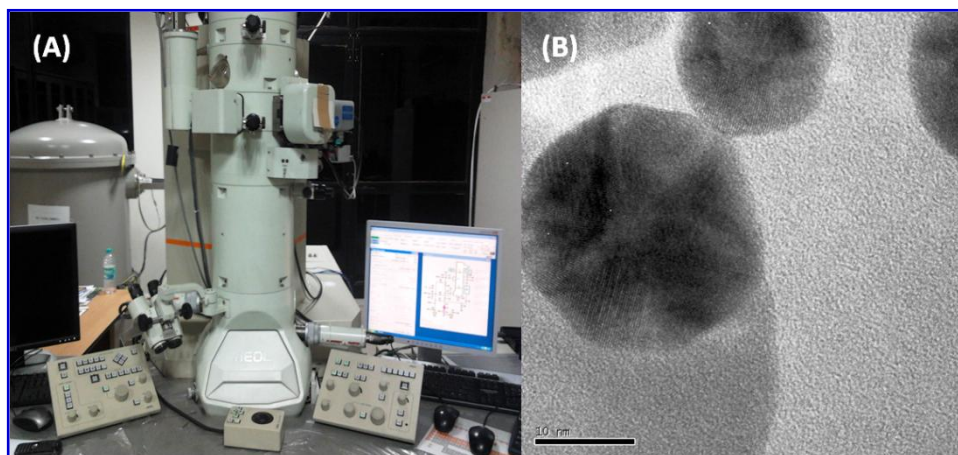


Figure 3.2.2(A) TEM instrument (TEM, JEOL JEM-2000 EX) and (B) TEM image of gold nanoparticles.

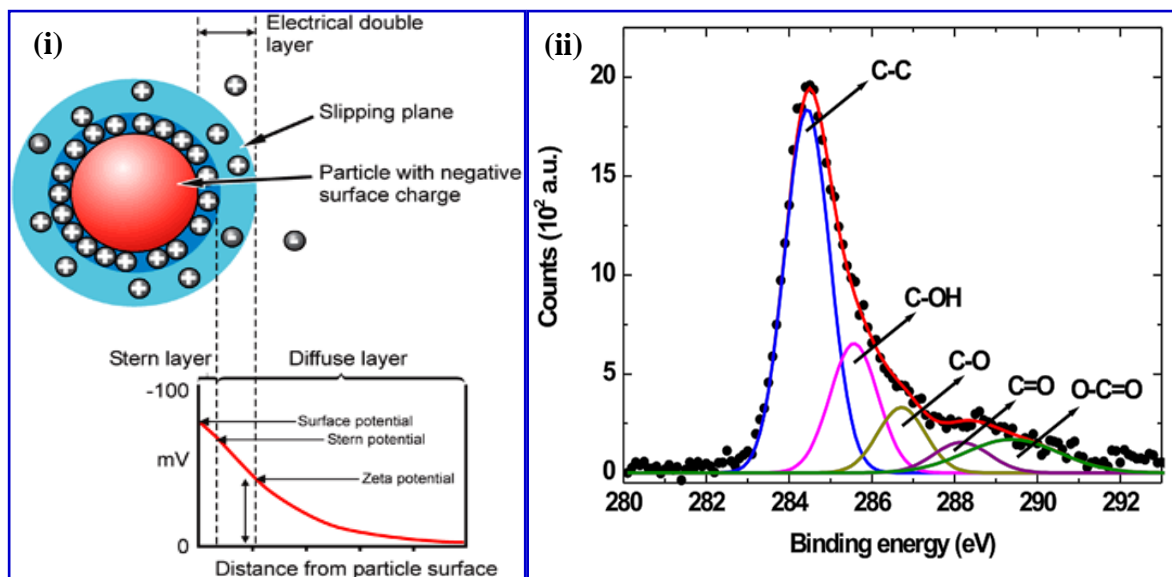


Figure 3.2.3 (i) Schematic representation of zeta potential (www.malvern.com) and (ii) XPS of the C1s region of rGO deconvoluted into characteristic peaks.

3.4.9 X-ray photoelectron spectroscopy (XPS)

XPS technique is a surface-sensitive quantitative method that measures the elemental composition at the parts per thousand range, empirical formula, chemical state and electronic state of the desired material [229]. XPS spectra can be obtained by irradiating the material with a beam of X-rays at ultra-high vacuum conditions in order to measure the kinetic energy and number of electrons that escape from the top 0 to 12 nm of the material being analyzed. It is a surface chemical analysis technique that can be used to analyze the surface chemistry of the material. It is used to measure: (a) elemental composition of the surface (top 1–10 nm), (b) empirical formula of pure materials, (c) elements that contaminate the surface, (d) chemical or electronic state of each element in the surface, (e) uniformity of elemental composition across the top surface (mapping) and (f) uniformity of elemental composition as a function of ion beam etching (or depth profiling). I have investigated the surface functionalization of ChEt-ChOx onto CH-TiO₂ and CNT-NiO surface. XPS of the C1s region of rGO is deconvoluted into characteristic peaks [Figure 3.2.3 (ii)].

3.5 Electrochemical techniques

Various electrochemical techniques such as cyclic voltammetry (CA), chronoamperometry (CA), impedance spectroscopy are used to characterize the electrochemical properties of the synthesized material [230].

3.5.1 Electrochemical cell

A basic circuit diagram for electrochemical measurement is shown in Figure 3.2.4. In potentiostatic mode, a potentiostat/galvanostat (PGSTAT) may be used to control the potential of the counter electrode (CE) against the working electrode (WE) accurately so that the potential difference between the WE and the reference electrode (RE) is well defined, and corresponds to the value specified by the user. In galvanostatic mode, the current flow between the WE and the CE is controlled. The potential difference between RE and WE and the current flowing between CE and WE are continuously monitored. By using a PGSTAT, the value specified by the user (i.e. applied potential or current) is accurately controlled, anytime during the measurement using a negative feedback mechanism.

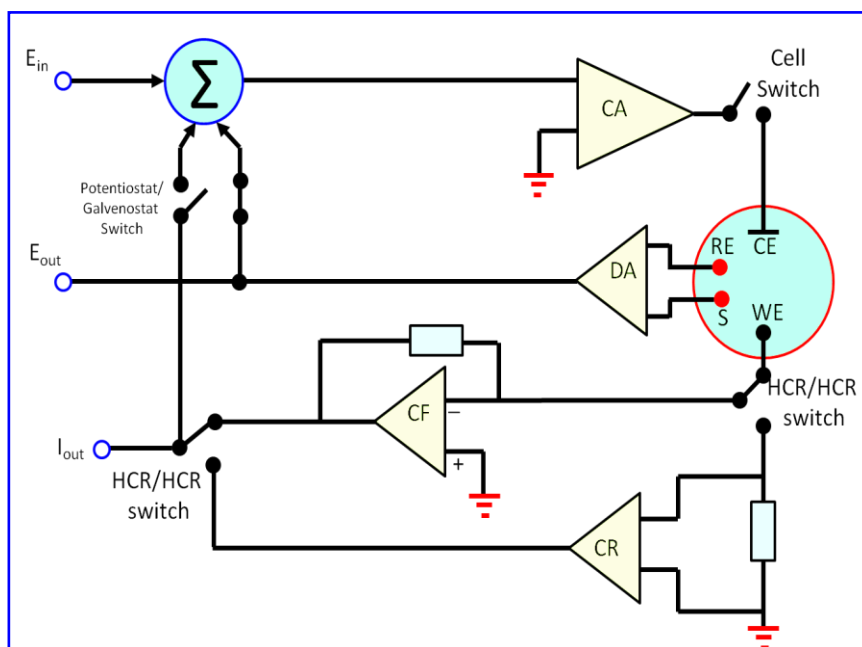


Figure 3.2.4 Electrochemical cell circuit for electrochemical measurement [source: <http://surface.metrohm.com>]

The CE is connected to the output of a control amplifier (CA) that forces the current to flow through the electrochemical cell. The value of the current is measured using a *current follower* (CF) or a shunt resistance (CR), for low and high currents, respectively. The potential difference is measured between the RE and S with a *differential amplifier* (DA). The PGSTAT switch is set depending on the mode the instrument is used (amperometry, potentiometry, chronoamperometry, impedance etc.) The signal is then input to the CA, along with the waveform E_{in} at by digital-to-analog converter through the summation point. The potential is measured between RE and S and the current is measured between WE and CE. The ground connector can be used to connect external devices to the same ground of the PGSTAT. The counter electrode, also known as “auxiliary electrode” is used to close the current circuit in the electrochemical cell. It is usually made of an inert material (Pt, ITO, Au, graphite, glassy carbon etc.) that does not participate in the electrochemical reaction. Because the current is flowing between the WE and the CE, the total surface area of the CE (source/sink of electrons) must be higher than that of the WE so that it will not be a limiting factor in the kinetics of the electrochemical process under investigation.

The reference electrode has a stable and well-known electrode potential and it is used as a point of reference in the electrochemical cell to control potential and current measurement. The high stability of the reference electrode potential is usually reached by employing a redox system with constant (buffered or saturated) concentrations of each participants of the redox reaction. Moreover, the current flow through

the reference electrode is kept close to zero (ideally, zero). which is achieved using the CE to close the current circuit in the cell together with a very high input impedance on the electrometer ($> 100 \text{ G}\Omega$). There are two commercially available types of reference electrodes, that are commonly used namely; Ag/AgCl and saturated-calomel electrodes.

(a) Ag/AgCl Electrode: There is a Ag wire that coated with AgCl and dipped into NaCl solution.



(b) Saturated-Calomel Electrode: Calomel is the other name of mercurous chloride (Hg_2Cl_2).



Working electrode is the electrode in an electrochemical system on which the reaction of interest occurs. In an electrochemical system with three electrodes, the working electrode can be referred to as either cathodic or anodic depending on whether the reaction on the working electrode is a reductive or an oxidative. One common working electrode can be made of inert materials such as Au, Ag, Pt, ITO, glassy carbon (GC) and Hg drop and film electrodes etc. The size and shape of the working electrode also varies depending on the application.

3.5.2 Cyclic voltammetry (CV)

CV is a technique that measures the current that develops in an electrochemical cell under conditions where voltage is in excess of that predicted by the Nernst equation [231]. CV can be performed by cycling the potential of a working electrode, and measuring the resulting current. CV is used to study the electrochemical properties of an analyte in a solution. The plot of the current at the working electrode vs. the applied voltage gives the CV of a redox reaction.

The potential of the working electrode is measured with respect to a reference electrode which maintains a constant potential and produces an excitation signal. Figure 3.2.5 (i) shows an input excitation signal for CV measurement and (ii) its output signal which is called CV resulting from a single electron reduction and oxidation.

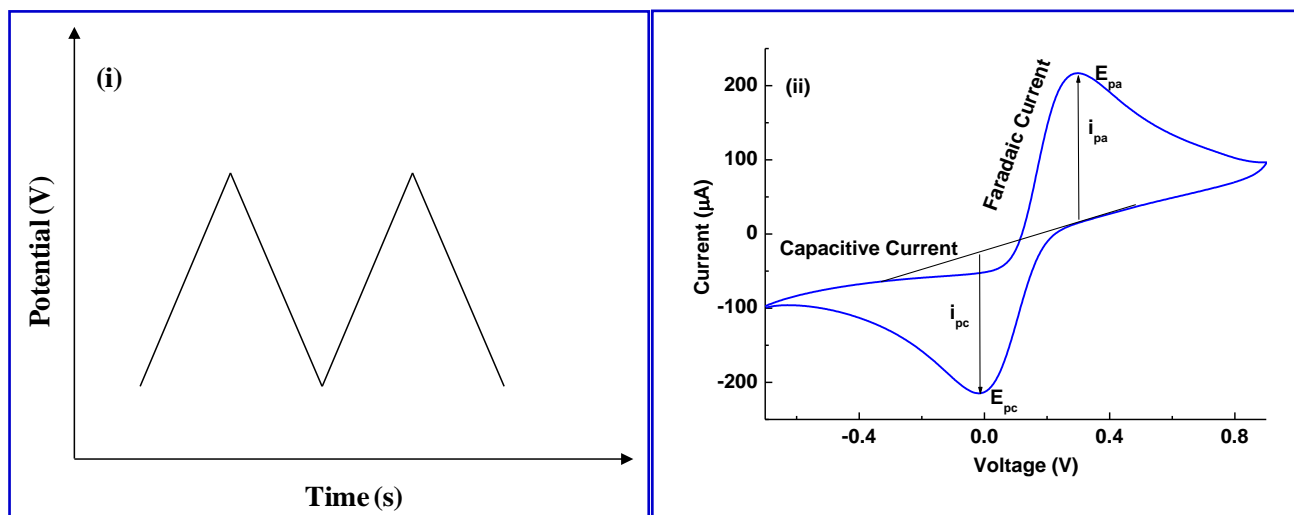


Figure 3.2.5 (i) Input signal or excitation signal for CV measurement and (ii) output signal of a CV .

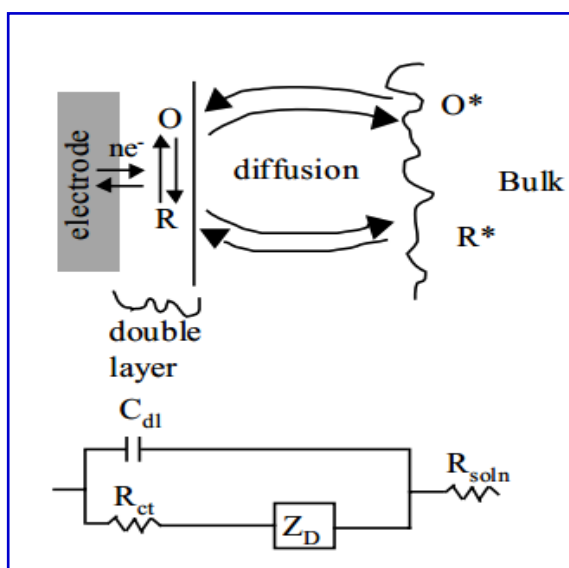
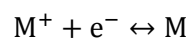


Figure 3.2.6 Electrochemical system that includes electron transfer along with its Randles equivalent circuit.

Consider the following reversible reaction:



Eq. 3.1.9

Electrode potential (E) is given by

$$E = E_i + vt \quad \text{Eq. 3.2.1}$$

where, E_i is the initial potential in volts, (v) is the sweep rate in volts s^{-1} , and t is the time in seconds. When the direction of the potential sweep is switched, the equation becomes,

$$E = E_s - vt \quad \text{Eq. 3.2.2}$$

where, E_s is the potential at the switching point. Electron stoichiometry (n):

$$E_p - E_{p/2} > \frac{0.056}{n} \quad \text{Eq. 3.2.3}$$

where (E_{pa}) is the anodic peak potential, (E_{pc}) is the cathodic peak potential, and (n) is the number of electrons participating in the redox reactions. Formal reduction potential (E°) is the mean of the E_{pc} and E_{pa} values: $E^\circ = (E_{pa} + E_{pc})/2$. Figure 3.2.6 describes the process that occurs in simple electrode reactions. In case of reduction, a species (O) capable of receiving an electron from the electrode diffuses to the surface, receives an electron and diffuses away from the surface. Current at the surface is generated by the transfer of electrons from the electrode to the redox species. In solution current is carried by migration of ions.

In a typical CV, the capacitive current is small compared to the current from electron transfer (Faradaic current). Faradaic current depends on two facts, the kinetics of electron transfer and the rate at which the redox species diffuses to the surface. For the redox couple $Fe(CN)_6^{3-/4-}$, the kinetics of electron transfer are reasonably fast, so that it can be assumed at least for the moment that, at the surface, the concentrations of $Fe(CN)_6^{3-}$ and $Fe(CN)_6^{4-}$ can be described by the Nernst equation as below

$$E = E^\circ - 0.056 \log \left\{ \frac{[Fe(CV)_6^{3-}]}{[Fe(CV)_6^{4-}]} \right\} \quad \text{Eq. 3.2.4}$$

where, E is the applied potential and E° is the formal electrode potential. When the concentration of $Fe(CN)_6^{3-}$ molecules decreases, potential of electrode surface becomes more negative. It is being reduced to $Fe(CN)_6^{4-}$. The peak current in a CV species is described by Randles-Sevcik Eq. 3.2.5.

$$i_p = (269,000)n^{3/2}AD^{1/2}Cv^{1/2} \quad \text{Eq. 3.2.5}$$

where i_p = redox peak current (A), n = number of electrons transferred in the redox event (1), A = electrode area (cm^2), D = diffusion coefficient (cm^2/s), C = surface concentration (mol), v = scan rate (mV/s)]. The cyclic voltammetry studies of the fabricated electrodes have been conducted in phosphate buffer (PBS, 50 mM, pH 7.0, 0.9% NaCl) at the potential range from -0.5V to +1.0V [Figure 3.2.7].

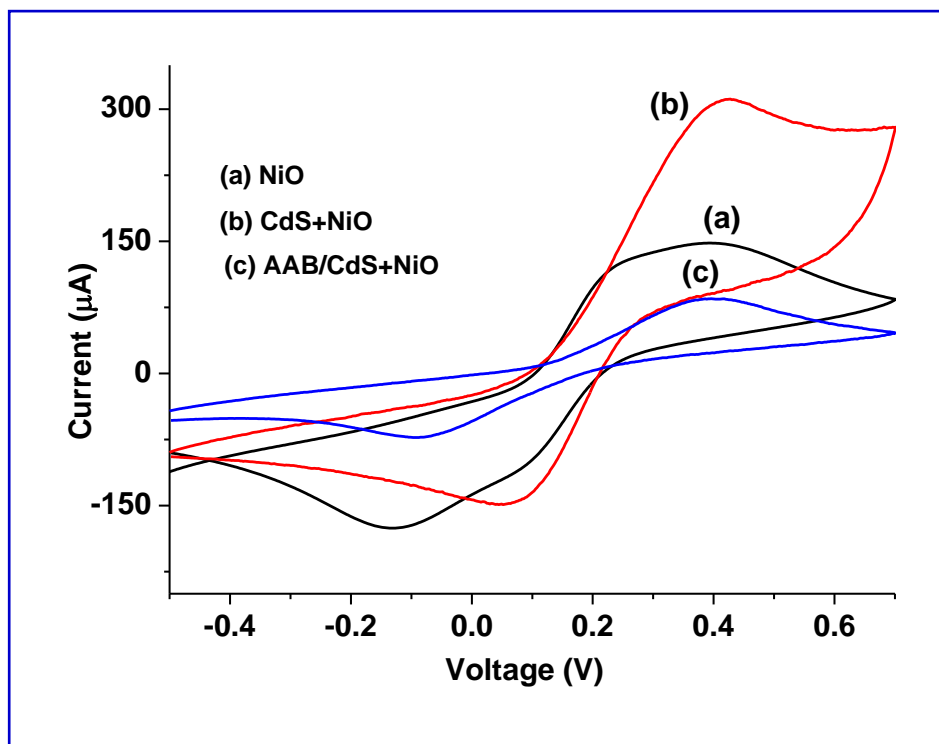


Figure 3.2.7 CV studies of various fabricated electrodes such as (a) NiO/ITO, (b) NiO-CdS/ITO and (c) AAB/NiO-CdS/ITO

3.5.3 Chronoamperometry and chronocoulometry

For chronoamperometric measurement, the steady state current is measured as a function of time while a potential is applied between the working and reference electrodes [232]. The input and output signal of a chronoamperometric measurement is shown in Figure 3.2.8(i). A diffusion layer is developed between the solution media and electrode surface. Diffusion controls the transfer of analyte from the bulk solution of higher concentration to the electrode. Thus, there is a concentration gradient from solution media to the electrode surface. Cottrell equation can be used to describe this situation. It defines the current-time dependence for linear diffusion control at an electrode.

$$i = nFAC_0\sqrt{\frac{D}{\pi t}} \quad \text{Eq. 3.2.6}$$

where, i is the current, n is the number of electrons transferred in the reaction, F is the Faraday constant, A is the electrode area, D is the diffusion coefficient, C_0 is the analyte concentration and t is the time. For example, the chronoamperometric response of rGO/ITO electrode have been conducted in PBS, 50 mM, pH 7.0, 0.9% NaCl at the potential -0.3 V [Figure 3.2.9].

Chronocoulometry [231] involves measurement of charge vs. time response to an applied potential step waveform [Figure 3.2.8(ii)]. The shape of the resulting chronocoulogram can be understood by considering the concentration gradients in the solution adjacent to the electrode surface. Chronocoulometry is useful for measuring electrode surface areas, diffusion coefficients, time window of an electrochemical cell, adsorption of electroactive species, and the mechanisms and rate constants for chemical reactions coupled to electron transfer reactions. The charge (Q) vs. time (t) curve (the Anson equation) is obtained by integrating the Cottrell equation is given by

$$Q = \frac{2nFAC_0D_0^{1/2}}{1/2}t^{1/2} \quad \text{Eq. 3.2.7}$$

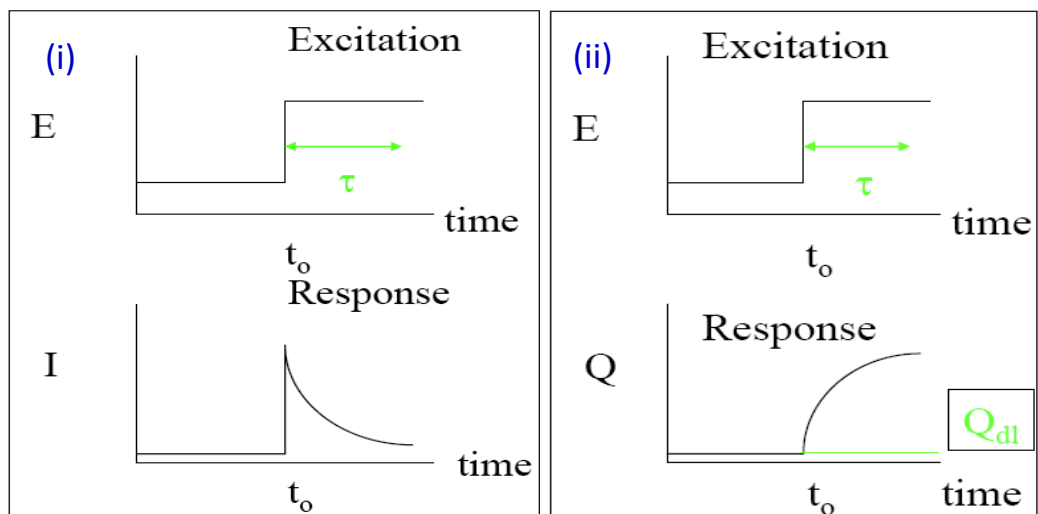


Figure 3.2.8(i) Current vs. time for chronoamperometric measurement and (ii) charge vs. time for chronocoulometric studies.

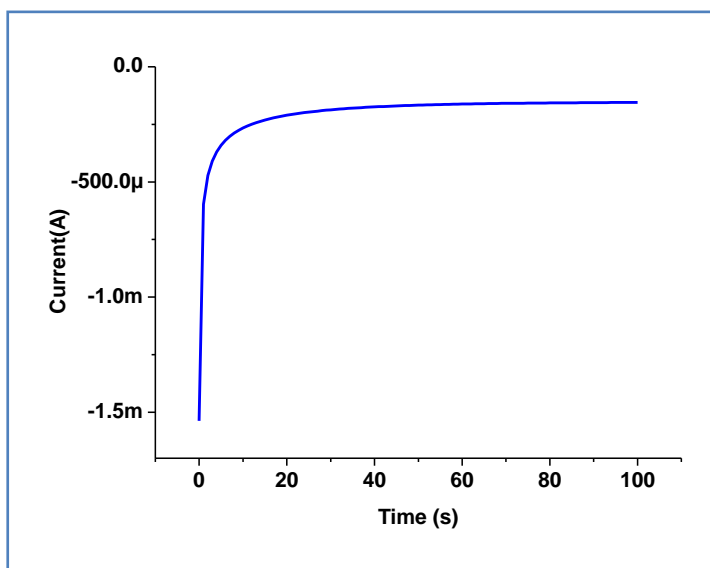


Figure 3.2.9 Chronoamperometric response of rGO/ITO electrode have been conducted in PBS, 50 mM, pH 7.0, 0.9% NaCl at the potential -0.3 V.

The Anson equation assumes the diffusion to a planar electrode following an instantaneous potential step, and it is instructive to see how accurate this assumption is. This can readily be achieved by a plot of Q/t vs. t , which should be constant if the Anson equation is obeyed.

3.5.4 Impedance spectroscopy

Impedance is a measure of the ability of a circuit to resist the flow of electrical current. Electrochemical impedance is usually measured by applying a sinusoidal AC potential to an electrochemical cell and then measuring the current through the cell [231-233]. The response to this potential is an AC current signal. This current signal can be analyzed as a sum of sinusoidal functions (a Fourier series). The excitation signal, expressed as a function of time, has the form

$$E_t = E_0 \sin(\omega t) \quad \text{Eq. 3.2.8}$$

where, E_t is the potential at time t , E_0 is the amplitude of the signal, and ω is the radial frequency. The relationship between radial frequency ω (radians/s) and frequency f (Hz) is given by

$$\omega = 2\pi f \quad \text{Eq. 3.2.9}$$

In a linear system, the response signal, I_t , is shifted in phase, ϕ and has a different amplitude, I_0

$$I_t = I_0 \sin(\omega t + \phi) \quad \text{Eq. 3.3.1}$$

The electrical impedance (Z) is the ratio of the incremental change in voltage, E_t to the resulting change in current, I_0 , and Z is given by Eq. 3.3.2.

$$Z = \frac{E_t}{I_0} = \frac{1}{Y} = \frac{E_0 \sin(2\pi ft)}{I_0 \sin(2\pi ft + \varphi)} = Z_0 \frac{\sin(2\pi ft)}{\sin(2\pi ft + \varphi)} \quad \text{Eq. 3.3.2}$$

where Y is the complex admittance and the impedance is described either by the modulus $|Z|$ and the phase shift φ or by its real (Z') and imaginary (Z''). The impedance is then represented as a complex number,

$$Z(\omega) = \frac{E}{I} = Z_0 \exp(j\varphi) = Z_0(\cos \varphi + j \sin \varphi) \quad \text{Eq. 3.3.3}$$

The most frequently used equivalent circuit for modeling the EIS experimental data is the Randles circuit that comprises of an electrolyte (R_s), in series with the double layer capacitance (C_{dl}), charge-transfer resistance (R_{CT}) and Warburg impedance (Z_w or Z_D). The Nyquist plot includes a semicircle region lying on the real axis followed by a straight line. The linear part ($\psi = \pi/4$), observed at the low frequency range, implies a mass-transfer limited process, whereas the semicircle portion, observed at high frequency range, implies a charge-transfer limited process [Figure 3.3]. The imaginary component, at high frequency falls to zero because it offers zero impedance. As the frequency drops, the capacitance C_{dl} offers high impedance and hence current flows mostly through R_{CT} and R_s . The double layer capacitance or constant phase element (CPE) can be calculated from the frequency at the maximum of the semicircle ($\omega = 2f = 1/R_{ct}C_{dl}$). The charge-transfer resistance R_{ct} and the double layer capacitance C_{dl} are the most important electrical parameters in analyzing the impedance signal change for antibody-antigen interaction. Figure 3.3.1 shows the EIS spectra of the Au (a), TGA/Au (b), CysCdS/Au (c) and AAB-CysCdS/Au electrodes in PBS solution (50 mM, pH 7.4, 0.9% NaCl) containing 5 mM $[\text{Fe}(\text{CN})_6]^{3-/4-}$. Both Nyquist and Bode plots are obtained and have been used to determine the relative change in surface-charge resistance. Interfacial R_{ct} and C_{dl} in Nyquist plot of impedance are obtained from real (Z') and imaginary ($-Z''$) impedance at different frequencies using the following equation (7) for a parallel RC circuit.

$$Z(\omega) = R_s + \frac{R_{ct}}{1 + j\omega R_{ct} C_{dl}} = R_s + \frac{R_{ct}}{1 + \omega^2 R_{ct}^2 C_{dl}^2} - \frac{j\omega R_{ct}^2 C_{dl}}{1 + \omega^2 R_{ct}^2 C_{dl}^2} = Z' + jZ'' \quad \text{Eq. 3.3.4}$$

where, R_s is the electrolyte solution resistance and R_{ct} is the charge transfer resistance or polarization resistance. The frequency associated with maximum $-Z''$ and R_{ct} are used to calculate C_{dl} using the following equation (8).

$$R_{ct} C_{dl} = \frac{1}{2\pi f_{\max}} = \tau \quad \text{Eq. 3.3.5}$$

where, τ is the time constant and f_{\max} is the maximum frequency. The Warburg resistance (Z_w) can be obtained through Nyquist plot and an equivalent circuit to describe the electrical response at electrode. In the plot, the Warburg impedance is expressed by an intercept of straight line having a slope of unity and can be derived from the following Eq. 3.3.6.

$$Z_w(\omega) = W_{\text{int}} + \left(\frac{R_{\text{ct}}\lambda}{\sqrt{2\omega}}\right) [1 - j]; \quad W_{\text{int}} = R_s + R_{\text{ct}} - R_{\text{ct}}^2\lambda^2 C_d \quad \text{Eq. 3.3.6}$$

where, $\lambda = \left(\frac{k_f}{\sqrt{D_0}} + \frac{k_b}{\sqrt{D_R}}\right)$, k_f and k_b are forward and backward electron-transfer rate constants, D_0 and D_R are the diffusion coefficients of oxidant and reductant. The R_s and $R_s + R_{\text{ct}}$ values are obtained from standard commercial software available with the instrument. The electron transfer rate (k_0) of an electrode can be calculated using charge transfer kinetics:

$$k_0 = \frac{RT}{n^2 F^2 A R_{\text{ct}} C} \quad \text{Eq. 3.3.7}$$

where R is the gas constant, T is the temperature, n is the electron transferring constant of the redox couple, F is Faraday constant, A is the effective area of the electrode, and C is the concentration of the redox couple in the bulk solution.

Electrolyte resistance: The resistance of an ionic solution depends on the ionic concentration, type of ions, temperature, and the geometry of the area through which current flows. The resistance can be defined as, $R = \rho l / A$, where, ρ is the solution resistivity, A is an area, and l is the length.

Double layer capacitance: An electrical double layer is an interface between the electrode and electrolyte solution. The charged electrode is separated from the charged ions which form a capacitor. The value of the double layer capacitance depends on many factors such as electrode potential, temperature, ionic concentrations, types of ions, oxide layers, electrode roughness, impurity adsorption, etc.

Charge transfer resistance: A resistance can be formed by a single kinetically controlled electrochemical reaction at equilibrium under a fixed potential. In a redox reaction, the electrons enter the electrode and the generated ions diffuse into the electrolyte. The relation between the potential and the current is given by

$$i = i_0 \left(\frac{C_0}{C_0^*} \exp\left(\frac{\alpha n F \eta}{RT}\right) - \frac{C_R}{C_R^*} \exp\left(\frac{-(1-\alpha) n F \eta}{RT}\right) \right) \quad \text{Eq. 3.3.8}$$

where, i_0 is the exchange current density, C_0 is the concentration of oxidant at the electrode surface, C_0^* is the concentration of oxidant in the bulk, C_R is the concentration of reductant at the electrode surface, η is the overpotential, α is the reaction order, T is the temperature and R is the gas constant. When the

concentration in the bulk is the same as at the electrode surface, $C_o = C_o^*$ and $C_R = C_R^*$, the Eq. 3.3.8 is called the Butler-Volmer equation.

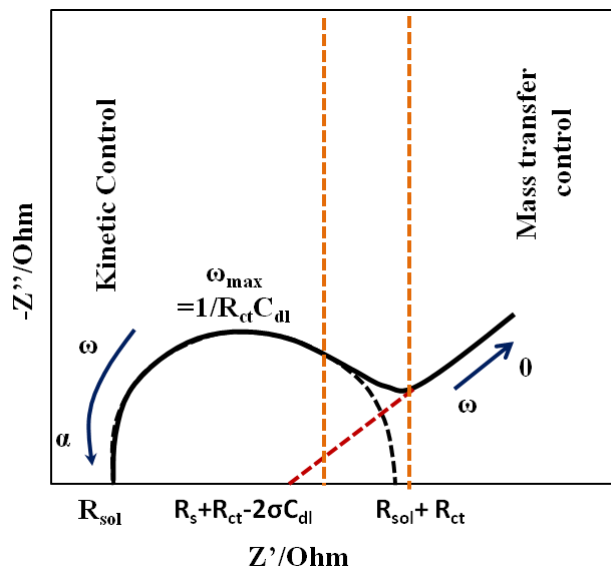


Figure 3.3 A Nyquist plot of EIS measurement, where, C_{dl} is the double-layer capacitor, R_{ct} is the polarization resistance, R_s is the solution resistance and Z_W is Warburg impedance.

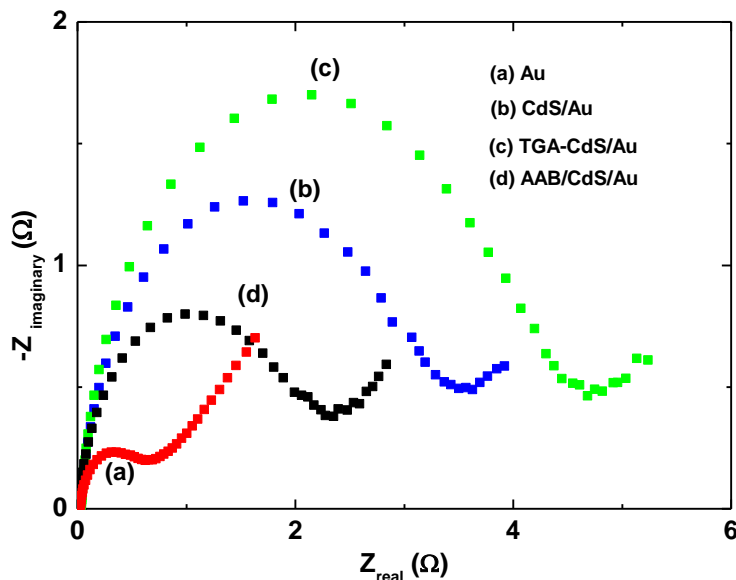


Figure 3.3.1 EIS spectra of various electrodes in PBS solution (50 mM, pH 7.4, 0.9% NaCl) containing 5 mM $[\text{Fe}(\text{CN})_6]^{3-/4-}$

Warburg impedance: Diffusion can create impedance which is called Warburg impedance and is dependent on the frequency of the potential perturbation. At low frequencies, the reactants diffuse which increases the Warburg-impedance while at high frequencies, the Warburg impedance is small. Warburg impedance is given by Eq. 3.3.6.

Constant phase element (CPE): In EIS experiments, capacitor is not behaved ideally. It acts like a constant phase element as defined below. The impedance of a capacitor is given by

$$Z_{\text{CPE}} = \frac{1}{(i\omega)^\alpha Y_0} \quad \text{Eq. 3.3.9}$$

where, Y_0 is the capacitance (C) and $\alpha = 1$ for an ideal capacitor.

3.6 Conclusions

The photolithography, soft lithography, and wet chemical etching techniques for PDMS microchannels and ITO microelectrodes have been illustrated in this Chapter. Various protocols followed for chemical synthesis of organic and inorganic nanomaterials and their composites for microfluidic devices have been illustrated. Different techniques such as SEM, TEM, AFM, XRD pattern, Zeta potential, UV-visible and FT-IR spectroscopy that are used to characterize the morphological and structural properties of synthesized nanomaterials and biofunctionalized microfluidic electrodes in this thesis has been explained. Also, electrochemical techniques such as CV, CC, CA and EIS employed to investigate the electrochemical properties of nanostructured materials, nanocomposite and bioelectrode have been explained. The next Chapter describes the results relating to the development of microfluidic cholesterol biosensors prepared using antTiO₂ and TiO₂-CH matrices.

CHAPTER 4

**Part I: Nanostructured anatase-TiO₂ based
microfluidic platform for free cholesterol estimation**

4.1 Introduction

Nanostructured metal oxides are well known to have unique abilities in promoting fast electron transfer kinetics between desired electrodes and active enzyme sites. In this chapter, an n type semiconductor nanocrystal TiO_2 is explored for potential use as a biosensor transducer material in microfluidic biosensor. TiO_2 has received significance research attention due to its unique properties like high surface area, structural uniformity, stability, negligible protein denaturation and excellent biocompatibility [234]. TiO_2 nanoparticles synthesized by numerous techniques provide superior electrical, optical and magnetic properties that are unlike from their bulk counterparts. The TiO_2 having a wide band gap of 3.2 eV for anatase and 3.05 eV for rutile and they are multifunctional materials. The nanostructured TiO_2 has been extensively used in tissue engineering, drug delivery, membranes, antimicrobial coating, photocatalysis, filters, solar cells, gas sensors and biosensors [235]. Among the various metal oxides, TiO_2 may play an important role as a transducer material for microfluidic biosensor because of their unique ability to promote faster electron transfer between electrode and active site of desired enzyme. Incorporation of nanostructured metal oxides onto the microfluidic electrode surface helps in increased loading of the desired biomolecules. The use of nanostructured TiO_2 may perhaps result in enhanced biomolecules adsorption and improved diffusion efficiency [236].

The functional properties of TiO_2 depend on its crystallographic structure. The crystallographic polymorphs of TiO_2 include rutile (tetragonal), anatase (tetragonal) and brookite (orthorhombic), and TiO_2 (B). Among the many polymorphs, anatase TiO_2 (*ant*- TiO_2) is known to be high-purity single crystal with a high percentage of reactive (001) facets that may cause enhanced catalytic activity, better stability and selectivity [236-238]. The formation of TiO_2 octahedrons is the key mechanism of anatase crystallization. The anatase polymorph of TiO_2 is formed by face sharing of TiO_2 octahedrons while rutile by edge sharing. The higher annealing temperature (greater than 650 °C) of titanium hydroxide can form rutile TiO_2 from anatase TiO_2 (less than 450 °C).

The nanostructured TiO_2 may induce a desired protein to be adsorbed on the nano-sized surface and may perhaps provide effective orientation for electron transfer between a desired protein and the electrode [239]. The *ant*- TiO_2 nanobelts have been used for electrochemical determination of the perfect match and mismatch of single nucleobases at the physiological pH [236]. It has been reported that porous nanocrystalline TiO_2 film not only retains biological activity of enzymes, but also can be used for increased loading capacity of enzyme molecules [235]. Various matrices including metal oxides and carbon nanotubes have been used to immobilize cholesterol oxidase (ChOx) for fabrication of cholesterol biosensor. Wang et al. have demonstrated TiO_2 nanowire bundle microelectrode-based impedance immunosensor for rapid and sensitive detection of *Listeria monocytogenes* [240]. However, the integration of nanostructured TiO_2 with a microfluidic device has not yet been explored. Moreover, the

oxygen containing antTiO_2 surface may lead to enhanced heterogeneous electron transfer rate leading to fast response times of the microfluidic sensor. The antTiO_2 nanoparticles can be used to electrochemically activate the active site of an enzyme due to the presence of gibbositities on the antTiO_2 surface resulting in decreased tunneling distance between active site of enzyme and electrode leading to enhanced electrochemical current. Part I of this Chapter discuss results of the studies relating to fabrication of a microfluidic cholesterol sensor based on ChOx functionalized with highly crystalline nanostructured ant-TiO_2 . In part II of this chapter, the mesoporous TiO_2 nanoparticles has been modified by chitosan for the fabrication of microfluidic biochip towards the detection of total cholesterol.

4.2.0 Experimental section

4.2.1 Fabrication of microfluidic biosensing platform

Details description and protocols for the fabrication of ITO microelectrodes and PDMS microchannels have been given in Chapter 3. The synthesis of ant-TiO_2 nanoparticles using sol gel technique has been also described in Chapter 3 (Section: 3.3.3). I have deposited Ti(OH)_4 sol on patterned ITO electrode via dip coating technique and utilized for biomolecule functionalization. The Ti(OH)_4 film is initially dried at $\sim 110^\circ\text{C}$ for about 1h and is finally annealed at 450°C for about 2h to obtain ant-TiO_2 . In order to immobilize ChOx, the stock solution of ChOx (1mgdl^{-1}) of 24Uml^{-1} is freshly prepared in phosphate buffer (50mM) at pH 7.0. The stock solution of cholesterol is prepared in 10% triton X-100 and was stored at 4°C . The proposed mechanism for preparation of ChOx/ ant-TiO_2 /ITO bioelectrode and immobilization of ChOx is shown in [Figure 4.1.1]. $10\ \mu\text{L}$ of ChOx solution is uniformly spread onto ant-TiO_2 /ITO electrode using physical adsorption technique and electrostatic interaction occurs between ChOx and ant-TiO_2 . This ChOx/ ant-TiO_2 /ITO bioelectrode is rinsed in 50 mM PBS (pH 7.0) in order to wash out any unbound ChOx from the electrode surface.

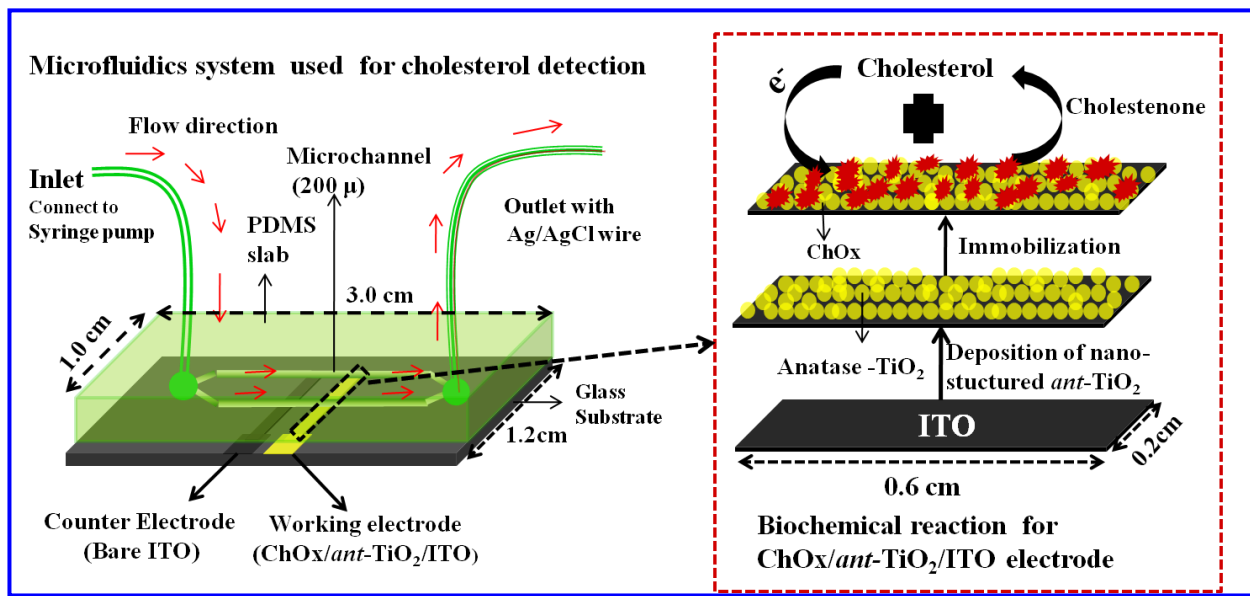


Figure 4.1.1 Pictorial representation of the microfluidic system for cholesterol detection

4.2.2 Precautions

- (i) Care should be taken while using nitric acid during synthesis of *ant*-TiO₂ nanoparticles.
- (ii) Care should be taken while using strong acid treatment for selectively etching the ITO from glass plate.

4.3.0 Results and discussion

4.3.1 X-ray diffraction studies

XRD pattern from *ant*-TiO₂ powder [Figure 4.1.2(a)] shows dominant peaks at 2θ: 25.4° and 48.2°, corresponding to the diffraction [101] and [200] planes indicating presence of the anatase phase of TiO₂. The diffraction pattern corresponding to [004], [105], [211], [204], [166] and [215] planes (JCPDS 89-4921, 89-6975) further supports the presence of anatase phase in TiO₂ with good crystalline structure. The crystallite size of anatase-TiO₂ nanoparticles obtained from the distinct peak (101) at 25.4° using Debye-Scherrer equation has been found to be 15.4 nm and the crystallite strain of anatase-TiO₂ has been estimated to be 2.9×10^{-3} using Williamson and Hall plot.

4.3.2 UV-Visible studies

The *ant*-TiO₂ has a broad absorption band from 280 to 400 nm in the UV region with a maximum absorption around 294 nm [Figure 4.1.2(b)]. A predominant blue shift in the absorption spectra due to quantum size effect of the nanocrystalline *ant*-TiO₂ compared to absorption spectra of the bulk TiO₂ is observed. The optical band gap energy of these TiO₂ nanoparticles has been estimated to be 3.4 eV which is slightly higher than that of bulk anatase phase (3.2 eV).

4.3.3 FT-IR studies

FT-IR spectra of *ant*-TiO₂/ITO exhibits characteristic peaks at 514 cm⁻¹ corresponding to vibrational bending of Ti-O bond in the finger print region [Figure 4.1.3(a)]. The peaks found at 844 and 1263 cm⁻¹ correspond to C-H and C-O stretching bonds, respectively. The band seen at 3600 cm⁻¹ is assigned to stretching and deformation of the O-H bond due to absorption of water molecules. The FTIR spectra of ChOx/*ant*-TiO₂/ITO film (b) exhibits band at 1637 cm⁻¹ arising due to N-H stretching in amide II indicating presence of ChOx on *ant*-TiO₂ film.

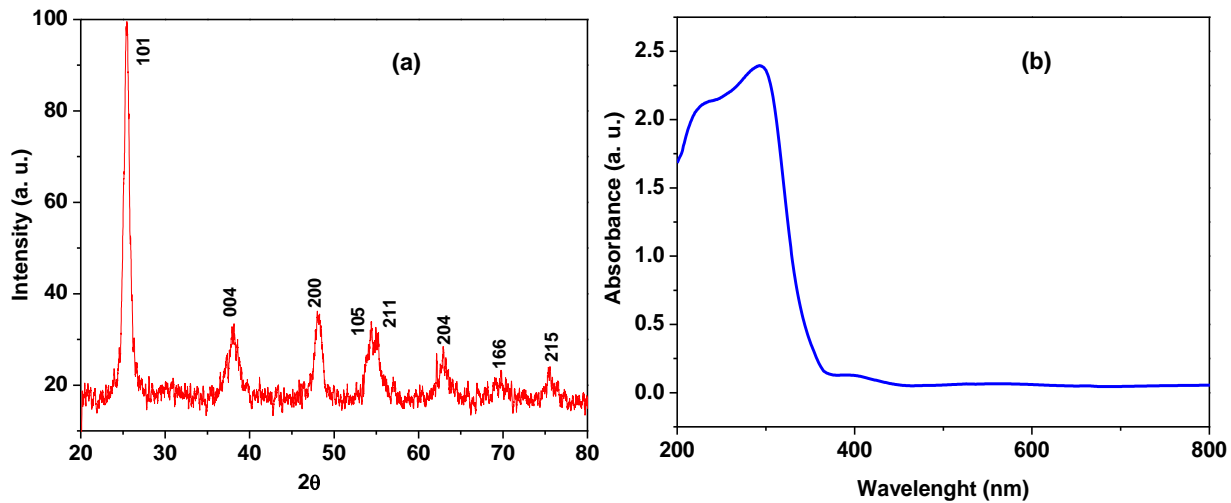


Figure 4.1.2 XRD spectrum of TiO₂ powder and (b) UV-visible spectra of ant-TiO₂/ITO film

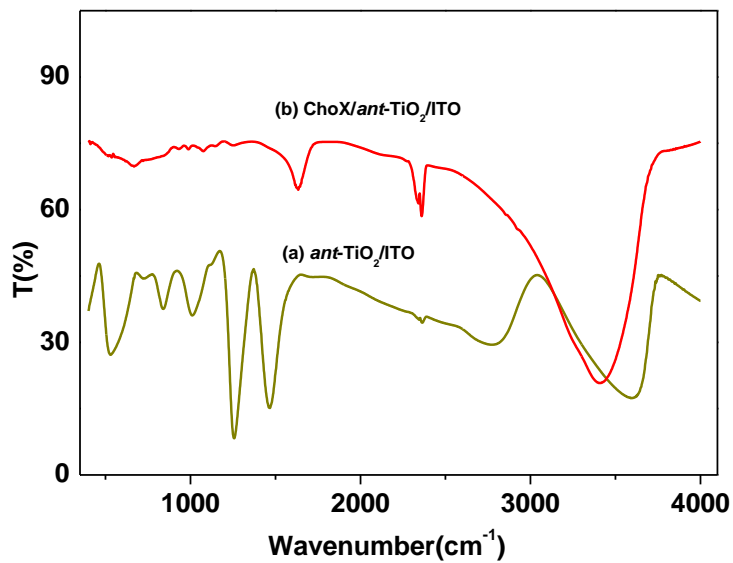


Figure 4.1.3 FT-IR studies of (a) ant-TiO₂/ITO and (b) ChoX/ant-TiO₂/ITO

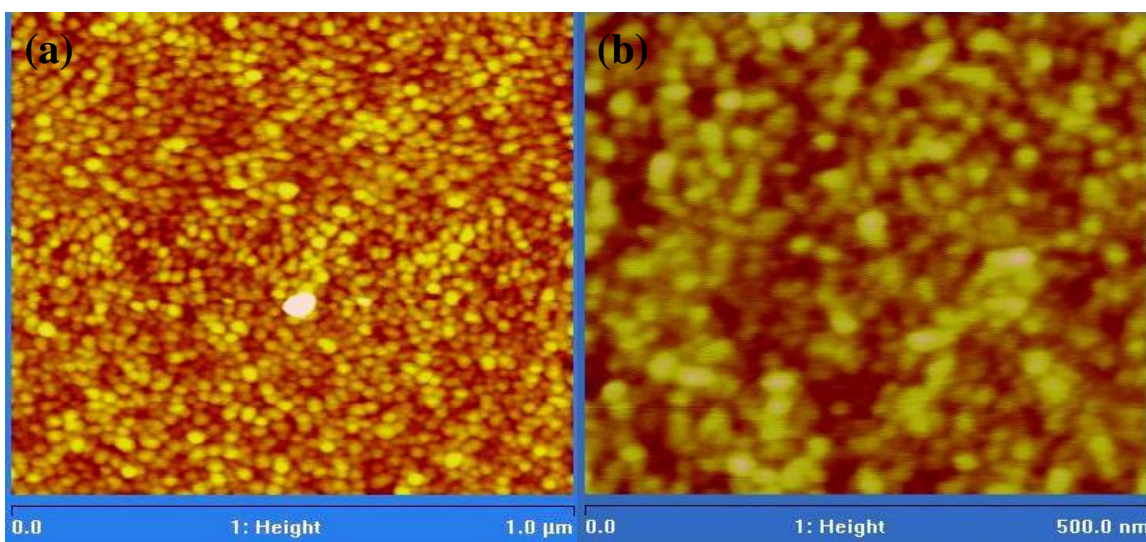


Figure 4.1.4 (a) AFM images for ant-TiO₂/ITO electrode and (b) AFM for ChOx/ant-TiO₂/ITO bioelectrode

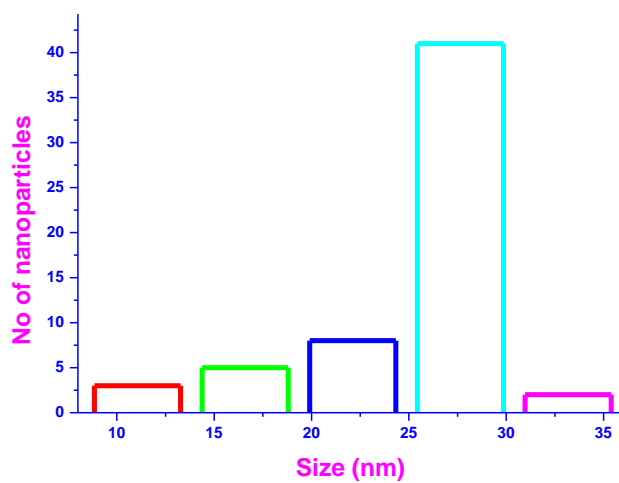


Figure 4.1.5 Histogram plot for average size of ant-TiO₂ nanoparticles

4.3.4 AFM studies

Figure 4.1.4 shows AFM images of nanostructured *ant*-TiO₂ on the ITO surface that are well-aligned, porous, monodispersed and uniformly distributed (image a and b). The average size of the *ant*-TiO₂ is found to be ~27 nm [Figure 4.1.5]. The rms surface roughness of *ant*-TiO₂ electrode is ~0.63 nm. The *ant*-TiO₂ surface gets uniformly covered after it is functionalized with ChOx [image b] and results in decreased roughness (0.49 nm) revealing that the nanosized *ant*-TiO₂ provides a favourable environment for adsorption of ChOx molecules via electrostatic interactions.

4.3.5 EIS studies

In electrochemical impedance spectroscopy (EIS), electron transfer resistance (R_{CT}) controls the electron transfer kinetics of the redox probe at the electrode interface and it is found to be 23.0 k Ω [Figure 4.1.6(i), curve a] for *ant*-TiO₂/ITO electrode. R_{CT} decreases to 10.2 k Ω in the case of ChOx/*ant*-TiO₂/ITO bioelectrode [curve b]. These results reveal that a regular arrangement in the *ant*-TiO₂ nanocrystalline film with restricted orientations provides direct and faster electron communication between enzyme and the electrode surface.

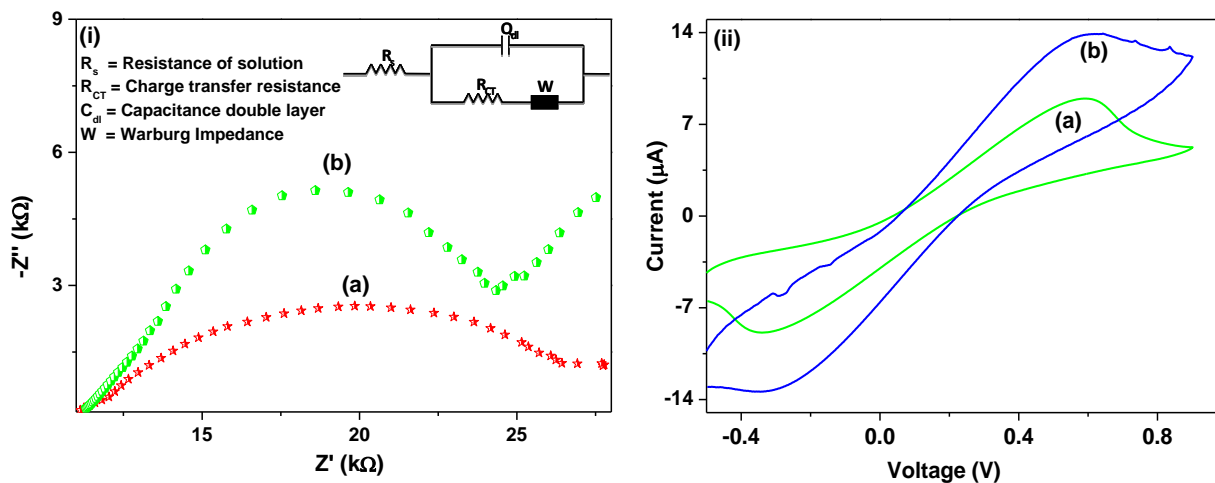


Figure 4.1.6(i) EIS studies of (a) *ant*-TiO₂/ITO electrode and ChOx/*ant*-TiO₂/ITO bioelectrode, (ii) The CV of (a) *ant*-TiO₂/ITO electrode and (b) ChOx/*ant*-TiO₂/ITO bioelectrode at scan rate (30 mV/s) in PBS (50 mM, pH 7.0, 0.9% NaCl) containing 5mM [Fe(CN)₆]^{3-/4-}.

4.3.6 CV studies

The CV studies have been conducted on *ant*-TiO₂/ITO (a) and ChOx/*ant*-TiO₂/ITO (b) in the potential range of -0.5V to +0.9V at constant flow rate [Figure 4.1.6 (ii)]. The anodic peak potential (E_{pa}) and cathodic peak potential (E_{pc}) for the ChOx/*ant*-TiO₂/ITO bioelectrode have been found to be respectively, 0.598V and -0.304V. The magnitude of peak current (1.33×10^{-5} A) is found to be higher after immobilization of ChOx compared to that of the *ant*-TiO₂/ITO electrode (8.99×10^{-6} A). This is attributed to the monodispersive nature of *ant*-TiO₂ that provides a suitable microenvironment for immobilization of ChOx. The observed excellent electrocatalytic characteristics of *ant*-TiO₂ reveal enhanced electron communication between active site of ChOx and the electrode. It can be speculated that these nanoparticles may directly communicate with the active sites of enzymes and act as electron mediators that establish electronic paths from the active sites of enzymes to the ITO electrode surface. Alternately, it may perhaps be assigned to the presence of strong electrostatic interactions and gibbosities on the *ant*-TiO₂ surface resulting in decreased tunneling distance between active site of ChOx and the electrode leading to enhanced peak current.

4.3.7 Scan rate studies

Cyclic voltammetry of ChOx/*ant*-TiO₂/ITO bioelectrode has been carried out as a function of scan rate from 20 to 80 mV/s at 30 μ L/min [Figure 4.1.7(i)]. A proportional increase of redox current (I_a is anodic) with respect to square root of scan rate is observed indicating diffusion-controlled system [inset: Fig. 3.7(i)]. It is found that ΔE_p increases with the scan rate revealing facile electron transfer between the redox probe and electrode. The surface concentration of ChOx/*ant*-TiO₂/ITO bioelectrode estimated from plot of I_p versus scan rate ($v^{1/2}$) using Brown–Anson model has been found to be 7.53×10^{-7} mol/cm². The value of diffusion coefficient of ChOx/*ant*-TiO₂/ITO bioelectrode has been found to be 3.38×10^{-4} cm²/sec estimated from the slope of I_p vs $v^{1/2}$ plot using Eq. 4.1.1

$$I_p = \frac{n^2 F^2 I^* A v}{4RT} \quad \text{Eq. 4.1.1}$$

where n is the number of electrons transferred, F is Faraday constant ($96485.34 \text{ C mol}^{-1}$), A is surface area (0.004 cm^2), R is gas constant ($8.314 \text{ J mol}^{-1} \text{ K}^{-1}$), I^* is surface concentration of bioelectrode (mol/cm^{-2}), T is 298K and I_p/v is the slope of calibration plot.

4.3.8 Effect of diffusion

The diffusivity of ions for *ant*-TiO₂/ITO electrode has been calculated using Randles–Sevcik equation from CV response at various flow rates (0-50 μ L/min) [Figure 4.1.7(ii)]. The plot between diffusivity and flow rate reveals that the diffusion near the electrode surface increases with the increase in the flow rate

of solution (inset). The higher diffusivity of the ions towards the electrode is perhaps responsible for faster response time and higher sensitivity.

4.3.9 Effect of pH

The effect of pH (5.0–8.0 at 25°C) on ChOx/*ant*-TiO₂/ITO bioelectrode has been investigated using CV to estimate optimum enzyme activity [Figure 4.1.8]. The highest current is obtained at pH 7.0 revealing that bioelectrode is most active at this pH [inset: Figure 4.1.8]. Thus, all the experiments are carried out at a pH of 7.0 at 25°C.

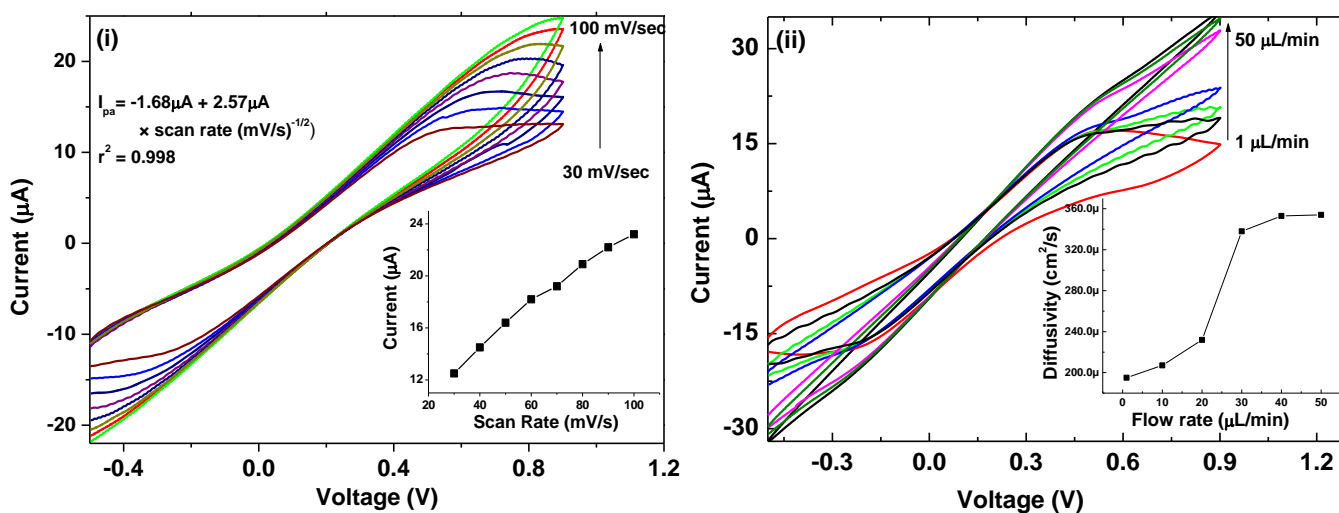


Figure 4.1.7(i) CV of ChOx/*ant*-TiO₂/ITO bioelectrode as a function of scan rate in PBS (50mM, pH 7.0, 0.9% NaCl) containing 5mM [Fe(CN)₆]^{3-/4-} and (ii) CV for different flow rates (0-50µL/min) as a function of flow rate [inset: Diffusivity for the *ant*-TiO₂/ITO electrode].

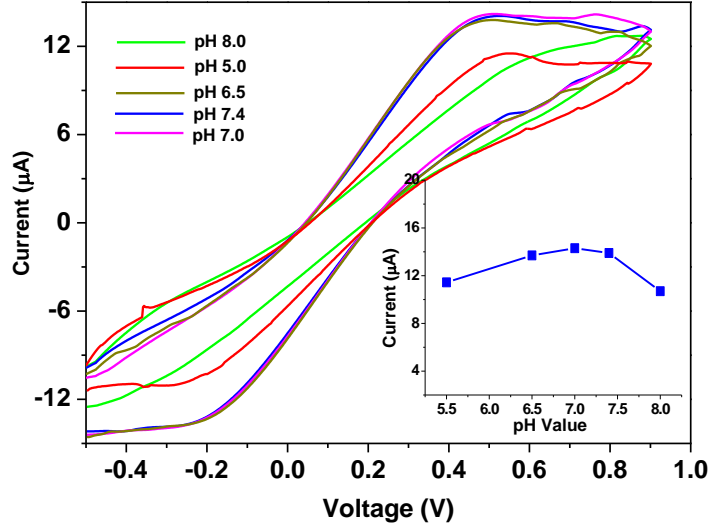


Figure 4.1.8 CV of ChOx/*ant*-TiO₂/ITO bioelectrode as a function of pH of the buffer solution (inset: plot between the current response and pH of solution).

4.4.0 Estimation of microfluidic parameters

The Reynolds number (R_e) is very important and is the most frequently used dimensionless number in fluid dynamics and defined as the inertial force to viscous forces. The flow of a fluid through a microfluidics channels can be characterized by R_e defined as Eq.4.1.1

$$R_e = \frac{LV_{avg}\rho}{\mu} \quad \text{Eq. 4.1.2}$$

where L is the characteristic length of channels, μ is the viscosity (10^{-3} Pa s), V_{avg} is average velocity of fluid (0.083×10^{-2} m/s) and ρ is fluid density ($\sim 10^3$ kg/m³) from which R_e number has been found to be 0.166 indicating that fluid flow is very low resulting in completely laminar. The surface to volume ratio (S/V) is calculated as 4997.5 cm^{-1} . This high value indicates large scale redox conversion leading to the higher sensitivity as compared to the conventional electrochemical cell.

4.4.1 Estimation of free cholesterol

Electrochemical response of the microfluidic sensor based on ChOx/*ant*-TiO₂/ITO bioelectrode as a function of cholesterol concentration (0.64–10.3 mM) is shown in Figure 4.1.9(a). During electrochemical measurements, various concentrations of cholesterol are injected into the microchannels (0.8 µL/each channel) at a constant flow rate of 30 µL/min. The observed increased oxidation peak current may perhaps be due to fast charge transfer from flavin adenine dinucleotide (FAD) center of ChOx to TiO₂

matrix (Figure 4.1.9). The anodic peak current is found to increase linearly on addition of cholesterol and the linearity is obtained as 1.3-10.3 mM [inset: Figure 4.1.9(a)]. The ChOx/*ant*-TiO₂ based-microsystem shows a better sensitivity of 94.65 $\mu\text{A}/\text{mM}/\text{cm}^2$ compared to those of other cholesterol biosensors (Table 4.1.1). The low value of Michaelis–Menten constant (K_m) obtained as 0.14 mM using Lineweaver–Burke plot reveals higher affinity between the active sites of ChOx onto the surface of *ant*-TiO₂ that perhaps directly participate in the biochemical reaction.

4.4.2 Selectivity studies

The selectivity of ChOx/*ant*-TiO₂/ITO bioelectrode has been determined by comparing magnitude of the current response by adding normal concentration of interferents such as glucose (5 mM), ascorbic acid (0.05 mM), uric acid (0.1 mM), urea (1 mM), and lactic acid (5 mM) to the cholesterol solution (2.6 mM) under microfluidics condition [Figure 4.1.9(b)]. The current response of this sensor chip remains nearly same except for lactic acid/ascorbic acid wherein there is increase of about 5% [inset: Figure 4.1.9(b)]. The bioelectrode achieves 95% of steady state current in less than 5s indicating fast electron exchange between electrode and enzymes. The reproducibility of different bioelectrode has been investigated using cholesterol concentration (2.6 mM) under identical conditions using CV response and it is found to be > 3% error [Figure 4.2(a)]. The storage stability of this bioelectrode has been determined by observing the current response using CV study at 2.6 mM cholesterol concentration at regular intervals of 7 days for about 35 days. The bioelectrode shows a 97% response [Figure 4.2(b)] in 35 days revealing very good shelf life.

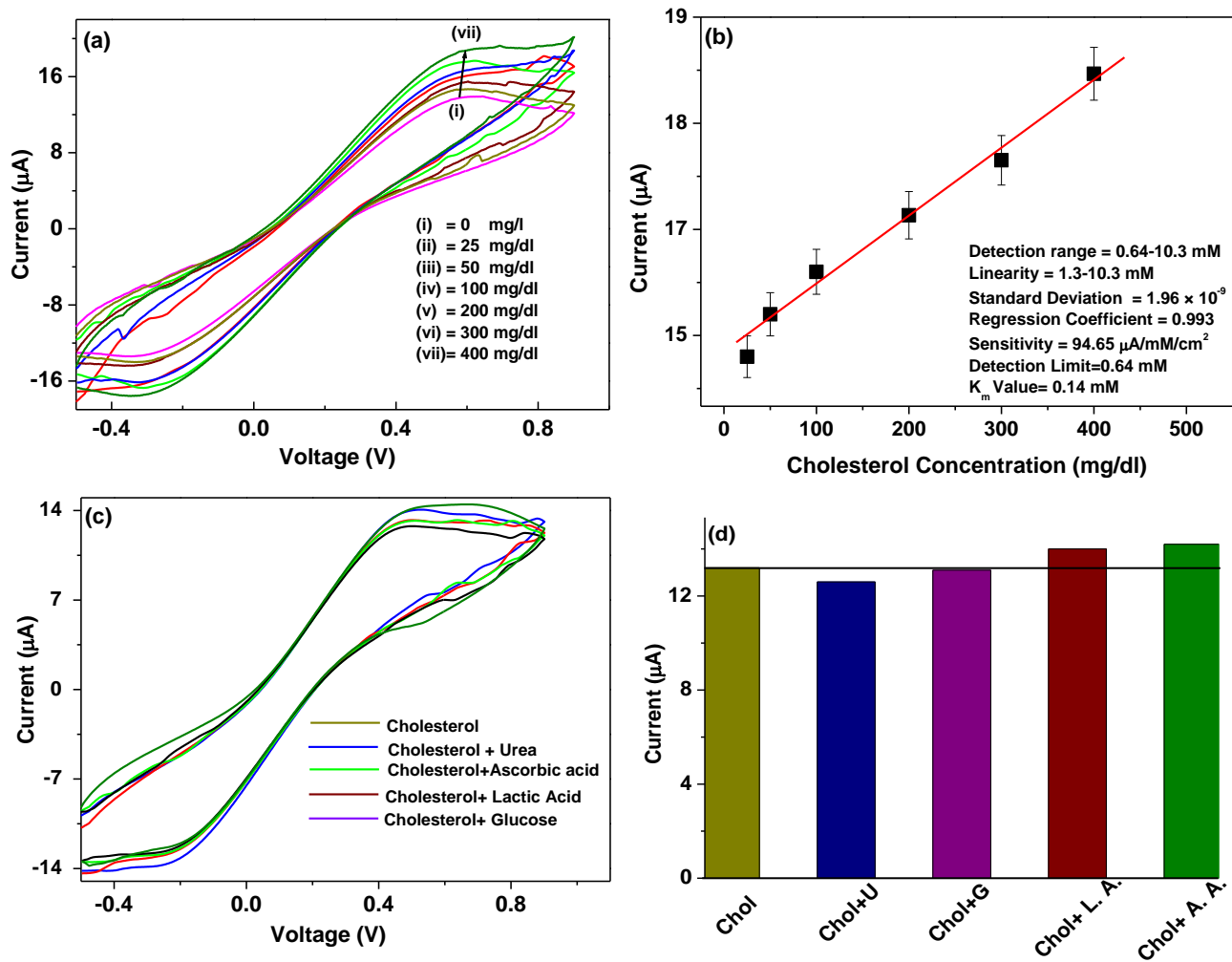


Figure 4.1.9(a) CV curves of ChOx/ant-TiO₂/ITO bioelectrode at different cholesterol concentration, (b) linear plot of response studies of ChOx/ant-TiO₂/ITO bioelectrode as a function of cholesterol concentration (50–400 mg/dl and (c) CV curves of ChOx/ant-TiO₂/ITO bioelectrode in presence of interferents. (d) Current responses of various interferents.

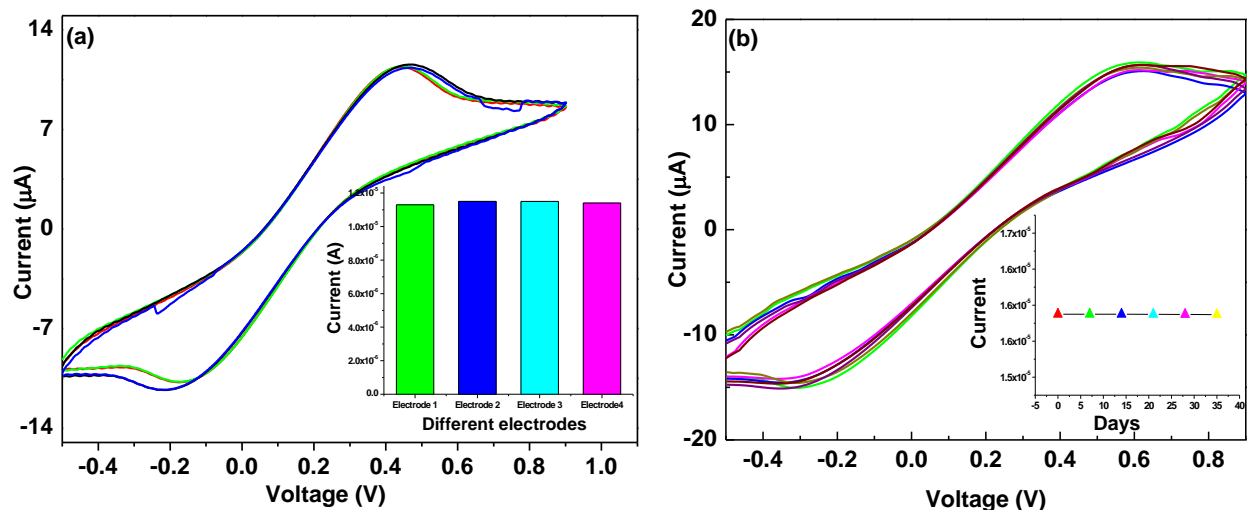


Figure 4.2.0 (a) Reproducibility studies for different bioelectrodes at same flow rate and (b) stability studies of the ChOx/*ant*-TiO₂/ITO bioelectrode (inset: current response vs days).

4.4.3 Potential merits and demerits of the ChOx/*ant*-TiO₂/ITO bioelectrode based microfluidic sensor

The fabricated ChOx/*ant*-TiO₂/ITO bioelectrode based microfluidics biosensor offers a suitable platform for free and total cholesterol detection. The high aspect ratio of this microfluidic device offers high sensitivity and selectivity to the amperometric detection of cholesterol compared to other reported literature (Table 4.1.1). This may be attributed to the small geometry of the device which offers a negligible capacitive current, reduced ohmic drop of potential, improved mass transfer and radial diffusion. The nanostructured TiO₂ plays an important role to enzyme (cholesterol esterase and cholesterol oxidase) immobilization and facilitate fast electron heterogeneous transfer from enzyme active site to electrode. The metastable anatase form is the most stable due to the lower average surface energy whose equilibrium crystal shape is largely dominated by the very stable (101) surface. The hydrophobic nature of PDMS microchannels into this electrode system offers low cost, flexibility, rapid prototyping and making it mainly suitable for aqueous applications. The flow rate of this microfluidic platform is an important parameter and plays a crucial role towards the wettability of the surface that can be controlled using surface chemical treatment. It has been observed that the ITO etching process is an inexpensive and low cost method compared to that of silicon and glass which is known to be expensive and time consuming. This microfluidic biosensor shows better reproducibility, low K_m value and suitable for detection of free and total cholesterol in physiological condition.

The direct attachment of biomolecules (such as cholesterol esterase and oxidase) with TiO₂ is a major problem due to low isoelectric point (~5.5) of TiO₂. The isoelectric point of enzyme molecules is found to be 4.5. This low isoelectric point of *ant*-TiO₂ nanomaterial on microfluidic transducer surface can cause a low adsorption capability of enzyme molecules leading to lesser sensitivity and poor film stability. It has been observed that this microfluidic biosensor shows a poor detection limit (1.2 mM for free and 3.8 mM for total cholesterol, respectively) compared to that in other reported literatures [Table 4.1.1].

Table 4.1.1 Characteristics of microfluidics based cholesterol biosensor along with those reported in literature

Working electrode	Microfluidic used	Detection range (mM)	Lower detection limit	Sensitivity	K _m value	References
CNT	Yes	1.25 -10.0	0.25 mM	0.0512 nA/mM/cm ²	241
Au wire	Yes	1.293 -6.4	0.1 mM	242
Gold nanoparticles	No	Up to 2.1	0.060 mM	0.13 μA/mM/cm ²	2.94 mM	243
ZnO	No	Upto 7.7	0.012 mM	1.53 nA/mM/cm ²	0.22 mM	244
Aligned Au nanowires	Yes	0.01–0.060	0.85 μA/mM/cm ²	17.1 mM	245
Anatase-TiO ₂	Yes	0.64-10.3	0.64 mM	94.65 μA/mM/cm ²	0.14 mM	Present work

4.4.4 Conclusions

The fabrication of a low cost microfluidics biosensor for free cholesterol detection has been demonstrated. The PDMS microchannel has been fabricated using soft lithography technique and ITO coated glass plate has been etched using a wet chemical etchant. Highly crystalline *ant*-TiO₂ nanoparticles are selectively deposited on microfluidic transducer surface for direct immobilization of cholesterol oxidase molecules. The integration of PDMS microchannel and electrodes (working and counter) on glass substrate has been carried out via conformal contact (reversible attachment) during amperometric measurement. This integrated microfluidics biosensor provides improved sensitivity and low K_m value

arising due to both higher surface-to-volume ratio of *ant*-TiO₂ nanocrystals and small geometry of the microfluidics system. The reproducibility studies on different *ant*-TiO₂ based bioelectrodes shows no significant change in current response. Effort will make to conduct the selectivity test of the fabricated biosensor in presence of albumin concentration. This miniaturized microfluidics sensor requires minimal instrumentation and can be readily integrated with micro-electronics in a chip-based format. The electrochemical response of this microfluidics sensor depends upon flow rate of the solution that influences response time and diffusion coefficient.

Surface modification of TiO₂ nanoparticles might be useful for improving the absorption of biomolecules onto the microfluidic transducer surface. Chitosan is a good candidate for this purpose. With this idea, chitosan modified TiO₂ nanoparticle is explored for electrode modification in a cholesterol biosensor. Due to reversible attachment between the microchannel and electrodes in this biosensor system, the same geometry of PDMS microchannel has been used for fabrication of micro-device. To overcome some of the demerits of this microfluidic biosensor, efforts have been made to utilize *ant*TiO₂-CH as transducer surface with similar geometry and the results have been described in Part II of this Chapter.

Part II: Mesoporous titania-chitosan composite based microfluidic biochip for cholesterol detection

4.5 Introduction

The experimental details relating to development of electrochemical microfluidic sensor based on anatase titania and chitosan nanocomposite for the estimation of total cholesterol is presented in the remaining sections. The anatase titania nanoparticles-grafted chitosan (antTiO₂-CH) has been selectively dip-coated onto ITO-patterned microelectrode and the surface is physically immobilized using the mixture of ChEt and ChOx.

The electroactive chitosan (CH) a deacetylation product of chitin, is a functional and basic polysaccharide composed of β -1,4-linked glucosamine that can be easily extracted from the exoskeleton of shrimps and crabs [246]. This biomaterial offers excellent film forming ability and acts as a stabilizing agent. Besides this, it is cost-effective, biocompatible and biodegradable. The nanoporous structure of CH can be used to obtain enhanced dispersion of the TiO₂ nanoparticles that may provide sufficient electron-conducting paths and high surface area for adsorption of biomolecules such as enzymes, proteins etc. [247]. The mesoporous structure of titania can promote adsorption of CH as well as biomolecules and improved electron diffusivity. The high porosity and excellent surface area of titania could thus provide a favorable platform for incorporation of CH resulting in higher loading of biomolecules. The available functional groups such as the amino (NH₂), hydroxyl (OH) etc. of CH offers a hydrophilic environment for loading of enzyme molecules on transducer surface. Feng et al. have developed a nanoporous metal oxide-CH matrix for immobilization of single stranded DNA probe for detection of a cancer gene [240]. Thus, the mesoporous structure of CH provides the fast heterogeneous electron transfer rate resulting in improved electrochemical properties. The direct attachment of biomolecules onto antTiO₂ surface is presently a major limitation as its surface can absorb only a limited number of desired biomolecules due to weak inter-molecular interactions with the biomolecules. This limitation can perhaps be overcome by using a nanocomposite material comprising of a biopolymer (e. g. chitosan) and antTiO₂ nanoparticles. The nanocomposite of TiO₂ with chitosan acts as a template for dispersion of antTiO₂ nanoparticles, thereby facilitating better enzyme functionalization.

The integration of the mesoporous antTiO₂-CH with microfluidic device may improve the biosensor efficacy due to improve electrochemical properties of nanocomposite for total cholesterol detection. Easy film forming ability, biocompatibility, higher enzymes loading capacity and cost

effectiveness of this mesoporous antTiO₂-CH nanocomposite provide a suitable platform to incorporate with microfluidic module for biomolecules detection. I have used the ac impedance spectroscopic technique for determination of total cholesterol concentration. The bienzyme functionalized antTiO₂-CH electrode has been characterized using electron microscopy, UV-visible spectroscopy, Brunauer–Emmett–Teller surface area, Fourier transform infra-red and X-ray photoelectron spectroscopy techniques.

4.5.1 Biosensing Platform

The selective deposition of antTiO₂-CH solution has been carried out on this fabricated patterned ITO electrode via dip coating. Initially, the glass substrate with ITO microelectrode is masked using a masking tape and only the desired electrode is selectively exposed by removing the masking tape over it. The substrate is then dried at 40°C for about 1 h after which the remaining masking tape film is removed from the substrate. Masking glue on substrate surface has removed using acetone treatment. This process results in a glass substrate containing antTiO₂-CH/ITO (unmasked region) and bare ITO electrode (masked region). The antTiO₂-CH/ITO film is washed with deionized water to remove any unbound particles.

The fresh solution of 1mg/ml cholesterol esterase (ChEt) and 1mg/ml cholesterol oxidase (ChOx) are mixed in the ratio 1:1 and 10µl solution of this mixture is uniformly spread onto antTiO₂-CH surface via physical absorption and is kept in a humid chamber for 12 h at 4°C. The surface charged antTiO₂ nanoparticles interact with –NH₂/OH groups of CH [cationic amine-rich polysaccharide (pH 4.2)] via electrostatic interactions and hydrogen bonding. The ChEt and ChOx are negatively charged at pH 7.0 and can be immobilized onto the positively charged antTiO₂-CH via electrostatic interaction. This ChEt-ChOx/antTiO₂-CH based bioelectrode is washed with 50 mM PBS (pH 7.0) in order to remove any unbound enzymes from the electrode surface. The bioelectrode is stored at 4°C when not in use. It has been found that the ChEt-ChOx/antTiO₂-CH/ITO bioelectrode shows very high catalytic behavior in phosphate buffer at pH 7.4 (50mM, 0.9% NaCl) containing [Fe(CN)₆]^{3-/4-} (5mM). The PDMS microchannel is reversibly sealed to a glass substrate comprising of ITO electrode and ChEt-ChOx/antTiO₂-CH/ITO bioelectrode, respectively. The various steps involved in the fabrication of the microfluidic device are shown in Figure 4.2.3. Electrochemical investigations for this impedimetric microfluidic chip have been carried out using an Autolab Potentiostat/Galvanostat (FRA analyzer) in phosphate buffer saline [PBS, (50 mM, pH 7.0, 0.9% NaCl)] containing [Fe(CN)₆]^{3-/4-} (5mM). The flow of buffer solution and analyte are optimized using electrochemical technique through this chip and 1µL/min is found to be optimum flow rate. The fabricated microfluidic biochip is shown in Figure 4.2.1. Figure 4.2.3 shows a photograph of microfluidic biochip.

Surface profiling and the thicknesses of the films of the film structure are carried out using an optical profiling system (NanoMap-D, Aep Technology, U.S.A.). The thicknesses are measured by an optical profiler in noncontact mode. Figure 4.2.2 shows an optical 3D profiling image of the ITO film coated on a glass in which the thickness was calculated $\sim 299 \pm 36$ nm. Then antTiO₂-CH was deposited on the ITO by dip coating method and the thickness was found $\sim 196 \pm 30$ nm.

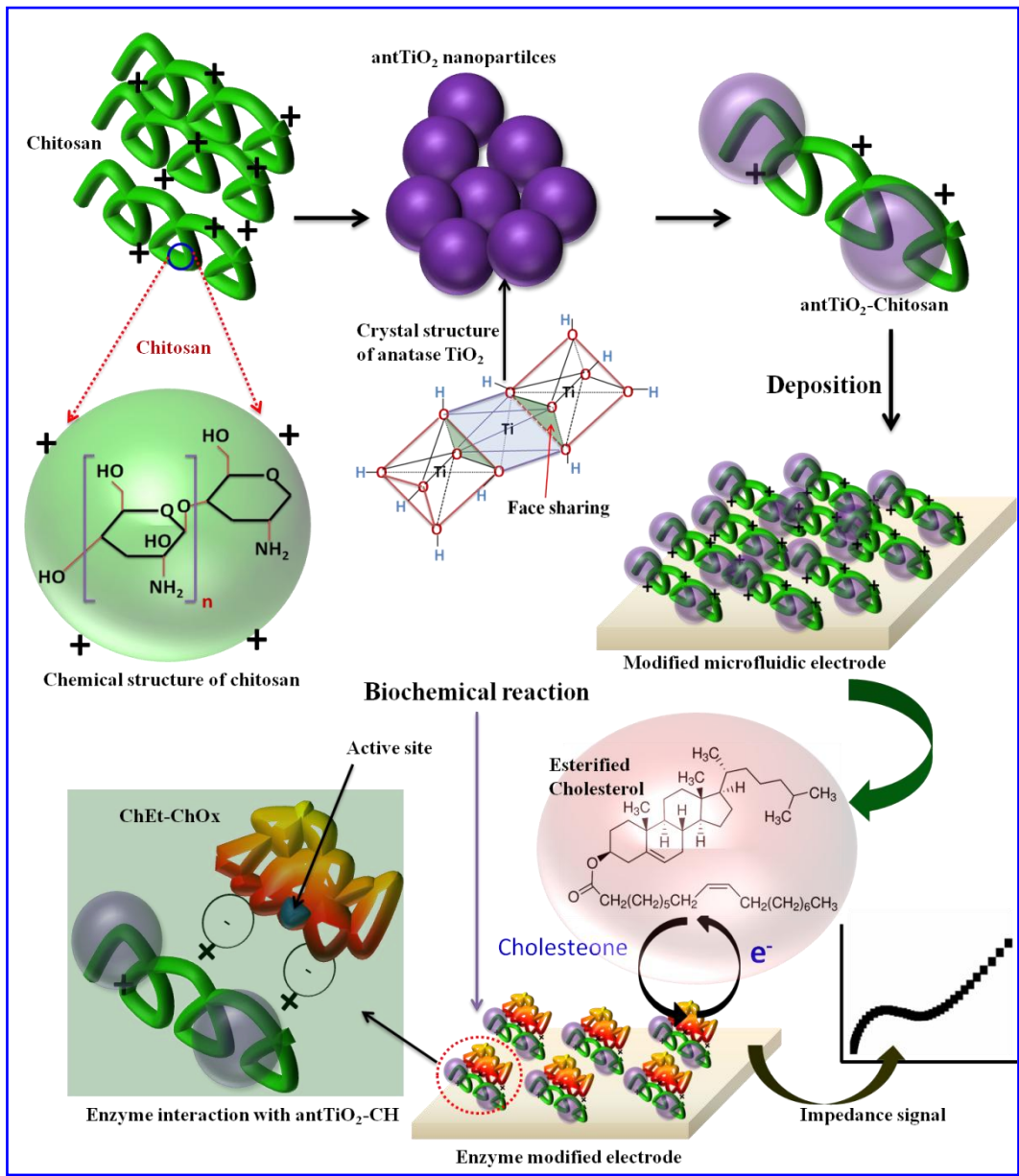


Figure 4.2.1 Functionalization of bienzyme onto antTiO₂-CH surface for cholesterol detection.

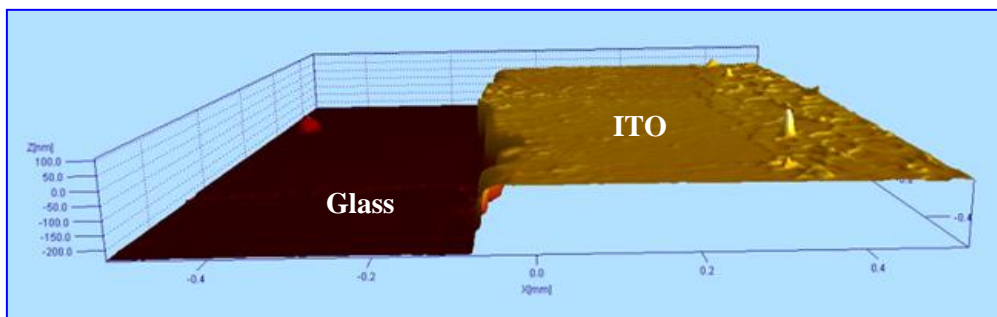


Figure 4.2.2: 3D optical profilometric image for (a) ITO on glass film

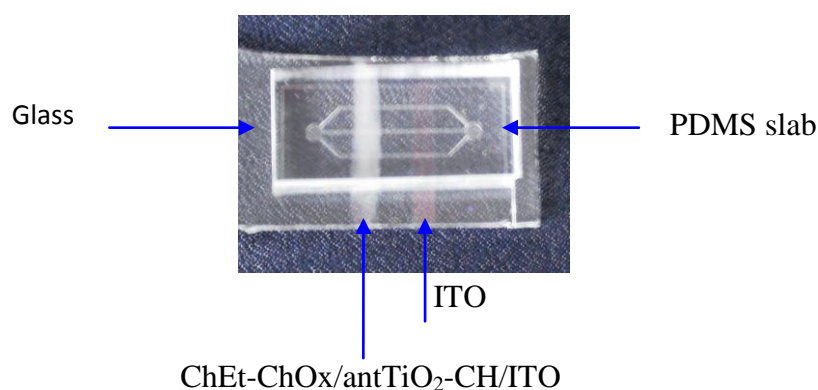


Figure 4.2.3 A photograph of the fabricated microfluidic biochip

4.6 Results and Discussion

4.6.1 UV-visible, FT-IR, Raman and BET surface analysis

The absorption spectrum of chitosan (curve a) solution shows a maximum absorption at 200 nm in the UV region due to presence of the functional groups ($-\text{NH}_2$ and $-\text{OH}$) of chitosan [Figure 4.2.4(i)]. The absorption of antTiO_2 nanoparticles begins from 352 nm and a maximum value is observed at 249 nm due to the band edge transition (curve b). The blue shift of the absorption edge is the evidence for the quantum confinement effect that occurs during the growth of nanoparticles. The absorption intensity is found to be higher in case of the antTiO_2 -chitosan (curve c) matrix due to electrostatic interaction between CH and antTiO_2 nanoparticles.

The FT-IR spectra of antTiO₂/ITO exhibits an IR peak at 523 cm⁻¹ in the finger print region due to vibrational band of Ti-O bond [Figure 4.2.4(ii), spectra a]. The peaks found at 819 and 1241 cm⁻¹ respectively, correspond to C-H and C-O stretching bonds. The band seen at 3593 cm⁻¹ is assigned to stretching and deformation of the O-H bond due to absorption of the water molecules. Figure 4.2.4(ii) shows the FT-IR spectra of CH (spectra b) that exhibits bands at 3200–3450 cm⁻¹ due to the stretching vibration mode of OH and NH₂ groups. The band at 1652 cm⁻¹ arises due to amide I group (C-O stretching along with N-H deformation mode). The 1564 cm⁻¹ peak is attributed to NH₂ group due to N-H deformation, 1400 cm⁻¹ peak is due to C-N axial deformation (amine group band), 1317cm⁻¹ peak is due to COO⁻ group in the carboxylic acid salt and 1063 cm⁻¹ is attributed to the stretching vibration mode of the hydroxyl group. The peak at 612 cm⁻¹ in the finger print region is attributed to antTiO₂ grafted CH. This absorption band occurs at a higher wavenumber than that of the pure antTiO₂ nanoparticles due to the interactions between CH and the antTiO₂. The presence of antTiO₂ nanoparticles in CH facilitates immobilization of ChEt-ChOx via amine and hydroxyl group. After immobilization of ChEt-ChOx on mesoporous antTiO₂-CH surface (spectra c), intensity of the absorption peaks becomes higher and broader due to overlap of the functional groups of enzymes corresponding to amide I (1652 cm⁻¹) and amide II (1545 cm⁻¹), respectively, indicating immobilization of the bienzyme (ChEt-ChOx) onto this matrix.

Raman spectral analysis [Wi, Tec, Gy] has been carried out at a wavelength of 532 nm. Figure 4.2.4(iii) illustrates the room temperature Raman spectra of the TiO₂ and antTiO₂-CH. The resultant spectra indicate the intensification of the lowest-frequency E_g mode. A strong Raman peak emerges at 196 cm⁻¹ at the high-frequency side of the E_g mode and which is assigned to the anatase phase of TiO₂. In addition, B_{1g}, A_{1g} and E_g modes are detected at 396, 517 and 642 cm⁻¹, respectively which also support the anatase phase of TiO₂ and antTiO₂-CH samples. It appears that, in the antTiO₂-CH structure, there is not much alteration detected when evaluated with bare TiO₂, signifying that the antTiO₂-CH synthesis did not destroy the characteristic structural morphology of TiO₂.

The specific surface area and porosity of the TiO₂ and antTiO₂-CH are studied by using the N₂ adsorption and desorption isotherms which is shown in Figure 4a. Table 1 shows the pore size distribution of the TiO₂ and antTiO₂-CH from Brunauer–Emmett–Teller (BET) measurements. It is found that the two isotherms of samples show stepwise adsorption and desorption branch belonging to type IV curves, hence representing the occurrence of mesoporous material. A hysteresis loop with a stepwise adsorption and desorption branch is observed at extensive range of pressure (P/P₀) for the mesoporous TiO₂ and antTiO₂-CH which indicates that the synthesized materials have extensive mesoporous structure. To examine pore size and pore volume distribution, a curve of the pore size distribution is inspected by desorption branch

of the BJH data as shown in the inset of the Figure 4.2.4(iv). The average pore diameter of mesoporous TiO_2 is found to be 6.287 nm with ~80% mesoporosity of total pore volume of 0.2961cc/g.

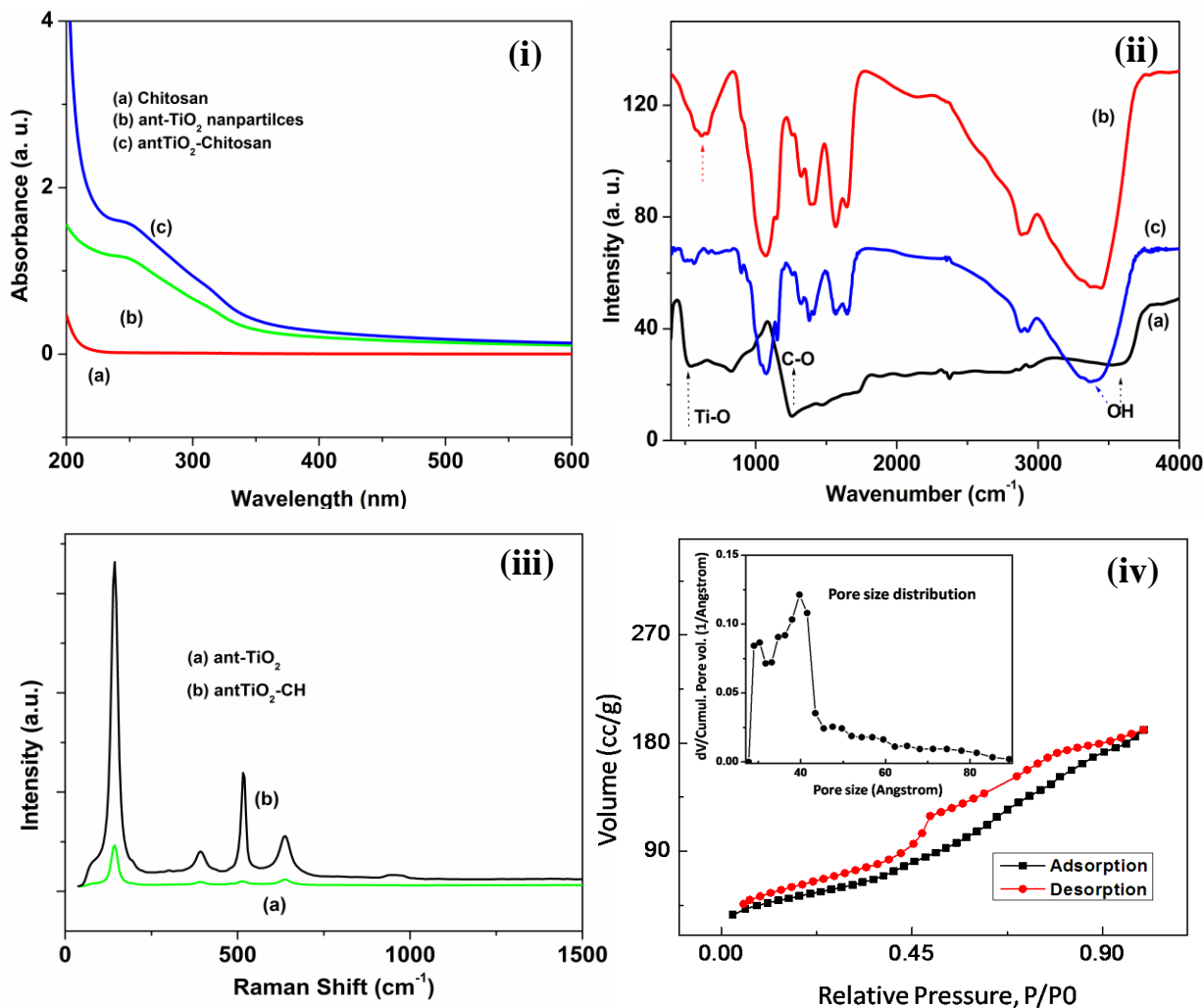


Figure 4.2.4(i) UV visible spectra of chitosan (a), ant TiO_2 nanoparticles (b) and ant TiO_2 -CH (c), (ii) FTIR spectra of (a) ant TiO_2 film, (b) ant TiO_2 -CH/ITO and (c) ChEt-ChOx/ant TiO_2 -CH/ITO film. (iii) Raman spectra of TiO_2 and ant TiO_2 -CH showing pure anatase phase. (iv) The N_2 adsorption and desorption isotherms of ant- TiO_2 nanoparticles, inset shows the pore size distribution of ant- TiO_2 nanoparticles.

The total pore volume of mesoporous ant TiO_2 -CH is 0.1265 cc/g and the mesoporosity of 83%. Analyzing BET results, it is perceived that titania nanoparticles have an elevated surface area of 188.2 m^2/g than ant TiO_2 -CH showing 90.83 m^2/g . The shrink in surface area of ant TiO_2 -CH is believably due to

the blocking tendency of pore entrances of TiO₂ particles by chitosan molecules. Table 4.1.2 shows the pore size distribution of antTiO₂ nanoparticles and chitosan modified antTiO₂ nanoparticles.

4.6.2 XPS studies

Figure 4.2.5(i) shows XPS wide scan spectrum obtained for the antTiO₂-CH/ITO (a) and ChEt-ChOx/antTiO₂-CH/ITO (b) electrodes. The peaks found at 199.5 eV, 284.2 eV, 496.5 eV and 530.5 eV are attributed to Cl 2p, C 1s, Sn 3d and O1s of antTiO₂-CH, respectively. In spectrum (b), the characteristic peak seen at 398.5 eV is assigned to the presence of N 1s present in the bienzyme (ChEt-ChOx). The additional peak found at 1069.5eV is assigned to Ti-Auger. The relative atomic concentration (%) and full width half maxima (FWHM) of the carbon, oxygen and nitrogen peaks are summarized in Table 4.1.3. The atomic concentration of N 1s of ChEt-ChOx/antTiO₂-CH/ITO bioelectrode increases to 2.48% compared to that of antTiO₂-CH/ITO electrode (1.23%). This indicates that antTiO₂-CH/ITO electrode surface facilitates immobilization of ChEt-ChOx via electrostatic interactions. The XPS spectra in the carbon 1s region of deposited antTiO₂-CH/ITO electrode [Figure 4.2.5(ii)], is deconvoluted into the characteristic peaks using Shirley type baseline and Lorentzian-Doniac-Sunsic curves with Gaussian profile. The deconvoluted C1s core-level spectrum of antTiO₂-CH sample consists of three peaks. The first, situated at 284.5 eV is assigned to the existence of the C-C and C-N binding in CH. The second peak, located at 286.3eV, is attributed to the chemical binding of the C in C-O and C-OH bonds, and the third peak is at 288.06 eV, is related to the N-C=O chemical binding in the acetamide group of CH. After bienzyme immobilization, the peaks found at 284.5 eV, 286.3eV and 288.06 eV are slightly shifted towards lower binding energy and one additional peak at 281.8 eV is observed [Figure 4.2.5(iii)]. After peak fitting of the N1s core-level spectrum of antTiO₂-CH, three peaks appear at 398.3, 401.4, and 406.2 eV [Figure 4.2.5(iv)].

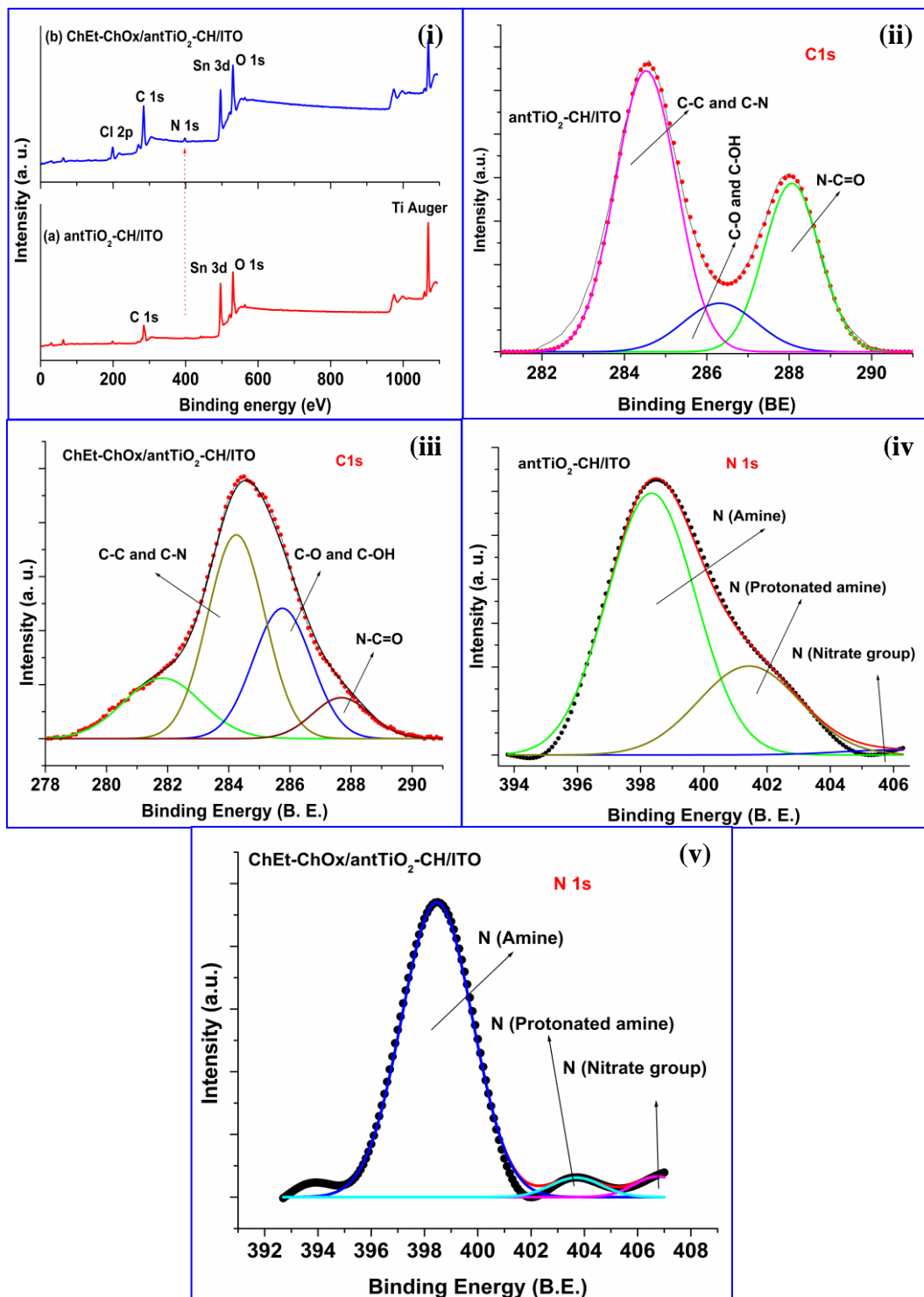


Figure 4.2.5 (i) Wide scan XPS of various films, (ii) XPS spectra of the C1s region of antTiO₂-CH film after deconvolution, (iii) the C1s region of ChEt-ChOx/antTiO₂-CH film, (iv) N 1s core level spectra of antTiO₂-CH film and (v) N 1s core level spectra of ChEt-ChOx/antTiO₂-CH film.

Table 4.1.2 Pore size distribution from BET data.

Sample details	p/p ₀	Total pore volume (cc/g)	BET area (m ² /g)	Macropore volume (cc/g)	Mesopore volume (cc/g)	Micropore volume (cc/g)	Average pore diameter (nm)
ant-TiO ₂	0.99707	0.2961	188.2	0.02286	0.2373317	0.0359083	6.287
antTiO ₂ -CH	0.99940	0.1265	90.83	0.00772	0.1059716	0.0128164	5.571

Table 4.1.3 The atomic concentration (%) and full width half maxima (FWHM) of C, O and N elements present in antTiO₂-CH/ITO and ChEt-ChOx/antTiO₂-CH/ITO electrodes from XPS analysis.

Elements/Atomic concentration (%)	C (FWHM)	O(FWHM)	N(FWHM)
antTiO ₂ -CH /ITO	43.3 (1.96)	34.8 (2.08)	1.23(3.6)
ChEt-ChOx/ antTiO ₂ -CH /ITO	61.3 (3.34)	25.7 (3.02)	2.48 (1.9)

The first peak is assigned to the chemical binding of N in the amine and acetamide (NH₂) groups, while the second peak is assigned to the chemical binding of the N in the protonated amine (NH₃⁺) groups. The third peak is attributed to chemical binding of the N in the nitrate group. In case of the biofunctionalized film, these peaks are slightly shifted towards higher binding energy [Figure 4.2.5 (v)]. And the atomic ratio of element (N) and peak intensity is found to be changed indicating bienzyme immobilization onto antTiO₂-CH surface via electrostatic interaction.

4.6.3 Morphological studies

The surface morphology of nanoparticles and chitosan coated nanoparticles are explored using field emission-scanning electron microscopy (FE-SEM). The titania nanoparticles are dispersed uniformly throughout the ITO surface with arrangement of aggregated nanoparticles. It also illustrates that the

nanoparticles are densely distributed with a slight range of dispersion. Nanosized particles exhibit smooth surface morphology. FE-SEM analysis of titania nanoparticles confirms their particle size ranging from 10 to 35 nm. The average diameter of the TiO_2 particles is calculated to be ~ 27 nm by analyzing the micrographs. The FE-SEM [Figure 4.2.6(a)] studies reveal the porous morphology of (ant TiO_2 -CH) film indicating the formation of ant TiO_2 -CH hybrid. This may be attributed to electrostatic interactions between cationic CH and surface charged ant TiO_2 nanoparticles grafted in the CH network [Figure 4.2.6(b)]. The micrograph reveals that the hybrid surface (Figure 4.2.6(b)) is coated with TiO_2 nanoparticles. After enzyme incorporation on ant TiO_2 -CH surface (image c), the film morphology has changed their structure. This may be due to the three dimensional environment of hybrid surface that promotes complex coating formation appear with number of apexes and voids. This may be due to porous surface structure of ant TiO_2 -CH provides increased loading capacity of the bienzyme (ChEt-ChOx).

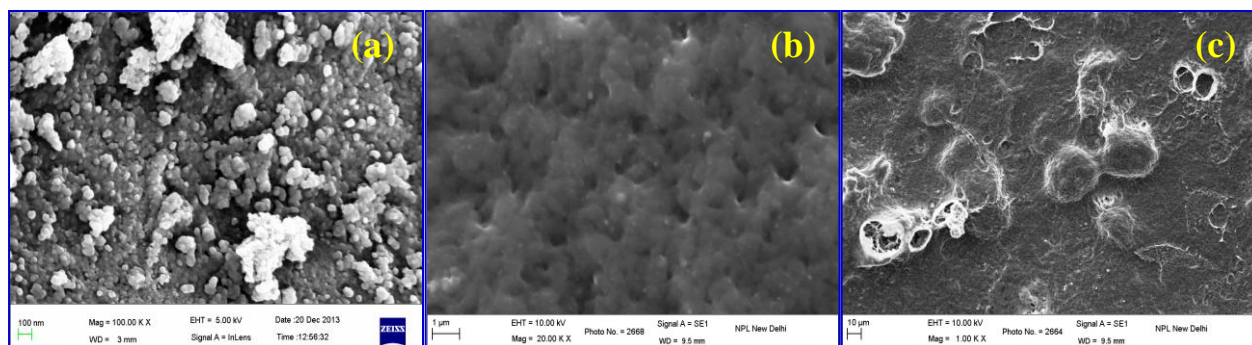


Figure 4.2.6(a) FE-SEM image of ant TiO_2 nanoparticles and (b) ant TiO_2 -CH. (c) FE-SEM image of ant TiO_2 -CH film with enzyme immobilization.

4.6.4 Cyclic voltammetric studies

Figure 4.2.7(i) shows the cyclic voltammogram of (a) ant TiO_2 -CH/ITO electrode and (b) ChEt-ChOx/ant TiO_2 -CH/ITO bioelectrode with potential range of -0.9V to $+1.0\text{V}$ conducted in PBS containing $5\text{ mM } [\text{Fe}(\text{CN})_6]^{3-/4-}$. The magnitudes of peak currents measured for the ant TiO_2 -CH/ITO electrode are found to be $7.43\ \mu\text{A}$ (anodic) and $-15.6\ \mu\text{A}$ (cathodic) with peak-to-peak separation voltage of 1.2V . The peak current (anodic) of ChEt-ChOx/ant TiO_2 -CH/ITO bioelectrode is higher ($11.9\ \mu\text{A}$; curve b) compared to that of the ant TiO_2 -CH/ITO (curve a) resulting in fast electron communication through ant TiO_2 -CH matrix and redox active site of ChEt-ChOx molecules. This indicates that nanoporous CH with ant TiO_2 facilitates activation of enzyme active sites resulting in enhanced current due to improved heterogeneous electron transfer. The high electrocatalytic activity of ant TiO_2 in presence

of bienzyme indicates superior performance of the redox process. The antTiO₂ nanoparticles can be used to activate active site of the enzyme leading to decreased tunneling distance for diffusion of electrons from bulk solution leading to enhanced current. The observed significant increase in the heterogeneous electron transfer rate results from the strong interaction of ChEt-ChOx with antTiO₂-CH based electrode as compared to that of antTiO₂-CH/ITO electrode.

The effect of the scan rate on the electrochemical response of bioelectrode is shown in Figure 4.2.7(ii). The peak current increases linearly with increase of the scan rate from 20 to 160 mVs⁻¹ (inset). The magnitude of current of both anodic peak (I_a) and cathodic peak (I_c) observed for ChEt-ChOx/antTiO₂-CH/ITO bioelectrode increases linearly with the scan rate (20-110 mV/s) indicating heterogeneous pseudo reversible fast electron-transfer process. The magnitude of I_a/I_c is calculated to be as 0.7<1. It can be seen that anodic potential shifts towards positive side and the cathodic peak potential [inset: Figure 4.2.7(ii)] shifts in the reverse direction indicating a surface-controlled process. The values of slope, intercept and correlation coefficient are given by Eq.4.1 (4 & 5)

$$I_a(\text{bioelectrode}) = 2.38\mu\text{A} + 1.21 \mu\text{A}(\text{s/mV})^{1/2} \times \text{scan rate (mV/s)}^{-1/2}; R^2 = 0.999 \quad \text{Eq. 4.1.4}$$

$$I_c(\text{bioelectrode}) = -5.92\mu\text{A} + [-1.02\mu\text{A}] (\text{s/mV})^{1/2} \times \text{scan rate (mV/s)}^{-1/2}; R^2 = 0.997 \quad \text{Eq. 4.1.5}$$

The magnitude of charge associated with the adsorption or desorption of an adsorbate gives an indication of the number of surface catalyst atoms present in the matrix. The electrical charge (Q) is defined as the integral of cell current (I) with respect to time (t) and is given by

$$Q = \int I dt \quad \text{Eq. 4.1.6}$$

The adsorption charge associated with a known adsorbate on the electrode surface (Q_m) and the charge associated with monolayer coverage of the said adsorbate (Q_{ad}), can be related to the electrochemical surface area, A_{ec} (cm²) by

$$A_{ec} = \frac{Q_{ad}}{Q_m} \quad \text{Eq. 4.1.7}$$

The concentration of electroactive bienzyme associated with the antTiO₂-CH surface can be determined by integrating the anodic peak according the Eq. 4.1.6

$$\Gamma = \frac{Q}{nFA_{ec}} \quad \text{Eq. 4.1.8}$$

where, Γ is the number of mol/cm², Q is the charge obtained by integrating the anodic peak, n is the number of electrons involved in the reaction (1) and F is Faraday's constant. It has been found that the surface concentration of the ChEt-ChOx/antTiO₂-CH/ITO is 5.3×10⁻⁹ mol/cm². The diffusion coefficient (or diffusivity) of the electrolyte containing redox species from CV response at different scan rate has

been estimated using the Eq. 3.2.5 (Chapter 3). The higher diffusivity ($76.37 \times 10^{-6} \text{ cm}^2/\text{s}$) of the redox species for ChEt-ChOx/antTiO₂-CH/ITO bioelectrode is responsible for faster response times.

4.6.5 Chronoamperometric studies

The effect of flow rate of this microfluidic sensor has been investigated using chronoamperometric technique. Figure 4.2.7(iii) shows chronoamperometric response of the antTiO₂-CH/ITO electrode (a) and ChEt-ChOx/antTiO₂-CH/ITO (b) as a function of flow rate (0.01-15 $\mu\text{L}/\text{min}$). It has been observed, that the chronoamperometric current increases with increasing flow rate (buffer solution) upto 5 $\mu\text{L}/\text{min}$ after which the current becomes saturated (curve a). It appears that the electrode exhibits higher diffusion with increasing flow rate. This is because the diffusivity of redox species increases with higher buffer flow rate due to improved mass transport resulting from the increased fluid velocity. In case of the ChEt-ChOx/antTiO₂-CH/ITO bioelectrode, the current initially rises with flow rate (buffer solution on addition of cholesterol (25 mg/dl) upto 1 $\mu\text{L}/\text{min}$ after which it decreases [Figure 4.2.7(iii), curve b]. This may perhaps be assigned to the retention time for flux of electro active species in the biochemical reaction. After 1 $\mu\text{L}/\text{min}$ flow rate, the retention time is found to be lesser resulting in decreased response current. It may perhaps be due to the fact that the cholesterol molecules move away from the sensing surface *via* microchannel prior to completion of the biochemical reaction onto the sensor surface resulting in decreased current. Thus, the electrochemical measurements have been carried out at the optimum flow rate 1.0 $\mu\text{L}/\text{min}$.

4.6.6 Electrochemical impedance spectroscopy (EIS) studies

The results of EIS studies conducted on this bioelectrode show two semicircles (charge transfer resistances) of Nyquist plots as shown in the Figure 4.2.9. The charge transfer resistances, R_{ct1} and R_{ct2} for both circuits of antTiO₂-CH/ITO electrode have been found to be as 22.0 k Ω and $3.1 \times 10^5 \Omega$, respectively, at 0.6V bias potential [Figure 4.2.7(iv), curve a]. This is because the antTiO₂-CH matrix has increased electroactive surface area of electrode resulting in easier electron transfer from the medium to electrode due to increased diffusion of redox species onto surface charged antTiO₂-CH surface. In particular, experimentally obtained R_{ct} in the antTiO₂-CH matrix can be explained as (i) diffusion of antTiO₂ nanoparticles into CH molecules to obtain changed oxidation state, and (ii) this diffusion may result in increased conductivity and hence compensate for the higher resistance of CH due to larger molecules. The R_{ct} further decreases ($R_{ct1}=16.8 \text{ k}\Omega$ and $R_{ct2}=2.7 \times 10^5 \Omega$ for both equivalent circuits) after the immobilization of ChEt-ChOx onto antTiO₂-CH surface revealing that mesoporous antTiO₂-CH provides a desirable microenvironment for the immobilization of bienzyme [Figure 4.2.7(iv), curve b]. The bienzyme (ChEt and ChOx) re-arranges its structure which presents better conformation onto antTiO₂-CH surface and the secondary and tertiary structure of ChEt-ChOx perhaps play important roles

towards the increased availability of the active sites. Thus, the ChEt-ChOx/antTiO₂-CH/ITO bioelectrode provides easier electron transfer due to increased active sites for electrical contact between electrode and the redox label in solution resulting in lower electrochemical impedance.

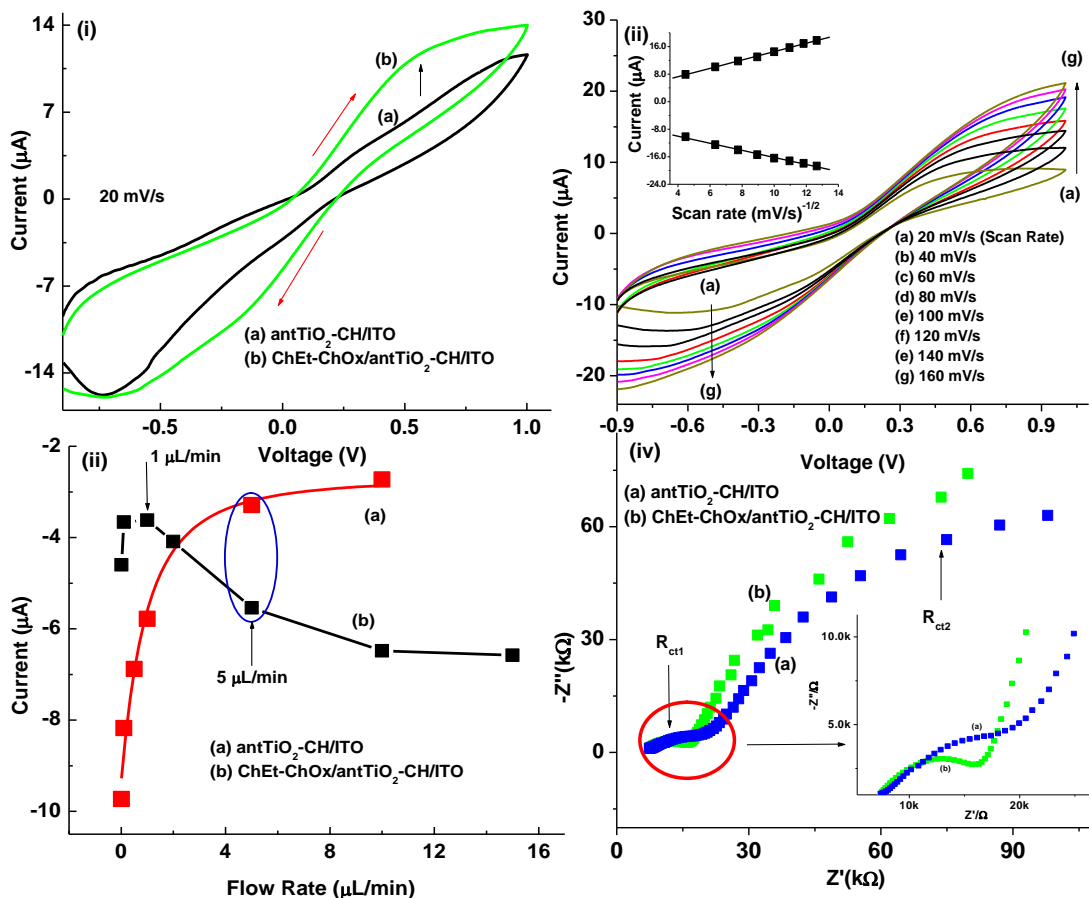


Figure 4.2.7(i) CV of (a) antTiO₂-CH/ITO electrode and (b) ChEt-ChOx/antTiO₂-CH/ITO bioelectrode in PBS solution (50 mM, pH 7.0, 0.9% NaCl) containing 5 mM [Fe(CN)₆]^{3-/4-}, (ii) CV of ChEt-ChOx/antTiO₂-CH/ITO bioelectrode as a function of scan rate [20-160 (mV/s)] in ascending order, inset: anodic and cathodic peak current vs scan rate (mV/s)^{-1/2}, (iii) chronoamperometric response current vs flow rate (µL/min) of (a) antTiO₂-CH/ITO electrode and (b) ChEt-ChOx/antTiO₂-CH/ITO bioelectrode, and (iv) electrochemical impedance spectroscopy (EIS) of (a) antTiO₂-CH/ITO electrode and (b) ChEt-ChOx/antTiO₂-CH/ITO bioelectrode, (inset: zoom image).

Figure 4.2.8(i) shows EIS spectra of ChEt-ChOx/antTiO₂-CH/ITO bioelectrode obtained as a function of flow rate (0.01- 5 µL/min). It has been observed that the R_{ct2} of the semicircle gradually increases, with increased flow rate of cholesterol solution containing [Fe(CN)₆]^{3-/4-} ions. This may be due

to increased number of $[\text{Fe}(\text{CN})_6]^{3-/4-}$ at the higher fluid velocity. After $1\mu\text{L}/\text{min}$, the impedance of ChEt-ChOx/antTiO₂-CH/ITO bioelectrode increases slowly and becomes saturated (inset). This optimum flow rate of $1\mu\text{L}/\text{min}$ has been used to conduct EIS measurements.

Figure 4.2.8(ii) shows EIS spectra of ChEt-ChOx/antTiO₂-CH/ITO bioelectrode as a function of applied potential (0 – 0.7 V). It has been seen that there are two semicircles that appear (zoom image) in low frequency region and high frequency region as shown in equivalent circuit model. The R_{ct2} values of semicircle 2 in low frequency region of the ChEt-ChOx/antTiO₂-CH/ITO bioelectrode have been found to increase linearly with increased potential [inset, Figure 4.2.8(ii)]. This reveals facile electron transfer kinetics wherein resistance controls the electron transfer kinetics of the redox probe at the electrode. The depression angle (δ) is an important parameter by which the semicircular displaced below the real axes is related to the width of the relaxation time distribution [6]. It can be seen that arc of the semicircle with least δ value, is less distorted from centre of the real axis and can be estimated using the relation $\delta = (1 - n)\pi/2$ where, n is the fractional exponent. Figure 4.3(i) shows the variation of depression angle (δ) for ChEt-ChOx/antTiO₂-CH/ITO bioelectrode as a function of applied potential. It is observed that values of (δ) for ChEt-ChOx/antTiO₂-CH/ITO bioelectrode decrease on increasing the potential from 0 to 0.7 V. The electric double layer or constant phase element (C_{dl}) has been found to decrease with increasing potential. This suggests that the resistance represented in the semicircle of the Nyquist plot depends on the bias voltage. Thus, the R_{ct2} values are found to increase at higher potential indicating that the charge transfer at low frequency is dependent on polarization potential, thus the high potential of 0.6V has been chosen for biosensing.

The bioelectrode has been further characterized by analyzing the following important parameters such as heterogeneous electron transfer rate constant (k_0) and time constant (τ) for redox probe containing $[\text{Fe}(\text{CN})_6]^{3-/4-}$ ions [31]. The corresponding k_0 of the modified electrode has been calculated using charge transfer kinetics. The k_0 value of the ChEt-ChOx/antTiO₂-CH/ITO bioelectrode obtained as 2.03×10^{-6} is higher than that for antTiO₂-CH/ITO electrode (1.7×10^{-6}), indicating a faster electron exchange between the redox probe. The ChEt-ChOx immobilization on antTiO₂-CH/ITO shows a sluggish electron charge transfer rate constant resulting in the generation of low capacitance at the electrode surface. The high value of time constant (τ) for the ChEt-ChOx/antTiO₂-CH/ITO compared to that of the antTiO₂-CH/ITO electrode is observed due to the slow diffusion of $[\text{Fe}(\text{CN})_6]^{3-/4-}$ ions at the electrode enzyme layer/solution interface. The surface coverage (θ), is calculated using the relation

$$\theta = 1 - \frac{R_{ct2(\text{electrode})}}{R_{ct2(\text{bioelectrode})}} \quad \text{Eq. 4.1.9}$$

where θ is the fraction of occupied binding sites. The $R_{ct2(\text{electrode})}$ and $R_{ct2(\text{bioelectrode})}$ are respectively, the surface specific charge transfer resistances of antTiO₂-CH/ITO electrode and ChEt-

ChOx/antTiO₂-CH/ITO bioelectrode. The value of θ has been determined to be as 0.87, indicating more than 87% surface coverage of the antTiO₂-CH/ITO electrode by ChEt-ChOx molecules.

4.6.7 Impedance response studies

The electrochemical impedimetric response of the microfluidic ChEt-ChOx/antTiO₂-CH/ITO bioelectrode obtained as a function of cholesterol concentration (2–500 mg/dl) in PBS solution containing [Fe(CN)₆]^{3-/4-} is shown in Figure 4.3(ii). During electrochemical measurements, various concentrations of cholesterol are injected into the microchannels at a constant flow rate of 1.0 $\mu\text{l}/\text{min}$. A Faradic impedance spectrum (Nyquist plot) includes two semicircle regions observed at higher and lower frequencies corresponding to electron-transfer limited process.

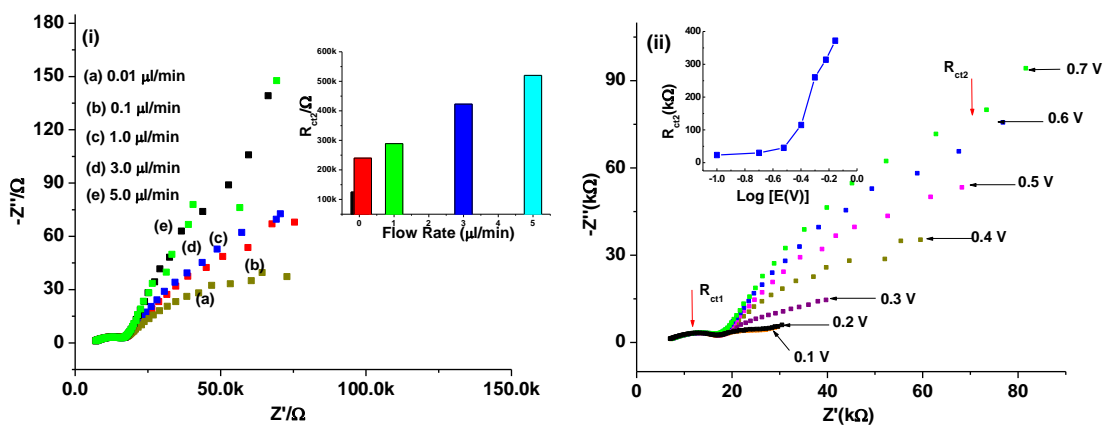


Figure 4.2.8(i) EIS spectra of ChEt-ChOx/antTiO₂-CH/ITO bioelectrode as a function of flow rate (0.01-5.0 $\mu\text{L}/\text{min}$), inset: plot between charge transfer resistance (R_{ct2}) and flow rate ($\mu\text{L}/\text{min}$) and (ii) EIS spectra of ChEt-ChOx/antTiO₂-CH/ITO bioelectrode at different potential (0.1-0.7 V), inset: the plot between R_{ct2} value and logarithm of potential.

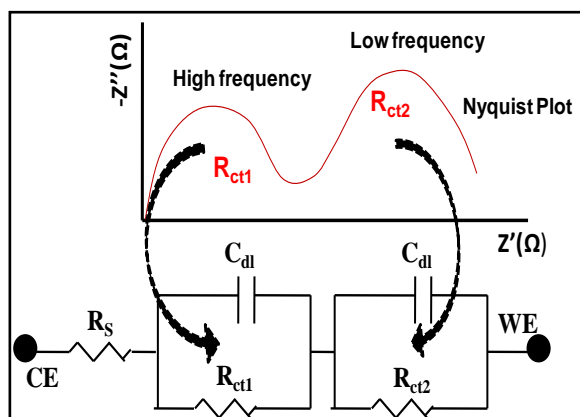


Figure 4.2.9 Randles equivalent circuit model for EIS measurement, where R_s = solution resistance, R_{ct} = charge transfer resistance, C_{dl} = constant phase element or double layer capacitance, W = Warburg impedance.

The electronic impedimetric circuit of the electrochemical system has been shown in Schematic 6.1.3. It can be seen that change in the second semicircle diameter (R_{ct2}) is higher compared to that of the first semicircle as shown in Figure 4.3(ii). The charge transfer resistance of microfluidic ChEt-ChOx/CH-antTiO₂/ITO bioelectrode (R_{ct2}) reveals electron-transfer kinetics of redox probe at the electrode interface which decreases with increasing cholesterol oleate concentration [Figure 4.3(iii)]. This can be attributed to the fact that in presence of ChEt on antTiO₂-CH /ITO electrode, the esterified cholesterol get converted to cholesterol and fatty acid. Again, ChOx converts cholesterol to choleste-4-ene-3-one and H₂O₂. The generated electrons during the re-oxidation of ChOx after enzymatic reaction are transferred to the CH-antTiO₂/ITO electrode via Fe(III)/Fe(IV) couples that help in enhanced charge transfer rate leading to decreased R_{ct2} value. A linear calibration curve [Figure 4.3(iv)] has been fitted between R_{ct2} and logarithm of cholesterol concentration revealing linearity from 2 to 400 mg/dl in the detection range of 2-500 mg/dl. The linear regression equation is $R_{ct2}(\Omega) = 27.9 \text{ k}\Omega - 6.77 \text{ k}\Omega \text{ mg}^{-1} \text{ dl} \times [\text{cholesterol oleate concentration (mg/dl)}]$ with a correlation coefficient of 0.996. The ChEt-ChOx/antTiO₂-CH/ITO based microfluidic chip yields excellent sensitivity (67.7 k Ω /mg/dl) compared to that in other literature [248]. The sensitivity of the mesoporous TiO₂ grafted CH microelectrode based impedance enzymatic sensor is several-folds higher, revealing that the combination of a microfluidic impedance sensor with biopolymer-nanostructured microelectrodes provides a technology for more sensitive detection of esterified cholesterol. The low apparent Michaelis–Menten constant (K_m^{app}) obtained (1.3 mg/dl) indicates that the ChEt-ChOx/antTiO₂-CH/ITO bioelectrode has higher affinity towards the esterified cholesterol compared to other reported literature. This may be due to the incorporation of mesoporous antTiO₂ nanoparticles

into chitosan matrix, that is capable of binding strongly with the desired enzyme. It has been observed that the reported cholesterol biosensors show poor detection limit, range and larger detection time as shown in Table 4.1.4. This proposed impedimetric microfluidic biosensor shows a lower detection limit of 0.2 mg/dl and a wide detection range of 2-500 mg/dl. The biosensing characteristics of ChEt-ChOx/antTiO₂-CH/ITO bioelectrode along with those reported in literature are summarized in Table 4.1.4. Thus, the method of detection (EIS) and the integration of antTiO₂-CH matrix to the microfluidic device is an efficient, fast and low cost technique for total cholesterol detection.

4.6.8 Reproducibility studies

The reproducibility of the ChEt-ChOx/antTiO₂-CH/ITO bioelectrode has been investigated at 100 mg/dl cholesterol concentration, no significant change in R_{ct2} value is observed after repeated for atleast 15 times as evidenced by the observed low standard deviation (RSD) of 3.19% (n=5) indicating good precision. The ChEt-ChOx/antTiO₂-CH/ITO bioelectrode shows good repeatability as indicated by the RSD 2.2 % (n = 15) for 100 mg/dl cholesterol concentration, after 15 times washing/repetition of the bioelectrode. No significant decrease in current is observed till repeated usage of 12 times, after which the bioelectrode shows slight decrease in current response that may be arising due to the denaturation of biomolecules.

4.6.9 Effect of stability and specificity

The shelf-life of the ChEt-ChOx/antTiO₂-CH/ITO bioelectrode measured in intervals of 1 week has been estimated to be 8 weeks. The decrease in the value of R_{ct2} has been found to be about 10% up to about 8 weeks after which the current decreases resulting in about 80% loss in about 10 weeks. The specificity of this enzymatic sensor is mainly dependent on the bienzyme (ChEt-ChOx) immobilized onto the sensor surface. To evaluate the specificity of the mesoporous antTiO₂-CH based impedance enzymatic sensor, glucose (5 mM), uric acid (0.1 mM), and urea (1 mM) analytes present in human serum sample, are tested at a concentration of 100 mg/dl (cholesterol oleate) using CV. No significant change in current response has been observed as evident by low relative standard deviation of 4.4 % [Figure 4.3.1].

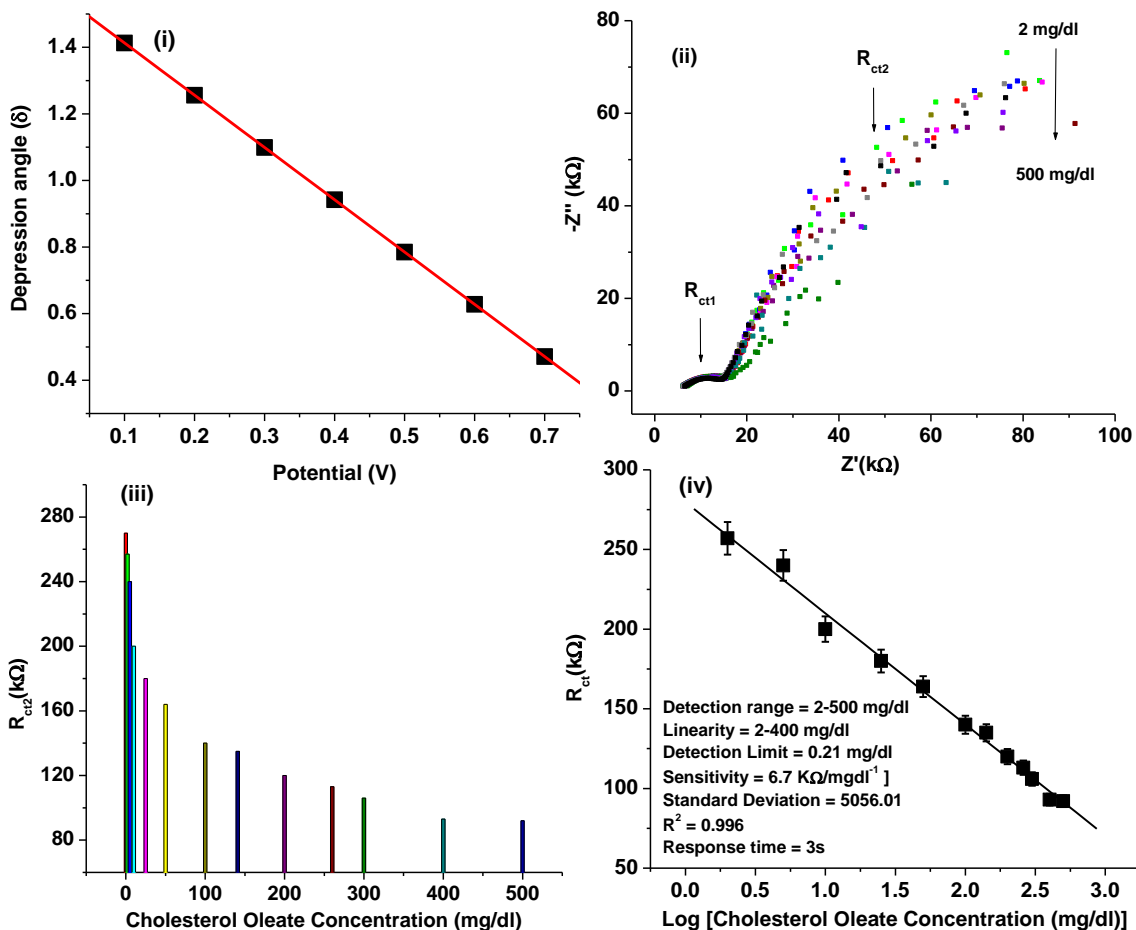


Figure 4.3 (i) Dispersion angles versus potentials for ChEt-ChOx/antTiO₂-CH/ITO bioelectrode, (ii) EIS response spectra of ChEt-ChOx/antTiO₂-CH/ITO bioelectrode as a function of cholesterol oleate concentration (at flow rate of 1 $\mu\text{L}/\text{min}$) (iii) plot between R_{ct2} and concentration of cholesterol oleate [2-500 mg/dl] and (iv) the microfluidic sensor linear fit curve between EIS response and logarithm of cholesterol oleate concentration in the range of 2-500 mg/dl.

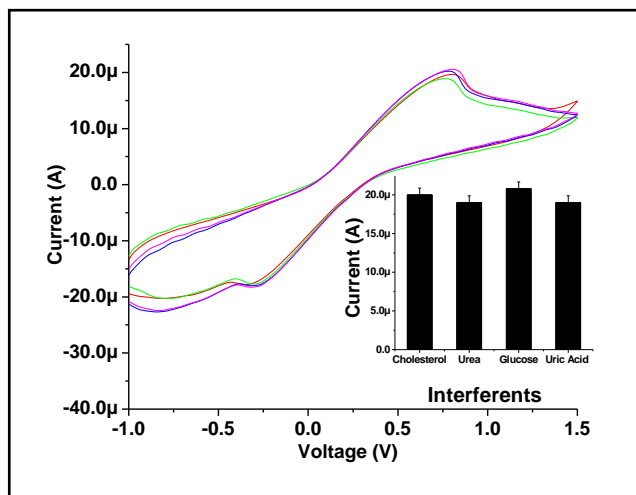


Figure 4.3.1 The selectivity studies in presence of various interferences.

Table 4.1.4 Sensing characteristics of cholesterol biosensor along with those reported in literature

Working electrode	Detection technique	Detection range (mg/dl)	Detection limit (mg/dl)	Sensitivity	K_m Value (mg/dl)	References
Fe_2O_3	EIS	0.25-400	0.24	$86\Omega/mg\ dl^{-1}$	0.08	[248]
Chitosan- CeO_2	CV	10-400	5.0	$47\ \mu A/mg\ dl^{-1}$	3.5	[249]
Chitosan- SnO_2	CV	5-400	5.0	$34.7\ \mu A/mg\ dl^{-1}$	146.9	[250]
Chitosan-ZnO	CV	3-300	$2.0\ \mu A/mg\ dl^{-1}$	8.8	[251]
TiO_2 -CH	EIS	2-500	0.20	$67.7\ k\ \Omega/mg\ dl^{-1}$	1.3	Present Work

4.7.0 Potential merits and demerits

This impedimetric microfluidic biosensor shows excellent sensing characteristics towards total cholesterol detection. It has been seen that biosensor characteristics using impedance (using EIS) method is improved compared to the amperometric detection (using CV) of cholesterol. Compared to other biosensors, this microfluidic biosensor exhibits very low detection limit with a wide detection range of 2-500 mg/dl. After chitosan incorporation onto titania, the pore volume decrease from 0.2961 cc/g to 0.1265 cc/g (i.e. 42.72% porosity or pore volume) and the surface area is also decreased due to chitosan coating which has blocked the pore entrances. It has been observed that the signal to noise ratio (SNR) is higher resulting in higher sensitivity. The incorporation of positively charged CH biopolymer onto mesoporous antTiO₂ matrix shows excellent adsorption ability of enzyme molecules resulting in improved stability. CH helps not only the dispersion of antTiO₂ nanoparticles but also results in enhanced electron transfer properties. It can be seen that the detection time for one impedance scan using frequency response analyzer is about 3 min, which is higher compared to that of CV scan (30 s) for one particular cholesterol concentration. Impedance is a complex analysis compared to amperometric analysis.

4.8 Conclusions

I have fabricated a microfluidic chip based on dispersive antTiO₂ nanoparticles grafted nanoporous CH for total cholesterol detection. Using ac impedance approach, the impedance changes due to catalytic reaction of enzymes and detectable cholesterol molecules in this enzymatic microfluidic chip has been investigated. The morphological (AFM, SEM) and spectroscopic (UV, FT-IR, XPS) investigations of antTiO₂-CH matrix indicate immobilization ChEt-ChOx and quantification of functional groups present in transducer surface. The electrochemical properties of the fabricated microfluidic chip have been investigated using CV, chronoamperometry and EIS techniques. This microfluidic chip showed excellent performance as a microscale platform. The impedance analysis of this microfluidic device offers small instrument size, low reagent consumption, and system automation, indicating that this microfluidic device has a high potential for the POC medical applications. The low cost, high sensitivity and low detection limit can be accounted for high electronic conductivity of antTiO₂ grafted CH and good catalytic activity of the nanoparticles. In addition, the CH not only enhances the electrode forming ability but also improves dispersion of antTiO₂ nanoparticles at surface.

The application of TiO₂ nanoparticles in the microfluidic platform for biofunctionalization is a major concern due to its low isoelectric point resulting in poor biomolecules absorption on transducer surface. There is a scope to utilize other metal oxides which having high isoelectric point for immobilization of biomolecules in order to improve sensitivity, detection limit and other related parameters. The antTiO₂-CH based microfluidic biosensor results in increased complexity for POC

applications. The higher potential of fabricated microfluidic system using antTiO₂-CH matrix is a limitation for POC application. Keeping this in view, nanostructured NiO having higher isoelectric point and better electrochemical properties has been explored for development of the microfluidic POC cholesterol biosensor. The next Chapter describes the fabrication and characterization of a microfluidic biochip using nanostructured NiO for total cholesterol estimation.

CHAPTER 5

**Highly efficient microfluidic biochip based on
nanostructured nickel oxide**

5.1 Introduction

This chapter describes results of the studies relating to the application of nickel oxide nanorods (NR-NiO) biosensor integrated with microfluidics for total cholesterol detection. First, I describe the integration of the microfluidic biosensor chip for total cholesterol detection. Attempts have been made to discuss the details relating to synthesis and characterization of nickel oxide nanorods, followed by the electrochemical characterization of the device. Finally, the merits and performance of this biosensor chip for total cholesterol estimation are compared with the studies described in the preceding Chapter.

Recent years have seen significant advances in the development of nanofluidics-based devices using one-dimensional (1D) nanostructured materials such as nanorods, nanotubes, nanowires and nanorings due to their novel properties [252, 253]. These 1D nanostructures act as “electronic wires” that can provide direct channels for electron transport from enzymes’ active sites to current collector leading to improved loading of biomolecules (enzymes) due to large-area scaffold. Among the 1D materials, the rod-like geometries with well-defined crystal surfaces have been reported as advantageous for transport of charge carriers such as electrons and ions [254]. The application of microfluidics-based devices to biosensing has recently grown exponentially because of their exceptional merits over conventional devices in terms of portability, microscale bioanalysis, automated drug discovery, lower cost, quick diagnosis, sample and reagent consumptions [75]. The integration of a microfluidics device (lab-on-a-chip) with 1D nanorods provides a promising approach in development of a smart biosensing chip that can be used to monitor desired analytes [255].

Many groups have reported the use of nanorods/nanotubes for bio-sensing, filtration and sample separation based on microfluidics devices [256]. Shi et al. have fabricated a low cost, high throughput and highly parallel mix-and-match nanodevices of integrated nanopillar arrays using soft UV nanoimprint lithography and reactive-ion-etch techniques for long DNA molecule separation [257]. Koto et al. have developed molecular sensor arrays composed of vertical germanium nanowires that function as a FET based microfluidic channel on silicon resulting in improved sensing performance with response time less than 10 s [258].

Nanostructured nickel oxide (NiO) is an antiferromagnetic semiconductor with a wide band gap of ~ 3.6 eV that can be used for fabrication of optoelectronic devices, FET and biosensors [259]. NiO with different morphologies, including nanoparticles, nanostrips, nanorods, nanosheets and hollow spheres have recently been reported for various applications including biosensing [260]. The rod-like nanostructured NiO has been found to be stable in air and does not degrade with immobilization of biomolecules. The selective binding of molecules to the nanostructured NiO and a Debye length

comparable to the nanostructure may perhaps strongly influence its surface, giving rise to enhanced sensitivity [261]. In addition, NiO nanorods offer attractive properties like high isoelectric point (IEP; 10.8), high electro-catalytic property and sensitivity that enhance the intensity of an electrochemical signal. However, 1D NiO platform offers higher accumulation of charges on the surface in comparison to the 2D nanostructured NiO due to its improved electrical properties. A nanostructured NiO based genosensor for diagnosing *Visceral Leishmaniasis* (Kala azar) has been demonstrated and it has been found to be an excellent matrix for immobilization of biomolecules [219]. Li et al. have used NiO hollow nanospheres due to their high specific active sites and electrocatalytic activity via controlled precipitation of metal ions with urea using carbon microspheres as templates for application to glucose biosensor [259].

The cholesterol biosensors based on gold nanowires have been fabricated by electroplating anodized alumina template integrated onto a microfluidic platform by dielectrophoresis coating [262]. Singh et al. have demonstrated that chitosan modified NiO nanoparticles can act as good acceptors of electrons generated during re-oxidation of cholesterol oxidase (ChOx) that are transferred to electrode via $\text{Ni}^{+2}/\text{Ni}^{+3}$ redox couple resulting in increased electrochemical current and exhibit the sensitivity upto $0.808 \mu\text{A}/(\text{mg dl cm}^2)$ [220]. This nanostructured chitosan-NiO matrix shows Michaelis–Menten constant (k_m) value of 0.67 mM attributed to favourable conformation of ChOx and higher loading onto transducer surface. However, there is a considerable scope to improve the biosensing performance in terms of sensitivity, K_m value, reducing use of reagents/samples, low cost and miniaturization for total cholesterol.

5.2 Experimental section

5.2.1 Fabrication of microfluidic biosensor

The synthesis of NR-NiO using co-precipitation method has been described in the third Chapter, (Section: 3.3.6). The transparent thick gel-like $\text{Ni}(\text{OH})_2$ solution is deposited onto patterned ITO on the glass substrate via dip coating. Finally, this glass substrate containing $\text{Ni}(\text{OH})_2/\text{ITO}$ and bare ITO electrodes are annealed at 400°C under ambient conditions for about 2 h to remove any solvent. ITO microelectrodes have been fabricated as described before. In order to immobilize the desired enzymes, 1 mg/ml cholesterol esterase (ChEt) and 1 mg/ml cholesterol oxidase (ChOx) are mixed in the ratio 1:1 and 10 μl solution of this mixture is uniformly spread onto NR-NiO/ITO microelectrode via physical adsorption (Figure 5.1.1) and is kept in a humid environment for 12 h at 4°C . The values of ionization electron potential (IEP) of NiO and enzymes (ChEt-ChOx) are found to be 10.8 and 5.3, respectively. The NiO matrix is positively charged in contrast to the enzymes that are negatively charged resulting in electrostatic interactions. This ChEt-ChOx/NR-NiO/ITO bioelectrode is washed with 50 mM PBS (pH 7.0) in order to remove any unbound enzymes from the electrode surface. The bioelectrode is stored at 4°C when not in use. Nickel oxide nanorods-based electrode is co-immobilized with ChEt-ChOx to serve

as the working electrode (ChEt-ChOx/NR-NiO/ITO) and bare ITO microelectrode serves as counter electrode. PDMS microchannels tightly sealed onto the glass substrate containing ITO and ChEt-ChOx/NR-NiO/ITO electrodes (Figure 5.1.1) via conformal contact (reversible sealing) act as the microfluidics biosensor chip. To avoid fluids leakage during experiment, the ITO substrate is clamped with PDMS slab. All the two electrodes and microchannel are embedded on the same chip.

5.2.2 Precautions

- (i) The temperature should be maintained constant during fabrication of PDMS microchannels. The oxidizing material which may cause a reaction with PDMS must be avoided.
- (ii) Direct contact of eye with PDMS may cause temporary redness and discomfort.
- (iii) The correct stoichiometry of precursor material is needed for co-precipitation of NiO.

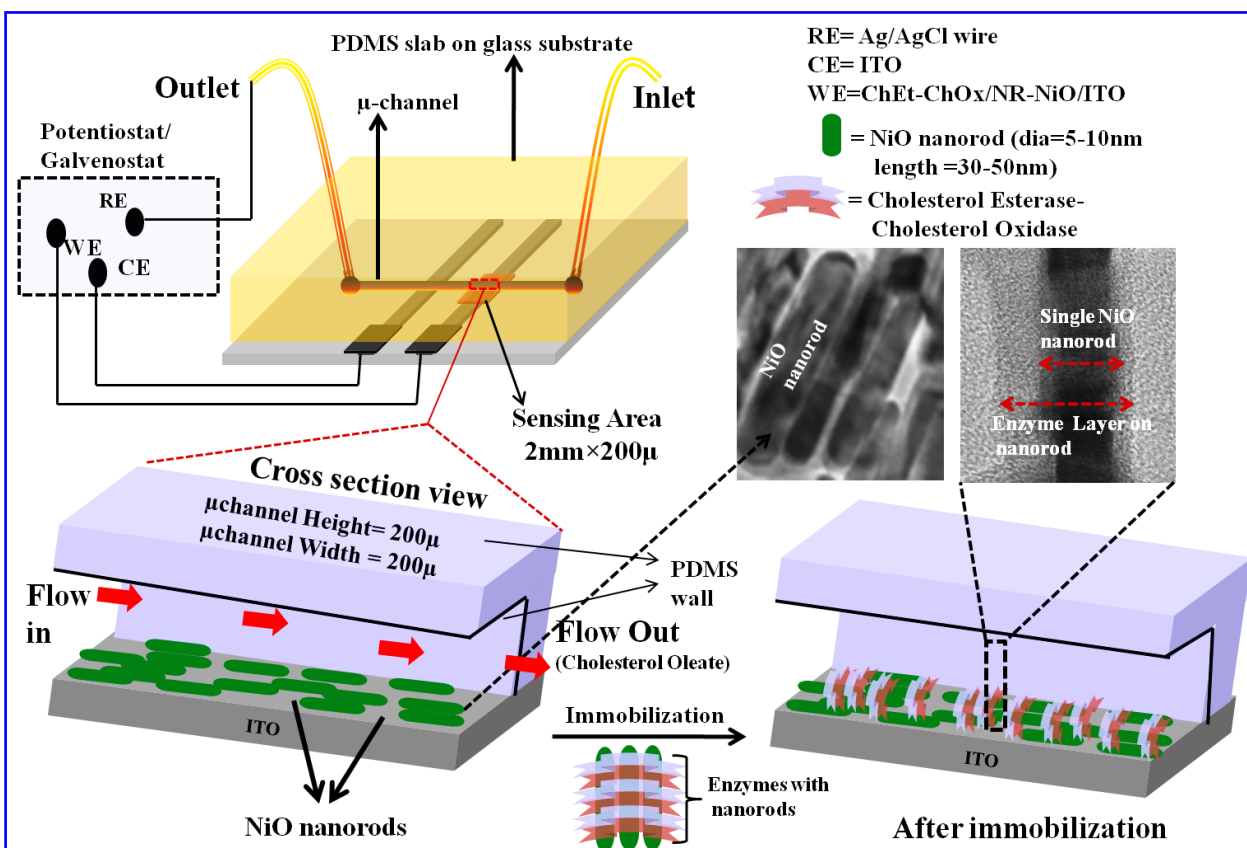


Figure 5.1.1 The microfluidic chip used for total cholesterol detection (ordered arrangement of nanorods on this chip is assumed for easy representation).

5.3 Results and discussions

5.3.1 XRD studies

The X-ray diffraction (XRD) studies [Figure 5.1.2] reveal the purity and crystallinity of the synthesized nickel oxide nanorods (NR-NiO) with the face-centred cubic (a) 4.1 Å and space group $Fm\bar{3}m$ (225), [JCPDS Card No. 78-0423]. All the peaks are assigned to the diffraction pattern resulting from the (111), (200), (220) and (222) planes of the cubic NiO, respectively. This observation indicates that the resultant NiO nanorods are mainly dominated by (111) facets. The intensity ratio between two planes (111) and (200) of NR-NiO [inset: Figure 5.1.2] calculated to be 5.2 is much higher than that of bulk NiO (1.45), indicating preferred crystallization along the plane (111). The d_{111} value of NiO nanorods is found to be 0.241nm for the plane (111) which is the same as from the HR-TEM studies. The peaks seen at 50.9° and 60.5° corresponding to the planes (124) and (143) are due to ITO coating on the glass substrate.

5.3.2 Raman studies

The Raman spectra of NR-NiO powder show several bands above 400 cm^{-1} at room temperature (25 °C) [Figure 5.1.3]. The vibrational band due to one phonon (1P) at 507 cm^{-1} corresponds to transverse optical (TO) mode arising due to excitation wavelength of 532 nm. This 1P band has very small intensity indicating good crystallinity. The peak due to two-phonon (2P) seen at ~713 cm^{-1} is assigned to 2TO modes and the at ~1090 cm^{-1} is attributed to the 2LO (longitudinal optical) mode. The band found at ~713 cm^{-1} exhibits low intensity at room temperature indicating presence of NR-NiO. In the ultra violet (UV)-visible spectra, a strong observation peak is observed at ~379 nm corresponding to intra-3d transition of Ni^{2+} in NiO structure [inset: Figure 5.1.3] as compared to that of the bulk NiO (484nm). This result shows blue shift to 105 nm indicating formation of the nanostructured NiO. This is because nanostructures are laterally quantum confined and occupy energy levels that are different from the traditional continuum of energy levels or bands found in a bulk material.

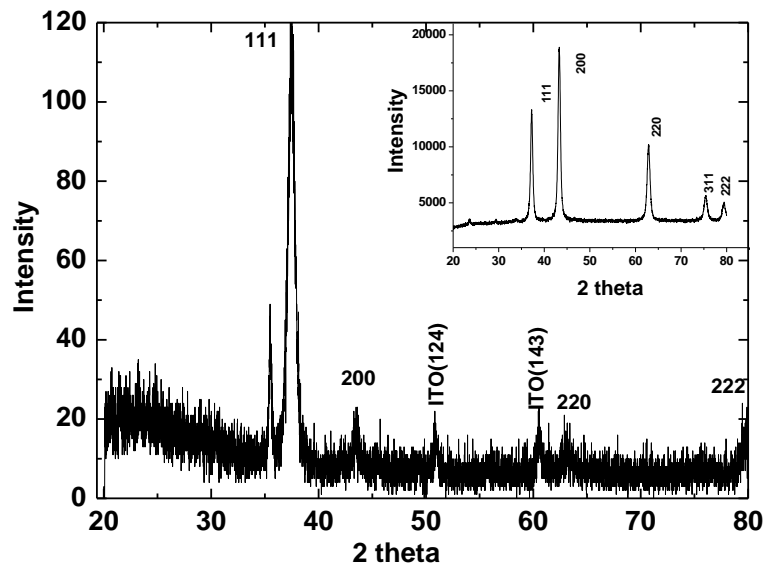


Figure 5.1.2 X-Ray diffraction pattern of NR-NiO nanorods onto ITO film (inset: powder XRD pattern of NiO nanorods)

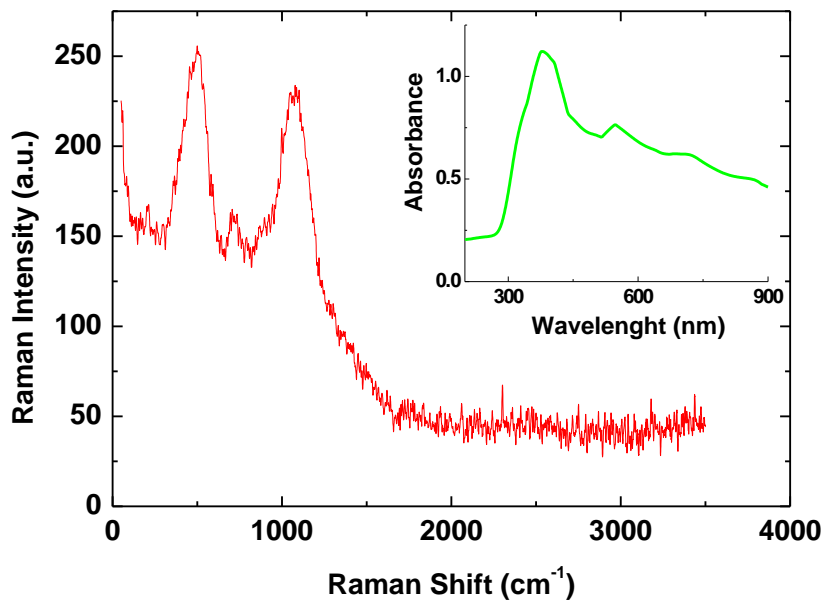


Figure 5.1.3 Raman spectroscopy studies of NiO nanorods (inset: UV-vis absorption spectrum of NR-NiO)

5.3.3 FT-IR studies

In FT-IR studies [Figure 5.1.4], the infrared peak found at 545 cm^{-1} in the fingerprint region (curve a) corresponds to vibrational bending of Ni-O. The dominant peak found at 1263 cm^{-1} arises due to the formation of bicarbonate (HCO_3) stretching on NR-NiO film. The absorption bands seen at $\sim 1000\text{--}2500\text{ cm}^{-1}$ are assigned to the O-C=O symmetric and asymmetric stretching vibrations and the C-O stretching vibration, which indicates that the NiO nanorods tend to strongly physically adsorb CO_2 . The presence of peak at 1632 cm^{-1} peak [curve (b)] corresponds to amide 1 band of ChEt and ChOx reveals immobilization of enzymes. The band found at 545 cm^{-1} for NiO is shifted to 600 cm^{-1} due to incorporation of the enzyme (ChEt and ChOx) molecules. The band found at ($3500\text{--}3700\text{ cm}^{-1}$) is assigned to the O-H stretching vibration in the NiO film.

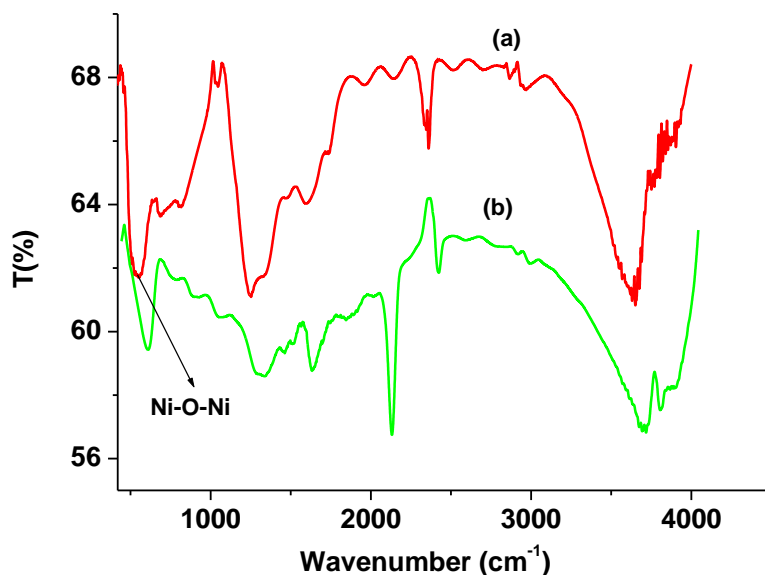


Figure 5.1.4 FT-IR spectra of (a) NR-NiO/ITO film and (b) ChEt-ChOx/NR-NiO/ITO film.

5.3.4 TEM studies

The high resolution-transmission electron microscopy (HR-TEM) studies have been conducted to unravel the NiO microstructure shape, size and surface morphology. For the HR-TEM studies, NiO nanorods dispersed in methanol are deposited onto the carbon coated copper grid by drop casting and dried in an open atmosphere. Figure 5.1.5(a) shows agglomeration of NiO nanorods. The majority of NiO nanorods exhibit nearly straight line appearance [inset: Figure 5.1.5]. The solid rods-like shapes tend to organise the long axes parallel to each other. The structural orientation of the individual nanorod of size (length=

~38nm; dia=~8nm) has been investigated via high-resolution TEM [Figure 5.1.5(b)] and it shows presence of moire fringes. These results reveal the presence of nanorods with conical tips in NiO. These NiO nanorods exhibit a low aspect ratio (length-to-width ratio) of ~4 indicating elongated nanostructure. The clear lattice fringes illustrate that the nanorods are highly crystalline in nature [Fig. 3(c)]. The spacing between the two adjacent fringes for different planes is found to be 0.245 nm and 0.20 nm [Figure 5.1.5(c)]. The interplanar spacing of 0.245 nm [inset: image c] corresponds to the (111) plane revealing anisotropic growth of the nanorod along (111) direction. The selected area electron diffraction (SAED) pattern consists of five diffraction rings with different radii [inset: Fig. 4.4(b)]. The diameter of the diffraction rings in the SAED pattern is proportional to $\sqrt{h^2 + k^2 + l^2}$. The 1st, 2nd, 3rd, 4th and 5th rings correspond to (111), (200), (220), (311), and (222) planes, respectively. These solid rod-like shapes of NiO may be beneficial for loading of enzymes due to higher surface area. However, a thick transparent layer of visible enzymes (ChOx-ChEt) containing consistent distribution of ChOx-ChEt is clearly visible on the individual nanorods [Figure 5.1.5 (b)]. These results indicate that NiO nanorods act as matrix or substrate for loading of biomolecules.

5.3.5 Electrochemical characterization

The EIS technique has been used to measure impedance of the electrode-electrolyte interface in response to a small AC signal as a function of frequency (0.01 to 10⁵ Hz) [Figure 5.1.6(i)]. The modification of electrode surface results in change in the value of charge transfer resistance (R_{CT}). The diameter of semicircle plot in EIS spectra gives a value of R_{CT} that reveals electron transfer kinetics of the redox probe at the electrode/electrolyte interface. The Nyquist diagram of the EIS curve shows that the R_{CT} value of NR-NiO/ITO electrode is 19 k Ω (curve a). This is due to presence of NiO nanorods on electrode surface that is insulating in nature thus impeding diffusion of the ferri/ferro cyanide $[\text{Fe}(\text{CN})_6]^{3-/4-}$ ions from bulk solutions to electrode surface resulting in enhanced charge transfer resistance. After co-immobilization of ChEt and ChOx on NR-NiO electrode surface, the charge transfer resistance (R_{CT}) decreases to 8.08 k Ω (curve b) implying that enzyme molecules are indeed absorbed onto NR-NiO/ITO surface suggesting that immobilized enzymes molecules bind strongly with NiO nanorods on the electrode surface. This low value of R_{CT} (curve b) is because of the enhanced catalytic activity of the enzyme and favourable electron transfer kinetics of NiO nanorods that enable rapid oxidation/reduction of the $[\text{Fe}(\text{CN})_6]^{3-/4-}$ ions that reach the electrode surface. In addition, NiO nanorods perhaps establish an electronic pathway that reduces the tunnelling distance to diffuse ions (or electrons) between enzymes active centre and electrode revealing that the bioelectrode is more conductive in nature in agreement with the results of the CV studies.

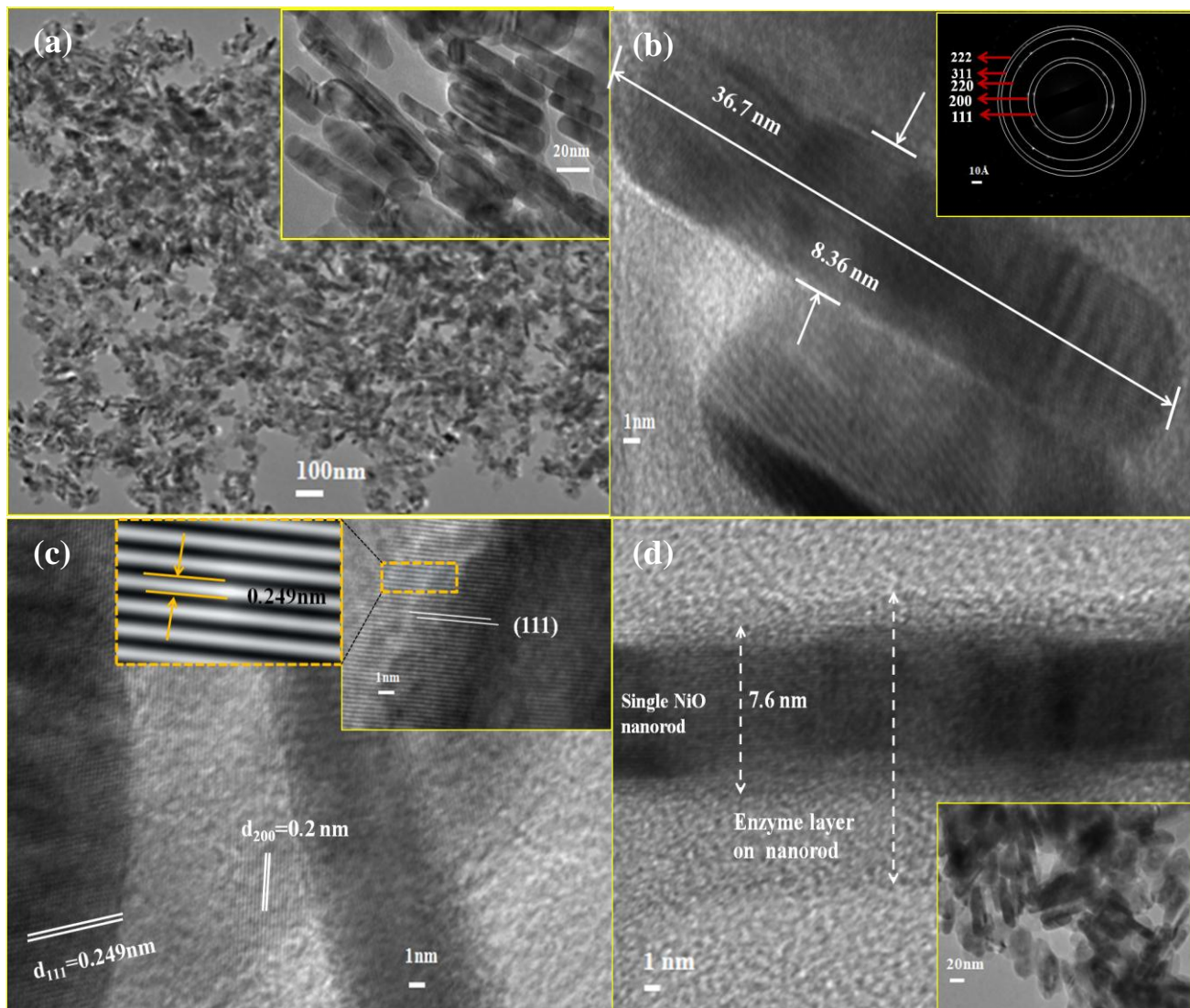


Figure 5.1.5 HR-TEM analysis of (a) synthesis NiO nanorods (inset: zoom image nanorods), (b) single nanorods micrograph with length 36.7nm and width 8.36nm (inset: SAED pattern of NiO nanorods), (c) lattice fringes of as-synthesis NR-NiO different planes (inset: lattice fringe for (111) plane and zoom image) and (d) ChEt-ChOx immobilization onto NR-NiO (inset: image at low resolution).

CV studies are carried on the NR-NiO/ITO electrode and the ChEt-ChOx/NR-NiO/ITO bioelectrode in the potential range from -0.8 V to +0.9 V in PBS buffer containing 5 mM $[\text{Fe}(\text{CN})_6]^{3-/4-}$ at a scan rate of 30 mV/s. [Figure 5.1.6(ii)]. In CV, the ChEt-ChOx/NR-NiO/ITO bioelectrode shows well-defined oxidation and reduction peaks at +0.399 V and -0.14 V, respectively, with peak-to-peak separation of 0.53 V. These anodic/cathodic peaks arise due to presence of the nanorods that provide confined 1D channels for transportation of electrons from enzyme active site to the electrode. The anodic peak current of ChEt-ChOx/NR-NiO/ITO bioelectrode is higher (curve b) compared to that of the NR-NiO/ITO electrode (curve a) resulting in fast electron communication towards the matrix and ChEt and ChOx molecules. This indicates that a larger surface area of nanorods facilitates higher mass diffusion efficiency due to electrochemical activation of the active sites of enzymes resulting in enhanced redox current. The high electrocatalytic activity of NiO nanorods results in a superior performance of the cholesterol biosensor.

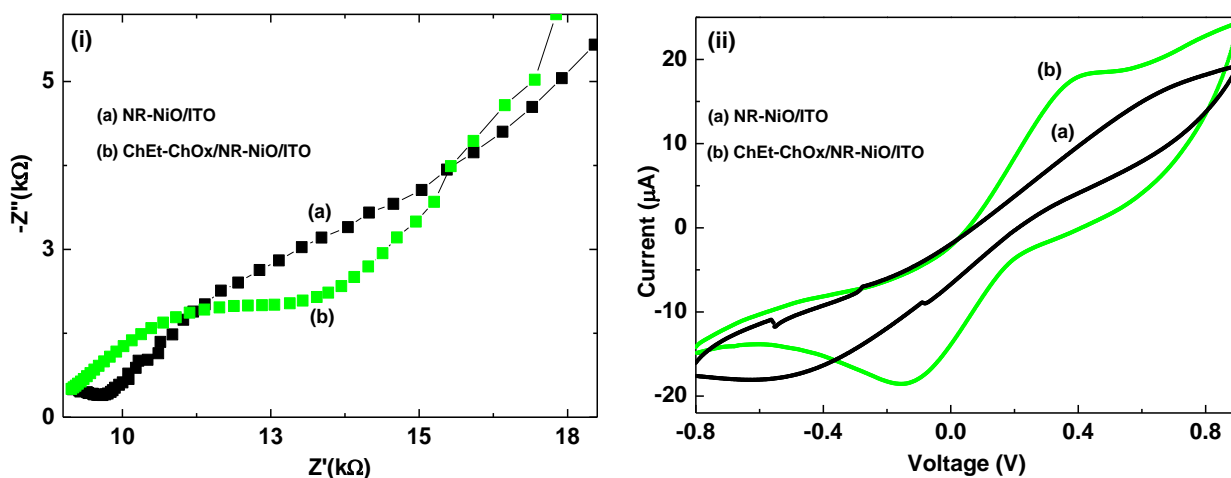


Figure 5.1.6(i) EIS of (a) NR-NiO/ITO electrode and ChEt-ChOx/NR-NiO/ITO bioelectrode and (ii) CV of (a) NR-NiO/ITO electrode and (b) ChEt-ChOx/NR-NiO/ITO bioelectrode in PBS solution (50 mM, pH 7.0, 0.9% NaCl) containing 5 mM $[\text{Fe}(\text{CN})_6]^{3-/4-}$.

5.3.6 Scan rate studies

The CV studies of the ChEt-ChOx/NR-NiO/ITO bioelectrode have been carried out as a function of scan rate (30-110 mV/s) [Figure 5.1.7]. The magnitude of current of both anodic peak (I_{pa}) and cathodic peak (I_{pc}) observed for ChEt-ChOx/NR-NiO/ITO bioelectrode increases linearly with scan rate (inset: Figure 5.1.7) indicating quasi-reversible diffusion controlled behaviour. It can be seen that anodic peak shifts towards positive side and the cathodic peak potential (inset: Fig. 4.6) shifts in the reverse direction. The values of the slope, intercept and correlation coefficient are given by Eq. (5.1.1-5.1.2).

$$I_{pa(\text{ChEt-CHOx/NR-NiO/ITO})} = 8.14\mu\text{A} + 0.243 \mu\text{A mV}^{-1}\text{s} \times \text{Scan Rate (mV/s)}; r^2 = 0.993 \quad \text{Eq. 5.1.1}$$

$$I_{pc(\text{ChEt-CHOx/NR-NiO/ITO})} = -9.6\mu\text{A} - 0.22 \mu\text{A mV}^{-1}\text{s} \times \text{Scan Rate (mV/s)}; r^2 = 0.990 \quad \text{Eq. 5.1.2}$$

The surface concentration (C_0^*) of ChEt-CHOx/NR-NiO/ITO bioelectrode has been estimated using the following Eq. 5.1.3

$$i_p = 0.227nFAC_0^*k^0 \exp\left[\frac{\alpha n_a F}{RT}(E_p - E'_0)\right] \quad \text{Eq. 5.1.3}$$

where i_p is the anodic peak current, n is the number of electrons transferred (1), F is the Faraday constant ($96485.34 \text{ C mol}^{-1}$), R is the gas constant ($8.314 \text{ J mol}^{-1} \text{ K}^{-1}$), A is the area of electrode surface (cm^2), C_0^* is the surface concentration of the ionic species in the film (mol/cm^2), E_p is the peak potential and E'_0 is the formal potential. $(\alpha n_a F/RT)$ and k^0 (rate constant) corresponds to the slope and intercept of $\ln(i_p)$ versus $(E_p - E'_0)$ curve at different scan rates. The value of surface concentration for ChEt-CHOx/NR-NiO/ITO bioelectrode has been found to be as $5.6 \times 10^{-7} \text{ mol/cm}^2$.

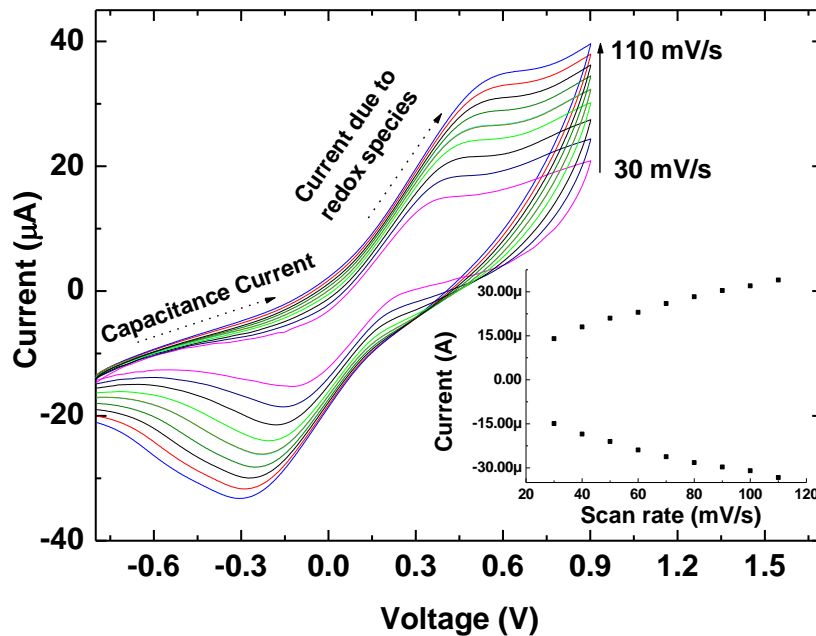


Figure 5.1.7 CV of ChEt-CHOx/NR-NiO/ITO bioelectrode as a function of scan rate $[30-110 \text{ (mV/s)}]^{-1/2}$ in ascending order in PBS solution containing $5 \text{ mM } [\text{Fe}(\text{CN})_6]^{3-/4-}$.

5.3.7 Effect of flow rate

Figure 5.1.8 shows the plot between diffusivity of $[\text{Fe}(\text{CN})_6]^{3-/4-}$ ions for the NR-NiO/ITO electrode and flow rate [10-70 $\mu\text{L}/\text{min}$] using CV in PBS (50mM, pH 7.0, 0.9% NaCl) at a scan rate of 30 mV/s. It has been found that the flow rate influences the diffusion of charge carriers (electrons) towards the electrode. The anodic current is found to increase with increasing flow rate of PBS buffer which is controlled by application of a positive pressure (syringe pump) [inset: Figure 5.1.8]. The diffusion coefficient (or diffusivity) of the electrolyte ions for each CV response at different flow rate has been estimated using Randles-Sevcik equation. It has been observed that diffusivity of the redox species increases at higher buffer flow rate due to improved mass transport resulting from increasing fluid velocity [263]. However, Collier et al. have demonstrated that response time decreases with increasing flow rate of buffer solution and have shown that the response time is inversely proportional to the flow rate [264] Thus, electrochemical studies have been carried out the at optimized flow rate of 10 $\mu\text{L}/\text{min}$.

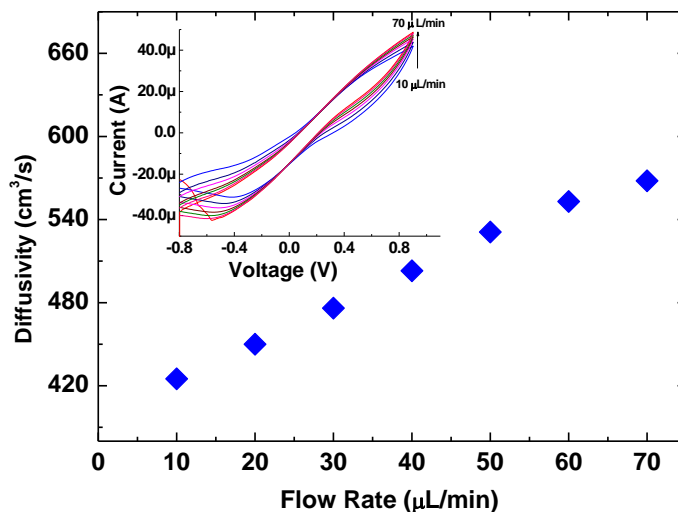


Figure 5.1.8 Diffusivity of NR-NiO/ITO electrode at different flow rates using syringe pump [inset: CV response of NR-NiO/ITO electrode at different flow rates (10-70 $\mu\text{L}/\text{min}$)].

5.3.8 Electrochemical response studies

The CV response of ChEt-ChOx/NR-NiO/ITO bioelectrode has been conducted with successive addition of cholesterol oleate at the inlet of the microchannel at a scan rate of 30 mV/s with optimum flow rate (10 $\mu\text{L}/\text{min}$) condition [inset: Figure 5.1.9]. It has been observed that the anodic peak current increases with increased concentration of cholesterol oleate (cholesterol esters) varying from 25 to 400 mg/dL [Figure

5.1.9]. In the proposed biochemical reaction, cholesterol esters (e.g. cholesterol oleate) are hydrolyzed via cholesterol esterase (ChEt) into cholesterol (or 3 β -hydroxysteroids) and fatty acid. Again utilizing flavin-adenine-dinucleotide (FAD), ChOx catalyses the oxidation and isomerization of 3 β -hydroxysteroids having *trans* double bond Δ^5 - Δ^6 of steroid ring corresponding to Δ^4 -3-ketosteroid and hydrogen peroxide (H₂O₂).³⁵ The H₂O₂ produce electrons via re-oxidation at 0.45 V. Thus during cholesterol detection, the NiO nanorods directly accept electrons from the reduced ChOx molecules in presence of [Fe(CN)₆]^{3-/4-} as mediator (Schematic S1, supplementary data). This integrated microfluidic sensor exhibits detection in the range, 0.65 mM to 10.3 mM with excellent sensitivity of 120 μ A/mgdl⁻¹/cm² compared to that of other microfluidic devices as shown in Table 5.1.1. The detection limit is found to be 0.64 mM and the value of the enzyme–substrate kinetics parameter (Michaelis–Menten constant, K_m) has been estimated using the Lineweaver–Burke plot [inset: Fig. 4.9(i)] revealing affinity of enzyme for desired analyte. It has been observed that the wide detection range of this biosensor for cholesterol is obtained compared to that using carbon nanotubes and gold nanowires based microfluidic devices (Table 5.1.1). The Lineweaver–Burke equation [Eq. 5.1.4] is given by the following as

$$\frac{1}{I_{ss}} = \frac{1}{I_{max}} + \frac{K_m^{app}}{I_{max}C} \quad \text{Eq. 5.1.4}$$

where I_{ss} is the steady-state current after addition of the substrate, C is the bulk concentration of the substrate, and I_{max} is the maximum current measured under saturated substrate conditions. It may be noted that K_m is dependent both on matrix and the method of immobilization of enzymes that may in turn bring about conformational changes resulting in different values of K_m. Besides this, the value of K_m for the bound enzyme can be lower or higher than that of purified enzyme. The obtained value of K_m for the ChEt-ChOx/NR-NiO/ITO bioelectrode (0.16 mM) is lower than the reported value [Table 5.1.1]. The lower K_m value indicates high affinity for cholesterol to ChOx and ChEt onto NR-NiO/ITO surface for faster biochemical reaction. This microfluidic sensor achieves 95% of the steady-state current in less than 5s indicating fast electron exchange between the ChEt-ChOx and NR-NiO/ITO electrode.

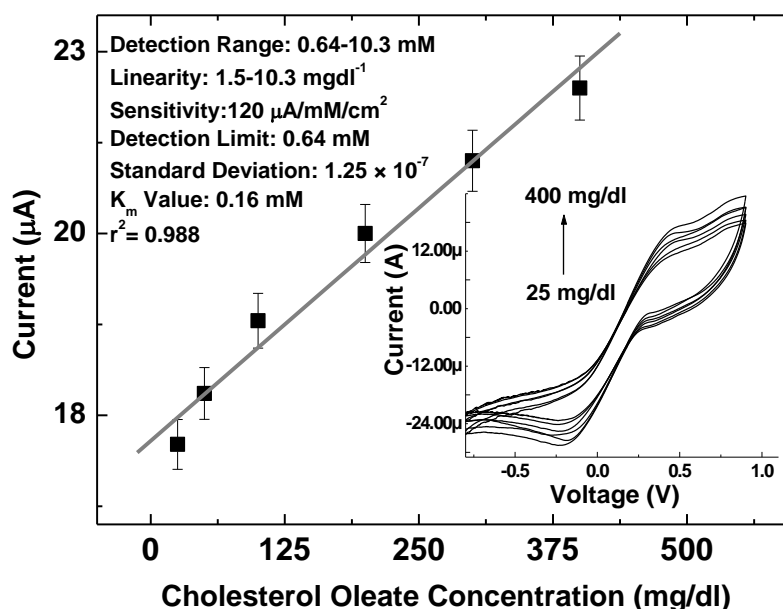


Figure 5.1.9 Calibration curve for this microfluidic biosensor between peak current and different concentration of cholesterol oleate (25-400 mg/dl) (inset: CV response of ChEt-ChOx/NR-NiO/ITO bioelectrode as a function of cholesterol oleate concentration).

5.3.9 Effect of interferents, stability and reproducibility

The effect of potential interferents such as ascorbic acid (AA), uric acid (UA), glucose (G), lactic acid (LA) and urea present in the blood samples at normal concentrations has been investigated on the response of ChEt-ChOx/NR-NiO/ITO bioelectrode using CV at the same flow rate [Figure 5.2.1(i)]. The change in the oxidation current has been measured in PBS containing equal amount (1:1) of cholesterol oleate (200 mg/dL) and interferent using the following Eq. 5.1.5

$$\%inter = I_{chol} - I_{Int}/I_{chol} \quad \text{Eq. 5.1.5}$$

where I_{chol} and I_{Int} are the changes in the current corresponding to the cholesterol oleate and the mixture of cholesterol oleate with desired interferents. As illustrated [Figure 5.2.1(ii)] the effects are negligible except in the case of uric acid. The storage stability of ChEt-ChOx/NR-NiO/ITO bioelectrode has been determined by measuring changes in the current response at regular intervals of 7 days for about 90 days [Figure 5.2.1(ii)]. This ChEt-ChOx/NR-NiO/ITO bioelectrode is stored at 4 °C when not in use. It has been found that bioelectrode exhibits 95% response after about 90 days.

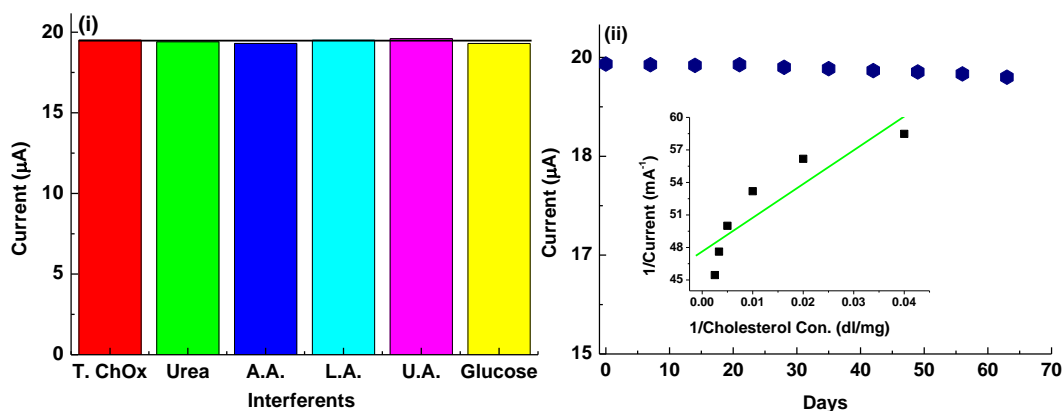


Figure 5.2.0 (i) Studies using different interferences for the ChEt-ChOx/NR-NiO/ITO bioelectrode. Current response is plotted as a function of different analytes. (ii) Stability studies of the ChEt-ChOx/NR-NiO/ITO bioelectrode as a function of days.

Table 5.1.1 Sensing characteristics of cholesterol biosensor along with those reported in literature

Working electrode	Microfluidics used	Detection range (mM)	Lower Detection limit (mM)	Sensitivity	K _m Value (mM)	Ref.
CNT	Yes	1.25 -10.0	0.25	0.0512 nA/mM	241
Au wire	Yes	1.293 -6.4	0.1	242
Gold nanoparticles	No	Up to 2.1	0.060	0.13µA/mM	2.94	243
ZnO	No	Upto 7.7	0.012	1.53 nA/mM	0.22	244
Aligned Au nanowires	Yes	0.01–0.060	0.85 µA/mM	17.1	245
Anatase-TiO ₂	Yes	0.64-10.3	0.64	94.65µA/mM	0.14	265 (Present work)
NiO nanorods	Yes	0.64-10.3	0.64	120 µA/mM	0.16	Present Work

5.4 Potential merits and demerits of this microfluidic biosensor

The proposed microfluidic system for total cholesterol detection is an efficient technique. The NiO nanorods integrated with the microfluidic system offer higher sensitivity and a low detection limits. The high isoelectric point of NiO can result in better stability and selectivity. Thus, this system provides improved biosensing characteristics as shown in Table 5.1.1. The higher sensitivity of this proposed microfluidic system can be attributed to the inherent properties of NiO nanorods on transducer surface

that enhance electron transfer kinetics. In addition, Ni(OH)₂ has uniform film forming ability, resulting in crack-free and better film formation and is easy to be integrated with microfluidic system. It is known that the direct functionalization of NiO with biomolecules is better due to positive surface potential which provides higher diffusion efficiency and better electrostatic interaction resulting in increased adsorption on sensor surface. However, this biosensing system offers higher K_m (enzyme kinetics) value as compared to that of previously described anatase TiO₂ integrated microfluidic system.

5.5 Conclusions

A microfluidic-based nano biosensor chip using nickel oxide nanorods functionalized with ChEt and ChOx has been presented for the detection of total cholesterol. These NiO nanorods have been successfully integrated with the microenvironment module to perform bioanalyte analysis as well as very precise and accurate detection. The laminar flow regime due to low Reynold number (0.82) at flow rate condition (10 μL/min) through microchannel influences diffusivity towards the electrode via nanorods and enzymes active sites. The flow rate is an important parameter in this microfluidic system. The NiO nanorods integrated with the miniaturized microfluidic device offer improved sensitivity for total cholesterol detection. Studies show no significant change in redox current of this microfluidics sensor on introducing interferents along with the analyte. Thus, a miniaturized and low cost sensor with improved biosensing parameters has been developed using this proposed microfluidic chip.

It is concluded that the NiO is a good nanostructured material suitable for the integration with microfluidic system as well as attachment of biomolecules. Thus, I have selected the NiO as a better candidate to form a composite material for this application. I have used carbon nanotubes for forming nanocomposite with NiO nanoparticles. Details of carbon nanotubes and NiO composite formation and integration with microfluidic assembly and detection are the topics of discussion for the next chapter.

CHAPTER 6

**Microfluidic biochip based on CNT-NiO
nanocomposite cholesterol estimation**

6.1. Introduction

This Chapter describes the results of studies relating to fabrication of a novel microfluidic nanobiochip based on a composite comprising of nickel oxide (NiO) nanoparticles and carbon nanotubes (CNTs). This microfluidic chip is utilized for detection of cholesterol and low density lipoproteins (LDL).

A nanocomposite is a multiphase material that incorporates nanosized particles into a matrix of standard material [266]. Recently, nanocomposites materials have gained much interest in various fields including biosensors, super-capacitors, battery, gas sensors and biomedical devices [267]. In particular, the characteristics of nanocomposites and the intrinsic benefits of microfluidics, including their laminar flow, low consumption of costly reagents and power, portability, minimal need for handling biohazardous materials, fast response time, multiplexing, and parallelization, are advantageous for the fabrication of a biochip [30, 268-270]. In this context, 1D structures, such as nanotubes, nanowires, and nanocomposites, composed of carbon materials can play an important role in medicinal chemistry and diagnostics, including the development of biochips for *in vitro* and *in vivo* investigations [270-272]. Carbon nanotubes (CNTs), allotropes of carbon originating from the fullerene family play an important role towards the development of biochips because of their high carrier mobility and tensile strength, as well as their high aspect ratio, which leads to quantum electron transport [271]. In addition, CNTs are non-reactive (like graphite) except at the nanotube caps located at ends (the tips when they are not cut), where the dangling bonds and edge-plane-like sites are open to reactions [273]. The CNTs are known to produce changes in energy bands close to the Fermi level [274]. The preferred electronic properties and high electrochemical reactivity of the enzymatic products suggest that fast electron transfer reactions occur when CNTs are used as electrodes in an electrochemical biochip [274].

Lin et al. have developed a microfluidic electrochemical sensor for on-site, non-invasive monitoring of Lead and Chlorophenols [275]. Wisitsoraat et al. have developed an electrochemical biochip for cholesterol detection that has a sensitivity of 0.0512 nA/mg/dl, which is based on the direct growth of CNTs on glass [241]. However, CNTs are known to agglomerate via *Van der Waals* interactions, resulting in poor film-forming ability. To overcome this problem, nanostructured metal oxides (NMOx) may be used to control the agglomeration of CNTs [276]. The covalent binding (or sidewall functionalization) of biomolecules (e.g., proteins, enzymes, and nucleic acids) to carboxyl-functionalized CNTs via diimide-activated amidation may provide improved stability and reproducibility [277]. In such a case, the large surface area of the CNTs and the presence of abundant functional groups may offer a suitable platform for biofunctionalization [278]. Additionally, CNTs may facilitate continuous conducting pathways to transport the charge carriers, leading to a higher sensitivity [279].

Shim et al. have used functionalized CNT for biomolecular recognition in a streptavidin/biotin approach to investigate the adsorption of proteins on the sidewalls of carbon nanotubes [277].

A biosensor based on nanostructured nickel oxide (NiO) has recently been explored to detect biomolecules such as DNA, antibody-antigen interactions, glucose, and cholesterol [219]. However, NiO-based biosensors have limited applications due to the inherently poor electrical conductivity of nNiO [280]. It has been shown that the non-covalent immobilization of enzymes onto NiO-based biochip results in poor stability of the desired biomolecules [172]. To improve the characteristics of a biosensing device, NiO can be integrated with CNT [281]. Zhang et al. have used CNT-NMOx to develop solar cells and gas sensors [282]. Chen et al. have reported the fabrication of a non-enzymatic electrochemical glucose sensor based on a MnO₂/CNT matrix [283]. Zhu et al. have utilized CNTs with ZnO nanoparticles for ultrafast, nonlinear optical switching [203].

The *sp*² hybridization and electronic properties of NiO coupled with the specific recognition properties of immobilized CNTs could lead to a miniaturized biochip [278]. Additionally, the toxicity effect of these synthesized CNT, NiO and CNT-NiO using A549 cell line, has been investigated. CNTs have been widely used for developing various nanomaterial based sensors but the toxicity associated with it had remained a cause of concern in biological applications or where the fabricated material may potentially come in direct contact with body fluids [284]. It has been found that these nanomaterials show a good performance for bio-application including *in situ* monitoring of biomolecules, especially for implantable devices without inducing remarkable deleterious effects. Thus, a systematic investigation relating to toxicity of the hybrid nanomaterials is required to understand the cells activities in order to develop the cell-based biosensors, LOC or implantable biosensor devices. The results presented here indicate that CNT-NiO nanocomposite-based microfluidic sensors as fabricated in the current study would be a better and safer choice for field applications.

Part I: CNT-NiO nanocomposite-based biochip for total cholesterol estimation

In this study, I discuss the fabrication of a novel CNT-NiO nanocomposite-based biochip for total cholesterol estimation. The biochip is immobilized with a bienzyme, composed of cholesterol esterase (ChEt) and cholesterol oxidase (ChOx), and integrated with PDMS microchannels. Unlike the conventional methods, this procedure results in bienzyme functionalization through carboxylation and amidation of the CNT-NiO nanocomposite that serves as the sensing interface.

6.2 Experimental

6.2.1 Cell proliferation studies

The effect of CNT, NiO nanoparticles or CNT-NiO nanocomposite on human cell line is studied using Methyl Thiazol Tetrazolium (MTT) assay and bright field microscopy. The lung epithelial cancer cell line A549 is used as a test cell line. The A549 cells were procured from NCCS, Pune, India. The cells are maintained in complete growth medium (RPMI -1640+10% FBS) at 37°C under humidified 5% CO₂ environment. For the assay, cells are plated at 5×10³ cell/well in 96-well tissue-culture plate and are allowed to attach for about 24 hours. Next day, the medium on the plated cells is replaced with fresh growth medium supplemented with CNTs, NiO or CNT-NiO nanocomposite. The nanoparticles of NiO, CNTs (1mg/ml) or their composite made of NiO and CNTs in the ratio 49:1 ratio were dispersed in de-ionized water by continuous sonication. These nanoparticles suspensions were kept at room temperature for 1 h to allow the undispersed material to settle down. Prior to the addition of dispersed nanoparticles to the growth medium, the nanoparticles are again dispersed by sonication using sonicator bath at room temperature (10 min at 40 W). The dispersed nanoparticles are added to the cell growth medium at various concentrations of 50, 25, 12.5 and 6.25 µg/ml.

After incubating for 24 hours, the medium on cells are replaced with RPMI-1640 medium containing MTT. The cells are further incubated for 1-2 hours at 37°C to allow reduction of MTT dye to formazan crystals. The cells are also observed under an inverted microscope prior to MTT addition and about 1-2 h later before solubilisation of cells with dimethyl sulfoxide (DMSO). The cells are solubilized in 100 µl of DMSO, followed by absorbance measurement at 540 nm. The absorbance value gives a measure of cell proliferation. The relative proliferation is calculated with respect to cells not exposed to any kind of nanoparticles. In each experiment, every treatment group is replicated in three independent wells. Each experiment is repeated three times, and the average proliferation was calculated.

6.2.2 Fabrication of microfluidic biochip platform

The CNTs (90%) are synthesized by catalytic CVD as discussed in Chapter 3. I have discussed the synthesis of CNT-NiO nanocomposite and modified microelectrode fabrication in the Material and Method Section: 3.3.8 (Chapter 3). A mixture of ChEt (1 mg/ml) and ChOx (1 mg/ml) in a 1:1 ratio is spread onto the CNT-NiO/ITO microelectrode via physical absorption [Figure 6.1.1]; the electrode is then kept in a humid chamber for 4 h at 4°C. The carboxyl-terminated CNTs and the NiO nanoparticles are respectively, negatively and positively charged resulting in increased electrostatic interactions. However, the carboxylic groups can undergo an amidation reaction with the amino acids of proteins. One approach to covalently bind proteins or enzymes utilizes the diimide-activated amidation of carboxylic acid functionalized carbon nanotubes. The COOH terminal group is activated using EDC (0.4 M) as the coupling agent and NHS (0.1 M) as the activator. The formation of strong covalent (C-N) amide bonds between the COOH groups of the CNTs and the NH₂ groups of the bienzyme [Figure 6.1.1] is confirmed via XPS studies. It is possible that the nNiO molecules with a high isoelectric point (an IEP of 10.0) interact with the bienzyme directly through electrostatic interactions due to their low IEP (5.5).

A PDMS microchannel slab is sealed temporarily with the ITO glass substrate containing the modified CNT-NiO and ChEt-ChOx electrodes [Figure 6.1.1]. The photograph of the fabricated microfluidic nanobiochip for cholesterol detection is shown in Figure 6.1.1(a). Figure 6.1.1 (b) shows the enlarged view of optical microscopic image of this microfluidic nanobiochip. The PDMS surface provides an adhesive layer that plays an important role, making the bonding with the glass substrate irreversible through weak *Van der Waal's* forces. The bare ITO acts as the counter electrode (CE), and the ChEt-ChOx/CNT-NiO/ITO bioelectrode is used as a sensor for total cholesterol detection. The glass substrate contained three electrodes and PDMS microchannels are embedded onto the same biochip.

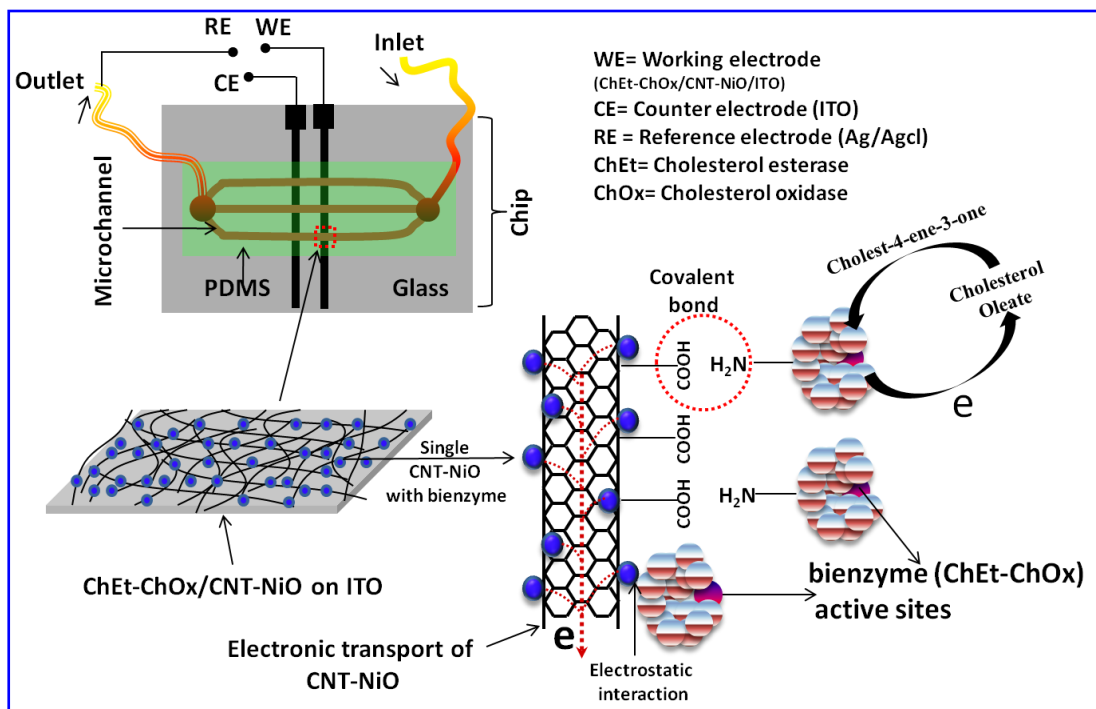


Figure 6.1.1 The schematic of the microfluidic biochip used for total cholesterol detection (the ordered arrangement of this microsystem is assumed).

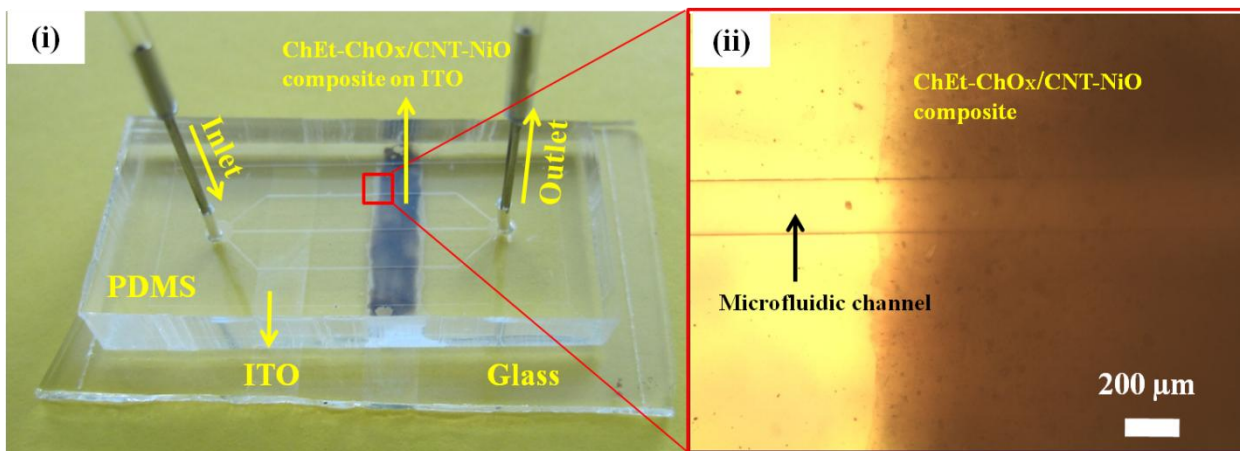


Figure 6.1.2(a) The photograph of the microfluidic biochip for cholesterol detection and (b) An enlarged view of the microfluidic channel.

3 Results and discussions

6.3.1 XRD studies

To confirm the formation of the nanocomposite (CNT-NiO) on the microfluidic electrode, X-ray diffraction (XRD), Raman spectroscopy, X-ray photoelectron spectroscopy (XPS), and zeta potential and electrochemical studies were performed. The XRD studies of the NiO-modified CNT [Figure 6.1.3(i)] revealed the purity and crystallinity of the synthesized NiO nanoparticles with the face-centered cubic (fcc) configuration (a) (4.1 Å) and space group $Fm\bar{3}m$ (225) (JCPDS Card No. 78-0423). Figure 6.1.3(i) reveals a peak at 26° (2θ value) due to the (002) plane (JCPDS Card No. 75-1261) of the CNTs. However, the peak intensity of the CNTs is lower compared to the other peaks due to the presence of defects. The other peaks observed in the diffraction pattern are attributed to the (111), (200), (220), (311), and (222) planes of the cubic NiO. The peak intensity observed for the (200) plane at 2θ (43.3°) is higher than that of the (111) plane, indicating that the growth is mainly dominated by the (200) facet. The d_{200} value of 0.20 nm corresponds to the hkl (200) plane.

6.3.2 Raman studies

The Raman studies [Figure 6.1.3(ii)] show several bands at 532 nm (the excitation wavelength). The vibrational band of NiO (spectra (a)), arising due to one phonon (1P) sampling at 494 cm^{-1} , corresponds to transverse optical (TO) mode. The two-phonon (2P) peak observed at approximately 746 cm^{-1} is assigned to the 2TO and 2LO (longitudinal optical) modes (at approximately 1027 cm^{-1}). The band observed at approximately 713 cm^{-1} exhibits lower intensity at room temperature (298 K), indicating the presence of NiO. In spectra (b), two sharp intense peaks attributed to G (graphite) and D (disorder) bands of CNT at 1342 cm^{-1} and 1580 cm^{-1} , respectively, can be observed. The 2D band is found at 2695 cm^{-1} (the second order of the D band). A small feature near 1617 cm^{-1} can be assigned to the G2 or D band. The peaks pertaining to the G+D band (approximately 2942 cm^{-1}), as well as a small peak approximately at 2450 cm^{-1} , can also be observed. The tangential G band (approximately 1580 cm^{-1}), derived from the graphite-like in-plane mode, splits into two distinct bands attributed to G1 (1577 cm^{-1}). The G2 (1610 cm^{-1}) peak arises due to changes in the curvature of the inner and outer cylinders of CNTs.

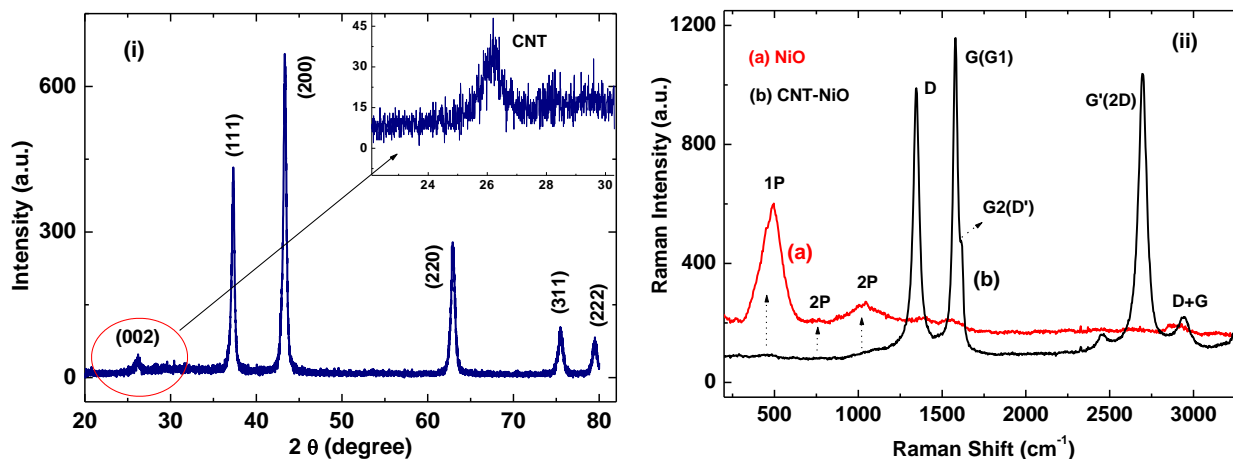


Figure 6.1.3(i) The X-ray diffraction pattern of CNT-NiO and (ii) the Raman spectroscopy spectra of (a) NiO nanoparticles and (b) CNT-NiO.

6.3.3 XPS studies

Figure 6.1.4(i) shows an XPS wide-scan spectrum obtained for the CNT-NiO/ITO (subfigure a) and ChEt-ChOx/CNT-NiO/ITO (sub-figure b) electrodes. The peaks found at 284.6 and 530.6 eV are attributed to the C1s and O1s of the COOH-functionalized CNTs. In spectrum (b), the characteristic peak observed at 399 eV is attributed to the presence of N1s in the bienzyme (ChEt-ChOx). The additional peaks found at 66.0, 112.6, 777.6, 870.6, and 1009.0 eV are assigned to Ni 3p³, Ni 3S, Ni-Auger, Ni 2p³, and Ni 2P¹, respectively. The Ni 2S peak is due to the incorporation of NiO nanoparticles onto the CNTs. The relative atomic concentrations (%) of carbon, nitrogen, oxygen, and nickel are summarized in Table 6.1.1. The atomic concentration of nitrogen in the ChEt-ChOx/CNT-NiO/ITO bioelectrode was found to be 9.93%. This result indicates that the CNT-NiO/ITO surface facilitates the covalent functionalization of ChEt-ChOx via EDC-NHS chemistry. The XPS spectra of the carbon 1s region of the deposited CNT-NiO electrode [Figure 6.1.4 (ii)] is deconvoluted into characteristic peaks using the Shirley-type baseline and Lorentzian-Doniac-Sunsic curves, with a Gaussian profile. The peak found at 284.1 eV is graphitic (sp²), the peak at 285.2 eV is due to a defect (sp³), the peak at 286.3 eV is attributed to a hydroxyl group, the peak at 287.3 eV is assigned to a carbonyl group and the peak found at 288.2 eV is attributed to the carboxyl group (-O-C=O).

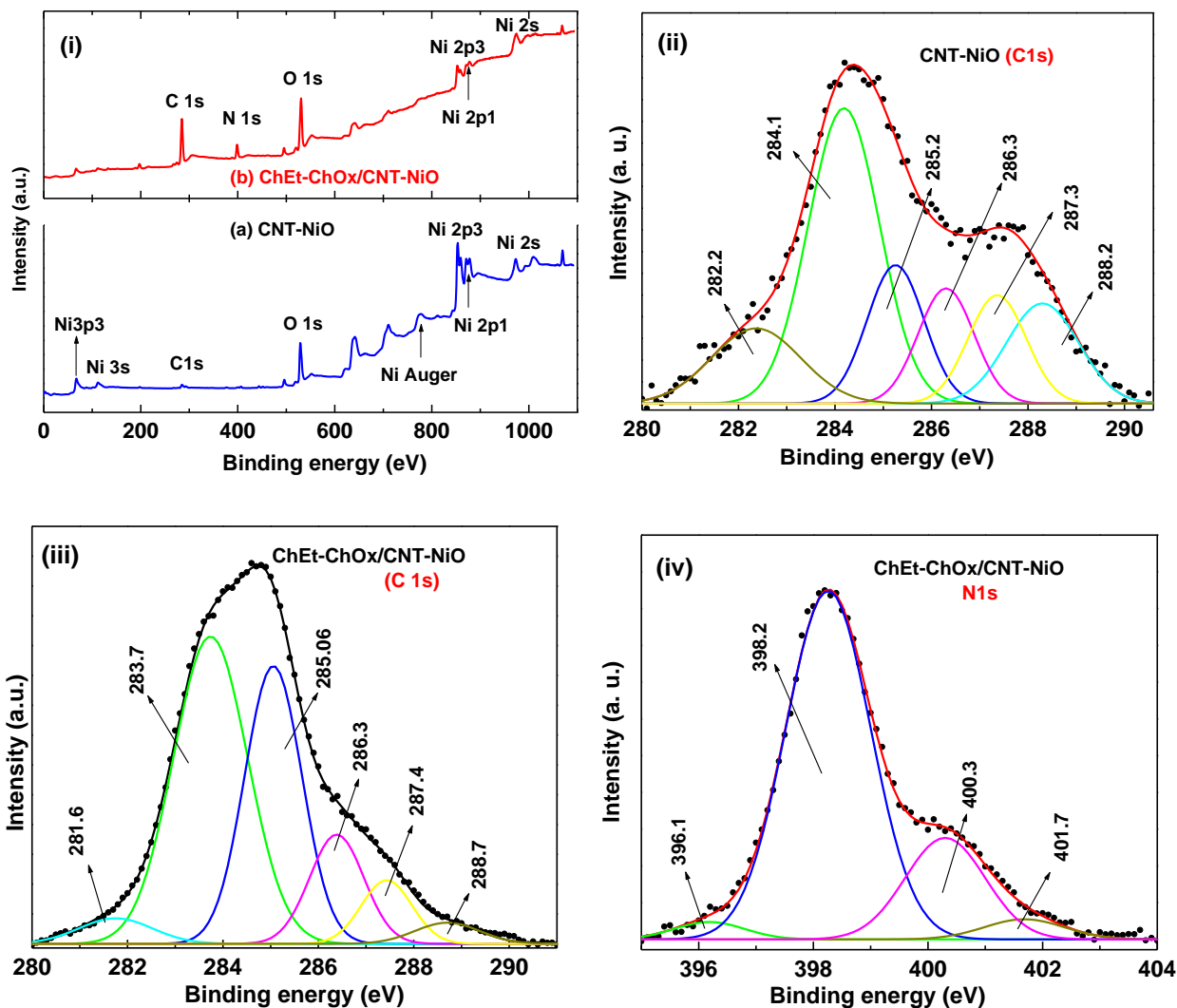


Figure 6.1.4 (i) The wide-scan X-ray photoelectron spectra (XPS) of various films. (ii) The XPS spectra of the C1s region of the CNT-NiO film after deconvolution; (iii) the C1s region of the ChEt-ChOx/CNT-NiO/ITO film; and (iv) the N1s core-level spectra of the ChEt-ChOx/CNT-NiO/ITO film.

In the ChEt-ChOx/CNT-NiO/ITO electrode [Figure 6.1.4(iii)], the binding energy peaks corresponding to functional groups are the same as those clearly visible in the spectra of the CNT-NiO/ITO electrode. The observed lower intensities of the ChEt-ChOx electrode, as well as the slight shift in its binding energy positions [Figure 6.1.4(iii)] compared with those of the CNT-NiO/ITO electrode [Figure 6.1.4(ii)], may perhaps be attributed to the covalent attachment of the bienzyme molecules to the film surface. In particular, the percentage of COOH groups decreased to 2.7% from the CNT-NiO/ITO film's value of 13%, indicating that most of the COOH functional groups have been used in bienzyme

attachment (ChEt-ChOx). The deconvoluted peak observed at approximately 282 eV in both the spectra may be due to the adsorption of NiO to the CNTs in the sample. In Figure 6.1.4(iv), the typical binding energy peak observed at 398.2 eV is due to the core-level electron of N1s. The peak found at 400.3 eV for the ChEt-ChOx/CNT-NiO bioelectrode corresponds to the amide nitrogen (CO-NH) present in the bienzyme molecules, whereas the peak observed at 401.7 eV, attributed to the $\equiv\text{N}$ species, confirms covalent functionalization.

Table 6.1.1 The atomic concentration (%) of the elements C, Ni, O, and N present in the CNT-NiO/ITO and ChEt-ChOx/CNT-NiO/ITO films obtained from XPS analysis.

Elements/atomic concentration (%)	C	Ni	O	N
nNiO-MWCNT/ITO	12.52	33.72	53.76	
ChEt-ChOx/nNiO-MWCNT/ITO	59.11	3.88	27.08	9.93

6.3.4 Zeta potential measurements

The value of the average surface potential of colloidal NiO nanoparticles is estimated to be +22.7 mV using zeta potential measurements. This value reveals that the NiO nanoparticles are positively charged [Figure 6.1.5(a)]. The average surface potential of the CNTs is measured to be -6.7 mV, indicating the presence of negatively charged groups on the sidewalls of the carbon nanotubes [Fig. 5.1.5(b)]. The positively charged NiO provides strong electrostatic interactions that link it to the negatively charged CNTs.

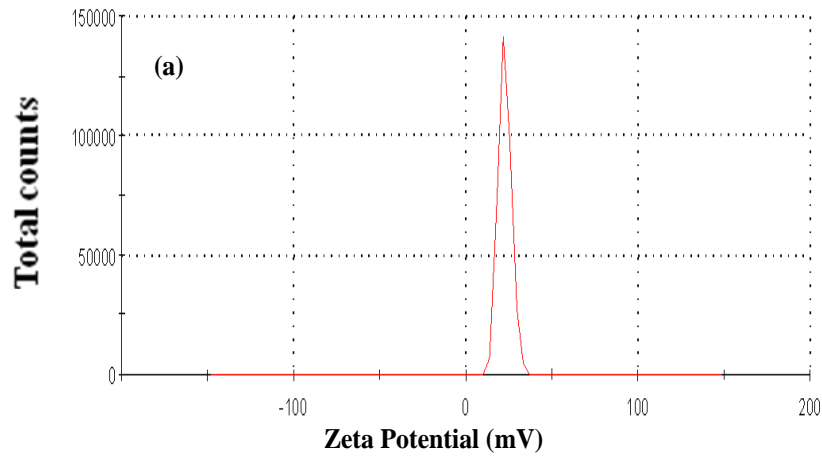


Figure 6.1.5(a) Zeta potential studies of dispersed NiO nanoparticles in water solution

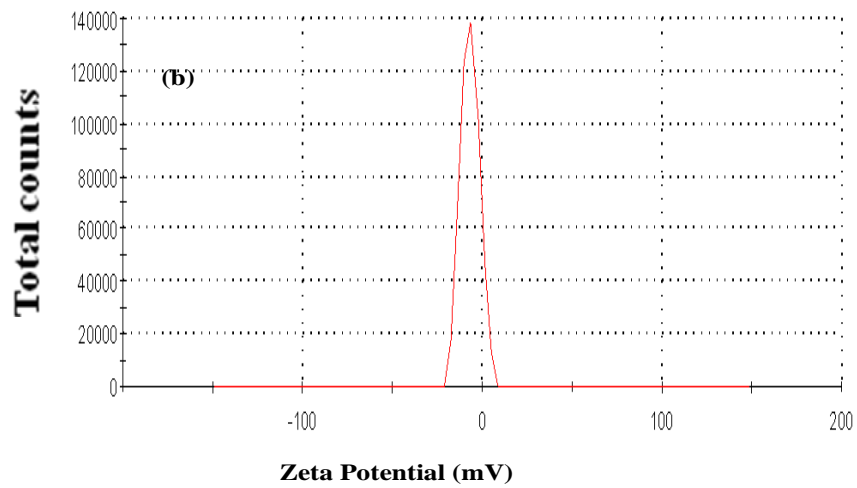


Figure 6.1.5(b) Zeta potential studies of dispersed CNTs in water solution

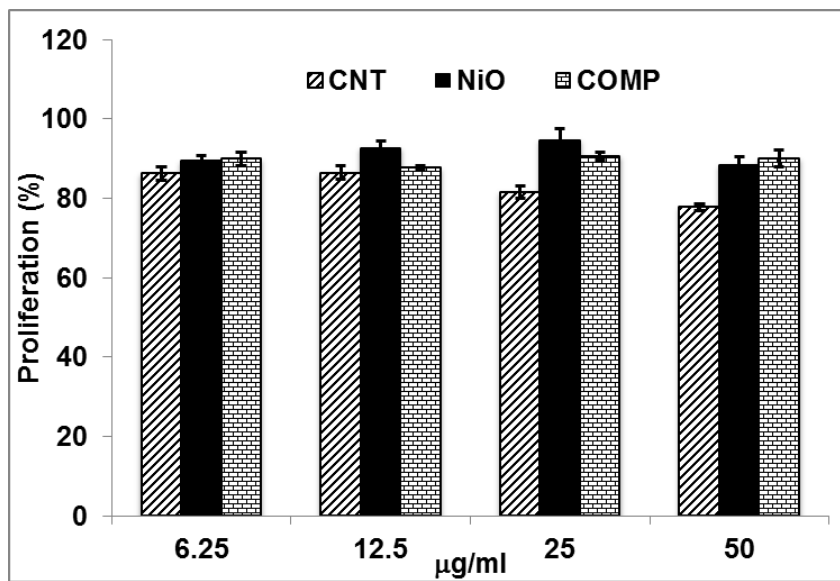


Figure: 6.1.6 CNT-NiO composite has reduced toxicity compared to CNTs alone. The A549 cells plated at 5×10^3 cells per well in 96 well tissue culture plate were exposed to growth medium containing indicated concentrations of nanoparticles for 24 hrs. The cells were treated with MTT for 1 hr and then relative reduction of MTT to formazan by cells was calculated. The relative reduction of MTT is presented as % proliferation with respect to cells not exposed to any nanoparticles (Ctrl). The error bars represent \pm average deviation (AVEDEV).

6.3.5 Cytotoxicity studies

The MTT assay reveals that nanoparticles of NiO and CNT-NiO nanocomposite had much reduced negative influence on the well being of A549 cells. Consequently the ability of cells to reduce MTT to formazan at all the concentrations has been investigated in comparison with CNTs [Figure 6.1.6]. The relative proliferation % is estimated with respect to growth of the control cells (Ctrl) that are not exposed to any nanoparticle. Though, the MTT assay [Figure 6.1.6] does not show much difference among the cells exposed to CNT, NiO or NiO-CNT composite upto 12.5 µg/ml concentration, further increase in the concentration showed incremental detrimental effect in case of CNT while others appear to have very little effect. The toxicity of CNT is more evident from the pattern of formazon crystal formation in CNT exposed cells as compared to NiO or CNT-NiO composite exposed cells. The CNT exposed cells progressively shows more diffuse formazon crystal formation and appearance of extracellular debris with increase in CNT concentration while NiO and NiO-CNT composite exposed cells are relatively unaffected in the concentration range studied [Figure 6.1.7].

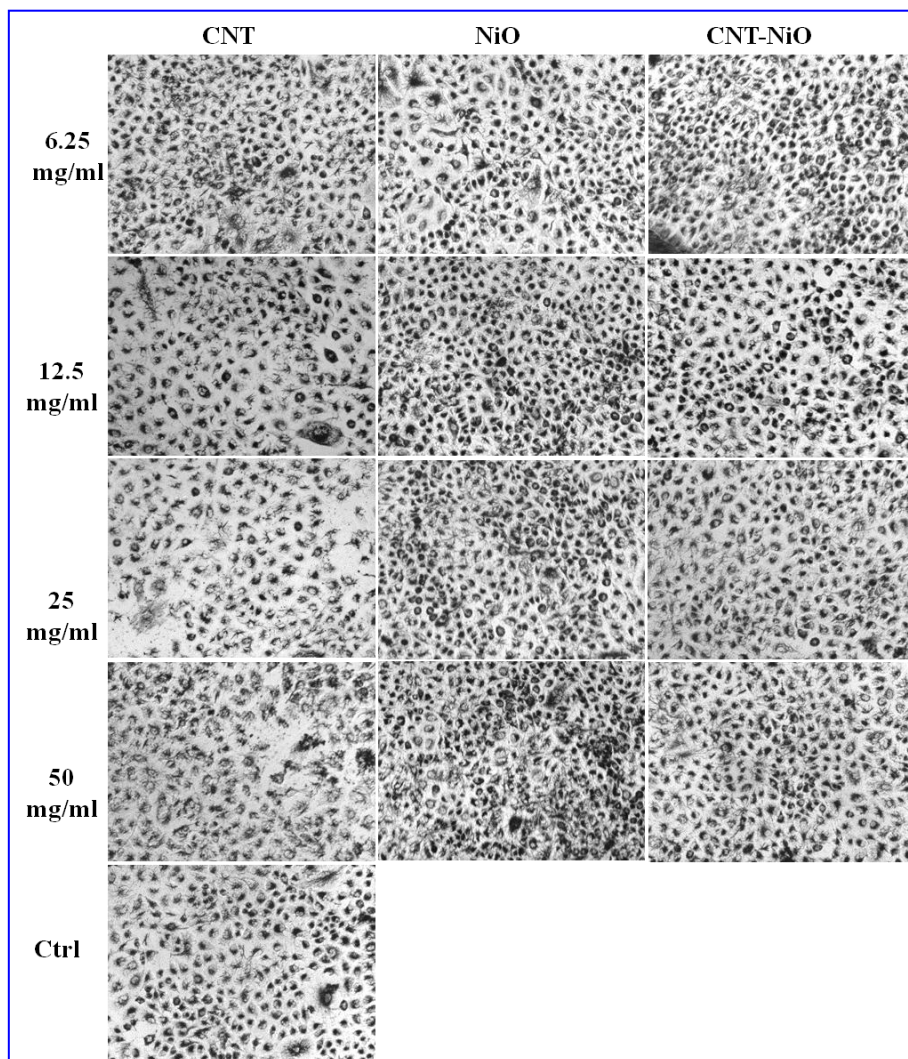


Figure 6.1.7 CNTs exposure significantly attenuates the ability of A549 cells to reduce MTT dye to formazan compared to NiO nanoparticles or CNT-NiO composite. A549 cells incubated with indicate concentration of CNTs, NiO nanoparticles or NiO-CNT composite for 24 hours and incubated in the presence of 1 mg/ml MTT for 1h. The cells are imaged using Nikon eclipse microscope at 100x magnification

6.3.6 Morphological studies analysis

The SEM studies [Figure 6.1.8] have been carried out for morphological observations at an accelerating voltage of 20 kV. The SEM image [Figure 6.1.8(i)] shows COOH-functionalized CNTs that are randomly oriented on the ITO substrate. The *in situ* incorporated CNTs along with deposited NiO nanoparticles are shown in Figure 6.1.8(ii). The NiO nanoparticles appear to be attached to the CNT, which are not agglomerated, indicating that the presence of NiO nanoparticles prevented their agglomeration. Figure 6.1.8(iii) shows the SEM image of NiO nanoparticles.

The TEM image shows spherical NiO nanoparticles with an average size <70 nm [Figure 6.1.9(i)]. The high-resolution image of the individual CNTs show outer and inner diameters of 34 and 12 nm, respectively. The selected area electron diffraction (SAED) pattern shows that graphitic (002) and (004) reflections are present in the CNTs [the inset in [Figure 6.1.9 (ii)]].

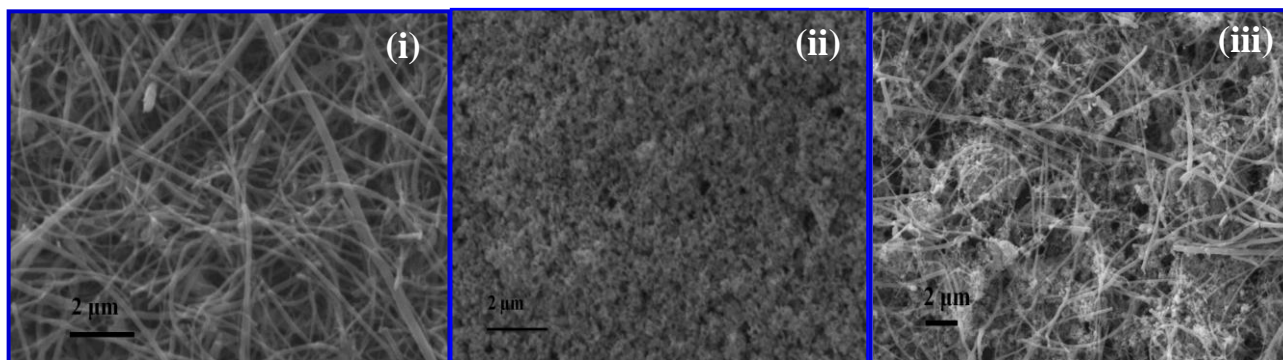


Figure 6.1.8 (i) SEM studies of COOH functionalized CNTs, (ii) CNT-NiO film on ITO coated glass substrate and (iii) SEM image of NiO nanoparticles.

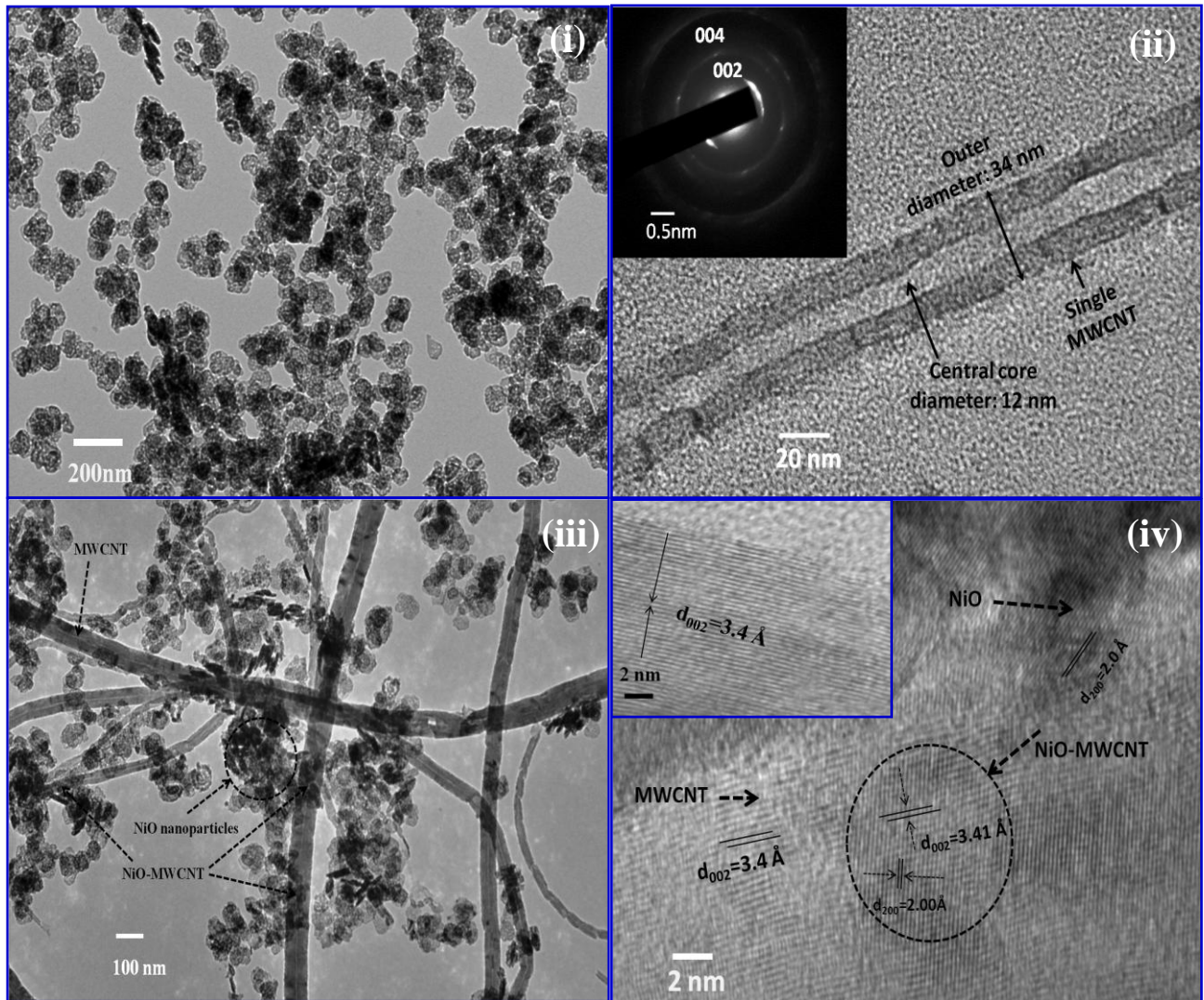


Figure 6.1.9 The HR-TEM analysis of (i) the NiO nanoparticles, (ii) an individual CNTs (inset: the SAED pattern of the CNTs), (iii) the CNTs modified with NiO nanoparticles, and (iv) an atomic-scale image of a CNT-NiO (inset: lattice fringes of the CNTs).

Figure 6.1.9(iii) shows that the well-dispersed COOH-functionalized tubular-shaped CNTs are entangled with NiO nanoparticles and randomly oriented. It appears that some of the NiO nanoparticles are aggregated on the CNTs surfaces. These CNTs are multi-walled in structure. A few NiO nanoparticles can be observed inside the carbon nanotubes [Figure 6.1.9(ii)]. The length range of the CNTs is several tens of micrometers, and they have an external diameter of approximately 20-80 nm. From the atomic-scale image of the CNT-NiO [Figure 6.1.9(iv)], it can be concluded that this nanocomposite is crystalline in nature, with an interlayer spacing of 3.41 Å (d_{002} for CNTs, shown in the subfigure inset, iv). The

lattice fringe spacing of the NiO nanocrystal is estimated to be 2.0 Å, which agrees with the results of the XRD studies. These results clearly reveal a successful and predictable formation of the CNT-NiO composite that can be used to fabricate the desired biochip.

6.3.7 Electrochemical properties

The electrochemical behaviour of the biochip, both before and after undergoing surface modification by the bienzyme (ChEt-ChOx), is investigated using CV in PBS, pH 7.0 containing ferro/ferricyanide (as a mediator) at a scan rate of 30 mV/s [Figure 6.2.1(i)]. The CV of the NiO/ITO electrode exhibits well-defined oxidation/reduction peaks in the -0.8 V to +0.9 V potential range, with a peak-to-peak separation (ΔE) of 0.115 V (a). After incorporation of NiO nanoparticles into the CNTs (1.0 %) (b), the electrochemical current increases to 28.0 μ A because CNTs are more conductive than the NiO/ITO electrode alone (23.0 μ A). The large number of edge plane sites along the surface of the tubes, as well as the presence of defects in the CNT, result in enhanced electrochemical behavior. In addition, the outer and inner surfaces of the carbon nanotubes are accessible to the electrolyte solution containing redox species ions and acts as pathways for the transport of electrons toward the electrode, resulting in an enhanced faradic current. In case of the CNT-NiO (2.0%) electrode (c), the peak current increases to 31.2 μ A. This increase is due to the presence of a large number of defect sites in the CNTs, leading to enhanced heterogeneous electron transfer. The resulting current can be controlled by varying the CNTs concentration (2.0%) in the nNiO matrix. Furthermore, a redox current of 14.0 μ A is obtained for the CNT-NiO/ITO electrode after bienzyme functionalization (d), which is lower than that of the CNT-NiO/ITO electrode; the bienzyme has insulating properties that block the transport of electrons toward the electrode. The magnitudes of the cathodic and anodic peaks increases linearly with the square root of the scan rate (30 to 100 mV s⁻¹), indicating a diffusion-controlled or quasi-reversible process and favourable electron transfer kinetics [Figure 6.2.2]. The values of the slope, intercept, and correlation coefficient of the ChEt-ChOx/CNT-NiO/ITO bioelectrode can be estimated using Eq. (6.1.1)-(6.1.4).

$$I_{pa} = 6.71 \mu\text{A} + 3.55 (\mu\text{AmV}^{-1}\text{s})^{1/2} [\text{scan rate (mV/s)}]^{1/2}; R^2 = 0.999 \quad \text{Eq. 6.1.1}$$

$$I_{pc} = -0.137 \mu\text{A} - 2.56 (\mu\text{AmV}^{-1}\text{s})^{1/2} [\text{scan rate (mV/s)}]^{1/2}; R^2 = 0.997 \quad \text{Eq. 6.1.2}$$

$$E_{pa} = 0.368 \text{ V} + 1.95 \text{ s}^{1/2} [\text{scan rate (mV/s)}]^{1/2}; R^2 = 0.998 \quad \text{Eq. 6.1.3}$$

$$E_{pc} = -0.235 \text{ V} - 1.54 \text{ s}^{1/2} [\text{scan rate (mV/s)}]^{1/2}; R^2 = 0.993 \quad \text{Eq. 6.1.4}$$

The anodic peak potential (E_{pa}) varied linearly with the natural logarithm of the scan rate ($\ln v$) and followed Eq. (6.1.5).

$$E_{pa} = 0.232 \ln v + 1.509 \quad \text{Eq. 6.1.5}$$

The surface concentration of the ChEt-ChOx/CNT-NiO/ITO bioelectrode was estimated using Laviron's theory Eq. (6.1.6), and the slope is given by Eq. (6.1.7):

$$RT/\alpha nF = 0.232 \quad \text{Eq. 6.1.6}$$

$$I_p = n^2 F^2 I^* / 4RT \quad \text{Eq. 6.1.7}$$

where α is the transfer coefficient, n is the number of electrons transferred (1 in this case), F is the Faraday constant (96485.34 C/mol), I^* is the surface concentration of the ChEt-ChOx/ CNT-NiO/ITO bioelectrode, v is the scan rate (mV s^{-1}), R is the gas constant ($8.314 \text{ J mol}^{-1} \text{ K}^{-1}$), and T is the absolute temperature (298 K). The i_p/v value can be calculated from the slope of the i_p versus v plot. The total surface concentration of the ChEt-ChOx/CNT-NiO/ITO bioelectrode is found to be $11.07 \times 10^{-6} \text{ mol/cm}^2$, indicating a high coverage of ChEt-ChOx on the CNT-NiO/ITO surface.

The flow rate is optimized for the ChEt-ChOx/CNT-NiO microfluidics biochip using the chronoamperometric technique [inset: Figure 6.2.1(ii and iii)]. The chronoamperometric current response of the CNT-NiO/ITO (ii) and ChEt-ChOx/CNT-NiO/ITO (iii) electrodes is obtained as a function of the flow rate (0.01-10 $\mu\text{L}/\text{min}$) and the corresponding current versus time, and the plots are shown in inset: Figure 6.2.1(ii and iii respectively). The chronoamperometric current increases for the CNT-NiO/ITO electrode with an increasing flow rate of the buffer solution. The maximum current is 0.1 $\mu\text{L}/\text{min}$, after which it reaches saturation (ii). This pattern is perhaps due to diffusivity of the redox species, which increases with a higher buffer flow rate because of the improved mass transport. At a flow rate of 0.1 $\mu\text{L}/\text{min}$, the response time of the microfluidics electrode is 2 s, after which, the amperometric current becomes saturated [inset: Figure 6.2.1(ii)].

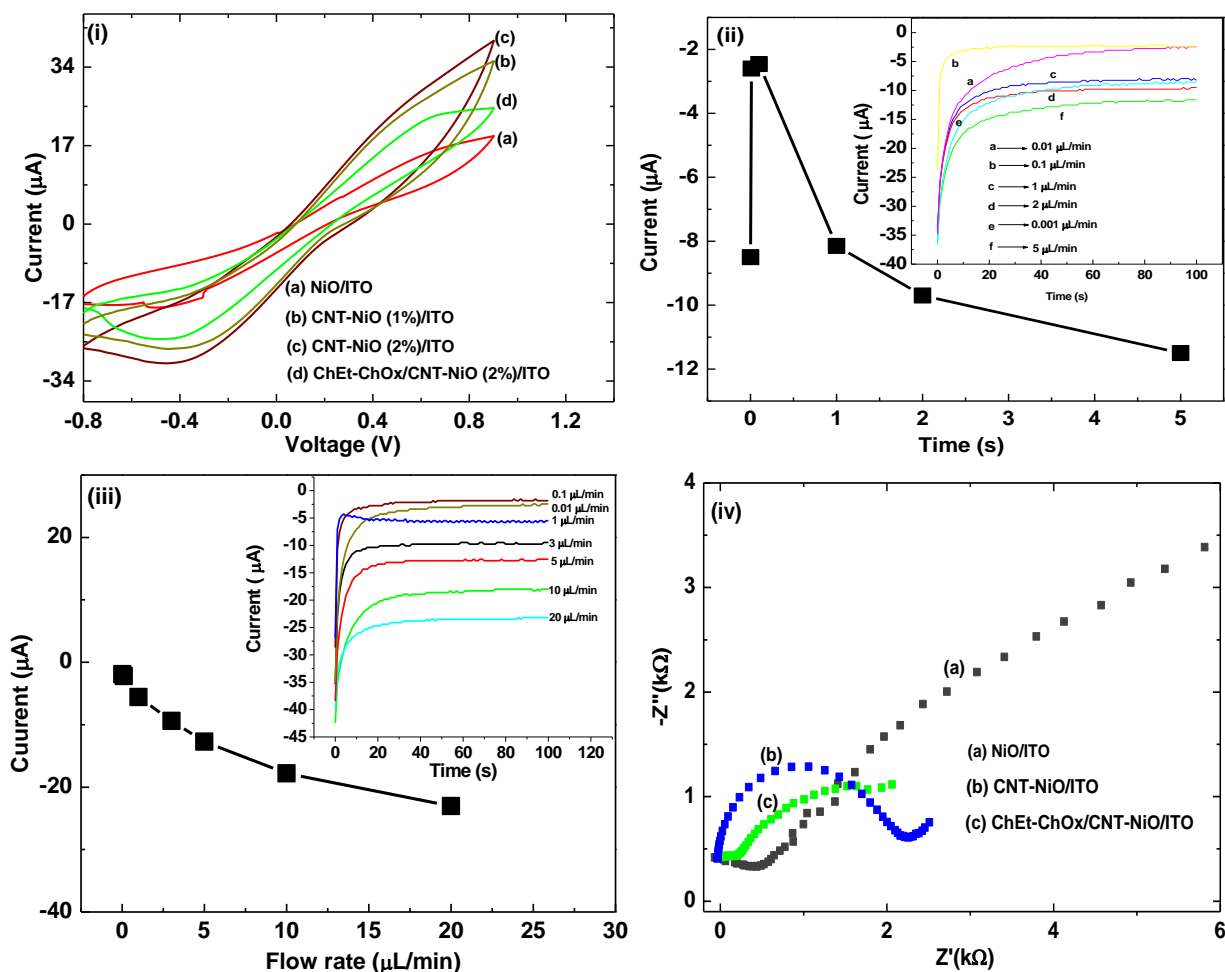


Figure 6.2.1(i) CV of different electrodes in PBS solution (50 mM, pH 7.0, 0.9% NaCl) containing 5 mM $[\text{Fe}(\text{CN})_6]^{3-/4-}$, (ii) the chronoamperometric (current-time) response of CNT-NiO/ITO electrode as a function of flow rate [0.01-5 $\mu\text{L}/\text{min}$], inset: current vs flow plot, (iii) the chronoamperometric response of ChEt-ChOx/CNT-NiO/ITO electrode as a function of flow rate [0.01-20 $\mu\text{L}/\text{min}$], inset: current vs flow plot and (iv) EIS spectra of electrodes.

After its ChEt-ChOx functionalization, the CNT-NiO/ITO electrode (iii) shows a high initial current decrease as the flow rate is increased [inset: Figure 6.2.1(iii)]. This response may be attributed to the retention time of the biocatalytic reaction. As the flow rate increases, the retention time becomes shorter, resulting in decreased response current. It appears that the cholesterol molecules move away from the biochip-sensing surface prior to the completion of the biochemical reaction. The diffusion time becomes maximum (approximately 3 s) at a flow rate of 1.0 $\mu\text{L}/\text{min}$, so the chronoamperometric measurements are carried out at this optimum flow rate. These results indicate that the fluid flow through the rectangular microchannel is laminar due to the low Reynolds number (0.082).

EIS studies have been carried out by applying a small-amplitude sinusoidal AC signal (with a bias voltage of 0.35 V) as a function of the frequency (0.01 to 10^5 Hz) [Figure 6.2.1(iv)] using a frequency response analyzer (FRA). The electrical impedance (Z) is the ratio of the incremental change in voltage, $V(t)$, to the resulting change in current, $I(t)$, and Z is given by Eq. (6.1.8).

$$Z = \frac{V(t)}{I(t)} = \frac{1}{Y} = \frac{V_0 \sin(2\pi ft)}{I_0 \sin(2\pi ft + \phi)} \quad \text{Eq. 6.1.8}$$

where, V_0 and I_0 are respectively, the maximum voltage and current signals, f is the frequency, t is the time, ϕ is the phase shift between the voltage-time and current-time function, and Y is the complex admittance. The impedance is described either by the modulus $|Z|$ and the phase shift ϕ or by its real (Z') and imaginary (Z''). The most frequently used equivalent circuit for modeling the EIS experimental data is the Randles circuit [inset: Figure 6.2.1(iv)] which contains the electrolyte (R_s) in series with a double-layer capacitance (C_{dl}), charge-transfer resistance (R_{CT}), and Warburg impedance (Z_w). The Nyquist plot includes a semicircle region lying on the real axis, which is followed by a straight line. The linear portion ($\psi = \pi/4$), observed in the low-frequency range, implies a mass-transfer limited process; the semicircle portion, observed in the high-frequency range, implies a charge-transfer-limited process. The imaginary component decreases to zero at a high frequency because it offers no impedance. As the frequency drops, the capacitance (C_{dl}) offers higher impedance and the current flows primarily through the R_{CT} and R_s segments. The R_{CT} value of the CNT-NiO/ITO electrode is 1.9 k Ω (shown in curve b), which is lower than the value of the NiO/ITO electrode (19 k Ω ; curve b).

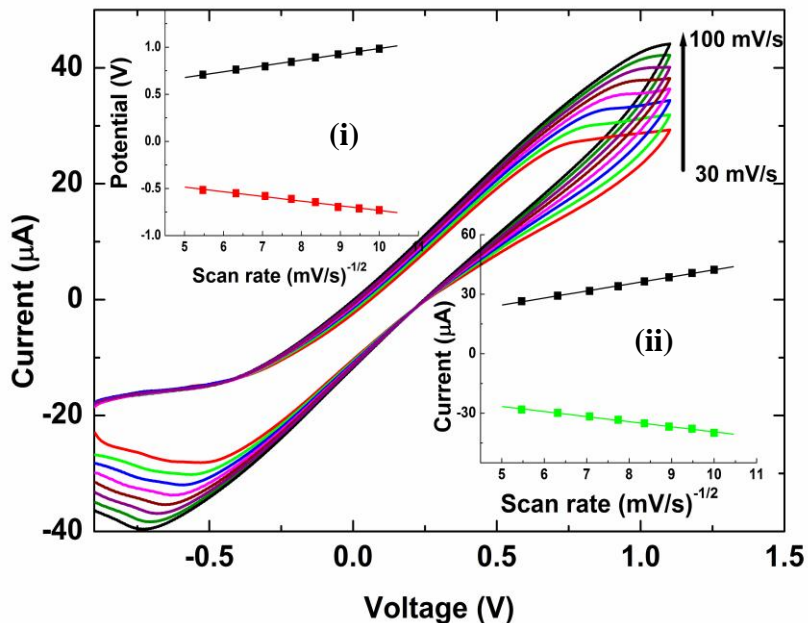


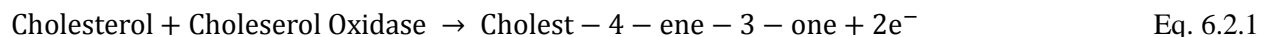
Figure 6.2.2 CV studies ChEt-ChOx/CNT-NiO/ITO bioelectrode as a function of scan rate [30-100 (mV/s)], inset: (i) anodic and cathodic peak current vs square root of scan rate and (ii) anodic and cathodic peak current vs square root of scan rate.

This result is due to the presence of the CNTs that causes enhanced catalytic activity and favorable electron-transfer kinetics; improved kinetics leads to a greater diffusion of the redox species ions from the bulk solution to the electrode surface. The R_{CT} value of the ChEt-ChOx/CNT-NiO/ITO bioelectrode increases to 3.9 k Ω (curve c), a value greater than that of the CNT-NiO/ITO (curve b) electrode, implying that the bienzyme absorbed onto the CNT-NiO surface provides steric hindrance to the diffusion of electrons through the electrode-electrolyte interface.

6.3.8 Chronoamperometric response studies

The chronoamperometric response of the biochip (ChEt-ChOx/CNT-NiO/ITO) has been measured [Figure 6.2.3(i)] as a function of the cholesterol oleate concentration (0.25-12.93 mM). During this chronoamperometric measurement, the solutions containing various concentrations of cholesterol oleate in PBS are injected through an inlet of the microchannel at regular intervals. The sensing potential is maintained at -0.4 V during the measurements, when the specific oxidative reaction of the bienzyme ChEt-ChOx was dominant. The chronoamperometric current of the microfluidics biochip increases linearly in the range of 0.25-12.93 mM, after which, it gets saturated [inset: Figure 6.2.3(i), curve a]. First, esterified cholesterol is converted into fatty acids and cholesterol in the presence of ChEt. ChOx molecules containing flavin-adenine-dinucleotide (FAD) sites react with the cholesterol to produce cholesterol-4-ene-3-one and H_2O_2 via catalytic conversion. The produced H_2O_2 further oxidized to H_2O

and oxygen by losing two electrons. These generated electrons (not mediated electrons) are responsible for the enhanced chronoamperometric current, and the current is directly proportional to the concentration of the injected esterified cholesterol. The enzymatic reactions used for total cholesterol detection are given by



A control experiment is conducted using the CNT-NiO/ITO electrode without bienzyme functionalization under similar conditions [inset: Figure 6.2.3(i), curve b]. No significant change in the current response of the CNT-NiO/ITO electrode has been observed with increasing concentrations of esterified cholesterol. These results reveal that the CNT-NiO/ITO electrode surface did not react with the esterified cholesterol molecules, and therefore, the electrochemical current remained unchanged.

In the clinical sample analysis, the response of the biochip (ChEt-ChOx/CNT-NiO/ITO) has been carried out in presence of clinical samples with varying cholesterol concentration. Various cholesterol concentrations are 149, 166, 193, and 230 mg/dl are obtained from a clinical diagnostics laboratory at New Delhi (India). In comparison to the standard cholesterol concentration, it has been observed that the ChEt-ChOx/CNT-NiO/ITO bioelectrode shows minute difference of 0.64-6.77 % during cholesterol detection presence in serum sample [Figure 6.2.3 (iii)]. Thus, these results indicate that this novel biosensor has potential to detect cholesterol directly in human serum sample.

Table 6.1.2 shows characteristics of the fabricated microfluidics biosensor along with those reported in the literature. It can be seen that the CNT-NiO composite-based microfluidic biodevice exhibits a much higher sensitivity ($2.2 \times 10^3 \mu\text{A}/\text{mM}/\text{cm}^2$), lower response time (2 s), lower K_m^{app} (0.22 mM), and more extended linearity (0.25-12.93 mM) than other total cholesterol sensors reported in the literature [285,288-285]. The observed low K_m^{app} value, obtained using the Lineweaver-Burk plot (1/concentration vs. 1/current) and the best linear fit (Table 6.1.2) indicates that ChEt-ChOx has a high affinity for cholesterol oleate and is properly functionalized onto the CNT-NiO surface. The 20-fold higher sensitivity, $2.2 \times 10^3 \mu\text{A}/\text{mM}/\text{cm}^2$, may be due to the integration of the high-aspect-ratio microfluidics device with the CNT-NiO matrix, as well as an improved biofunctionalization of the bienzyme. The composite material (CNT-NiO) results in enhanced electrochemical properties, and the micro-dimensions of the fabricated electrode perhaps cause improved electron diffusion. Additionally, the CNTs provide a channel for electron conduction with long electron mean free paths towards the electrode and thus have the capability to support very large current densities. The detection limit of this nanobiochip is found to be a cholesterol concentration of $0.03 \times 10^{-3} \text{ M}$, which corresponds to a

physiological range of 2.07-6.2 mM in human blood. The comparatively higher detection limit of the ChEt-ChOx/CNT-NiO/ITO microfluidic total cholesterol sensor may be caused by either insufficient electrical conductivity of the nNiO or the morphological changes arising as a result of interactions between the bienzyme (ChEt-ChOx) and the CNT-NiO nanocomposite surface [285].

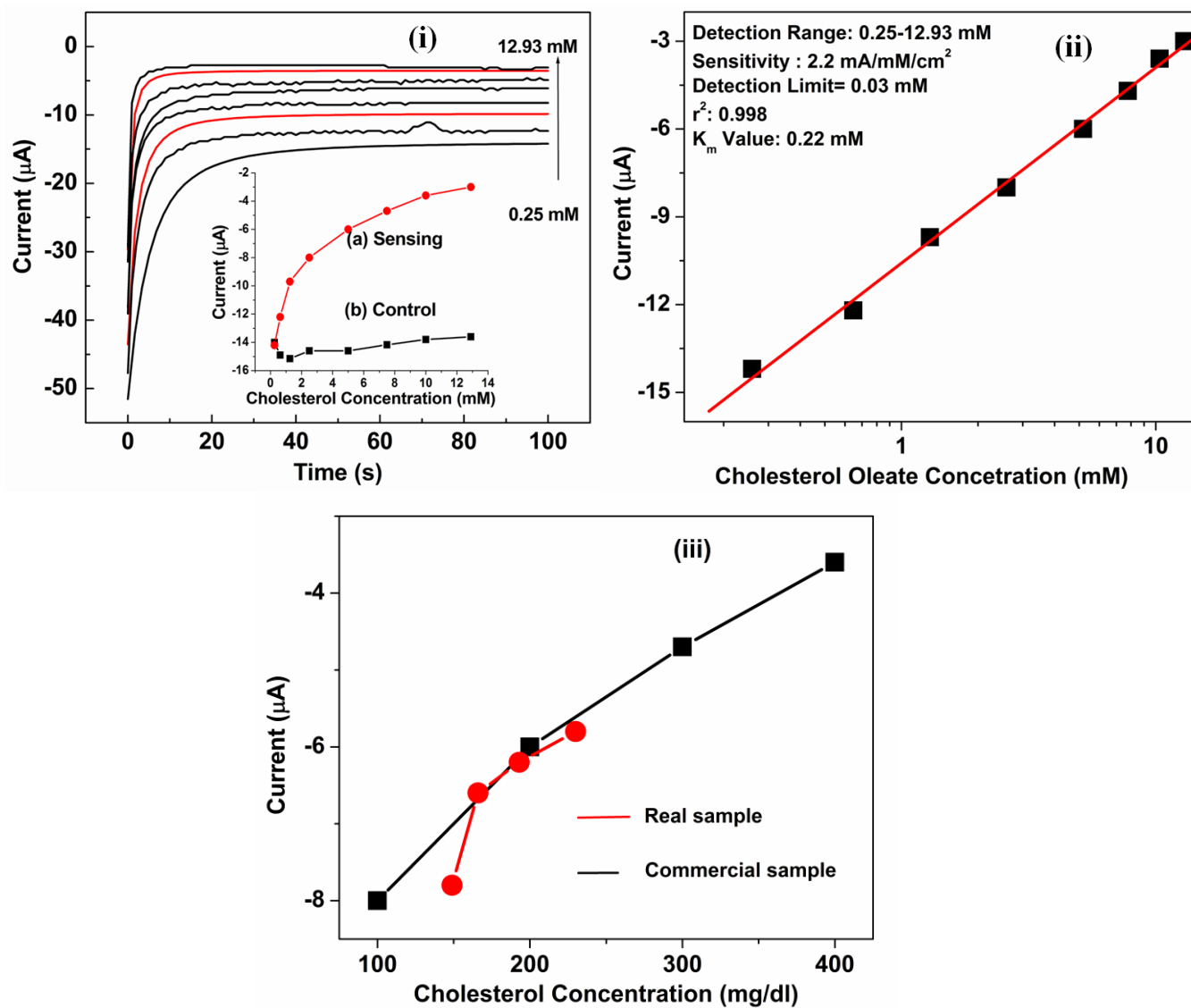


Figure 6.2.3 (i) The chronoamperometric response of the ChEt-ChOx/CNT-NiO/ITO-based biochip as a function of the cholesterol oleate concentration (0.25-12.93 mM) in a PBS solution containing 5 mM of $[\text{Fe}(\text{CN})_6]^{3-/4-}$. The experiment is controlled using a syringe pump attached to the inlet of the microsystem (inset: the response current as a function of the cholesterol concentration obtained for both (a) ChEt-ChOx/CNT-NiO/ITO and (b) CNT-NiO/ITO electrodes). (ii) A calibration plot showing the logarithm of the cholesterol concentration (mM) and the amperometric current of the biochip during sensing. (iii) Serum (real) sample analysis.

Table 6.1.2 The sensing characteristics of the ChEt-ChOx/CNT-NiO/ITO based biochip designed for total cholesterol estimation.

Electrode materials	Microfluidic used	Detection limit (M)	Sensitivity (/mM/ cm ²)	Detection range	K _m Value (mM)	Stability (days)	Ref.
CNT	Yes	0.25×10 ⁻³	0.0512 nA	1.25 -10.0mM	[241]
Anatase-TiO ₂	Yes	0.64×10 ⁻³	0.094 mA	0.64-10.3 mM	0.14 mM	35	Present work
nNiO	Yes	0.64×10 ⁻³	0.12 mA	0.64-10.3 mM	0.16 mM	60	Present work
ZnO	No	37 ×10 ⁻⁹	23.7 μA	1.0 to 500.0 nM	4.7 mM	50	[286]
Pt nanoparticles	No	0.2 ×10 ⁻⁶	2.07 μA	Upto 4.0 μM	5 mM	3	[287]
Polyelectrolyte-MWCNT	No	0.2 ×10 ⁻³	0.559 μA	Upto 6.0 mM	7.17 mM	[288]
Chitosan/silica-MWCNT	No	1 ×10 ⁻⁶	1.55 μA	4.0 μM-0.7mM	0.24 mM	50	[285]
CNT-NiO	Yes	0.03×10 ⁻³	2.2 mA	0.25-12.93 mM	0.22 mM	40	Present Work

6.3.9 Reproducibility studies

The ChEt-ChOx/CNT-NiO/ITO based biochip shows good reproducibility for cholesterol concentrations of 2.59 and 5.18 mM [Figure 6.2.4(i)] as is evidenced by the low standard deviations (RSD) found (4.19% and 2.13%, n=5), indicating good precision. The ChEt-ChOx/CNT-NiO/ITO bioelectrode also shows good repeatability, as evidenced by its low RSD of 1.12% (n = 15) for a cholesterol concentration of 2.50 mM. No significant decrease in the current is observed after 12 uses. In further procedures, the bioelectrode showed slight decreases in its current response possibility due to the denaturation of the biomolecules [Figure 6.2.4(ii)].

6.4.0 Selectivity and stability studies

The selectivity of the ChEt-ChOx/CNT-NiO/ITO bioelectrode is demonstrated using lactic acid (LA), glucose (G), ascorbic acid (AA), uric acid (UA), and other interferents in a buffer solution. The present bioelectrode is highly specific to total cholesterol (5.18 mM) and shows a negligible change in its response current in the presence of other analytes (interferents) [Figure 6.2.4(iii)]. The shelf life of this biochip is determined by measuring the change in the current response at regular 5-day intervals for approximately 3 months; the chip exhibited a 93.7% response after approximately 40 days. The ChEt-ChOx/CNT-NiO/ITO bioelectrode is stored at 4°C when not in use. This integrated microfluidics

nanobiochip reached 92% of its steady-state current in less than 2 s, indicating that a fast electron exchange is occurring between the active sites of the bienzyme and the CNT-NiO/ITO electrode.

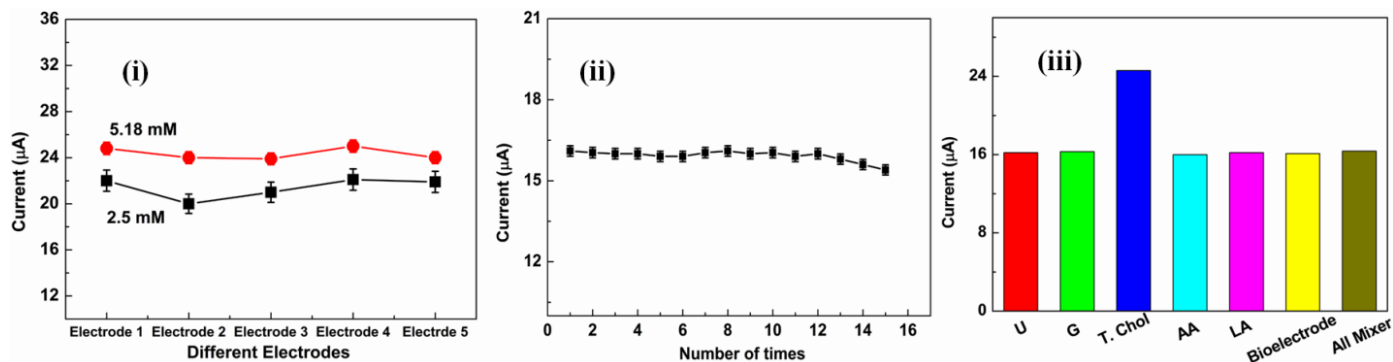


Figure 6.2.4(i) Reproducibility studies of the ChEt-ChOx/CNT-NiO/ITO microfluidics bioelectrodes under similar conditions. (ii) Stability studies of the ChOx-ChEt/CNT-NiO/ITO bioelectrode and (iii) selectivity studies of the ChOx-ChEt/CNT-NiO/ITO-based biochip.

6.5 Conclusions

In summary, the miniaturized microfluidics-integrated biochip based on a CNT-NiO composite allows for the rapid detection of biomolecules at a low cost. The NiO serves as a support for the dispersion of CNT and helps exfoliate smaller bundles or individual nanotubes. The covalent functionalization through reactions of desired chemical groups onto the π -conjugated skeleton of this CNT-NiO composite matrix offers considerable advantages for the development of a nanobiochip to detect molecules such as cholesterol. In particular, the COOH groups on the CNT provide simple biofunctionalization and a higher loading capacity of biomolecules on the microfluidic transducer surface. The 9.3% of the carboxyl groups present on the CNT-NiO surface are used to covalently bind with the bienzyme. The synergistic electrocatalytic activity of the CNT provides straight conducting pathways for carriers such as electrons and ions, resulting in a higher sensitivity than NiO-based biochips. This bienzyme functionalized and integrated microfluidic biochip is highly sensitive to cholesterol oxidation and is both highly reproducible and stable, allowing it to be utilized for total cholesterol monitoring. This microfluidic platform exhibits improved detection limits and faster response times. This highly efficient composite microfluidics biochip could be used to monitor low-density lipoproteins molecules based on antigen-antibody reaction. Details have been discussed in the next part.

Part II: CNT-NiO nanocomposite based impedimetric-Lab on a chip for LDL detection

In this part, an impedimetric-Lab on a chip (*i*LOC) immunosensor for the label free detection of blood low density lipoprotein (LDL) using the proposed CNT-NiO nanocomposite. In this *i*LOC, the immunoelectrode has been fabricated using anti-apolipoprotein B 100 (AAB) functionalized carbon nanotubes-nickel oxide (CNT-NiO) patterned onto ITO substrate.

6.6 Biosensing platform

In previous Section, I have discussed the fabrication of patterned microelectrode based on CNT-NiO nanocomposite. The AAB solution (10 μ l) is spread onto the CNT-NiO/ITO microelectrode surface via physical absorption followed by EDC-NHS chemistry and kept for 4 h in humid chamber (4°C). The carboxylic groups can further undergo an amidation reaction with the amino acids of the proteins. One approach for covalent binding of proteins or enzymes utilizes the diimide-activated amidation of carboxylic acid functionalized carbon nanotubes. The COOH terminal has been activated using EDC (0.4M) as the coupling agent and NHS (0.1M) as activator. The strong covalent (C-N) bond formed between –COOH group of CNT and –NH₂ group of enzymes that has been confirmed via XPS studies. Finally, the BSA solution has been used for blocking the nonspecific site of antibody functionalized surface. Hence, the prepared BSA-AAB/CNT-NiO/ITO immunosensor is kept at 4 °C when not in use.

6.7 Results and discussions

6.7.1 FT-IR studies

The FT-IR spectrum of various electrodes is shown in the Figure 6.2.5. The absorption peak at 503cm⁻¹ (curve a) in the finger print region corresponds to Ni-O vibration band (a). The characteristic absorption seen at 2839 cm⁻¹ and 2917 cm⁻¹ are attributed to CH stretching of COOH-CNTs. The band seen at 1562.5 cm⁻¹ arises due to the C=C stretching that forms the framework of the CNT sidewall. The bands observed in the range of 2500-3000 cm⁻¹ wave number results from the carboxylic acid O-H stretching. The absorption bands seen at ~1000–2500 cm⁻¹ are assigned to the O–C=O symmetric and asymmetric stretching vibrations and the C–O stretching vibration indicating CO₂ absorption on CNT-NiO film. After immobilization of BSA-AAB onto CNT-NiO/ITO electrode surface (curve b), the peak found at 850 cm⁻¹ is assigned to the aromatic C-H bending. The peak at 1040 cm⁻¹ is due to C-OH stretching vibration. The band seen at 3300 cm⁻¹ is attributed to the OH stretching on film surface. The bands seen at 1248 cm⁻¹ and 1650 cm⁻¹ are due to amide III and amide I of BSA-AAB proteins molecules.

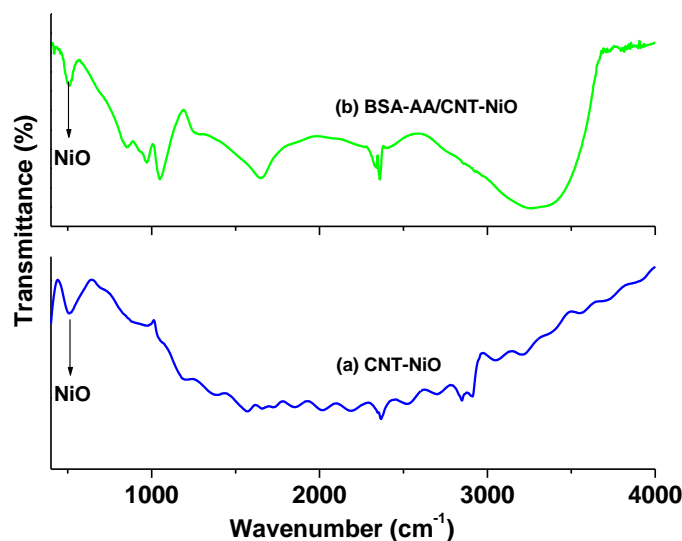


Figure 6.2.5 FT-IR spectra of (a) CNT-NiO/ITO film and (b) BSA-AAB/CNT-NiO/ITO film.

6.7.2 UV-Vis studies

The results of UV-Visible spectroscopic studies of NiO nanoparticles (i), CNTs (ii) and CNT-NiO (iii) carried out in water are shown in the Figure 6.2.6 (A). The strong absorption peak seen at 330 nm (curve i) corresponds to intra-3d transition of Ni^{++} in the cubic structure of NiO. The blue shift of the absorption edge compared to bulk NiO reveals the quantum size effect that might occur at the time of particle growth. Figure 6.2.6(B) shows the extrapolation for the determination of direct band gap, where $(\alpha h\nu)^2$ plots versus energy from the intercept with the x -axis using the following Tauc Eq. Eq. 6.2.2

$$(\alpha h\nu)^2 = k(h\nu - E_g) \quad \text{Eq. 6.2.2}$$

where α is absorbance, h is Plank's constant and k is a constant. The direct band gap (E_g) of synthesized nanostructured NiO is found to be 3.29 eV [Figure 6.2.6B (a)]. In addition to the fundamental absorption of NiO, it has been found that the band edge (broadened line; shown by dotted mark) shows an absorption which fall slightly below the conduction band of NiO that is arising due to exciton (electron-hole pair) that interacts with impurities. The energy of photon involved in exciton absorption is given by $h\nu = E_g - E_{\text{ex}}$, where E_{ex} is the exciton binding energy (0.01 eV). The absorption peak at 266 nm arises from a π - π^* transition due to an unshared pair of electrons of the $-\text{C}=\text{O}$ bond in the carbonyl group ($-\text{COO}$) terminated CNT [Figure 6.2.6B, curve b)]. The band gap of synthesis COOH functionalized CNTs is found to be 2.1 eV [Figure 6.2.6B, curve b)]. In case of CNT-NiO the absorption peak found at 307 nm which is red shifted compared to that of CNTs results from incorporation of NiO onto CNTs [Figure 6.2.6A, curve c)]. The energy gap of synthesized NiO has been tuned to 3.17eV due to incorporation of

CNTs and exhibits higher conductivity. This shifting of energy band of NiO indicates the presence of CNT-NiO composite.

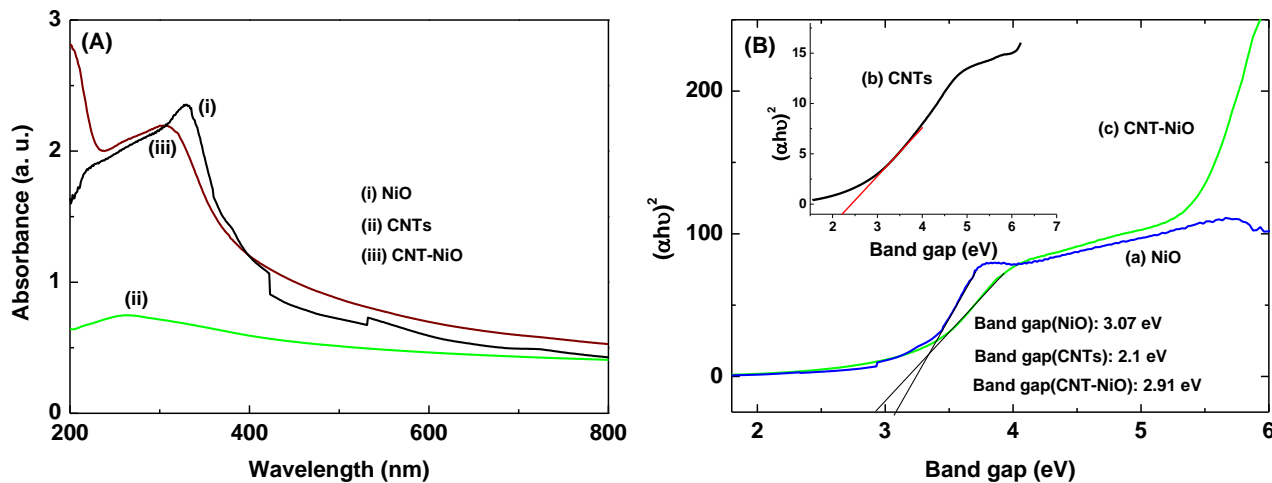


Figure 6.2.6(A) UV-Visible studies and (B) $(\alpha h\nu)^2$ versus energy plots of various films

6.7.3 Chronocoulometric studies

In order to measure the electrode surface areas, diffusion coefficients and charges with respect to time and the mechanisms and rate constants for chemical reactions coupled to electron transfer reactions, the chronocoulogram (CC) have been carried out for various electrodes at same step potential of waveform (2V) as shown in Figure 6.2.7(i). Typical CC plots (charge-time) for both (a) CNT-NiO/ITO electrode and (b) BSA-AAB/CNT-NiO/ITO bioelectrode are shown in Figure 6.2.7(i) and indicates charge-time dependence for linear diffusion control. It has been observed that the BSA-AAB/CNT-NiO immunoelectrode shows less charges value at each time compared to that of CNT-NiO/ITO electrode. The analysis of the chronocoulometric data is based on the Anson equation (Eq. 6.2.3) which defines the charge-time dependence for linear diffusion control:

$$Q = 2nFACD^{1/2}\pi^{1/2}t^{1/2} \quad \text{Eq. 6.2.3}$$

where, Q represents the charge (coulombs). A plot of Q vs. $t^{1/2}$ is referred as the Anson plot Fig. 5.2.3(ii), where the slope (a) can be determined by the following Eq.6.2.3 and 6.2.4

$$a = 2nAFCD^{1/2}/\pi^{1/2} \quad \text{Eq. 6.2.4}$$

n and A represent respectively, the number of electrons transferred and the real electrochemical surface area of the electrode (cm²). F is the Faraday's constant (96,485 coulombs/mole).

The concentration of the mediator is denoted by C and the diffusion coefficient of the mediator (cm²/sec) and time (sec) are denoted by D and t, respectively. Therefore, the real electrochemical surface area of the electrode (A_{ec}) can be calculated from the slope in Eq.6.2.4, provided the other four parameters (n, F, C and D) are known.

$$A = a/(2nFCD^{1/2}/\pi^{1/2}) \quad \text{Eq. 6.2.5}$$

The calculation of the diffusion coefficient (D) of the mediator for the (a) CNT-NiO/ITO electrode and (b) BSA-AAB/CNT-NiO/ITO bioelectrode are found to be respectively, 6.29×10^{-9} cm²/s and 2.82×10^{-9} cm²/s. The electrochemical active surface area (A_{ec}) are found to as 1.9×10^{-2} cm² and 2.0×10^{-2} cm² for the (a) CNT-NiO/ITO electrode and (b) BSA-AAB/CNT-NiO/ITO bioelectrode, respectively.

Figure 6.2.8(i) shows potential-dependent chronocoulometric responses recorded for the BSA-AAB/CNT-NiO/ITO bioelectrode at different potential (1.0-5.0 V). It has been seen that that the charge-time responses increases with increasing potential. Again, I have recorded CC curves at different flow rates (0.01-15 μL/min) and are shown in Figure 6.2.8(ii). The Q vs. t^{1/2} plot for different flow rates [Figure 6.2.8(iii)] and slope of chronocoulometric curves vs. flow rates are shown inset [Figure 6.2.8(iii)]. At flow rate 1.0 μL/min, the slope value is found to decrease and after that the slope value of bioelectrode increases to saturated value.

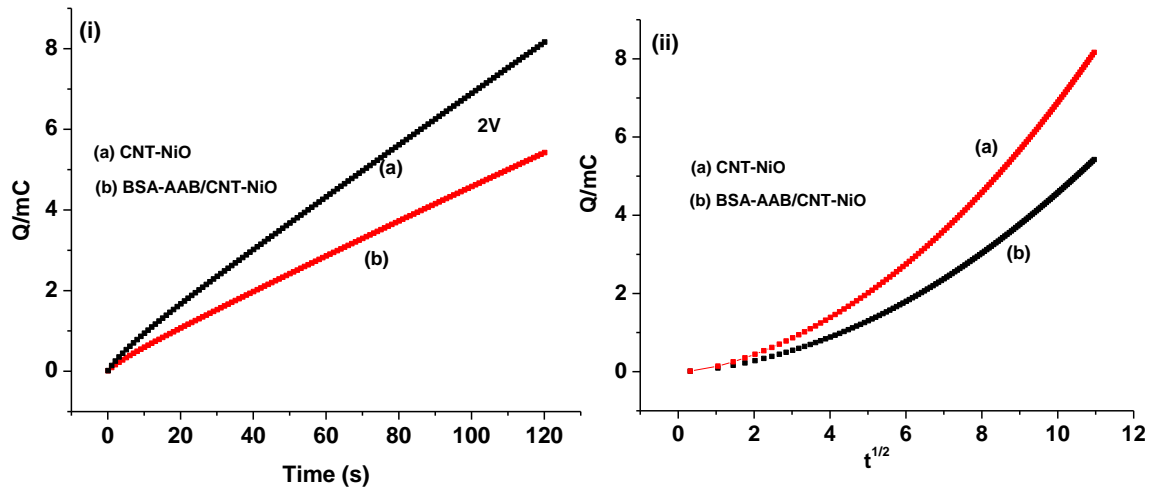


Figure 6.2.7(i) CC plots (charge-time) for CNT-NiO/ITO (a) electrode and BSA-AAB/CNT-NiO/ITO (b) bioelectrode, and (ii) charge (Q) vs. t^{1/2} plot of CNT-NiO/ITO (a) electrode and BSA-AAB/CNT-NiO/ITO (b) bioelectrode.

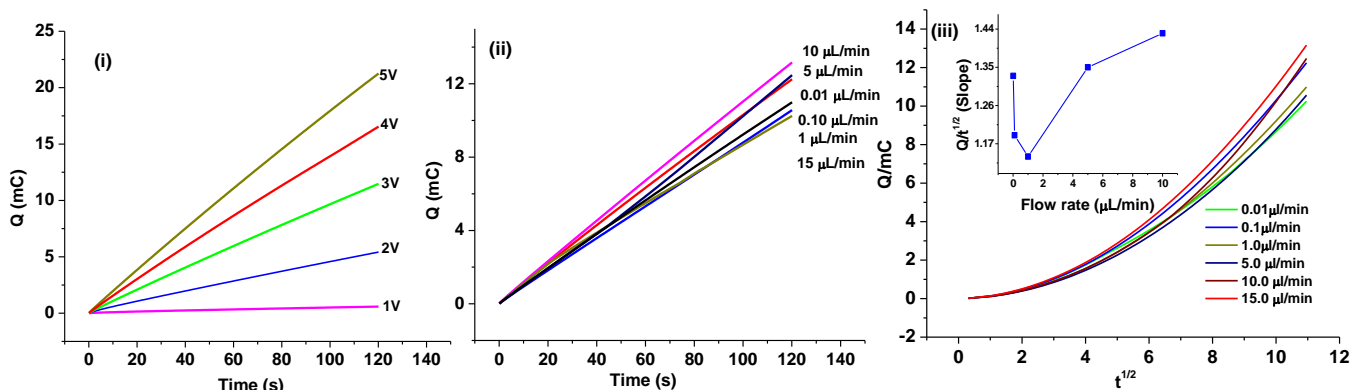


Figure 6.2.8(i) Potential-dependent chronocoulometric responses for the BSA-AAB/CNT-NiO/ITO bioelectrode at different potential (1.0-5.0 V), (ii) chronocoulometric responses at different flow rate (0.01-15 $\mu\text{L}/\text{min}$) and (iii) Q vs. $t^{1/2}$ plot for different flow rates (inset: slope; $Q/t^{1/2}$ vs flow rate plot).

6.7.4 Electrochemical impedance properties of *i*LOC

In order to investigate the antigen-antibody interaction, the impedance analysis can employ by applying a small amplitude sinusoidal AC signal as function of frequency 0.01– 10^5 Hz at fixed bias potential. The impedance can be measure by the real part (Z') and the imaginary part (Z'') of the Nyquist plot. A typical shape of Nyquist plot includes a semicircle region lying on the real axis followed by a straight line. The linear part observed in the low frequency range implies a mass-transfer limited process, where the semicircle portion observed in high frequency range, implies a charge-transfer limited process. The imaginary component, at high frequency falls to zero because it offers no impedance. As the frequency drops, the capacitance C_{dl} offers high impedance and hence current flows mostly through R_{ct} and R_s . The double layer capacitance or constant phase element (CPE) can be calculated from the frequency at the maximum of the semicircle ($\omega = 2f = 1/R_{ct}C_{dl}$). The charge-transfer resistance (R_{ct}) and the double layer capacitance (C_{dl}) are the most important electrical parameters in the analyses of the change in impedance signal for antibody-antigen interaction. The parameter of interest here is R_{ct} , which can be extracted from the fitted circuit model. Figure 6.2.9(a) shows the R_{ct} value of the CNT-NiO/ITO (i) is 2.4 k Ω . This is due to the fact that CNT-NiO act as mediators for electron transfer and reduces the electron tunnelling distance from the redox probe $[\text{Fe}(\text{CN})_6]^{3-/4-}$ in bulk solution to the electrode resulting in decreased R_{ct} . The C_{PE} value of CNT-NiO/ITO is found to be higher (10.0 μF) compared to that of the bioelectrode (4.6 μF) arising due to the AAB-BSA incorporation onto CNT-NiO/ITO surface that enhances the

dielectric thickness. After BSA-AAB immobilization onto CNT-NiO/ITO surface, the R_{ct} value increases to 11.2 k Ω (ii). This is attributed to the antibody and CNT-NiO interaction that impedes the ions transfer from bulk solution to the electrode. Antibody and BSA act as insulating materials, which covalently bind with CNT-NiO/ITO resulting in blocking the charge transfer through the diffusion layer.

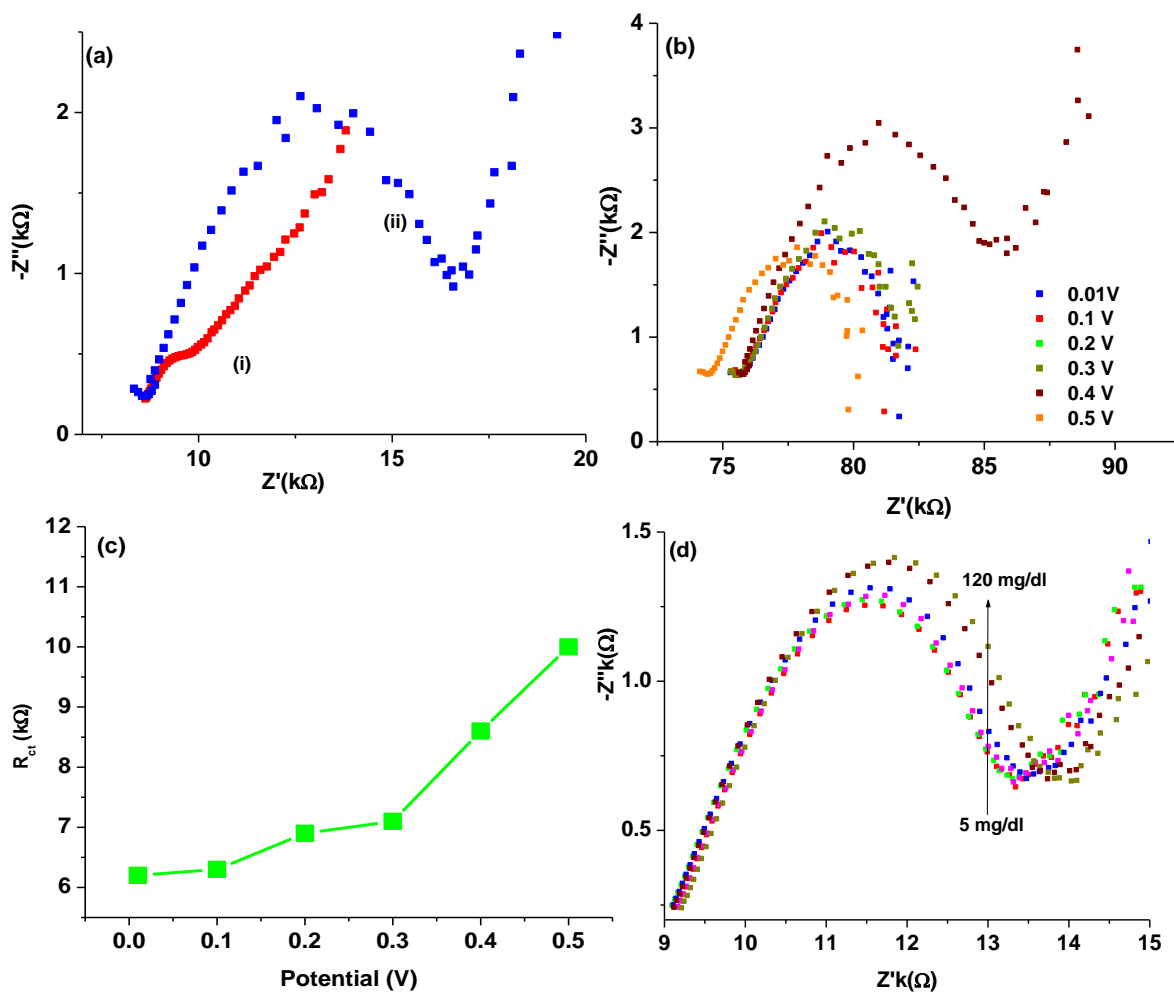


Figure 6.2.9(a) EIS spectra of CNT-NiO/ITO electrode (i) and BSA-AAB/CNT-NiO/ITO bioelectrode (ii), (b) EIS spectra of BSA-AAB/CNT-NiO/ITO bioelectrode as a function of potential (V), (c) plot between charge transfer resistance (R_{ct}) and potential (V) and (d) EIS responses of BSA-AAB/CNT-NiO/ITO bioelectrode as function of LDL concentration.

The bioelectrode is characterized by analyzing the following important parameters such as heterogeneous electron transfer rate constant (k_0) and time constant (τ) for redox probe containing redox species. These parameters provide the information relating to the interfacial interactions of biomolecules as well as for explaining the mechanisms of chemical processes occurring at the electrode/solution interfaces. The corresponding k_0 of the modified electrodes has been calculated by using Eq. 3.3.5 and Eq. 3.3.7 (Chapter 3). The k_0 value of the BSA-AAB/CNT-NiO/ITO bioelectrode is 23.0×10^{-8} /s, which is higher than that for CNT-NiO/ITO electrode (1.4×10^{-8} /s), indicating a faster electron exchange between the redox probe and electrode. The BSA-AAB immobilization on CNT-NiO/ITO shows a sluggish electron charge transfer rate constant resulting in the generation of low capacitance at the electrode surface. The high value of time constant (τ) for the BSA-AAB/CNT-NiO/ITO is estimated as 5.15×10^{-2} due to the slow diffusion of $[\text{Fe}(\text{CN})_6]^{3-/4-}$ ions at the electrode enzyme layer/solution interface compared to that of the CNT-NiO/ITO (2.4×10^{-2}) electrode. The surface coverage (θ), is calculated using the Eq. 4.1.9 (Chapter 4). The value of θ is estimated to be 0.8, indicating more than 80% surface coverage of the CNT-NiO/ITO electrode by BSA-AAB molecules. Figure 6.2.9(b) shows EIS spectra of *i*LOC as a function of potential (0.01 – 0.5 V). It has been seen that there are two semicircles appears in low frequency region as shown in equivalent circuit model. The R_{ct} values of semicircles in low frequency region of the *i*LOC has been found to increase linearly with increased potential [Figure 6.2.9(c)]. This reveals facile electron transfer kinetics wherein resistance controls the electron transfer kinetics of the redox probe at the electrode. It suggests that the resistance represented in the semicircle of the Nyquist plot depends on the bias voltage. The electric double layer or constant phase element (C_{dl}) has been found to decrease with increasing potential. Thus, the R_{ct} values are found to increase at higher potential indicating that the charge transfer at low frequency is dependent to the polarization potential, thus the high potential of 0.5V has been chosen for biosensing.

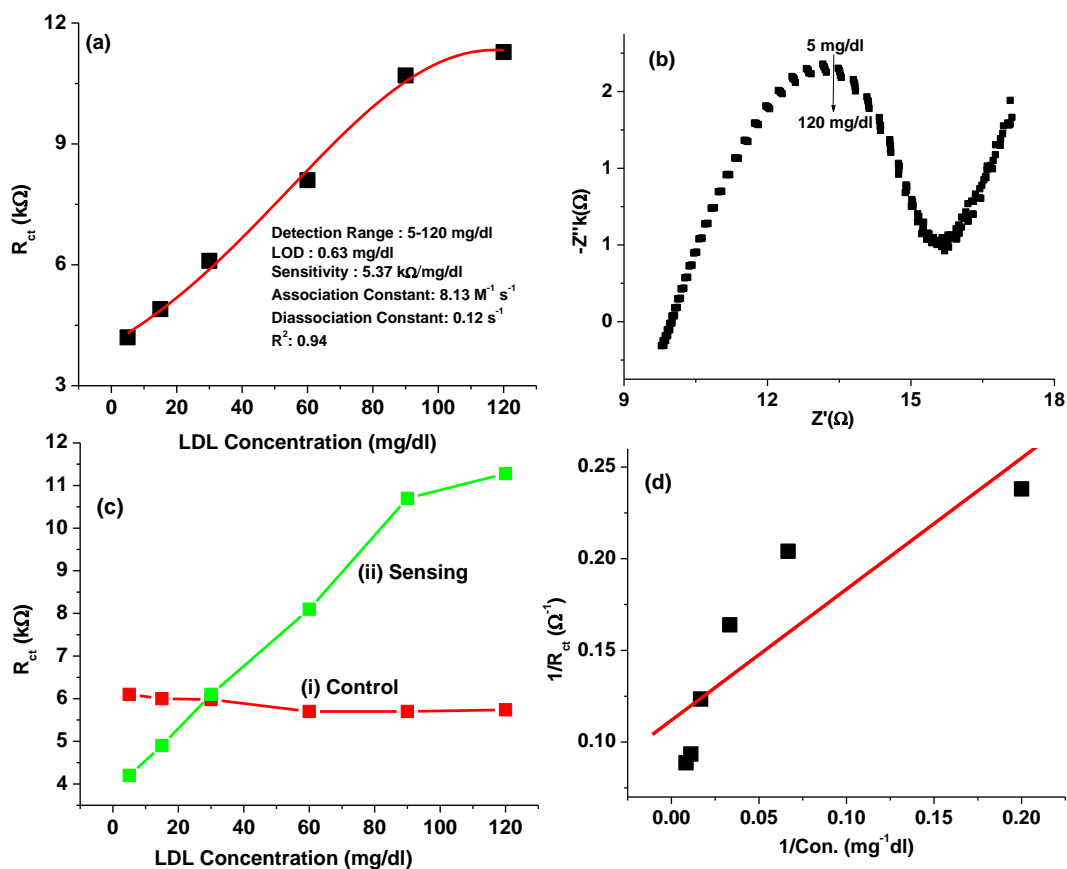


Figure 6.3.1(a) Linear sensor calibration plot of *i*LOC, (b) EIS spectra of *i*LOC without BSA-AAB for control experiment, (c) sensing and control experiment plots as a function of LDL concentration and (d) $1/R_{ct}$ and $1/\text{concentration}$ plot for association constant.

6.7.5 Impedimetric response of *i*LOC

The impedimetric response for the *i*LOC (BSA-AAB/CNT-NiO/ITO bioelectrode) measured as a function of lipid (LDL) concentration [5-120 mg/dl] in PBS containing $[\text{Fe}(\text{CN})_6]^{3-/4-}$ with incubation time of about 5 minutes [Figure 6.2.9(d)]. The changes in the R_{ct} value or dielectric/blocking properties of the BSA-AAB/CNT-NiO/ITO bioelectrode arise from antigen-antibody interaction at electrode/electrolyte interface.

The magnitude of charge transfer resistance (R_{ct}) value increases linearly for the *i*LOC on addition of LDL concentration [Figure 6.3.1(a)]. The increased R_{ct} value indicates that presence of the insulating layer of LDL molecules onto BSA-AAB/CNT-NiO/ITO bioelectrode surface inhibits penetration of the redox species towards the electrode, resulting in higher diameter of EIS spectra. The

negative charges carried by the LDL phospholipids coating perhaps block the electron transfer of the $[\text{Fe}(\text{CN})_6]^{3-/4-}$ redox couple resulting in higher impedance. The bioelectrode when treated with the 0.2 M glycine solution of pH 2.4 for about two minutes results in 95 % of the regenerated bioelectrode. The plot between R_{ct} value and LDL concentration (5-120 mg/dl) yields, $R_{CT}(\Omega) = -0.66(\text{k}\Omega) + 5.3 \text{ k}\Omega \text{ mgdl}^{-1} \times \text{LDL concentration}$. The impedimetric sensitivity of this *i*LOC is obtained to be as high as 5.3 k Ω /mg/dl with regression coefficient (r^2) as 0.94. It has been found that the impedimetric *i*LOC exhibits improved characteristics such as low detection limit of 0.63 mg/dl using $3\sigma_b/m$ criteria, where m is slope of the calibration graph and σ_b is standard deviation.

A control experiment is carried out using the CNT-NiO/ITO electrode without BSA-AAB functionalization under similar conditions. EIS spectra of each concentration are shown in the Figure 6.3.1(b and c)]. I have observed a slight change in the impedance value of the CNT-NiO/ITO electrode with increasing concentration of LDL [Figure 6.3.1(b and c)]. These results reveal that the CNT-NiO/ITO electrode surface does not interact with the LDL molecules, and therefore, the electrochemical impedance remain unchanged. The association and dissociation constant of this *i*LOC are estimated as 8.13 $\text{M}^{-1}\text{s}^{-1}$ and 0.12 s^{-1} , respectively, indicating that LDL molecules have higher affinity towards this *i*LOC [Figure 6.3.1(d)].

6.7.6 Stability and selectivity studies

Stability of this proposed biochip has been evaluated for 100 days. This chip shows an excellent stability upto 60 days with 95% response of R_{ct} value, after which the response is decreased to 78 %. The BSA-AAB/CNT-NiO immunoelectrode is stored at 3°C when not in use. The reproducibility of the working electrodes that are produced under same conditions has been observed. The changes in impedance (R_{ct}) values for electrodes used in the chip are negligible as indicated by the relative standard deviation (RSD) of 3.44 %. In order to determine the selectivity of the *i*LOC for LDL (90 mg/dl) detection, I have performed EIS studies by incorporating the other analytes including triglyceride (150 mg/dl), free cholesterol (150 mg/dl), and total cholesterol (150 mg/dl) and all mixed together. In this study, a low RSD value (4.3 %) has been observed which indicates a negligible interference with other analytes. Thus, this proposed biochip shows excellent selectivity and stability.

6.7.7 Potential merits of this fabricated microfluidic platform

The CNT-NiO nanocomposite can be easily integrated with microfluidic transducer through functionalization of biomolecules such as enzyme, antibodies. Sensitivity and other biosensing parameters are improved due to this CNT-NiO nanocomposite and low aspect ratio of microfluidic device. This CNT-NiO nanocomposite can be used for enzymatic analysis as well as antibody-antigen kinetics

analysis. The amperometric detection of the nanocomposite based electrode offers highly sensitivity to impedance in microchannel solution. The selectivity and stability of biofunctionalized electrode is found to be higher. A label free immunosensor for LDL monitoring indicates that this platform is suitable for the detection of antibody-antigen interaction.

6.8 Conclusions

In summary, an *i*LOC based on anti-apolipoprotein B 100 functionalized CNT-NiO has been described. This *i*LOC has been used to evaluate antigen-antibody binding kinetics as well as blood LDL detection *via* EIS technique. The observed higher value of association and dissociation rate constants with this *i*LOC indicates strong binding affinity between AAB functionalized CNT-NiO nanocomposite and LDL molecules. The BSA-AAB/CNT-NiO immunoelectrode is found to be highly selective for LDL and exhibits detection range of 5-120 mg/dl within the physiological range of LDL in blood/serum in human body. The CNT-NiO composite provides a biocompatible and favourable environment due to high surface-to-volume ratio resulting in enhanced loading capacity of AAB. Low cost, low reagent/power consumption and high specificity are the main advantages of this proposed *i*LOC. This BSA-AAB/CNT-NiO immunoelectrode shows higher sensitivity as 5.3 k Ω /mg/dl and faster response. The application of CNT-NiO composite not only improves the electrochemical properties but also result in enhanced loading capacity of antibodies. This CNT-NiO nanocomposite shows less toxicity effect with human cells compared to that of only using CNT. The high sensitivity combined with specificity of LDL-AAB binding, towards LDL detection using CNT-NiO is a promising platform that can be used to detect other lipids such as VLDL, triglyceride etc. The impedimetric measurements have been carried out by introducing three electrode systems in microchannels. The impedance depends on the charge transfer property of solution as well as the electrode assembly. This chapter demonstrated the amperometric detection of enzymatic microfluidic biosensor for cholesterol as well as impedance detection of LDL via antigen-antibody interaction.

CHAPTER 7

Summary of the work and future prospects

7.1 Summary of the work

Microfluidic devices are capable of, detecting and analyzing small sample volumes, and provide automated sample preparation and reduced processing times at the consumption of lowest amounts of expensive reagents. These advantages promote the integration of microfluidic biosensors for POC diagnostic applications. Several intrinsic characteristics of microfluidic devices such as laminar flow, minimal handling of hazardous materials, and multiplexed and parallel sample detection, portability and versatility can be in-built in a POC testing system. This work reported here is an effort to explore the feasibility of microfluidic chips in detecting concentration of specific analyte rapidly, accurately and at a low cost in a desired test sample.

In this thesis, I have demonstrated the design and fabrication of the microfluidic biosensor systems using soft lithographic technique for free cholesterol, total cholesterol and LDL detection via electrochemical techniques. In these microfluidic biochips, the ITO electrodes have been utilized as supporting material for integration of nanomaterials as well as for immobilization of biomolecules. The chemical etching, which is a low cost technique, was employed for fabrication of ITO. The fabricated ITO electrodes on glass substrate were easily coupled with PDMS microchannels through the reversible sealing. In addition, the physical adsorption method for modification of ITO electrode shows an excellent absorption of nanomaterials which facilitate the immobilization of biomolecules. A systematic protocol was tested and followed for modification of ITO microelectrodes using nanomaterials to improve the biosensor characteristics. The model enzymes such as cholesterol oxidase and cholesterol esterase were used in these biochips for accurate identification of cholesterol. In these microfluidic biosensors, the binding kinetics of biomolecular interactions has revealed the association and dissociation rates of enzymes interaction with cholesterol molecules. The surface modification of enzymes on these microfluidic transducers via covalent interaction (EDC/NHS coupling chemistry) improved the detection parameters like detection limit, sensitivity, stability etc. of the biosensors. In addition to enzymatic analysis, these microfluidic biochips served as provide an ideal platform for applications such as detection of LDL molecules via antigen-antibody interaction and study their binding kinetics.

The fabricated microfluidic biosensor platforms offered numerous advantages compared to other traditional methods such as ultracentrifugation, electrophoresis, NMR etc. These proposed devices are capable of high-throughput analysis and massive parallelization due to compactness. Excellent reproducibility, high selectivity, accuracy, reliability, ease of use, portability, small size and cost effectiveness are main advantages of these microfluidic devices for detection of cholesterol and LDL molecules. Additionally, these microfluidic devices have been observed as safer platforms, which can precisely control and manipulate the various body fluids such as blood serum and other chemical fluids

(like buffer solution). The results from these microfluidic biosensors indicate a promising technological innovation for the next generation of analytical miniaturized systems towards POC diagnostics.

Selection of materials is very important in designing microfluidic devices. I have focused on PDMS-based microchannels to control the biological fluids in the fabricated microfluidic devices. PDMS offer good mechanical and optical properties, flexibility, transparency and rapid prototyping compared to silicon and glass. The PDMS behaves like an elastic solid material that maintains its molded structure. PDMS can reduce time and complexity for fabrication of microfluidic devices, which are compatible with aqueous media and biological samples prepared in aqueous solutions. In addition, it can be molded at low temperature and thus, researchers working in benchtop can construct devices easily and rapidly. PDMS is an ideal and robust material for fabrication of microfluidic biochips and its channels, reservoirs, holes etc. can make easy for alignment and reversible/irreversible sealing with ITO microelectrode.

The size of the electrode in electrochemical microfluidic biochip is one of the key design issues. The size of electrode may affect the mass transport of ions to and from the electrode surface in the bulk solution, which in turn may influence the electrochemical response. The planer diffusion of ions occurs in the case of macro-electrodes in a conventional biosensor. The micro-dimensions of the electrode in a microfluidic device is known to facilitate spherical or radial diffusion arising due to the diffusion from different directions of the surrounding bulk solution towards the electrode resulting in improved mass transfer towards the electrode. In addition, the microelectrode provides small capacitive-charging currents, reduced ohmic drop of potential (iR) and steady-state diffusion currents leading to improved biosensor sensitivity. Some of the other important parameters such as detection time and limit also can be improved to better numbers in a microfluidics device.

In this thesis, the synthesis of various type metal oxides (anatase TiO_2 and NiO) and their composite with chitosan and carbon nanotubes for fabrication of microfluidic biochips have also been described. These synthesized nanomaterials were integrated with the fabricated microfluidic systems in order to improve the biosensor efficacy and efficient loading of biomolecules such as cholesterol oxidase, cholesterol esterase and anti-apolipoproteins. The large surface-to-volume ratio, excellent catalytic properties, non-toxicity, biocompatibility, high chemical and thermal stability, negligible swelling in both aqueous and non-aqueous solvents, and high electron transfer communication are the potential merits of these nanomaterials to be integrated with microfluidic biosensors. In particular, these nanomaterials act as mediators that accelerate generated electrons from active site of proteins to the electrodes during electrochemical detection. These nanomaterials provide a friendly environment for loading of enzymes or antibodies without any loss of their biological activities. Incorporation of these nanomaterials in these

microfluidic chips have enhanced the electrochemical current, leading to higher sensitivity and lower detection limits. This thesis presented a new microfluidic biosensor chip platform using nanostructured materials that can be used for the detection of clinically important analytes such as free cholesterol, esterified cholesterol and LDL molecules.

The results relating to the fabrication of nanostructured anatase-TiO₂ nanoparticle-based microfluidic platform for free cholesterol estimation were described in Chapter 3. The sol-gel synthesized monodisperse TiO₂ nanoparticles uniformly absorb the cholesterol oxidase molecules in the microfluidic transducer surface. The use of crystalline nanostructured anatase-TiO₂ improved the charge transfer properties in this microfluidic device resulting in enhanced sensitivity towards free cholesterol detection. The response of this microfluidic biosensor depends on flow rate of the buffer solution, which influences response time and diffusivity through the diffusion layer. Good reproducibility, high selectivity and low K_m value of the proposed biosensor were observed. This miniaturized microfluidic biosensor requires minimal instrumentation and can be readily integrated with micro-electronics in a chip-based format.

In the next chapter, we explored the possibility of using TiO₂ composite with CH. In order to improve the biosensor efficacy, the TiO₂ nanoparticles have been modified with chitosan molecules. The mesoporous structure of TiO₂-CH nanocomposite and available functional groups such as the amino, hydroxyl etc. enhanced adsorption capacity and created a hydrophilic environment for loading enzyme molecules on transducer surface. This TiO₂-CH nanocomposite in this microfluidic device contained ~80% of mesoporosity of total pore volume of 0.2961cc/g. The integration of the mesoporous anatase-TiO₂-CH with this microfluidic device improved the biosensor characteristics due to excellent electrochemical properties for total cholesterol detection. An XPS study of the microfluidic biosensor was used to quantify the used functional groups before and after enzyme immobilization. The results reported from this study have shown that the sensitivity of mesoporous TiO₂-CH based microfluidic device is several-folds higher, indicating that the combination of impedimetric detection with biopolymer-nanostructured microelectrode provides a technology that is more sensitive towards esterified cholesterol. This microfluidic biosensor showed a lower detection limit of 0.2 mg/dl in a wide range (2-500 mg/dl) of cholesterol detection. Additionally, the K_m value of this microfluidic biosensor was found to be lower, indicating a strong affinity of CH-TiO₂ based microfluidic bioelectrode to the cholesterol.

In the next experiment, I have explored NiO nanorods as another candidate for microfluidic bioelectrode modification. Utilization of nickel oxide nanorods to the microfluidic biosensor for total cholesterol detection facilitated the direct enzyme immobilization on transducer surface due to its high

isoelectric point. The nanorod shape geometries and well-defined crystal surfaces of NiO in the microfluidic device enhanced the electrons transfer from bulk solution to electrode. Nanostructured NiO acted as good acceptors of electrons generated during re-oxidation of cholesterol oxidase that transfer to electrode via $\text{Ni}^{+2}/\text{Ni}^{+3}$ redox couple resulting in increased sensitivity compared to using TiO_2 nanoparticles in microfluidic system. It was observed that this NiO based microfluidic device shows excellent sensitivity and high adsorption ability of biomolecules on transducer surface. Thus, it can be concluded that the NiO is a good candidate for the integration with microfluidic system as well as attachment of biomolecules for cholesterol detection.

In addition to these modifications, CNTs were used to form CNT-NiO nanocomposite and were integrated with microfluidic device for detection of cholesterol and LDL. The smart CNT-NiO nanocomposite matrix with microfluidic assembly showed better biosensing characteristics compared to using single component such as TiO_2 and NiO nanoparticles. In this microfluidic biosensor, the toxicity effect of the CNT-NiO composite was found to be lesser compared to CNTs and NiO nanoparticles. The application of CNT-NiO composite in this device improved the electrochemical properties as well as loading capacity of antibody/enzyme. Surface immobilization of cholesterol oxidase and cholesterol esterase was carried out on CNT-NiO composite via covalent interaction for estimation of total cholesterol molecules. In this strategy, a 20-fold of sensitivity (2.2 mA/mM/cm^2) enhancement for cholesterol monitoring was observed. The low detection limit (0.03 mM) and fast detection time (2 s) are quite remarkable for detection of cholesterol molecules using this microfluidic biosensor. This may be due to the available functional groups of CNTs utilized in this microfluidic biosensor. In this same microfluidic biosensor, we carried out an anti-apolipoprotein immobilization in place of cholesterol oxidase and esterase to convert this to an immunosensor for the detection of LDL molecules. The results relating to the detection of LDL molecules using this microfluidic biosensor showed good selectivity, stability, reproducibility and can detect LDL molecules within its physiological range. Higher values of association and dissociation constants indicated strong binding affinity between AAB functionalized CNT-NiO nanocomposite and LDL molecules. Sensitivity and othered biosensing characteristics were improved due to the covalently bind AAB molecules to CNT-NiO nanocomposite on microfluidic transducer. The label free detection of LDL molecules in this microfluidic device offered higher selectivity and stability. The CNT-NiO composite based microfluidic device facilitated detection of cholesterol as well as LDL molecules in an efficient manner.

Thus to be conclusive, the main focus of this thesis was to develop POC microfluidic platforms for detection of biomolecules. Efforts have been made to critically evaluate biosensing parameters and

optimize of detection cholesterol and LDL via electrochemical techniques. Starting from the microfabrication, synthesis and characterization of nanoparticles, their immobilization etc. this thesis has explained every step in the development of a novel microfluidic platform with nanostructured materials. For fabrication of cholesterol microfluidic biosensor, we used various immobilization matrices such as TiO₂, NiO, CNT-NiO and CH-TiO₂ to increased stability, reusability, ordered arrangement and high reproducibility. They facilitated the immobilization of biomolecules without denaturation and provided fast electron transfer between biomolecules and electrode surface. The functional properties of biomolecules and nanostructured materials were easily manipulated to make them compatible for immobilization of biomolecules with better orientation.

These demonstrated microfluidic systems can address the problems like miniaturization, cost effectiveness, compactness, reagent/power consumption, detection time and sensitivity to be greater extent. Additionally, the simplicity and basic fundamentals of electrochemistry can improve our device fabrication in fluidic-format. These proposed biochips could positively create a new direction in future medical health-care diagnostics.

7. 2 Future prospects

The basic design of a microfluidic biosensor needs microstructures to control fluidic operations as well as the bioelectrode. The bioelectrode should be attached with biological receptor coupled to an electronic transducer that converts a biological event into a measurable signal. The problems can arise due to limited functional stability of immobilized biomolecules and electrical interference of signal transduction. To overcome these problems, the selection of a suitable matrix for immobilization of desired biomolecules can play an important role. The fabricated microfluidic devices for detection of cholesterol are greatly benefitted from the use of nanoparticles, particularly from the use of CNTs. Efforts are still in progress to utilize graphene oxide sheets as detectors in lab-on-a-chip devices.

Using a syringe pump may be a limitation for fluidic manipulation towards the point-of-care diagnostics. The disadvantages include large dead volumes and significant flow hysteresis. To obviate this problem, the passive mixing elements that exploit liquid movement in the geometries of the microchannels to induce fluid mixing can be proposed. Passive mixers are generally reliable, low cost, can be easily fabricated and integrated onto POC diagnostic devices. The typical driving forces for propelling fluids in passive microfluidic devices are dependent on chemical gradients, osmotic pressure, and capillary forces etc. Thus, these microfluidic devices offer portability, reduced cost, minute dead volumes and low power consumption. However, a major limitation relates to the flow rates of these devices that can only be presently varied to a limited degree.

The PDMS behaves like an elastic solid material that maintains its molded structure. It offers low cost, flexibility, and rapid prototyping. PDMS has poor chemical compatibility with many organic solvents as it tends to swell upon contact, making it mainly suitable for aqueous applications. PDMS adsorbs small molecules and it can be deformed under pressure of pneumatic valves. It can become a significant issue for high pressure operation as it leads to a large alteration of channel geometry. Though, PDMS has gained widespread acceptance in the field, glass and silicon certainly still have increased utility in microfluidics device fabrication. The permanent modification of PDMS surface using various chemical treatments has been investigated. In Chapter 2 (Section 2.3), I have described relating to the modification of PDMS surface via chemical treatment over some period. Researchers are trying to find a solution using self assembled monolayer (SAM) onto PDMS surface to reduce swelling and obtain improved stability. PDMS can be modified by conversion of chemical bonding from Si-CH₃ (hydrophobic) to Si-OH (hydrophilic) which can reduce the use of syringe pump in the proposed microfluidic system to develop a hand-held compact device.

It is proposed to detect multi-analytes such as LDL, cholesterol and triglycerides, using same microfluidic detection system with minor modifications. In this proposed microfluidic system, fabrication of a suitable electrode array and selective deposition of biofunctionalized nanomaterials is proposed to detect desired analytes. Advances in microfluidic technologies have provided an exciting opportunity to integrate photonics and microfluidics at micron-size scales to leverage the combined advantages resulting in a totally new area of research termed as 'optofluidics'. Non-contact label-free measurements and microscopic optical imaging based on microfluidics have attracted the attention of researchers in this field as most effective ways for fast, real-time and high sensitivity detection of biomolecules. Optofluidic elements that can manipulate light inside a microchannel have also been demonstrated. Principles of optical microscopic imaging coupled with fluorescence tags and SPR-based detection have been explored and demonstrated as effective biosensing platforms for detection and quantification of various biomolecules. In SPR measurements, resonance angle is very sensitive to the change in refractive index and SPR shift in millidegrees (m°), due to the change in refractive index, is used as the response to quantify the binding of macromolecules at the sensor surface. SPR patterned Au electrode on glass can be used to functionalize biomolecules and PDMS microchannel will be used to control biological fluids for desired analyte on this SPR electrode. The SPR signal can be recorded as a typical sensogram.

Microfluidics systems have been adapted for imaging intracellular events like cell division, migration etc. The nanotechnology developments and a wide variety of nanoparticulate imaging contrast agents have significantly contributed to the development of nanoparticles based biosensors both *in vitro*

as well as *in vivo* levels. Thus, using a microscope in combination with optofluidic channels is likely to create new possibilities towards POC diagnostics for human health care.

References

1. C. H. Ahn, J.-W. Choi, G. Beaucage, J. H. Nevin, J.-B. Lee, A. Puntambek, and J. Y. Lee. Disposable smart lab on a chip for point-of-care clinical diagnostics. *Proc. Of the IEEE* 92, (2004) 154-173.
2. M. Barbaro, A. Bonfiglio, L. Raffo, A. Alessandrini, P. Facci, and I. Barák. A CMOS, Fully Integrated Sensor for Electronic Detection of DNA Hybridization. *IEEE Electron Device Lett.* 27, (2006) 595-597.
3. X. Cheng, A. Gupta, C. Chen, R. G. Tompkins, W. Rodriguez, and M. Toner. Enhancing the performance of a point-of-care CD4+ T-cell counting microchip through monocyte depletion for HIV/AIDS diagnostics. *Lab Chip* 9, (2009) 1357–1364.
4. H. Dong, C.-M. Li, Y.-F. Zhang, X.-D. Cao, and Y. Gan. Screen-printed microfluidic device for electrochemical immunoassay. *Lab Chip* 7, (2007) 1752–1758.
5. L. Gervais, and E. Delamarche. Toward one-step point-of-care immunodiagnostics using capillary-driven microfluidics and PDMS substrates. *Lab Chip* 9, (2009) 3330–3337.
6. L. Gervais, N. Rooij, and E. Delamarche. Microfluidic chips for point-of-care Immunodiagnostics. *Adv. Mater.* 23, (2011) H151–H176.
7. V. Gubala, L. F. Harris, A. J. Ricco, M. X. Tan, and D. E. Williams. Point of care diagnostics: status and future. *Anal. Chem.* 84, (2012) 487–515.
8. W. H. Grover, R. H. C. Ivester, E. C. Jensen and R. A. Mathies. Development and multiplexed control of latching pneumatic valves using microfluidic logical structures. *Lab Chip* 6, (2006) 623–631.
9. S. Haeberle, and R. Zengerle. Microfluidic platforms for lab-on-a-chip applications. *Lab Chip* 7, (2007) 1094–1110.
10. V. Linder. Microfluidics at the crossroad with point-of-care diagnostics. *Analyst* 132, (2007) 1186–1192.
11. F. B. Myers, and L. P. Lee. Innovations in optical microfluidic technologies for point-of-care diagnostics. *Lab Chip* 8, (2008) 2015–2031.
12. A. Sandhu, H. Handa, and M. Abe. Synthesis and applications of magnetic nanoparticles for biorecognition and point of care medical diagnostics. *Nanotechnology* 21, (2010) 442001.
13. A. J. Tüdos, G. A. J. Besselink and R. B. M. Schasfoort. Trends in miniaturized total analysis systems for point-of-care testing in clinical chemistry. *Lab on a Chip* 1, (2001) 83–95.

14. J. Wang. Electrochemical biosensors: towards point-of-care cancer diagnostics. *Biosensor. Bioelectron.* 21, (2006) 1887–1892.
15. L. Gervais. Capillary microfluidic chips for point-of-care testing: from research tools to decentralized medical diagnostics. Ph.D. thesis, École polytechnique fédérale de Lausanne, the Switzerland, 2011.
16. P. K. Sorger, Microfluidics closes in on point-of-care assays. *Nat. Biotechnol.* 26, (2008) 1345-1346.
17. G. Russo, C. Zegar, and A. Giordano. Advantages and limitations of microarray technology in human cancer. *Oncogene* 22, (2003) 6497–6507.
18. C. D. Chin, V. Linder, and S. K. Sia. Commercialization of microfluidic point-of-care diagnostic devices. *Lab Chip* 12, (2012) 2118–2134.
19. G. J. Kost, N. K. Tran, and R. F. Louie. Point-of-care testing: Principles, practice, and critical-emergency-disaster medicine. *Encyclopedia of Anal. Chem.* 2008.
20. A. F Rossi, and D. Khan, Point of care testing: improving pediatric outcomes. *Clinical Biochemistry* 37, (2004) 456-461,
21. J. H. Nichols. Point-of-care testing. New York: Marcel Decker, Inc. 2003.
22. N. K. Tran, and G. J. Kost. Worldwide point-of-care testing: compendiums of POCT for mobile, emergency, critical, and primary care and of infectious diseases tests. *Point of Care: The Journal of Near-Patient Testing & Technology* 5, (2006) 84–92.
23. A. K. Yetisen, M. S. Akram, and C. R. Lowe. Paper-based microfluidic point-of-care diagnostic devices. *Lab Chip* 13, (2013) 2210-2251.
24. O. Edwin, and A. V. Berg, Lab-on-a-chip: miniaturized systems for (bio) chemical analysis and synthesis. Elsevier Science, 2003.
25. V. Srinivasan, V. K. Pamula, and R. B. Fair. An integrated digital microfluidic lab-on-a-chip for clinical diagnostics on human physiological fluids. *Lab on a Chip* 4, (2004) 310-315.
26. H. Chong, Y. Koo, B. Collins, F. A. Gomez, Y. Yun, and J. Sankar. Paper-based microfluidic point-of-care diagnostic devices for monitoring drug metabolism. *J. Nanomed. Biotherapeut. Discov.* 3, (2013) 1-2.
27. S. A. Soper, K. Brown, A. Ellington, B. Frazier, G. G.-Manero, V. Gau, S. I. Gutman, D. F. Hayes, B. Korte, J. L. Landers, D. Larson, F. Ligler, A. Majumdar, M. Mascini, D. Nolte, Z. Rosenzweig, J. Wang, and D. Wilson, Point-of-care biosensor systems for cancer diagnostics/prognostics. *Biosens. Bioelectron.* 21, (2006) 1932-1942.

28. J. Wang. Electrochemical biosensors: Towards point-of-care cancer diagnostics. *Biosens. Bioelectron.* 21, (2006) 1887–1892.
29. C. D. Chin, V. Linder, and S. K. Sia. Commercialization of microfluidic point-of-care diagnostic devices. *Lab on a Chip* 12, (2012) 2118-2134.
30. S. Choi, M. Goryll, L. Y. M. Sin, P. K. Wong, and J. Chae. Microfluidic-based biosensors toward point-of-care detection of nucleic acids and proteins. *Microfluid. Nanofluid.* 10, (2011) 231-247.
31. P. Tabeling, *Introduction to microfluidics*. Oxford University Press, 2005.
32. P. Gravesen, J. Branebjerg, and O. S. Jensen. Microfluidics-a review. *J. Micromech. Microeng.* 3, (1993) 168.
33. S. C. Terry, J. H. Jerman, and J. B. Angell. A gas chromatographic air analyzer fabricated on a silicon wafer. *IEEE Electron Device Lett.* 26, (1979) 1880-1886.
34. A. Manz, N. Graber, and H. M. Widmer. Miniaturized total chemical analysis systems: a novel concept for chemical sensing. *Sensor. Actuat. B-Chem.* 1, (1990) 244-248.
35. D. C. Duffy, O. J. A. Schueller, S. T. Brittain, and G. M. Whitesides. Rapid prototyping of microfluidic switches in poly(dimethylsiloxane) and their actuation by electroosmotic flow. *J. Micromechan. Microeng.* 9, (1999) 211-217.
36. Y. Xia, J. J. McClelland, R. Gupta, D. Qin, X.-M. Zhao, L.L. Sohn, R.J. Celotta, and G. M. Whitesides. Replica molding using polymeric materials: A practical step toward nanomanufacturing. *Adv. Mater.* 9, (1997) 147-149.
37. D. Qin, Y. Xia, and G. M. Whitesides. Elastomeric light valves. *Adv. Mater.* 9 (1997) 407-410.
38. G. M. Whitesides, The origins and the future of microfluidics. *Nature* 442, (2006) 368-373.
39. B. Kirby, *Micro-and nanoscale fluid mechanics*. New York: Cambridge University Press, 2010.
40. S. D. Minteer, *Microfluidic techniques: reviews and protocols*. Springer 321, (2006)
41. H. A. Stone, A. D. Stroock, and A. Ajdari. Engineering flows in small devices: microfluidics toward a lab-on-a-chip. *Annu. Rev. Fluid Mech.* 36 (2004) 381-411.
42. M. Mir, A. Homs, and J. Samitier. Integrated electrochemical DNA biosensors for lab-on-a-chip devices. *Electrophoresis* 30, (2009) 3386-3397.
43. H. Craighead. Future lab-on-a-chip technologies for interrogating individual molecules. *Nature* 442, (2006) 387-393.
44. H. Mao, T. Yang, and P. S. Cremer. Design and characterization of immobilized enzymes in microfluidic systems. *Anal. Chem.* 2 (2002) 379-385.

45. N. V. Zaytseva, N. G. Vasiliy, A. R. Montagna and A. J. Baeumner. Development of a microfluidic biosensor module for pathogen detection. *Lab on a Chip* 5 (2005) 805-811.
46. I. Meyvantsson and D. J. Beebe. Cell culture models in microfluidic systems. *Annu. Rev. Anal. Chem.* 1 (2008) 423-449.
47. H. Song, J. D. Tice, and R. F. Ismagilov. A microfluidic system for controlling reaction networks in time. *Angew. Chem.* 115 (2003) 792-796.
48. T. Velten, H. H. Ruf, D. Barrow, N. Aspragathos, P. Lazarou, E. Jung, C. K. Malek, M. Richter, J. Kruckow, and M. Wackerle. Packaging of bio-MEMS: strategies, technologies, and applications. *IEEE Trans. Adv. Packag.* 28 (2005) 533-546.
49. L. Malic, D. Brassard, T. Veres, and M. Tabrizian. Integration and detection of biochemical assays in digital microfluidic LOC devices. *Lab on a Chip* 10 (2010) 418-431.
50. D. R. Reyes, D. Iossifidis, P.-A. Auroux, and A. Manz. Micro total analysis systems. Introduction, theory, and technology. *Anal. Chem.* 74 (2002) 2623-2636.
51. J. M. Bustillo, R. T. Howe and R. S. Muller. Surface micromachining for microelectromechanical systems. *Proc. of the IEEE* 86 (1998) 1552-1574.
52. V. Hessel, H. Löwe, and F. Schönfeld. Micromixers—a review on passive and active mixing principles. *Chem. Eng. Sci.* 60 (2005) 2479-2501.
53. J. E.-Ali, Peter K. Sorger, and Klavs F. Jensen. Cells on chips. *Nature* 442, (2006) 403-411.
54. C. Monat, P. Domachuk, and B. J. Eggleton. Integrated optofluidics: A new river of light. *Nat. photonics* 1, (2007) 106-114.
55. D. Erickson, and D. Li. Integrated microfluidic devices. *Anal. Chim. Acta* 507 (2004) 11-26.
56. H. Andersson, and A. V. Berg. Microfluidic devices for cellomics: a review. *Sensor. Actuat. B-Chem.* 92, (2003) 315-325.
57. T. V. -Dinh, G. Griffin, D. L. Stokes, and A. Wintenberg. Multi-functional biochip for medical diagnostics and pathogen detection. *Sensor. Actuat. B-Chem.* 90, (2003) 104-111.
58. M. L. Kovarik, P. C. Gach, D. M. Ornoff, Y. Wang, J. Balowski, L. Farrag, and N. L. Allbritton. Micro total analysis systems for cell biology and biochemical assays. *Anal. Chem.* 84, (2011) 516-540.
59. L. Kang, B. G. Chung, R. Langer, and A. Khademhosseini. Microfluidics for drug discovery and development: from target selection to product lifecycle management. *Drug Discovery Today* 13, (2008) 1-13.

60. D. B. Weibel, and G. M. Whitesides. Applications of microfluidics in chemical biology. *Curr. Opin. Chem. Biol.* 10, (2006) 584-591.
61. C. Hansen, and S. R. Quake. Microfluidics in structural biology: smaller, faster... better. *Curr. Opin. Chem. Biol.* 13, (2003) 538-544.
62. G. S. Fiorini, and D. T. Chiu. Disposable microfluidic devices: fabrication, function, and application. *BioTechniques* 38, (2005) 429-446.
63. S. Borgmann, A. Schulte, S. Neugebauer, and W. Schuhmann. Amperometric biosensors. *Bioelectrochemistry: Fundamentals, Applications and Recent Developments.* (2011).
64. G. G. Guilbault, G. Palleschi, and G. Lubrano. Non-invasive biosensors in clinical analysis. *Biosen. Bioelectron.* 10, (1995) 379-392.
65. L. C., Clark, and C. Lyons. Electrode systems for continuous monitoring in cardiovascular surgery. *Ann. N. Y. Acad. Sci.* 102, (1962) 29-45.
66. K. Cammann, Bio-sensors based on ion-selective electrodes. *Fresenius J. Anal. Chem.* 287, (1977) 1-9.
67. W. Zhang, and G. Li. Third-generation biosensors based on the direct electron transfer of proteins. *Anal. Sci.* 20, (2004) 603-609.
68. J. Wang, Electrochemical glucose biosensors. *Chem. Rev.* 108, (2008) 814-825.
69. M. Pumera, S. Sanchez, I. Ichinose, and J. Tang. Electrochemical nanobiosensors. *Sensor. Actuat. B-Chem.* 123, (2007) 1195-1205.
70. G. Chornokur, S. K. Arya, C. Phelan, R Tanner, and S. Bhansali. Impedance-Based Miniaturized biosensor for ultrasensitive and fast prostate-specific antigen detection. *Journal of Sensors* 2011, (2011).
71. E. Dubuisson, Z. Yang, and K. P. Loh. Optimizing label-free DNA electrical detection on graphene platform. *Anal. Chem.* 83, (2011) 2452-2460.
72. S. Chandra, N. Barola, and D. Bahadur. Impedimetric biosensor for early detection of cervical cancer. *Chem. Comm.* 47, (2011) 11258-11260.
73. G. Jie, J. Zhang, D. Wang, C. Cheng, H.-Y. Chen, and J.-J. Zhu. Electrochemiluminescence immunosensor based on CdSe nanocomposites. *Anal. Chem.* 80, (2008) 4033-4039.
74. K. V. Singh, D. K. Bhura, G. Nandamuri, A. M. Whited, D. Evans, J. King, and R. Solanki. Nanoparticle-enhanced sensitivity of a nanogap-interdigitated electrode array impedimetric biosensor. *Langmuir* 27, (2011) 13931-13939.

75. V. N. Goral, N. V. Zaytseva, and A. J. Baeumner. Electrochemical microfluidic biosensor for the detection of nucleic acid sequences, *Lab Chip* 6, (2006) 414.
76. J. Min and A. J. Baeumner. Characterization and optimization of interdigitated ultramicroelectrode arrays as electrochemical biosensor transducers. *Electroanalysis* 6, (2004) 9.
77. F. Lisdat, and D. Schäfer. The use of electrochemical impedance spectroscopy for biosensing. *Anal. Bioanal. Chem.* 391, (2008) 1555–1567.
78. J. S. Daniels, and N. Pourmand, Label-free impedance biosensors: opportunities and challenges, *Electroanalysis*, 19, (2007) 1239–1257.
79. A. Bonanni, and M. del Vallea. Use of nanomaterials for impedimetric DNA sensors: A review, *Anal. Chim. Acta* 678, (2010) 7–17.
80. L. C. Clark, R. Wolf, D. Granger, and Z. Taylor. Continuous recording of blood oxygen tensions by polarography. *J. Appl. Physiol.* 6, (1953) 189-193.
81. R. S. Yalow, and S. A. Berson. Immunoassay of endogenous plasma insulin in man. *Obes. Res.* 4, (1996) 583-600.
82. S. A. Katz, and G. A. Rechnitz. Direct potentiometric determination of urea after urease hydrolysis. *Fresenius J. Anal. Chem.* 196, (1963) 248-251.
83. S. J. Updike, and G. P. Hicks. Reagentless substrate analysis with immobilized enzymes. *Science* 158, (1967) 270-272.
84. S. R. Betso, Michael H. Klapper, and L. B. Anderson. Electrochemical studies of heme proteins. Coulometric, polarographic, and combined spectroelectrochemical methods for reduction of the heme prosthetic group in cytochrome c. *J. Am. Chem. Soc.* 94, (1972) 8197-8204.
85. M. Hikuma, H. Obana, T. Yasuda, I. Karube, and S. Suzuki. A potentiometric microbial sensor based on immobilized *Escherichia coli* for glutamic acid. *Anal. Chim. Acta* 116, (1980) 61-67.
86. R. G. Nuzzo, and D. L. Allara. Adsorption of bifunctional organic disulfides on gold surfaces. *J. Am. Chem. Soc.* 105, (1983) 4481-4483.
87. H. Huck, and H.-L. Schmidt. Chloranil as a catalyst for the electrochemical oxidation of NADH to NAD⁺. *Angew. Chem. Int. Ed.* 20, (1981) 402-403.
88. B. Liedberg, C. Nylander, and I. Lunström. Surface plasmon resonance for gas detection and biosensing. *Sensor. Actuat.* 4 (1983) 299-304.
89. A. E. G. Cass, G. Davis, G. D. Francis, H. Allen O. Hill, W. J. Aston, I. John Higgins, E.V. Plotkin, L. D. L. Scott, and A. P. F. Turner. Ferrocene-mediated enzyme electrode for amperometric determination of glucose. *Anal. Chem.* 56, (1984) 667-671.

90. E. Csoeregi, D. W. Schmidtke, and A. Heller. Design and optimization of a selective subcutaneously implantable glucose electrode based on "wired" glucose oxidase. *Anal. Chem.* 67, (1995) 1240-1244.
91. T. Ikeda, F. Fushimi, K. Miki, and M. Senda. Direct bioelectrocatalysis at electrodes modified with D-gluconate dehydrogenase. *Agric. Biol. Chem.* 52, (1988) 2655-2658.
92. P. N. Bartlett, V. Q. Bradford, and R. G. Whitaker. Enzyme electrode studies of glucose oxidase modified with a redox mediator. *Talanta* 38, (1991) 57-63.
93. D. R. Thevenot, K. Toth, R. A. Durst, and G. S. Wilson. Electrochemical biosensors: recommended definitions and classification. *Pure Appl. Chem.* 71, (1999) 2333-2348.
94. C. Kurzawa, A. Hengstenberg, and W. Schuhmann. Immobilization method for the preparation of biosensors based on pH shift-induced deposition of biomolecule-containing polymer films. *Anal. Chem.* 74, (2002) 355-361.
95. R. L. Weinstein, S. L. Schwartz, R. L. Brazg, J. R. Bugler, T. A. Peyser, and G. V. McGarraugh. Accuracy of the 5-day free style navigator continuous glucose monitoring system comparison with frequent laboratory reference measurements. *Diabetes Care* 30, (2007) 1125-1130.
96. B. He, T. J. Morrow, and C. D. Keating. Nanowire sensors for multiplexed detection of biomolecules. *Curr. Opin. Chem. Biol.* 12, (2008) 522-528.
97. W.-C. Law, K.-T. Yong, A. Baev, and P. N. Prasad. "Sensitivity improved surface plasmon resonance biosensor for cancer biomarker detection based on plasmonic enhancement. *ACS nano* 5, (2011) 4858-4864.
98. J. C. Claussen, A. D. Franklin, A. Haque, D. M. Porterfield, and T. S. Fisher. Electrochemical biosensor of nanocube-augmented carbon nanotube networks. *ACS Nano* 3, (2009) 37-44.
99. H. Wang, R. Yang, L. Yang, and W. Tan. Nucleic acid conjugated nanomaterials for enhanced molecular recognition. *ACS nano* 3, (2009) 2451-2460.
100. V. A. Zamolo, G. Valenti, E. Venturelli, O. Chaloin, M. Marcaccio, S. Boscolo, V. Castagnola. Highly sensitive electrochemiluminescent nanobiosensor for the detection of palytoxin. *ACS nano* 6, (2012) 7989-7997.
101. S. Siddiqui, P. U. Arumugam, H. Chen, J. Li, and M. Meyyappan. Characterization of carbon nanofiber electrode arrays using electrochemical impedance spectroscopy: effect of scaling down electrode size. *ACS nano* 4, (2010) 955-961.
102. K. A. Mahmoud, S. Hrapovic, and J. H. T. Luong. Picomolar detection of protease using peptide/single walled carbon nanotube/gold nanoparticle-modified electrode. *ACS nano* 2, (2008) 1051-1057.

103. F. N. Ishikawa, H.-K. Chang, M. Curreli, H.-I. Liao, C. A. Olson, P.-C. Chen, R. Zhang. Label-free, electrical detection of the SARS virus N-protein with nanowire biosensors utilizing antibody mimics as capture probes. *ACS nano* 3, (2009) 1219-1224.
104. D. Luo, L. Wu, and J. Zhi. Fabrication of boron-doped diamond nanorod forest electrodes and their application in nonenzymatic amperometric glucose biosensing. *ACS nano* 3, (2009) 2121-2128.
105. B. G. Choi, H. Park, T. J. Park, M. H. Yang, J. S. Kim, S.-Y. Jang, N. S. Heo, S. Y. Lee, J. Kong, and W. H. Hong. Solution chemistry of self-assembled graphene nanohybrids for high-performance flexible biosensors. *ACS nano* 4, (2010) 2910-2918.
106. D. S. Lee, Y. Q. Fu, S. Maeng, X. Y. Du, S. C. Tan, J. K. Luo, and A. J. Flewitt. Integrated ZnO surface acoustic wave microfluidic and biosensor system. *Int. El. Devices Meet* (2007) 851-854.
107. S. K. Arya, M. Datta, and B. D. Malhotra. Recent advances in cholesterol biosensor. *Biosen. Bioelectron.* 23, (2008) 1083-1100.
108. M. Poirot, S. Silvente-Poirot and R. R. Weichselbaum, Cholesterol metabolism and resistance to tamoxifen. *Curr. Opin. Pharmacol.* 12, (2012) 683–689.
109. T. E. S. Faulin, M. C. C. Garcia, and D. S. P. Abdalla. Recent advances on detection of modified forms of low-density lipoproteins. *Recent Patents on Endocrine, Metabolic & Immune Drug Discovery* 3, (2009) 28-34.
110. T. Ahmadraji and A. J. Killard. The evolution of selective analyses of HDL and LDL cholesterol in clinical and point of care testing. *Anal. Methods* 5, (2013) 3612.
111. N. Ruecha, W. Siangproh and O. Chailapakul, A fast and highly sensitive detection of cholesterol using polymer microfluidic devices and amperometric system. *Talanta* 84, (2011) 1323-8.
112. P. R. Solanki, C. Dhand, A. Kaushik, A. A. Ansari, K. N. Sood, and B. D. Malhotra, Nanostructured cerium oxide film for triglyceride sensor, *Sensor. Actuat. B-Chem* 141, (2009) 551-556.
113. A. Kaushik, R. Pratima, K. Kaneto, C. G. Kim, S. Ahmad, and B. D. Malhotra Nanostructured iron oxide platform for impedimetric cholesterol detection. *Electroanalysis* 22, (2010) 1045–1055.
114. C. Dhand, P. R. Solanki, M. K. Pandey, M. Datta, and Bansi D. Malhotra. Electrophoretically deposited polyaniline nanotubes based film for cholesterol detection. *Electrophoresis* 31, (2010) 3754-62.

115. D. Mark, S. Haeberle, G. Roth, F. V. Stetten, and R. Zengerle. Microfluidic lab-on-a-chip platforms: requirements, characteristics and applications. *Chem. Soc. Rev.* 39, (2010) 1153-1182.
116. R. F. Ismagilov. Integrated microfluidic systems. *Angew. Chem. Int. Ed.* 42, (2003) 4130-4132.
117. A. Persat, M. E. Suss, and J. G. Santiago. Basic principles of electrolyte chemistry for microfluidic electrokinetics. Part II: Coupling between ion mobility, electrolysis, and acid–base equilibria. *Lab on a Chip* 9, (2009) 2454-2469.
118. A. E. Kamholz, and P. Yager. Theoretical analysis of molecular diffusion in pressure-driven laminar flow in microfluidic channels. *Biophys. J.* 80, (2001) 155-160.
119. N. Pamme. Magnetism and microfluidics. *Lab on a Chip* 6, (2006) 24-38.
120. Y. Z. Liu, B. J. Kim, and H. J. Sung. Two-fluid mixing in a microchannel. *Int. J. Heat Fluid Flow* 25, (2004) 986-995.
121. A. P. Sudarsan, and V. M. Ugaz. Fluid mixing in planar spiral microchannels. *Lab on a Chip* 6, (2006) 74-82.
122. J. Koo, and C. Kleinstreuer. Liquid flow in microchannels: experimental observations and computational analyses of microfluidics effects. *J. Micromech. Microeng.* 13, (2003) 568.
123. P. Gravesen, J. Branebjerg, and O. S. Jensen. Microfluidics-a review. *J. Micromech. Microeng.* 3, (1993): 168.
124. H. B. Squire. On the stability for three-dimensional disturbances of viscous fluid flow between parallel walls. *Proc. R. Soc. London* 142, (1933) 621-628.
125. C. Yang, and D. Li. Electrokinetic effects on pressure-driven liquid flows in rectangular microchannels. *J. Colloid Interface Sci.* 194, (1997) 95-107.
126. S. K. Sia, and G. M. Whitesides. Microfluidic devices fabricated in poly (dimethylsiloxane) for biological studies. *Electrophoresis* 24, (2003) 3563-3576.
127. R. Gorkin, J. Park, J. Siegrist, M. Amasia, B. S. Lee, J.-M. Park, J. Kim, H. Kim, Marc Madou, and Y.-K. Cho. Centrifugal microfluidics for biomedical applications. *Lab on a Chip* 10, (2010) 1758-1773.
128. V. Studer, A. Pepin, Y. Chen, and A. Ajdari. Fabrication of microfluidic devices for AC electrokinetic fluid pumping. *Microelectron. Eng.* 61, (2002) 915-920.
129. T. Thorsen, S. J. Maerkl, and S. R. Quake. Microfluidic large-scale integration. *Science* 298, (2002) 580-584.
130. T. M., Squires, and S. R. Quake. Microfluidics: Fluid physics at the nanoliter scale. *Rev. Mod. Phys.* 77, (2005) 977.

131. S. Jamal, and Y. K. Agrawal. Advances in microfluidics: Lab-on-a-chip to point of care diagnostic devices. *A. S. E. M.* 5, (2013) 385-394.
132. J. Yang, F. Lu, L. W. Kostiuk, and D. Y. Kwok. Electrokinetic microchannel battery by means of electrokinetic and microfluidic phenomena. *J. Micromech. Microeng.* 13, (2003) 963.
133. J. C. McDonald, and G. M. Whitesides. Poly (dimethylsiloxane) as a material for fabricating microfluidic devices. *Acc. Chem. Res.* 35, (2002) 491-499.
134. H. Becker, and L. E. Locascio. Polymer microfluidic devices. *Talanta* 56, (2002): 267-287.
135. Z. Nie, F. Deiss, X. Liu, O. Akbulut, and G. M. Whitesides. Integration of paper-based microfluidic devices with commercial electrochemical readers. *Lab on a Chip* 10, (2010) 3163-3169.
136. C. D. David, J. C. McDonald, O. J. A. Schueller, and G. M. Whitesides. Rapid prototyping of microfluidic systems in poly (dimethylsiloxane). *Anal. Chem.* 70, (1998) 4974-4984.
137. A. Plecis, and Y. Chen. Fabrication of microfluidic devices based on glass-PDMS-glass technology. *Microelectron. Eng.* 84, (2007) 1265-1269.
138. S. R. Quake, and Axel Scherer. From micro-to nanofabrication with soft materials. *Science* 290, (2000) 1536-1540.
139. D. Bodas, and C. K. Malek. Formation of more stable hydrophilic surfaces of PDMS by plasma and chemical treatments. *Microelectron. Eng.* 83, (2006) 1277-1279.
140. Y. Wu, Y. Huang, and H. Ma. A facile method for permanent and functional surface modification of poly (dimethylsiloxane). *J. Am. Chem. Soc.* 129, (2007) 7226-7227.
141. I. Wong and C.-M. Ho. Surface molecular property modifications for poly (dimethylsiloxane)(PDMS) based microfluidic devices. *Microfluid. Nanofluid.* 7, (2009) 291-306.
142. D. R. Thévenot, K. Toth, R. A. Durst, and G. S. Wilson. Electrochemical biosensors: recommended definitions and classification. *Biosens. Bioelectron.* 16, (2001) 121-131.
143. D. Grieshaber, R. MacKenzie, J. Vörös, and E. Reimhult. Electrochemical biosensors-Sensor principles and architectures. *Sensors* 8, (2008) 1400-1458.
144. J. Wang, Carbon-nanotube based electrochemical biosensors: A review. *Electroanalysis* 17, (2005) 7-14.
145. J. Wang, G. Rivas, X. Cai, E. Palecek, P. Nielsen, H. Shiraishi, N. Dontha. DNA electrochemical biosensors for environmental monitoring. A review. *Anal. Chim. Acta* 347, (1997) 1-8.

146. S. Mao, K. Yu, J. Chang, D. A. Steeber, L. E. Ocola, and J. Chen. Direct growth of vertically-oriented graphene for field-effect transistor biosensor. *Sci. Rep.* 3 (2013) 1-6.
147. J. S. Daniels, and N. Pourmand. Label-Free Impedance Biosensors: Opportunities and Challenges. *Electroanalysis* 19, (2007) 1239-1257.
148. J. A. Lee, S. Hwang, J. Kwak, S. Park, S. S. Lee, and K.-C. Lee. An electrochemical impedance biosensor with aptamer-modified pyrolyzed carbon electrode for label-free protein detection. *Sensor. Actuat. B-Chem.* 129, (2008) 372-379.
149. K.-H. Lee, J.-O. Lee, M.-J. Sohn, B. Lee, S.-H. Choi, S. K. Kim, J.-B. Yoon, and G.-H. Cho. One-chip electronic detection of DNA hybridization using precision impedance-based CMOS array sensor. *Biosens. Bioelectron.* 26, (2010)1373-1379.
150. R. Wang, C. Ruan, D. Kanayeva, K. Lassiter, and Y. Li. TiO₂ nanowire bundle microelectrode based impedance immunosensor for rapid and sensitive detection of *Listeria monocytogenes*. *Nano Lett.* 8, (2008) 2625-2631.
151. A. J. Haes, and R. P. V. Duyne. A nanoscale optical biosensor: sensitivity and selectivity of an approach based on the localized surface plasmon resonance spectroscopy of triangular silver nanoparticles. *J. Am. Chem. Soc.* 124, (2002) 10596-10604.
152. J. C. Riboh, A. J. Haes, A. D. McFarland, C. R. Yonzon, and R. P. V. Duyne. A nanoscale optical biosensor: real-time immunoassay in physiological buffer enabled by improved nanoparticle adhesion. *J. Phys. Chem. B* 107, (2003) 1772-1780.
153. J. Homola, S. S. Yee, and G. Gauglitz. Surface plasmon resonance sensors: review. *Sensor. Actuat. B-Chem.* 54, (1999) 3-15.
154. P. Pattnaik. Surface plasmon resonance. *Appl. Biochem. Biotechnol.* 126, (2005) 79-92.
155. J. Homola. Present and future of surface plasmon resonance biosensors. *Anal. Bioanal. Chem.* 377, (2003) 528-539.
156. B. Johnsson, S. Löfås, and G. Lindquist. Immobilization of proteins to a carboxymethyl-dextran-modified gold surface for biospecific interaction analysis in surface plasmon resonance sensors. *Anal. Biochem.* 198, (1991) 268-277.
157. B. N. Feltis, B. A. Sexton, F. L. Glenn, M. J. Best, M. Wilkins, and T. J. Davis. A hand-held surface plasmon resonance biosensor for the detection of ricin and other biological agents. *Biosens. Bioelectron.* 23, (2008) 1131-1136.
158. Y. Luo, F. Yu, and R. N. Zare. Microfluidic device for immunoassays based on surface plasmon resonance imaging. *Lab on a Chip* 8, (2008) 694-700.

159. G. G. Guilbault. Detection of formaldehyde with an enzyme-coated piezoelectric crystal detector. *Anal. Chem.* 55 (1983) 1682-1684.
160. S. Kumar, S. Kumar, M. A. Ali, P. Anand, V. V. Agrawal, R. John, S. Maji, and B. D. Malhotra. Microfluidic-integrated biosensors: Prospects for point-of-care diagnostics. *Biotechnol. J.* 8, (2013) 1267-1279.
161. H.-H. Hou, Y.-N. Wang, C.-L. Chang, R.-J. Yang, and L.-M. Fu. Rapid glucose concentration detection utilizing disposable integrated microfluidic chip. *Microfluid. Nanofluid.* 11, (2011) 479-487.
162. J. Yu, R. L. Roux, Y. Gu, K. Yunus, S. Matthews, J. G. Shapter, and A. C. Fisher. Integration of enzyme immobilised single-walled carbon nanotube arrays into microfluidic devices for glucose detection. *ICONN* (2008) 137-140.
163. A. Ali, A. A. Ansari, A. Kaushik, P.R. Solanki, A. Barik, M. K. Pandey, and B. D. Malhotra. Nanostructured zinc oxide film for urea sensor. *Mater. Lett.* 63, (2009) 2473-2475.
164. S. Srivastava, P. R. Solanki, A. Kaushik, M. A. Ali, A. Srivastava, and B. D. Malhotra. A self assembled monolayer based microfluidic sensor for urea detection. *Nanoscale* 3, (2011) 2971-2977.
165. R. K. Srivastava, S. Srivastava, T. N. Narayanan, B. D. Mahlotra, R. Vajtai, P. M. Ajayan, and A. Srivastava. Functionalized multilayered graphene platform for urea sensor. *ACS nano* 6, (2011) 168-175.
166. C. A. Rowe, S. B. Scruggs, M. J. Feldstein, J. P. Golden, and F. S. Ligler. An array immunosensor for simultaneous detection of clinical analytes. *Anal. Chem.* 71, (1999) 433-439.
167. A. Bange, H. B. Halsall, and W. R. Heineman. Microfluidic immunosensor systems. *Biosens. Bioelectron.* 20, (2005) 2488-2503.
168. S. R. Mikkelsen. Electrochemical biosensors for DNA sequence detection." *Electroanalysis* 8, (1996) 15-19.
169. X. Chen, Y.-H. Lin, J. Li, L.-S. Lin, G.-N. Chen, and H.-H. Yang. A simple and ultrasensitive electrochemical DNA biosensor based on DNA concatamers. *Chem. Commun.* 47, (2011) 12116-12118.
170. A. O. Olaniran, L. Hiralal, and B. Pillay. Whole-cell bacterial biosensors for rapid and effective monitoring of heavy metals and inorganic pollutants in wastewater. *J. Environ. Monit.* 13, (2011) 2914-2920.

171. M. Gerard, A. Chaubey, and B. D. Malhotra. Application of conducting polymers to biosensors. *Biosens. Bioelectron.* 17, (2002) 345-359.
172. P. R. Solanki, A. Kaushik, V. V. Agrawal, and B. D. Malhotra. Nanostructured metal oxide-based biosensors. *NPG Asia Mater.* 3, (2011) 17-24.
173. C.-C. Chang, N.-F. Chiu, D. S. Lin, Y. C.-Su, Y.-H. Liang, and C.-W. Lin. High-sensitivity detection of carbohydrate antigen using a gold/zinc oxide thin film surface plasmon resonance-based biosensor. *Anal. Chem.* 82, (2010) 1207-1212.
174. M. Ahmad, C. Pan, L. Gan, Z. Nawaz, and J. Zhu. Highly sensitive amperometric cholesterol biosensor based on Pt-incorporated fullerene-like ZnO nanospheres. *J. Phys. Chem. C* 114, (2009) 243-250.
175. F. Xiao, Y. Li, X. Zan, K. Liao, R. Xu, and H. Duan. Growth of metal-metal oxide nanostructures on freestanding graphene paper for flexible biosensors. *Adv. Funct. Mater.* 22, (2012) 2487-2494.
176. P. M. Levine, P. Gong, R. Levicky, and K. L. Shepard. Real-time, multiplexed electrochemical DNA detection using an active complementary metal-oxide-semiconductor biosensor array with integrated sensor electronics. *Biosens. Bioelectron.* 24, (2009) 1995-2001.
177. H. Kim, S. H. Yoon, H. N. Choi, Y. Lyu, and W. Lee. Amperometric glucose biosensor based on sol-gel-derived zirconia/nafion composite film as encapsulation matrix. *Bull. Korean Chem. Soc.* 27, no. 1 (2006): 65.
178. M.-A. Neouze, and U. Schubert. Surface modification and functionalization of metal and metal oxide nanoparticles by organic ligands. *Monatsh. Chem.-Chem. Month.* 139, (2008) 183-195.
179. S. N. S. A. Ayob, and U. Hashim. The synthesis and fabrication of Titanium dioxide nanowires-based biosensor. *ICSE* (2012) 145-148.
180. S.-J. Bao, C. M. Li, J.-F. Zang, X.-Q. Cui, Y. Qiao, and J. Guo. New nanostructured TiO₂ for direct electrochemistry and glucose sensor applications. *Adv. Funct. Mater.* 18, (2008) 591-599.
181. P. M. Chavhan, V. Reddy, and C. G. Kim. Nanostructured titanium oxide platform for application to ascorbic acid detection. *Int. J. Electrochem. Sci* 7, (2012) 5420-5428.
182. E., G. Jardinier, Pandraud, M. H. Pham, P. J. French, and P. M. Sarro. Atomic layer deposition of TiO₂ photonic crystal waveguide biosensors. *J. P. C. S* 187, (2009) 012043.
183. J. Li, S. Wang, I. M. Ayoub, and C. F. Yang. A TiO₂-sol-gel derived prussian blue nanoparticles-based glucose biosensor. In *Sensors Applications Symposium, IEEE* (2007) 1-6.

184. M. Liu, G. Zhao, Y. Tang, H. Shi, and N. Yang. Direct electrochemistry of hemoglobin on vertically aligned carbon hybrid TiO₂ nanotubes and its highly sensitive biosensor performance. *Chin. J. Chem.* 31, (2013) 215–220.
185. P. Si, Shujiang Ding, Jun Yuan, Xiong Wen Lou, and Dong-Hwan Kim. Hierarchically structured one-dimensional TiO₂ for protein immobilization, direct electrochemistry, and mediator-free glucose sensing. *ACS nano* 5, (2011) 7617-7626.
186. S. Carrara, V. Bavastrello, D. Ricci, E. Stura, and C. Nicolini. Improved nanocomposite materials for biosensor applications investigated by electrochemical impedance spectroscopy. *Sensor. Actuat. B-Chem.* 109, (2005) 221-226.
187. M. Tak, V. Gupta, and M. Tomar. Zinc oxide–multiwalled carbon nanotubes hybrid nanocomposite based urea biosensor. *J. Mater. Chem. B* 1, (2013) 6392-6401.
188. K.-J. Feng, Y.-H. Yang, Z.-J. Wang, J.-H. Jiang, G.-L. Shen, and R.-Q. Yu. A nano-porous CeO₂/Chitosan composite film as the immobilization matrix for colorectal cancer DNA sequence-selective electrochemical biosensor. *Talanta* 70, (2006) 561-565.
189. B. D. Malhotra, and A. Kaushik. Metal oxide–chitosan based nanocomposite for cholesterol biosensor. *Thin Solid Films* 518, (2009) 614-620.
190. A. Salimi, E. Sharifi, A. Noorbakhsh, and S. Soltanian. Immobilization of glucose oxidase on electrodeposited nickel oxide nanoparticles: direct electron transfer and electrocatalytic activity. *Biosen. Bioelectron.* 22, (2007) 3146-3153.
191. H. Pang, Q. Lu, Y. Zhang, Y. Li, and F. Gao. Selective synthesis of nickel oxide nanowires and length effect on their electrochemical properties. *Nanoscale* 2, (2010) 920-922.
192. X. Niu, Minbo Lan, Hongli Zhao, and Chen Chen. "Highly Sensitive and Selective Nonenzymatic Detection of Glucose Using Three-Dimensional Porous Nickel Nanostructures. *Anal. Chem.* 85, no. 7 (2013): 3561-3569.
193. T. Kavitha, and H. Yuvaraj. A facile approach to the synthesis of high-quality NiO nanorods: electrochemical and antibacterial properties. *J. Mater. Chem.* 21, (2011) 15686-15691.
194. S. Xiong, C. Yuan, X. Zhang, and Y. Qian. Mesoporous NiO with various hierarchical nanostructures by quasi-nanotubes/nanowires/nanorods self-assembly: controllable preparation and application in supercapacitors. *CrystEngComm* 13, (2011) 626-632.
195. S. K. Yadav, J. Singh, V. V. Agrawal, and B. D. Malhotra. Nanostructured nickel oxide film for application to fish freshness biosensor. *App. Phys. Lett.* 101, (2012) 023703-023703.
196. H. Muguruma. Amperimetric biosensor based on carbon nanotube and plasma polymer. (2010).

197. S. Timur, U. Anik, D. Odaci, and L. Gorton. Development of a microbial biosensor based on carbon nanotube (CNT) modified electrodes. *Electrochem. Commun.* 9, (2007) 1810-1815.
198. M. T. Martínez, Y.-C. Tseng, N. Ormategui, I. Loinaz, R. Eritja, and J. Bokor. Label-free DNA biosensors based on functionalized carbon nanotube field effect transistors. *Nano Lett.* 9, (2009) 530-536.
199. M. Abdolahad, M. Taghinejad, H. Taghinejad, M. Janmaleki, and S. Mohajezadeh. "A vertically aligned carbon nanotube-based impedance sensing biosensor for rapid and high sensitive detection of cancer cells. *Lab on a Chip* 12, (2012) 1183-1190.
200. J. Wang, Carbon-nanotube based electrochemical biosensors: A review. *Electroanalysis* 17, (2005) 7-14.
201. J. Prasek, J. Drbohlavova, J. Chomoucka, J. Hubalek, O. Jasek, V. Adam, and R. Kizek. Methods for carbon nanotubes synthesis—review. *J. Mater. Chem.* 21, (2011) 15872-15884.
202. P. Ayala, F. L. Freire Jr, L. Gu, David J. Smith, I. G. Solorzano, D. W. Macedo, J. B. V. Sande, H. Terrones, J. R.-Manzo, and M. Terrones. Decorating carbon nanotubes with nanostructured nickel particles via chemical methods. *Chem. Phys. Lett.* 431, (2006) 104-109.
203. Y. Zhu, H. I. Elim, Y.-L. Foo, T. Yu, Y. Liu, W. Ji, J.-Y. Lee. Multiwalled carbon nanotubes beaded with ZnO nanoparticles for ultrafast nonlinear optical switching. *Adv. Mater.* 18, (2006) 587-592.
204. W.-D. Zhang, J. Chen, L.-C. Jiang, Y.-X. Yu, and J.-Q. Zhang. A highly sensitive nonenzymatic glucose sensor based on NiO-modified multi-walled carbon nanotubes. *Microchim. Acta* 168, (2010) 259-265.
205. J. C. Claussen, A. D. Franklin, A. Haque, D. M. Porterfield, and T. S. Fisher. Electrochemical biosensor of nanocube-augmented carbon nanotube networks. *ACS Nano* 3, (2009) 37-44.
206. E. R. Pennell, and J. Pennell. *Lithography and lithographers: some chapters in the history of the art.* MacMillan Comapny, 1915.
207. Y. Xia, and G. M. Whitesides. Soft Lithography. *Angew. Chem. Int. Ed.* 37, (1998) 550 -575
208. M. Shikida, K. Sato, K. Tokoro, and D. Uchikawa. Surface morphology of anisotropically etched single-crystal silicon. *JMEMS* 10, (2000) 522.
209. B. Bahadur. *Liquid crystals: Applications and uses world scientific.* 1, (1990).183.
210. Z. Calahorra, E. Minami, R. M. White, and R. S. Muller. Reactive ion etching of indium tin oxide films. *J. Electrochem. Soc.* 136, (1989) 1839-1840.

211. H. Schmidt. Nanoparticles by chemical synthesis, processing to materials and innovative applications. *Appl. Organomet. Chem.* 15, (2001) 331-343.
212. B. H. Kim, M. J. Hackett, J. Park, and T. Hyeon, Synthesis, characterization, and application of ultrasmall nanoparticles. *Chem. Mater.* (2013).
213. L. L. Hench, and J. K. West. The sol-gel process. *Chem. Rev.* 90, (1990) 33-72.
214. H. Dislich. New routes to multicomponent oxide glasses. *Angew. Chem. Int. Ed.* 10, (1971) 363-370.
215. C.-C. Wang, and J. Y. Ying. Sol-gel synthesis and hydrothermal processing of anatase and rutile titania nanocrystals. *Chem. Mater.* 11, (1999) 3113-3120.
216. Y. Masuda and Kazumi Kato. Synthesis and phase transformation of TiO₂ nano-crystals in aqueous solutions. *Ceram. Soc. Jpn.* 117, (2009) 373-376.
217. C. H. Kim, J. W. Choi, H. J. Chun, and K. S. Choi. Synthesis of chitosan derivatives with quaternary ammonium salt and their antibacterial activity. *Polym. Bull.* 38, (1997) 387-393.
218. J. A. Dean. *Analytical Chemistry Handbook*. 2nd edition, McGraw-Hill, 2005.
219. S. Mohan, P. Srivastava, S. N. Maheshwari, S. Sundarb, and R. Prakash. Nano-structured nickel oxide based DNA biosensor for detection of visceral leishmaniasis (Kala-azar). *Analyst* 136, (2011) 2845-2851.
220. J. Singh, P. Kalita, M. K. Singh, and B. D. Malhotra, Nanostructured nickel oxide-chitosan film for application to cholesterol sensor. *App. Phys. Lett.* 98, (2011) 123702-123702.
221. P. Jeevanandam, and V. R. R. Pulimi. Synthesis of nanocrystalline NiO by sol gel and homogeneous precipitation method. *Indian J. Chem.* 51A, (2012) 586-590.
222. R. B. Mathur, S. Chaterjee, and B. P. Singh. Growth of carbon nanotubes on carbon fibre substrates to produce hybrid/phenolic composites with improved mechanical properties. *Compos. Sci. Technol.* 68, (2008) 1608-1615.
223. Skoog, A. Douglas, F. J. Holler, and T. A. Nieman. *Principles of instrumental analysis*. Principles of Instrumental Analysis, 6th edition, Thomson Brooks/Cole, 1998.
224. P. Griffiths, and J. A. de Hasseth, *Fourier Transform Infrared Spectrometry*. 2nd edition, Wiley-Blackwell, 2007
225. D. J. Gardiner. *Practical Raman spectroscopy*. Springer-Verlag, 1989.
226. R. Egerton. *Physical principles of electron microscopy*. Springer, 2005.

227. K.M. Lang, D. A. Hite, R. W. Simmonds, R. McDermott, D. P. Pappas, and J. M. Martinis. Conducting atomic force microscopy for nanoscale tunnel barrier characterization. *Rev. Sci. Instrum.* 75, (2004) 2726–2731.
228. R. Greenwood, and K. Kendall. *J. Eur. Ceram. Soc.* 19, (1999) 479–488.
229. J. F. Watts, and J. Wolstenholme. *An Introduction to Surface Analysis by XPS and AES.* Wiley & Sons, 2003.
230. A. J. Bard and L. R. Faulkner. *Electrochemical Methods Fundamentals and Applications.* 2nd edition. John Wiley & Sons, 2001.
231. R. S. Nicholson, and I. Shain. Theory of stationary electrode polarography. Single scan and cyclic methods applied to reversible, irreversible, and kinetic Systems. *Anal. Chem.* 36, (1964) 706–723.
232. Zoski, and G. Cynthia. *G. Handbook of Electrochemistry.* Elsevier Science, 2007.
233. F. Kremer, A. Schonhals and W. Luck. *Broadband Dielectric Spectroscopy.* Springer-Verlag, 2002.
234. Q. Li, G. Luo, J. Feng, Q. Zhou, L. Zhang, and Y. Zhu. Amperometric detection of glucose with glucose oxidase absorbed on porous nanocrystalline TiO₂ film. *Electroanalysis* 13, (2001) 5.
235. E. Topoglidis, A. E. G. Cass, G. Gilardi, S. Sadeghi, N. Beaumont, and J. R. Durrant. Protein adsorption on nanocrystalline TiO₂ films: An immobilization strategy for bioanalytical devices. *Anal. Chem.* 70, (1998) 5111.
236. J. Cui, D. Sun, S. Chen, W. Zhou, P. Hu, H. Liu, and Z. Huang. Enhancement of selective determination of the perfect match and mismatch of single nucleobases with a biosensing electrode based on surface-coarsened anatase TiO₂ nanobelts. *J. Mater. Chem.* 21, (2011) 10633-10636.
237. S. Yurdakal, G. Palmisano, V. Lodo, V. Augugliaro, L. Palmisano, Nanostructured rutile TiO₂ for selective photocatalytic oxidation of aromatic alcohols to aldehydes in water. *J. Am. Chem. Soc.* 130, (2008) 1568-1569.
238. D. Chen, F. Huang, Y.-B. Cheng, and R. A. Caruso. Mesoporous anatase TiO₂ beads with high surface areas and controllable pore sizes: a superior candidate for high-performance dye-sensitized solar cells. *Adv. Mater.* 21, (2009) 2206–2210.
239. Q. Li, G. Luo, J. Feng, Q. Zhou, L. Zhang, and Y. Zhu. Amperometric detection of glucose with glucose oxidase absorbed on porous nanocrystalline TiO₂ film. *Electroanalysis* 13, (2001) 5.

240. R. Wang, C. Ruan, D. Kanayeva, K. Lassiter, and Y. Li. TiO₂ nanowire bundle microelectrode based impedance immunosensor for rapid and sensitive detection of *Listeria monocytogenes*. Nano Letter. 8, (2008) 2625-2631.
241. A. Wisitsoraat, P. Sritongkham, C. Karuwan, D. Phokharatkul, T. Maturros, and A. Tuantranont, Fast cholesterol detection using flow injection microfluidic device with functionalized carbon nanotubes based electrochemical sensor. Biosens. Bioelectron. 26, (2010) 1514.
242. N. Ruecha, W. Siangproh, and O. Chailapakul, Polydimethylsiloxane microchip capillary electrophoresis for determination of cholesterol. J. Electron. Sci. Tech. 8, (2010) 82.
243. A. Parra, E. Casero, E. Pariente. L. Vazquez, and E. Lorenzo. Cholesterol oxidase modified gold electrodes as bioanalytical devices. Sens. Actuat. B 124, (2007) 30.
244. P. R. Solanki, A. Kaushik, A. A. Ansari, and B. D. Malhotra, Nanostructured zinc oxide platform for cholesterol sensor. Appl. Phy. Lett. 94, (2009) 143901.
245. S. Aravamudhan, N. S. Ramgir and S. Bhansali. Electrochemical biosensor for targeted detection in blood using aligned Au nanowires. Sens. Actuat. B 127, (2007) 29.
246. K.-J. Feng, Y.-H. Yang, Z.-J. Wang, J.-H. Jiang, G.-L. Shen, and R.-Q. Yu. A nano-porous CeO₂/chitosan composite film as the immobilization matrix for colorectal cancer DNA sequence-selective electrochemical biosensor, Talanta 70, (2006) 561–565.
247. A. Kaushik, Raju Khan, P. R. Solanki, P. Pandey, J. Alam, S. Ahmad, B.D. Malhotra, Iron oxide nanoparticles–chitosan composite based glucose biosensor. Biosen. Bioelectron. 24, (2008) 676–683.
248. A. Kaushik, P. R. Solanki, K. Kaneto, C. G. Kim, S. Ahmad, B. D. Malhotra. Nanostructured iron oxide platform for impedimetric cholesterol detection. Electroanalysis 22, (2010), 1045-1055.
249. B. D. Malhotra and A. Kaushik, Metal oxide-chitosan based nanocomposite for cholesterol biosensor. Thin Solid Films 518, (2009) 614-620.
250. A. A. Ansari, A. Kaushik, P. R. Solanki and B. D. Malhotra, Electrochemical cholesterol sensor based on tin oxide-chitosan nanobiocomposite. Electroanalysis, 21, (2009) 965.
251. R. Khan, A. Kaushik, P. R. Solanki, A. A. Ansari, M. K. Pandey. and B.D. Malhotra. Zinc oxide nanoparticles-chitosan composite film for cholesterol biosensor. Anal. Chem. Acta 616, (2008) 207.
252. H.-M. Kim, T. W. Kang, and K. S. Chung. Nanoscale ultraviolet-light-diodes using wide band gap gallium nitrides nanorodes. Adv. Mater. 15, (2003) 567.

253. Y. Huang, X. Duan, Y. Cui, L. J. Lauhon, K.-H. Kim, and C. M. Lieber. Logic gates and computation from assembled nanowire building blocks. *Science*, 294, (2001) 1313.
254. R. Wang, C. Ruan, D. Kanayeva, and K. Lassiter. TiO₂ nanowire bundle microelectrode based impedance immunosensor for rapid and sensitive detection of *Listeria monocytogenes*. *Nano Lett.* 8, (2008) 2625.
255. J. Kim, Z. Li, and I. Park. Direct synthesis and integration of functional nanostructures in microfluidic devices. *Lab Chip* 11, (2011) 1946.
256. J. Chen, J. Lib, and Y. Sun. Microfluidic approaches for cancer cell detection, characterization, and separation. *Lab Chip* 12, (2012) 1753.
257. J. Shi, A. P. Fang, L. Malaquin, A. Pépin, D. Decanini, J. L. Viovy, and Y. Chen, Highly parallel mix-and-match fabrication of nanopillar arrays integrated in microfluidic channels for long DNA molecule separation. *Appl. Phys. Lett.* 91, (2007) 153114.
258. M. Koto, P. W. Leu, and P. C. McIntyre, Vertical germanium nanowire arrays in microfluidic channels for charged molecule detection. *Journal of the Electrochemical Society* 156, (2009) K11.
259. C. Li, Y. Liu, L. Li, Z. Du, S. Xu, M. Zhang, X. Yin, and T. Wang, A novel amperometric biosensor based on NiO hollow nanospheres for biosensing glucose. *Talanta* 77, (2008) 455.
260. H. Pang, Q. Lu, Y. Zhang, Y. Li, and F. Gao. Selective synthesis of nickel oxide nanowires and length effect on their electrochemical properties. *Nanoscale* 2, (2010) 920
261. J.-W. Lang, L.-B. Kong, W.-J. Wu, Y.-C. Luo, and L. Kang. Facile approach to prepare loose-packed NiO nano-flakes materials for supercapacitors. *Chem. Commun.* (2008) 4213.
262. S. Aravamudhan, A. Kumar, S. Mohapatra, and S. Bhansali. Sensitive estimation of total cholesterol in blood using Au nanowires based micro-fluidic platform. *Biosens. Bioelectron.* 23, (2007) 2289.
263. P. Chandani, W. Chen, and A. Chandani. Flow injection amperometric enzyme biosensor for direct determination of organophosphate nerve agents. *Environ. Sci. Technol.* 35, (2001) 2562.
264. W. A. Collier, and A. L. Hart. Electrochemical detection in microfluidic devices. *Int. Conf. Sens. Tech.* (2005) 21.
265. Md. A. Ali, S. Srivastava, P. R. Solanki, V. V. Agrawal, R. John, and B. D. Malhotra. Nanostructured anatase-titanium dioxide based platform for application to microfluidics cholesterol biosensor. *Appl. Phys. Lett.* 101, (2012) 084105.
266. E. Manias. Nanocomposites: Stiffer by design. *Nat. Materials* 6, (2007) 9–11.

267. M. Y. Wing, Y. Zhongzhen, X. Xiaolin, Z. Qingxin, and M. A. Jun. Polymer nanocomposites and their applications. *HKIE Transactions* 10, (2003) 67-73.
268. C. Hansen, and S. R. Quake. Microfluidics in structural biology: smaller, faster, better. *Curr. Opin. Struct. Biol.* 13, (2003) 538–544.
269. A. G. Crevillen, M. Avilla, M. Pumera, M. C. Gonzalez, and A. Escarpa. Food analysis on microfluidic devices using ultrasensitive carbon nanotubes detectors. *Anal. Chem.* 79, (2007) 7408–7415.
270. R. Bashir, BioMEMS: state-of-the-art in detection, opportunities and prospects. *Adv. Drug. Deliv. Rev.* 56, (2004) 1565–1586.
271. Q. Fu, and J. Liu. Integrated single-walled carbon nanotube/microfluidic devices for the study of the sensing mechanism of nanotube sensors. *J. Phys. Chem. B* 109, (2005) 13406–13408.
272. W. Wei, A. Sethuraman, C. Jin, N. A. Monteiro-Riviere, and R. J. Narayan. Biological properties of carbon nanotubes. *J. Nanosci. Nanotechnol.* 7, (2007) 1284–97.
273. X. Chen, G. S. Lee, A. Zettl, and C. R. Bertozzi. Biomimetic engineering of carbon nanotubes by using cell surface mucin mimics. *Angew. Chem. Int. Ed.* 43, (2004) 6111–6.
274. K. Balasubramanian, and M. Burghard. Chemically functionalized carbon nanotubes. *Small* 1, (2005) 180–192.
275. K. Balasubramanian, and M. Burghard. Biosensors based on carbon nanotubes. *Anal. Bioanal. Chem.* 385, (2006) 452–468.
276. Y. Lin, C. A. Timchalk, D. W. Matson, H. Wu, and K. D. Thrall. Integrated microfluidics/electrochemical sensor system for monitoring of environmental exposures to lead and chlorophenols. *Biomed. Microdevices* 3, (2001) 331–338.
277. Y. Zhu, H. I. Elim, Y.-L. Foo, T. Yu, Y. Liu, W. Ji, J.-Y. Lee, Z. Shen, A. T. S. Wee, J. T. L. Thong, and C.H. Sow. Multiwalled carbon nanotubes beaded with ZnO nanoparticles for ultrafast nonlinear optical switching. *Adv. Mater.* 18, (2006) 587–592.
278. M. Shim, N. W. S. Kam, R. J. Chen, Y. Li, and H. Dai. Functionalization of carbon nanotubes for biocompatibility and biomolecular recognition. *Nano Lett.* 2, (2002) 285–288.
279. D. Tasis, N. Tagmatarchis, A. Bianco, and M. Prato. Chemistry of carbon nanotubes. *Chem. Rev.* 106, (2006) 1105–1136.
280. S. K. Vashist, D. Zheng, K. Al-Rubeaan, J. H. T Luong, and F.-S. Sheu. Advances in carbon nanotube based electrochemical sensors for bioanalytical applications. *Biotech. Adv.* 29, (2011) 169–188.

281. Md. A. Ali, S. srivastava. P. R. Solanki, V. V. Agrawal, R. John, and B. D. Mlhotra. A highly efficient microfluidic nano biochip based on nanostructured nickel oxide. *Nanoscale* 5, (2013) 2883–2891.
282. W.-D. Zhang, J. Chen, L.-C. Jiang, Y.-X. Yu, and J.-Q. Zhang. A highly sensitive nonenzymatic glucose sensor based on NiO-modified multi-walled carbon nanotubes. *Microchim. Acta* 168, (2010) 259–265.
283. W.-D. Zhang, B. Xu, and L.-C. Jiang. Functional hybrid materials based on carbon nanotubes and metal oxides. *J. Mater. Chem.* 20, (2010) 6383–6391.
284. J. Chen, W.-D. Zhang, and J.-S. Ye, Nonenzymatic electrochemical glucose sensor based on MnO_2 /MWNTs nanocomposite. *Electrochem. Commun.* 10, (2008) 1268–1271.
285. Y. Zhang , S. F. Ali , E. Dervishi, Y. Xu , Z. Li , D. Casciano, and A. S. Biris. Cytotoxicity effects of graphene and single-wall carbon nanotubes in neural phaeochromocytoma-derived PC12 cells. *ACS Nano*, 4, (2010) 3181–3186.
286. X. Tan, M. Li, P. Cai, L. Luo, and X. Zoua, An amperometric cholesterol biosensor based on multiwalled carbon nanotubes and organically modified sol-gel/chitosan hybrid composite film. *Anal. Biochem.* 337, (2005) 111–120.
287. A. Umar, M. M. Rahman, M. Vaseem, and Y.-B. Hahn. Ultra-sensitive cholesterol biosensor based on low-temperature grown ZnO nanoparticles. *Electrochem. Commun.* 11, (2008) 118–121.
288. R. S. Dey and C. R Raj. Development of an amperometric cholesterol biosensor based on graphene-Pt nanoparticle hybrid material. *J. Phys. Chem. C* 114, (2010) 21427–21433.
289. M. Guo. J. Chen, J. Li, L. Nie, and S. Yao. Carbon nanotubes-based amperometric cholesterol biosensor fabricated through layer-by-layer technique. *Electroanalysis* 16, (2004) 23.

Publications (thesis)

1. **Md. Azahar Ali**, S. Srivastava, P. R. Solanki, V. Reddy, V. V. Agrawal, C. Kim, R. John, B. D. Malhotra, Highly efficient bienzyme functionalized nanostructured nickel oxide–multiwalled carbon nanotubes composite biochip integrated with microfluidics for cholesterol detection, **Nature: Scientific Reports** 2013, 3 : 2661, DOI: 10.1038/srep02661, (IF:2.9).
2. **Md. Azahar Ali**, P. R. Solanki, M.K. Patel, H. Dhayani, V.V. Agrawal, R. John, B. D. Malhotra, Highly efficient microfluidics nano biochip based on nanostructured nickel oxide, **Nanoscale**, 2013, 5, 2883-2891 (IF: 6.23).
3. **Md. Azahar Ali**, S. Srivastava, P. R. Solanki, V V Agrawal, R. John and B. D. Malhotra, Nanostructured anatase-titanium dioxide based platform for application to microfluidics cholesterol biosensor, **Applied Physics Letters**, 2012, 101, 084105 (IF: 3.79).
4. S. Dev, S. Kumar, **Md. Azahar Ali**, P. Anand, V. V. Agrawal, R. John, B. D. Malhotra, Microfluidics-integrated biosensors: prospects for point-of-care diagnostics, **Biotechnology Journal**, 2013, 8, 11, (IF: 3.46).
5. **Md. Azahar Ali**, S. Srivastava, M. K. Pandey V. V. Agrawal, R. John, B. D Malhotra, Protein–conjugated quantum dots interface: binding kinetics and label free lipid detection, **Analytical Chemistry**, 2014, 86 (3), 1710–1718 (IF: 5.6).
6. **Md. Azahar Ali**, K. Kamil Reza, S. Srivastava, M. K. Pandey V. V. Agrawal, R. John, B. D Malhotra, Functionalized reduced graphene oxide based interface for label free low density lipoprotein detection, **Langmuir**, 2014, 30 (14), 4192–4201 (IF: 4.1).
7. **Md. Azahar Ali**, P. R. Solanki, S. Singh, S. Srivastava, V. V. Agrawal, R. John, B. D. Malhotra, Nanostructured carbon nanotubes-nickel oxide platform: cell proliferation, electrochemistry and immuno chip application, to be communicated.
8. **Md. Azahar Ali**, S. Srivastava, P. M. Chavhan, V. V. Agrawal, R. John, B. D. Malhotra, Surface functionalized antase titania composite based biochip: microfluidics, electrochemistry and biomedical application, to be communicated.
9. **Md. Azahar Ali**, Ved V Agrawal, Renu John, Bansi D Malhotra, Bioconjugated CdS QDs-nickel oxide nanorods platform for low density lipoprotein detection, to be communicated.
10. **Md. Azahar Ali**, N. Singh, S. Srivastava, V. V. Agrawal, R. John, B. D. Malhotra, Carbon Nanotubes Based Nanocomposite for Low Density Lipoprotein Detection. **Applied Biochemistry and Biotechnology**, Under Review.

Publications (not included in thesis)

1. **Md. Azahar Ali**, C. Singh, V. V. Agrawal, R. John, B. D. Malhotra, Reduced graphene oxide based nanocomposite platform for low density lipoprotein detection, to be communicated.

2. R. Sharma, **Md. Azahar Ali**, N. Selvi, V. Singh, R. Sinha, Ved V. Agrawal, Electrochemically assembled gold nanostructures platform: electrochemistry, kinetic analysis and biomedical application, **The Journal of Physical Chemistry C**, 2014, 118 (12), 6261–6271 (IF: 4.8).
3. P. R. Solanki, S. Srivastava, **Md. Azahar Ali**, R. K. Srivastava, G. Sumana, A. Srivastava, B. D. Malhotra, Protein conjugated reduced graphene oxide-titania platform for label-free biosensor application, **Biosensor and Bioelectronics**, Under review (IF: 5.4).
4. B. D. Malhotra, S. Srivastava, **Md. Azahar Ali**, C. Singh, Carbon nanomaterials based biosensors for food toxins detection, **Applied Biochemistry and Biotechnology**, 2014, Accepted (IF: 1.8).
5. S. Srivastava, **Md. Azahar Ali**, S. Omrao, U. Parashar, A. Srivastava, G. Sumana, S. S. Pandey, S. Hayase, B. D. Malhotra, Graphene oxide based biosensor for food toxin detection, **Applied Biochemistry and Biotechnology**, 2014, Accepted, (IF: 1.8).
6. K. Mondal, **Md. Azahar Ali**, V. V. Agrawal, B. D. Malhotra, A. Sharma, Highly sensitive biofunctionalized mesoporous nanofibers based interface for biomedical application, **ACS Applied Material Interface**, 2014, 6, 2516–2527 (IF: 5.008).
7. P. R. Solanki, **Md. Azahar Ali**, A. Kaushik, B.D. Malhotra, Label-free capacitive immunosensor based on nanostructured cerium oxide, **Advanced Electrochemistry**, 2014, 1, 1-6, doi:10.1166/adel.2014.1016.
8. P. R. Solanki, **Md. Azahar Ali**, Ved V. Agrawal, A. K. Srivastava, R. K. Kotnala, B. D. Malhotra, Highly sensitive biofunctionalized nickel oxide nanowires based immunosensor for cholera detection, **RSC Advances**, 2013, 3 (36), 16060 – 16067 (IF: 2.56).
9. M. K. Patel, **Md. Azahar Ali**, S. Srivastava, V. V. Agrawal, S.G. Ansari, B. D. Malhotra, Magnesium oxide grafted carbon nanotubes based impedimetric genosensor for biomedical application, **Biosensors and Bioelectronics**, 50 (2013) 406–413 (IF: 5.4).
10. C. Singh, S. Srivastava, **Md. Azahar Ali**, T. K. Gupta, G. Sumana, A. Srivastava, R. B. Mathur, B. D. Malhotra, Carboxylated multiwalled carbon nanotubes based biosensor for aflatoxin detection, **Sensors & Actuators B**, 2013, 185, 258–264 (IF: 3.5).
11. M. K. Patel, **Md. Azahar Ali**, V. V. Agrawal, Z. A. Ansari, B. D. Malhotra, S. G. Ansari, Nanostructured magnesium oxide biosensing platform for cholera detection, **Applied Physics Letters**, 2013, 102, 144106 (IF: 3.79).
12. A. C. Roy, Nisha V. S., C. Dhand, **Md. Azahar Ali**, B. D. Malhotra, Molecularly imprinted polyaniline-polyvinyl sulphonic acid composite based sensor for para-nitrophenol detection, **Analytical Chimica Acta**, 2013, 777, 63–71 (IF: 4.3).
13. M. K. Patel, **Md. Azahar Ali**, Md. Zafaryab, V. V. Agrawal, M. M. A. Rizvi, Z. A. Ansari, S. G. Ansari, B. D. Malhotra, Biocompatible nanostructured magnesium oxide-chitosan platform for genosensing applications, **Biosensors and Bioelectronics**, 2013, 45, 181–188 (IF: 5.4).
14. S. Srivastava, V. Kumar, **Md. Azahar Ali**, P. R. Solanki, A. Srivastava, G. Sumana, P. S. Saxena, B. D. Malhotra, Electrophoretically deposited reduced graphene oxide platform for food toxin detection, **Nanoscale**, 2013, 5, 3043-3051(6.23).
15. S. Srivastava, **Md. Azahar Ali**, P.R. Solanki, P.M. Chavhan, M. K. Pandey, A. Mulchandani, A. Srivastava and B. D. Malhotra, Mediator-free microfluidics biosensor based on titania–zirconia nanocomposite for urea detection, **RSC Advances**, 2013, 3, 228 (IF: 2.56).

16. S. Srivastava, P. R. Solanki, A. Kaushik, **Md. Azahar Ali**, A. Srivastava, B. D. Malhotra, A Self assembled monolayer based Microfluidic sensor for urea detection, **Nanoscale**, 2011, 3, 2971-7 (IF: 6.23).
17. H. Dhyani, **Md. Azahar Ali**, M. K. Pandey, B.D. Malhotra and P. Sen, Electrophoretically deposited CdS quantum dots based electrode for biosensor application, **J. Mater. Chem.**, 2012, 22, 4970 (IF: 6.1).
18. **Md. Azahar Ali**, A. Ansari, A. Kaushik, P. Solanki, A. Barek, B. D. Malhotra, Nanostructured Zinc Oxide Film for Urea Sensor” **Materials Letters**, 2009, 63, 2473–2475 (IF: 2.22).
19. Abdul Barik, P R. Solanki, A. Kaushik, **Md. Azahar Ali**, M. K. Pandey, B. D. Malhotra. Ponyaniline- carboxymethyl cellulose nanocomposite for cholesterol detection, **J. Nanosci. Nanotechnol.**, 2010, 10, 6479-88 (IF: 1.9).
20. Anees A Ansari, **Md. Azahar Ali** and B. D. Malhotra, Electrochemical Urea Biosensor Based on Sol-gel Derived Nanostructured Cerium Oxide, **Journal of Physics: Conference Series**, 2012, 358, 012006
21. Hemant Dhyani, Saurabh Srivastava, **Md. Azahar Ali**, B. D. Malhotra and Prasenjit Sen, Fabrication of nanocrystalline CdS electrode via chemical bath deposition technique for application to cholesterol sensor, **Journal of Physics: Conference Series**, 2012, 358, 012008.
22. P. Nath, M. Datta, A. Barik, **Md. Azahar Ali**, H. K. Singh , A K. Kalita, P Datta, Cobalt chloride doped polymer film for relative humidity measurement, **Proc. of SPIE**, 2008, 662404.

Conferences

1. **Md. Azahar Ali**, V. V. Agrawal, R. John, B D Malhotra, India-Japan Workshop on Biomolecular Electronics & Organic Nanotechnology for Environment Preservation (IJWBME -2013), Department of Biotechnology, Delhi Technological University, Delhi, India, December, 13-15, 2013
2. **Md. Azahar Ali**, V. V. Agrawal, R. John, B D Malhotra, National Conference on Biomedical Science and Technology-2013, CSIR-National Physical Laboratory, November, 21-22, 2013
3. **Md. Azahar Ali**, R. John, V.V. Agrawal, B D Malhotra, NATIONAL SEMINAR ON PHYSICS AND TECHNOLOGY OF SENSORS (NSPTS-2013), Jamia Milia Islamia, New Delhi, India, March 11-13 , 2013.
4. **Md. Azahar Ali**, R. John, V.V. Agrawal, B D Malhotra, National symposium on Nanobiotechnology (NSNT-2012), Indian Institute of Technology Mandi, Himachal Pradesh, India, June, 1-2 , 2012.
5. **Md. Azahar Ali**, V. V. Agrawal, R. John, B D Malhotra, India-Japan Workshop on Biomolecular Electronics & Organic Nanotechnology for Environment Preservation (IJWBME -2011), Department of Electrical Engineering and Computer Science, University of Hyogo, Himaji, Japan, Dec-7, 2011.
6. Pratima R. Solanki, **Md. Azahar Ali**, B D Malhotra, National symposium on Nanobiotechnology (NSNT-2012), IIT Mandi, Himachal Pradesh, India, June, 1-2 , 2012.
7. M. K. Patel, **Md. Azahar Ali**, P. R. Solanki, V.V. Agrawal, S. G. Ansari, and B.D. Malhotra, International Conference on Bio-Materials and Implants: Prospects & Possibilities In the New Millennium (BIO-2011), Central Glass and Ceramic Research Institute (CGCRI), Kolkata, INDIA, 21-23 July 2011.

8. **Md. Azahar Ali**, A. A. Ansari, A. Barik, B. D. Malhotra, APAM (1^{8th}) organized at National Physical Laboratory, New Delhi, India.